

University of  
**Strathclyde**  
**Glasgow**

Microfluidic Flow of Colloidal Particles  
in Nematic Liquid Crystals

Magdalena Lesniewska

A thesis presented for the degree of  
Doctor of Philosophy

Department of Physics  
University of Strathclyde  
United Kingdom

2024

# Declaration of Authenticity and Author's Rights

This thesis is the result of the author's original research. It has been composed by the author and has not been previously submitted for examination which has led to the award of a degree.

The copyright of this thesis belongs to the author under the terms of the United Kingdom Copyright Acts as qualified by University of Strathclyde Regulation 3.50. Due acknowledgement must always be made of the use of any material contained in, or derived from, this thesis.

Chapter 5 describes work that has been published in the research article [1]. Chapter 6 describes work presented in the research article [2]. The results contained in the published research articles are the author's original research in collaboration with the article's co-authors, namely Professor Nigel Mottram and Dr Oliver Henrich.

Signed:

Date:



# Acknowledgements

I would like to take the opportunity to deeply thank my supervisors Dr Oliver Henrich and Prof Nigel Mottram for their guidance and support throughout my studies. Thank you, Oliver, for your enthusiasm, and for your boundless soft matter and software development knowledge. Thank you, Nigel, for your extensive knowledge of and connections in the liquid crystal field, and for always knowing what to say. Thank you both for your unwavering belief in me, and for going above and beyond.

I would also like to acknowledge the support from the United Kingdom Engineering and Physical Sciences Research Council (EPSRC), the University of Strathclyde, the Scottish Universities Physics Alliance (SUPA), the HPC facilities ARCHER, Cirrus, and Archie-West.

And last but not least, I would like to thank all my friends and family who have been there for me through this experience. There are too many of you to name, and I would not be where I am without you. A special mention goes to Mónica and Laurine: while the path of our doctoral journeys has diverged, our friendship never did.

# Abstract

This thesis presents the result of research conducted on the behaviour of colloidal particles in nematic liquid crystal flow for a wide range of parameters in microfluidic channels and ducts. We study the change in structure of defects and molecular orientation around a static particle, particle migration in microfluidic channels, morphology of Saturn ring defects and director structure in ducts of comparable size to the particle, and many particle migration and advection in large scale systems of differing colloidal densities. We observe elongation of the defect lines around a static colloidal particle, novel positional control of individual colloidal particle and also colloidal densities in microchannels through tunable driving pressure, and non monotonic dependence of the differential velocity of particle and fluid in highly confined ducts on Ericksen number.

# Contents

<b>1</b>	<b>Introduction</b>	<b>1</b>
1.1	Liquid crystal fluids . . . . .	1
1.2	Microfluidics and rheology . . . . .	3
1.3	Motivation and aims . . . . .	4
1.4	Thesis outline . . . . .	5
<b>2</b>	<b>Theory of liquid crystals</b>	<b>7</b>
2.1	History of the mesophase . . . . .	7
2.1.1	Liquid crystal categories . . . . .	10
2.2	Modelling of nematic phases . . . . .	11
2.3	Molecular order . . . . .	14
2.3.1	Notation . . . . .	15
2.4	Q-tensor . . . . .	17
2.5	Frank Oseen elastic energy . . . . .	19
2.6	Landau de Gennes theory . . . . .	22
2.6.1	Nematic to isotropic phase transition . . . . .	23
2.6.2	Landau de Gennes free energy . . . . .	26
2.7	Boundary conditions . . . . .	26
2.7.1	Surface anchoring . . . . .	26
2.8	Topological defects . . . . .	30
2.9	Viscosity . . . . .	32
2.10	Fluid dynamics . . . . .	34

2.10.1	Basic theory of fluid dynamics . . . . .	34
2.10.2	Beris-Edwards model . . . . .	39
2.10.3	Dimensionless numbers . . . . .	43
2.11	Nematic liquid crystal colloids . . . . .	46
2.12	Experimental background of liquid crystal microfluidics . . . . .	49
<b>3</b>	<b>Simulation methods</b>	<b>53</b>
3.1	Fluid dynamics and simulation approaches . . . . .	53
3.1.1	Boltzmann equation . . . . .	55
3.2	Lattice Boltzmann method: an outline . . . . .	56
3.2.1	Connecting the lattice Boltzmann equation to the Navier Stokes equations . . . . .	61
3.2.2	A simple lattice Boltzmann algorithm . . . . .	62
3.3	Discretisation in velocity . . . . .	63
3.3.1	Velocity Sets . . . . .	68
3.4	Discretisation in space and time . . . . .	72
3.5	Boundary conditions . . . . .	82
3.6	Liquid crystal inclusion . . . . .	85
3.6.1	Landau de Gennes . . . . .	85
3.7	<i>Ludwig</i> code . . . . .	86
3.7.1	Parameter Mapping to Physical Units . . . . .	89
3.7.2	Using <i>Ludwig</i> . . . . .	90
3.7.3	Technical limitations . . . . .	91
<b>4</b>	<b>Static particle in liquid crystal flow</b>	<b>93</b>
4.1	Simulation set up . . . . .	93
4.2	Homeotropic wall anchoring . . . . .	95
4.2.1	Defect structure . . . . .	97
4.2.2	Director field . . . . .	103
4.3	Summary . . . . .	110

<b>5</b>	<b>Particle migration in liquid crystal flow</b>	<b>112</b>
5.1	Simulation set up . . . . .	112
5.2	Particle migration . . . . .	114
5.2.1	Segré Silberberg effect . . . . .	114
5.2.2	Migration in a nematic . . . . .	116
5.2.3	Force effects . . . . .	123
5.3	Summary . . . . .	127
<b>6</b>	<b>Particle advection in confined liquid crystal flow</b>	<b>129</b>
6.1	Simulation set up . . . . .	129
6.2	Defect structure influenced by the director and fluid velocity fields . . .	133
6.3	Advection behaviour . . . . .	146
6.4	Summary . . . . .	149
<b>7</b>	<b>Many particle liquid crystal flow</b>	<b>151</b>
7.1	Simulation set up . . . . .	151
7.2	Particle Migration . . . . .	153
7.2.1	Low colloidal density . . . . .	154
7.2.2	High colloidal density . . . . .	157
7.3	Colloid velocity and defects . . . . .	161
7.4	Summary . . . . .	167
<b>8</b>	<b>Conclusions and Future work</b>	<b>169</b>
8.1	Conclusions . . . . .	169
8.2	Future Work . . . . .	171
<b>A</b>	<b>Chapman-Enskog analysis</b>	<b>173</b>
A.1	Connecting the lattice-Boltzmann and Navier Stokes equations . . . . .	173
<b>B</b>	<b>Hermite Polynomials</b>	<b>180</b>
B.1	Expansion of the equilibrium and particle distribution functions . . . . .	180



# Chapter 1

## Introduction

### 1.1 Liquid crystal fluids

Fluids of all types are commonly present in every day life, with water being an example of a fluid vital to all forms of life on Earth. Functionally, water is a simple fluid which in classical terms is defined as a system of atoms or molecules whose microscopic interactions with each other depend on their relative distances [3]. The question of simplicity is an interesting one from a philosophical perspective - which meaningful measures should be taken to define what is a simple fluid can vary[4] as initial assumptions can lead to differing results. Simplicity in the macroscopic behaviour of a liquid is usually described through its equation of state, viscosity, and diffusion constant. Since Sir Isaac Newton originated the concept of viscosity, fluids that can be categorised through the relationship between the shear stress and the rate of strain are often called Newtonian and non-Newtonian [5]. For Newtonian (viscous) fluids the stress is directly proportional to the rate of strain and for non-Newtonian fluids that is not the case. Complex fluids that is, mixtures that coexist between two or more phases, exhibit non-Newtonian behaviour through their nonlinear response to shear. They are common with many biological compounds, food items, and personal care products exhibiting non-Newtonian behaviour. The properties of a complex fluid also include high disorder and clustering on multiple length scales. Complex fluid behaviour has its uses

in engineering applications, for example small amounts of polymers in water can reduce turbulent drag [6], reducing the power needed to be used. As a result of the geometrical constraints, the mechanical response in complex fluids results in solid-like and fluid-like behaviour at different times. Generally, at short time scales, solid properties manifest more, while at long timescales (anywhere from seconds to days) the overall flow behaviour is more visible. The differences in the time scales are a feature of this non-linear mechanical response (i.e. deformation) of complex fluids under shear stress leading them to be termed as ‘viscoelastic’ [7]. A viscoelastic material is one that has both viscous and elastic responses when subjected to deformation resulting in time-dependent strain, leading to the its defining properties of hysteresis on the stress-strain curve, occurrence of stress relaxation and creep, and the strain rate influencing the stiffness of the material.

Liquid crystals are an intermediate state of matter with characteristics between an ordered solid phase (like a crystal) and a disordered liquid phase (isotropic). Standard viscoelastic liquids are isotropic, while liquid crystals are anisotropic due to their spontaneously broken internal symmetry [8]. As such, liquid crystals have properties arising from both their hydrodynamic properties as complex fluids, and their anisotropy due to inherent order present in the geometry. This internal orientational order affects the elasticity, viscosity, and other physical properties of the liquid crystals. Those properties are crucial for varied kinds of applications, the most well known being liquid crystal displays [9]. For a long time this single application has dominated the international research efforts of the field in academic and industrial research contexts. Due to the commercial success of liquid crystal display technology and their development in the 1970s, modern day display research is mainly done in industrial settings. Academic liquid crystal science has moved away from display to other uses in nano-/micro manipulation, novel composites, and biotechnology [10] creating emerging novel research with new kinds of potential applications. Flow of such anisotropic fluids gives rise to investigations into spectacular phenomena resulting from the competing viscous, elastic, and inertial effects.



## 1.2 Microfluidics and rheology

As suggested by the title of this thesis, the research presented here falls into the category of microfluidic rheology. Microfluidics is a science of systems that process small amounts ( $10^{-9} - 10^{-18}$  liters) of fluids using small channels with sizes of tens to hundreds of micrometers [11]. Such confinements can be capillaries, channels, ducts or networks of such geometries. Microfluidics exploits its most obvious characteristic — small size — to offer a fundamentally new control capability over concentrations of molecules in space and time. Since its development in the 1990s [12] microfluidics has seen increased interest in many fields of modern science and technology. This has resulted in contributions to growing interdisciplinary research - joining together physics, chemistry, biology, and engineering into a common platform of interest. The main advantage of microfluidics is the ability of precise control and manipulation of flows. Through a variety of methods [12] systems with high precision can be fabricated, including morphological structures if required, that allow for flow manipulation. These systems include micro-pumps, micro-valves, guiding paths etc. [13], which can subsequently can be put together to created large scale networks with differing complexity to create lab-on-a-chip devices [14].

Rheology is a branch of physics that deals with the deformation and flow of materials that have a complex microstructure, and whose viscosity changes with the strain rate (the relative flow velocity) [5]. Hence, it focuses on the non-Newtonian fluids by characterizing functions needed to relate the stresses with the rate of change of strain. In functional terms, rheology aims to extend continuum mechanics to describe the flow of materials combining elastic, viscous and plastic behaviour. As the response to stress of such materials can be very different, this allows for abundant investigations into novel phenomena exhibited by the complex non-Newtonian flow.

### 1.3 Motivation and aims

Liquid crystals have fascinated generations of scientists from the time of their discovery in the late 19<sup>th</sup> century[15]. This interest and focus has undergone many transformations over the last century, going from the initial investigations into fundamental properties through to the ubiquity of liquid crystal displays in the modern world. While liquid crystals were synthesised for their commercially viable properties and behaviours in the display fields, there is still more to be discovered about their characteristics in other contexts.

Here, we focus on exploring the liquid crystalline behaviour when introducing colloidal particles to the region. The liquid crystal therefore acts as a unique, due to its anisotropy and non-Newtonian properties, continuous phase that affects the dispersed particles. Activity and interest in such combination of particles and liquid crystals has been growing over the last 25 years [10] becoming a well-established and fast-growing area of soft matter research [16]. Early research explored ways of creating new types of dense soft materials based on liquid crystal and colloid composites [17] [18], with later studies focusing on creating structures within a liquid crystal environment. In general, one of the main goals of colloidal science is to imitate the diversity of atomic element organisation to obtain structured composite materials through self-assembly (i.e. local interactions of disordered states leading to organised structures without external direction). Self-organization of colloidal nanometer- and micrometer-sized particles dispersed in a liquid crystal is a promising approach [16]. To this end, there were a number of experimental studies of different types of colloids looking at the possibilities of self-assembly [19] [20] [21] and interactions between the colloidal particles in the liquid crystal environment [22] [23] [24] [25] [26]. The emerging scientific understanding shows promise for significant new discoveries and applications. Using the fundamental knowledge of self-assembly in complex fluids could lead to applications such as metamaterial and photonic crystal fabrication, or energy conversion.

The field of nematic colloidal composites is well established with studies done through experiments, simulations and theory. However, fully three dimensional sim-

ulations of microfluidic flows including nematic liquid crystals and colloidal particles are uncommon. What initially started as an investigation of large scale microfluidics of colloid-liquid crystal composite materials by the thesis author lead to a focus on individual particle behaviour. As the highly complex large scale flows have many interconnected phenomena happening at the same time, it is important to be able to focus on individual effects before being able to accurately attribute the contributing factors of bulk behaviour. Hence, the goal of the thesis is to achieve a fundamental level of understanding of novel phenomena occurring in microfluidic flow of colloidal particles in nematic liquid crystals. This will be achieved through contemporary simulations of such systems. This leads to twofold project aims: to define the factors strongly influencing particle migration and to better understand liquid crystal defect behaviour in flow. The potential impacts of this work include the stimulation of further experimental activity and developing mechanisms of particle migration control.

## 1.4 Thesis outline

This thesis is divided into eight chapters. Chapter 2 serves as an introduction to liquid crystal theory, an introduction into fluid dynamics, and theoretical description of the rheology of nematic liquid crystal colloids. Chapter 3 focuses on the lattice Boltzmann simulation method and the inclusion of a particular solver (*Ludwig*) that includes the fluid dynamics, liquid crystal properties and incorporates the colloidal particles into its model. The *Ludwig* code is used in the thesis to investigate the complex behaviour of nematic liquid crystals colloids.

Chapters 4, 5, 6, 7 present the main results of this thesis. Chapter 4 discusses the behaviour of a liquid crystal with a fixed spherical particle subjected to flow. We will focus on the defect behaviour and influence of the anchoring type on the system. The novel findings include the elongation of defects and In Chapter 5 we shall examine the behaviour of a dynamic particle placed in a channel resulting in controllable migration. Order-flow interactions facilitated by the defect structure will be of particular interest. This lead to the observation of novel positional control of a colloidal particle, and was

subsequently published [1]. This poses future possibilities for tailored particle separation. Chapter 6 will present an investigation into the effects of confinement on a single particle in a duct. We aim to investigate the effect of defects on the advection behaviour of colloidal particles and address some knowledge gaps related to the combination of the pressure driven flow and moderate to large confinement. Finally, Chapter 7 will present early research on large scale systems of colloidal liquid crystal flows. The investigation into the large scale colloidal systems is rarely conducted. We aim to change that by providing a foundation level of insight into the novel effects occurring in such systems including particle migration and percolating clusters of colloidal particles.

Chapter 8 shall conclude the thesis with final remarks on the work done in the previous results chapters. We will summarise the individual chapter findings with original contributions from the thesis author, suggest the different directions the research could be expanded upon in future work, and highlight the potential applications.

## Chapter 2

# Theory of liquid crystals

### 2.1 History of the mesophase

The three most commonly known states of matter are solid, liquid, and gas with substances able to transition between the different states by changes in temperature or pressure. While useful, this classification is simplified and not generally accurate for many substances. A liquid crystal (LC) phase is a state of matter with properties between that of a solid and a liquid. Liquid crystals are in fact examples of mesophases (also: mesomorphic phases), as they are intermediate states of matter. Even though they can flow, they still possess some kind of internal ordering and certain optical responses that makes them akin to crystals - the name liquid crystal is an expression trying to tie those ideas together. In most basic terms it can be looked at as a phase of a material made up of elongated rod-like or disk-like molecules that on average has some preferred orientation. Not all materials have a mesophase and the occurrence of the phases is dependant on the temperature or solvent concentration. The temperature dependent phases, also called thermotropic LCs, are the ones focused on in this work. When a solid is heated up until it melts into an isotropic liquid it may go through the liquid crystal phase (or phases) with the transition temperatures depending on the material used. When talking about an isotropic liquid in this context, it means that there is no average orientation of the molecules, whereas an anisotropic liquid would

be one where an average orientation can be defined. This change of internal ordering is shown in Fig. 2.1, with the molecules being graphically represented as ellipsoids.

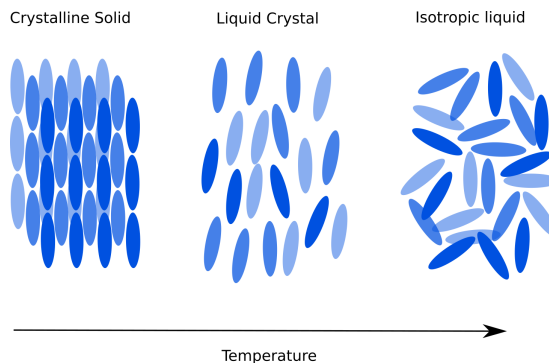


Figure 2.1: Phase transition from a solid to an isotropic liquid with increasing temperature (left to right). Liquid crystal mesophase exists within a temperature range dependent on material characteristics, with some materials going through different types, for example smectic and nematic.

The discovery of liquid crystals is credited to a botanist Friedrich Reinitzer, who reported his observations of two melting points of cholesteryl benzoate in 1888. While heating up the solid at room temperature material, it turned into a cloudy liquid at  $144.5^\circ$  and at  $178.5^\circ$  became transparent [15]. The cloudy liquid was subsequently called a cholesteric liquid crystal, and in later years alternatively described as a chiral nematic liquid crystal. The higher melting point is now referred to as the clearing point. Reintizer recognized some connection of his work to the work of Otto Lehmann, and established correspondence to talk about his experiments. Lehman then constructed an instrument with a polarising microscope with a precise temperature control stage, allowing him to observe the similarities in properties of his samples and the ones received from Reinitzer. Over time he was convinced that the opaque phase in his experiments was a distinct and uniform phase of matter, with properties somewhere between liquids and solids. Lehmann seems to be the first to use the term ‘flowing crystal’ to describe this type of materials in 1889 and 1900, and also introduced the general term ‘liquid crystal’ which is now commonplace. His work was influential in the field, and a French research group continued to run their own experiments eventually culminating with a classification scheme presented in 1922 by Georges Freidel. This scheme proposed

categorisation into 3 different types: nematic, smectic, and cholesteric [27].

At the same time as German scientists were conducting research on this interesting state of matter, the subject also became of interest to Friedel around 1907. In 1922, he contributed a 200 page work on the ‘Mesomorphic States of Matter’ to ‘Annales des Physiques’ which established in depth terminology for the description of what he called the mesomorphic phases of matter. He was against using the oxymoronic colloquial term ‘liquid crystal’, and instead favoured using the term ‘mesophase’, believing it more sound and accurate. There have been further critiques of using the colloquial name liquid crystal instead of the apt mesophase by Prost and de Gennes, in their ‘The Physics of Liquid Crystals’ [8]. While in some fields of chemistry ‘mesophase’ became the prevalent term, it seems that the ‘liquid crystal’ prevails in both academic and popular science circles. During the 1930s and 1940s more work was done, focusing on elastic properties, and effects of magnetic and electric fields [28]. In the post war years liquid crystals became quite niche as there were no applications of them at the time and the existing textbooks did not mention them.

Then, in the 1960s there was renewed interest in the materials in places like the United Kingdom, the United States, and the Soviet Union, perhaps wanting to find some application for these unusual materials. During that time, an American chemist Glenn Brown founded the Liquid Crystal Institute at Kent State University and in the same year organised the first International Liquid Crystal Conference which continues biennially to this day attracting scientists from all over the world to discuss their research [29]. A continent away, a British chemist George Gray published a full length book on liquid crystals based on his reliable and systematic investigations relating the structures of the liquid crystals with their behaviour and properties. It is said that no other author in the history of the subject has published about more new liquid crystals [30]. He and his team at Hull University were instrumental in developing novel liquid crystals for flat-panel displays in the 1970s [31]. Igor G. Chistyakov was instrumental in the revival and further development of the field in the USSR, establishing laboratories and a research group first in Ivanovo and later in Moscow. Advancement of the field was rapid and consequential, with the first demonstration of a liquid crystal display

creating pressure to further develop the technology.

Further work by Vorländer in 1974 outlined the fundamental discovery of rod-like molecules being a critical condition for observance of two melting points. Future studies expand the vital condition to be that of molecular anisotropy, as disc-like and banana-like molecules that have two melting points have been found since. The assumption of rod-like molecules was instrumental for the theoretical description of liquid crystals, as the resulting molecular structure approach became to mathematically describe the materials as rod-like. This approach is still prevalent today, in conjunction with more complex descriptions of molecular shapes.

### 2.1.1 Liquid crystal categories

There are various types of the LC phases and different ways of categorising them, with the main three types distinguished by the main factors that have an effect on the orientation of the molecules. Thermotropic liquid crystals go through phase changes with variation in temperature, lyotropics exhibit phase transitions due to temperature and concentration in a solvent, and metallotropic do so as a function of temperature and the organic to inorganic ratio. In this work, we focus on thermotropic liquid crystals. As mentioned before, they exhibit liquid crystalline behaviour as a function of temperature, with each material having a specific range. If it is heated up above it, the material will behave as an isotropic liquid, when cooled below the threshold usually it will form a crystal. Different materials can go through a number of different liquid crystal phases as temperature is increased before transitioning to a conventional isotropic. The possible phases include nematic, smectic, cholesteric, blue and others.

The nematic phase is the simplest case, with the molecules having long-range orientational order, but no positional order. Nematics are commonly uniaxial, with the average direction of the main axis being called the ‘director’. As for their properties, nematics are readily influenced by external electric and magnetic fields, and due to their optical responses they are commonly used in liquid crystal displays.

Smectic phases, as well as possessing orientational order, are positionally ordered in one direction, forming layers that can glide over each other. As usual, the different



types of smectic phases are distinguished by the degrees of positional and orientational order. The most well known smectics include smectic A and C, with molecules inside the layers arranged parallel to the normal in the former, and tilted away from it in the latter.

Cholesterics exhibit chirality, that is handedness, named after being initially observed in cholesterol compounds. In this phase, the molecules twist in a direction perpendicular to the director and possess long-range order. Alternatively, they are also referred to as chiral nematics. In this phase, the distance over which the molecules go through a full  $360^\circ$  is called the chiral pitch,  $p$ . As the molecules are modelled to be uniaxial, the same pattern is repeated every half pitch. The length of the pitch changes with, for example, temperature, making it tunable. Together with some unique optical properties, cholesterics have been used for many applications such as light modulators, UV detectors, dye lasers, and luminescent displays [32].

The differences in between the different phases can be observed under a microscope and due to the birefringence of the materials visually stunning images can be obtained as shown in Fig. 2.2.

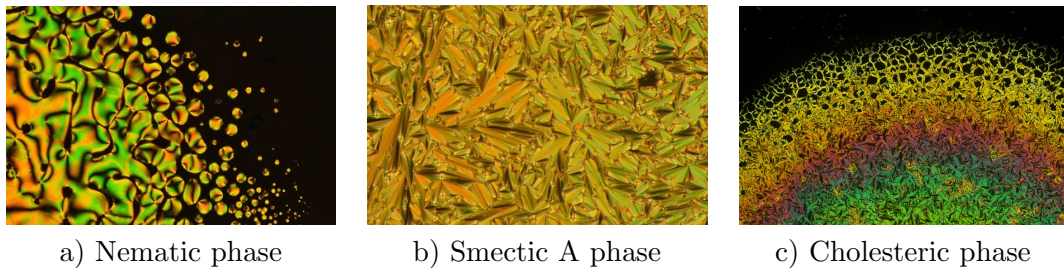


Figure 2.2: Microscopic images of liquid crystal a) nematic, b) smectic A, and c) cholesteric phases. Reproduced with permission from Vance Williams, Department of Chemistry, Simon Fraser University [33]

## 2.2 Modelling of nematic phases

Molecular order is just one of the properties of liquid crystals. In this thesis we focus on the nematic phase specifically, and now we will explore different ways of describing it theoretically. Modelling liquid crystals in a mathematically rigorous way comes with

challenges and there are different theoretical models of various accuracy that can be used. In general, simpler models are advantageous as they are easier to understand and implement but lose a lot of accuracy. More complex approaches can result in great accuracy, but require more computational resources to fully resolve. At the most basic level, fluids can either be treated as made up of individual molecules or as a continuum medium giving rise to different ways of modelling depending on how the material is described. As such, depending on the approach used, the models are referred to by their approach giving rise to molecular models [34, 35] or continuum models [8, 36]. Following on the experimental work on the at the time recently discovered mesophases, Oseen laid the groundwork for the theoretical underpinnings and description of what is now accepted as the continuum theory of liquid crystals [37]. This static continuum theory used a unit vector, called the director, to describe the average local direction preferred by the nematic molecules. This was based on a common understanding that the molecules of nematics have a degree of local ordering, which direction was called the anisotropic axis [36]. The director formulation can account for properties such as anisotropic elasticity, body forces, and surface effects. Through its simplicity and ease of use, it is still commonly used today [36].

The work of Oseen on the static theory was then further expanded upon by Frank in 1958 [38], into what is now called the Oseen-Frank theory. This theory can be applied to many problems that involve nematic phases [36, 37], and has been particularly advantageous due to its ability to describe the Fréedericksz transition. The Fréedericksz transition is a phase transition effect occurring for an undisturbed liquid crystal subjected to a sufficiently strong electric or magnetic field. It is named in honour of the Russian/Soviet physicist Vsevolod Fréedericksz (whose name is sometimes also romanised as Frederiks). Well below the threshold, there is no observed change in the orientation of the director, with the nematic sample orienting itself according to its preferred alignment in the undisturbed state. As the magnitude of the field is gradually increased from the critical value (called the Fréedericksz threshold), the director attempts to twist until it aligns with the applied electric or magnetic field. Through this transition three different configurations can occur, called the splay, twist,

and bend.

While the static Oseen-Frank theory is very useful and widely applied, more work needed to be done to develop a dynamic continuum theory of nematics. Such a theory requires the inclusion of the viscoelastic properties of liquid crystals into the model, maintaining the conservation laws and also general dynamics. In his 1961 publication [39], Ericksen laid out the balance laws for the conservation of linear and angular momentum. A couple of years later, Leslie formulated the constitutive equations first for anisotropic fluids [40] and then for liquid crystals [41]. The resultant theory using the descriptions of these balance laws was then named the Ericksen-Leslie theory, and it uses the conservation of mass, linear and angular momentum to describe the pairing of the director, the fluid velocity, and fluid pressure [36]. Early corroboration of this theory was done by Atkin [42] in 1970 for flow of a nematic due to a pressure gradient in both a stationary capillary tube and two coaxial stationary tubes. The scaling accomplished in Atkin's work was consistent with experimental observations of Fisher and Frederickson [43] made a year earlier for nematic flow between coaxial cylinders. The resulting Ericksen-Leslie theory has been in use for various problems involving flow, electric and magnetic fields, and free surfaces [36].

A notable complication of both the Oseen-Frank static theory and the Ericksen-Leslie dynamic theory is the challenge in describing the so-called defects (or disclinations) that are present in liquid crystals. A disclination in a liquid crystal is a type of topological defect where the rotational symmetry is violated, meaning that the director is undefined in a particular position. It is important to keep in mind that these defects are not flaws in a material that can be fixed, but rather an important feature of nematics. These defects have a profound role to play and influence the behaviour and properties of a system in which they occur. Ericksen proposed a continuum model that includes disclinations [44] in 1991, that expanded the understanding of moving defects. At the time the static theory of point defects was well developed as described in for example the survey by Kinderlehrer [45]. The general static theory for the nematic phase that includes the director and the resulting defects is based on the Q-tensor formulation that is the foundation of the Landau de Gennes theory [8]. It considers the

the behaviour of the director and the variable referred to as the scalar order parameter, the latter describing the propensity of the molecules to align with the director. A comprehensive review of the background and development of the continuum model can be found in [46], while the mathematical underpinnings are reviewed in detail in [47]. An adaptation of the Landau de Gennes theory into a dynamic form is called the Beris-Edwards theory, based on the equation of the same name [48].

For additional particulars of the history and development of mathematical models used to describe liquid crystals, an interested reader is guided to a review by Carlsson and Leslie [37]. The systems in this thesis are dynamic and fully three dimensional, using the Beris-Edwards approach for the behaviour of the nematic phase. Nonetheless, it is important to have a good understanding of the static theory as well as the dynamic adaptation in order to recognise how the systems in this thesis are modelled.

## 2.3 Molecular order

As liquid crystals exhibit some amount of orientational order, a common way to describe this is to define a unit vector  $\mathbf{n}$  called a director which gives the direction of the average molecular orientation. For rod-like molecules, this will be the average orientation of the long axis. The director can vary over time. Therefore, the director is both space and time dependent. To measure the level of orientation about the director it is standard to use a scalar order parameter  $S$ , which is equal to 0 in a disordered phase, and nonzero otherwise. It is defined as the weighted average of the molecular orientation angle  $\theta$  between the long axis and the director

$$S = \frac{1}{2} \langle 3 \cos^2 \theta - 1 \rangle = \frac{1}{2} \int (3 \cos^2 \theta - 1) f(\theta) dV, \quad (2.1)$$

where  $\langle \rangle$  is the thermal average, and  $f(\theta)$  is the statistical orientational distribution function. As mentioned before when  $S = 0$  the internal order is fully disordered and indicates an isotropic phase. The maximum value of  $S$  is +1, which happens when all molecules are perfectly aligned along the director. When all molecules are perfectly

aligned perpendicularly to the director,  $S = -\frac{1}{2}$ , meaning that the order parameter  $S$  is bound by the interval  $[-\frac{1}{2}, 1]$ . This measure of order is an appropriate approximation in most cases, with Eq. (2.1) being a second order Legendre polynomial. In some cases, for example where higher accuracy is required, a higher order polynomial should be used. Connecting the  $S$  values to real-world scenarios, for a liquid crystal in equilibrium it is more usual for the order parameter to be positive, and a typical  $S$  value in the middle of the phase region might be  $S = 0.6$  [47].

By using a rod-like model to describe the ordering, there are two possibilities for how the material might behave - biaxially or uniaxially. In a biaxial system, there is no axis of rotation that does not cause a change in the system, while a uniaxial system has a symmetry axis. Uniaxiality is common in liquid crystals, and usually for modelling purposes it is assumed. The uniaxiality leads to birefringence, as there are different refractive indices observed perpendicularly and in parallel to the optical axis. For biaxial materials, this leads to trirefringence with three unique refractive indices for the three orthogonal directions.

### 2.3.1 Notation

With vectors being ubiquitous in the mathematical description of liquid crystals, the question of notation and commonly used convention needs exploring. In the literature both direct vector and index notations are used. In many cases, for the purposes of brevity, the Einstein summation convention is used. For a given vector  $\mathbf{a}$ , it can be expressed by its components and a set of basis vectors  $\{\mathbf{e}_1, \mathbf{e}_2, \mathbf{e}_3\}$  in  $\mathbb{R}^3$ , such that

$$\mathbf{a} = a_1\mathbf{e}_1 + a_2\mathbf{e}_2 + a_3\mathbf{e}_3 = \sum_{i=1}^3 a_i\mathbf{e}_i. \quad (2.2)$$

The terms  $a_i, i = 1, 2, 3$  are the Cartesian components of  $\mathbf{a}$ . The sum in Eq. (2.2) can be expressed as

$$\mathbf{a} = a_i\mathbf{e}_i \quad (2.3)$$

with the underlying assumption that the repeated index  $i$  is summed over, and obeys the following rule; when any index appears twice (and only twice) in the same term summation is implied over all the contributions of that index using all of its possible values. This is the Einstein summation convention, and can be used for vectors, matrices, and tensors. We can further introduce a set of useful quantities written in the summation convention - the Kronecker delta  $\delta_{ij}$  and the alternator  $\epsilon_{ijk}$ , with  $i, j, k$  each being able to take values from 1 to 3. The Kronecker delta is defined by

$$\delta_{ij} = \begin{cases} 1 & \text{if } i = j, \\ 0 & \text{if } i \neq j, \end{cases} \quad (2.4)$$

and the alternator is defined by the following

$$\epsilon_{ijk} = \begin{cases} 1 & \text{if } i, j \text{ and } k \text{ are unequal and in cyclic order,} \\ -1 & \text{if } i, j \text{ and } k \text{ are unequal and in non-cyclic order,} \\ 0 & \text{if any two of } i, j \text{ or } k \text{ are equal.} \end{cases} \quad (2.5)$$

Some examples using the above definitions are:  $\delta_{13} = 0$ ,  $\delta_{11} = 1$ ,  $\epsilon_{123} = \epsilon_{321} = \epsilon_{312} = 1$ ,  $\epsilon_{132} = \epsilon_{213} = \epsilon_{321} = -1$ ,  $\epsilon_{221} = 0$ . A particularly effective result that ties the Kronecker delta and the alternator is

$$\epsilon_{ijk}\epsilon_{ipq} = \delta_{jp}\delta_{kq} - \delta_{jq}\delta_{kp}, \quad (2.6)$$

and it is generally called the contraction rule for alternators. Another widely used convention is: when including partial derivatives with respect to some variable, place a comma before it. For example  $m_{,i}$  means a partial derivative of some quantity  $m$  with respect to the  $i^{\text{th}}$  variable, and  $b_{i,j}$  means the partial derivative of the  $i^{\text{th}}$  component of some vector  $\mathbf{b}$  with respect to the  $j^{\text{th}}$  variable.

## 2.4 Q-tensor

An alternative approach used to describe the internal order of a liquid crystal is by using a tensor order parameter, rather than a scalar. The advantage of using a tensor over a scalar is that it has an additional dimension and can in this case be used to describe collective ordering in space. To achieve this, let us consider a Cartesian system of coordinates with a director  $\mathbf{n}$  parallel to the  $z$ -axis. The orientation of individual molecules, described by some vector  $\mathbf{s}$ , that can be parameterised by

$$s_1 = \sin \theta \cos \phi, \quad s_2 = \sin \theta \sin \phi, \quad \text{and} \quad s_3 = \cos \theta \quad (2.7)$$

where  $\theta$  and  $\phi$  are the angular deviations of the molecule along the polar and azimuthal directions respectively. The probability  $d\Psi$  of finding the molecule oriented within a solid angle  $d\Omega$  is given by

$$d\Psi = \frac{1}{4\pi} f(\theta, \phi) d\Omega \quad (2.8)$$

where  $f(\theta, \phi)$  is the distribution function describing the general state of the molecular orientation. For uniaxial nematics, that are axially symmetric about the director  $\mathbf{n}$ ,  $f(\theta, \phi) = f(\theta)$  holds true. In fact, the distribution function  $f(\theta)$  can be expanded by using the Legendre polynomials to form a sum

$$f(\theta) = \sum_{n=0}^{\infty} f_n P_n(\cos(\theta)). \quad (2.9)$$

The term  $P_n(x)$  is the  $n^{\text{th}}$  Legendre polynomial and

$$f_n = \frac{2n+1}{2} \int_{-1}^1 f(\theta) P_n(\cos(\theta)) d(\cos \theta). \quad (2.10)$$

Operating under the assumption of uniaxiality, that is  $\mathbf{s} = -\mathbf{s}$ , it means that  $f(\theta) = f(\pi - \theta)$ . As such, the non-zero contributions will be due to even terms alone, with

$f_0 = 1$  Hence, the scalar order parameter  $S$  is defined by a quadrupolar term

$$S = \frac{1}{5}f_2 = \frac{1}{2} \int_{-1}^1 f(\theta)P_2(\cos \theta)d(\cos \theta) = \langle P_2(\cos \theta) \rangle . \quad (2.11)$$

Through this definition, the scalar order parameter lies within the interval  $-\frac{1}{2} \leq S \leq 1$ , with  $S = 1$  meaning all molecules being perfectly aligned along the director  $\mathbf{n}$ ,  $S = 0$  indicating the case with an isotropic state with no order, and the lower bound  $S = -\frac{1}{2}$  that all the molecules are aligned along a plane perpendicular to the director. This information can be expressed by a single variable, by combining the director field  $\mathbf{n}$ , with the degree of local order  $S$  into a second-rank tensor. Following convention, it is called the Q-tensor, and it describes both the degree of local order and the director. It is obtained by looking at the orientational probability function, in terms of  $S$ , up the second order

$$f(\theta) = 1 + 5SP_2(\cos \theta) = 1 + \frac{5}{2}S(3(\mathbf{n} \cdot \mathbf{s})^2 - 1) \quad (2.12)$$

$$= 1 + \frac{5}{2}S(3n_\alpha n_\beta - \delta_{\alpha\beta})s_\alpha s_\beta = 1 + 5Q_{\alpha\beta}s_\alpha s_\beta \quad (2.13)$$

where Q-tensor is described as

$$Q_{\alpha\beta} = \frac{S}{2}(3n_\alpha n_\beta - \delta_{\alpha\beta}). \quad (2.14)$$

with  $\delta_{\alpha\beta}$  being the Kronecker delta. For the director  $\mathbf{n}$ , the Cartesian components are given by  $n_\alpha$  and  $\alpha = 1, 2, 3$ . Einstein summation notation is used in Eq. (2.14), and this is a traceless uniaxial tensor with the largest eigenvalue  $S$  going along the director. When adding external electric or magnetic fields the local ordering may no longer be uniaxial and instead be in a biaxial form [49], which can be described by

$$Q_{\alpha\beta} = \frac{S}{2}(3n_\alpha n_\beta - \delta_{\alpha\beta}) + \frac{P}{2}(e_\alpha^{(1)}e_\beta^{(1)} - e_\alpha^{(2)}e_\beta^{(2)}) \quad (2.15)$$

as the two degenerate eigenvalues become different. In the expression above,  $e^{(1)}$  is a unit vector along the symmetry axis of the molecule,  $e^{(2)} = \mathbf{n} \times e^{(1)}$  is the secondary



director, while  $P = \langle \sin^2 \theta \cos(2\Phi) \rangle$ . In a biaxial case, the order parameter is a real, symmetric, and traceless tensor that has three distinct eigenvalues. The first is equal to  $S$ , the same as in a uniaxial case, with the corresponding eigenvector along the director. The director field specifies the direction of the largest tensor eigenvalue. The other two eigenvalues are  $-\frac{1}{2}(S + P)$  and  $-\frac{1}{2}(S - P)$ , with the complementary eigenvectors specifying the orientation and the biaxiality  $P$  of the order parameter tensor. The biaxiality  $P$  describes the loss of uniaxiality and the discontinuity of the rotational symmetry around the director. The possible values of  $P$  lie in the interval  $[-\frac{3}{2}, +\frac{3}{2}]$ , with unique values of  $P = 0$  reproducing the uniaxiality and  $|P| = \frac{3}{2}$  meaning the complete ordering along the secondary director  $\mathbf{e}^{(1)}$ . In bulk, the recognized nematic phases are uniaxial however local biaxiality can and does develop in confined nematics - especially in the cores of topological defects. This means that the tensorial ordering field displays non-trivial behaviour.

## 2.5 Frank Oseen elastic energy

In a nematic with no external influences the uniform director orientation comes from the global minimum of its free energy. The expression for the free energy can include the director. This director, upon which the static theory of liquid crystals is based, can be expressed by the unit director field  $\mathbf{n}$ . Since it is a unit vector,  $\mathbf{n} \cdot \mathbf{n} = 1$ . This mean alignment has some amount of elasticity, and it is known that in the liquid crystal tends to return to its initial uniform alignment after the removal of disturbances [36]. Therefore, the assumption is that there exists a free energy density associated with the distortions of the anisotropy such that

$$\omega = \omega(\mathbf{n}, \nabla \mathbf{n}), \quad (2.16)$$

where  $\nabla = (\frac{\partial}{\partial x}, \frac{\partial}{\partial y}, \frac{\partial}{\partial z})$ , with a total elastic free energy being given by

$$\mathcal{F} = \int_V \omega(\mathbf{n}, \nabla \mathbf{n}) dV. \quad (2.17)$$

The additional assumptions include the incompressibility of the liquid crystal, that is a constant mass density and the uniaxiality of the director implying that  $\omega(\mathbf{n}, \nabla \mathbf{n}) = \omega(-\mathbf{n}, -\nabla \mathbf{n})$ . Following the approach adopted by Frank [38], a local system of Cartesian coordinates  $x, y, z$  is introduced, with  $z$  parallel to  $\mathbf{n}_0 = (0, 0, 1)$ . Small changes in any direction induce three possible types of changes in orientation that lead to six components of curvature. These fundamental distortions about the equilibrium state lead to

$$\omega = k_i a_i + \frac{1}{2} k_{ij} a_i a_j \quad \text{for } i, j = 1, \dots, 6. \quad (2.18)$$

The distortions are usually referred to as splay, twist, and bend, with their components given by

$$\text{splay: } a_1 = \frac{\partial n_1}{\partial x}, \quad a_6 = \frac{\partial n_2}{\partial y} \quad (2.19)$$

$$\text{twist: } a_2 = \frac{\partial n_1}{\partial y}, \quad a_4 = \frac{\partial n_2}{\partial x} \quad (2.20)$$

$$\text{bend: } a_3 = \frac{\partial n_1}{\partial z}, \quad a_5 = \frac{\partial n_2}{\partial z} \quad (2.21)$$

with  $k_i$  and  $k_{ij}$  being the curvature constants [36]. Using further assumptions of indifference of frame under reflection or rotation, and also the invariance of the nematic phase the elastic curvature constants most of them will be equal to zero [36]. The remaining elastic constants are known as the Frank elastic constants  $k_{11}, k_{22}, k_{33}, k_{24}$ . Commonly they are rewritten as

$$K_1 = k_{11}, \quad K_2 = k_{22}, \quad K_3 = k_{33}, \quad K_4 = k_{24}. \quad (2.22)$$

We can now join the Frank elastic curvature constants and the six fundamental distortions  $a_i$  to obtain the free energy density. This bulk free energy density is called the Frank-Oseen elastic energy density and becomes

$$\omega = \frac{1}{2}(K_1 - K_2 - K_4)n_{i,j}n_{j,j} + \frac{1}{2}K_2n_{i,j}n_{i,j} + \frac{1}{2}K_4n_{i,j}n_{j,i} + \frac{1}{2}(K_3 - K_2)n_jn_{i,j}n_kn_{i,k}. \quad (2.23)$$

It can be thus presented in vector form as [36]

$$\begin{aligned} \omega = & \frac{1}{2}K_1(\nabla \cdot \mathbf{n})^2 + \frac{1}{2}K_2(\mathbf{n} \cdot \nabla \times \mathbf{n})^2 + \frac{1}{2}K_3(\mathbf{n} \times \nabla \times \mathbf{n})^2 \\ & + \frac{1}{2}(K_2 + K_4)\nabla \cdot ((\mathbf{n} \cdot \nabla)\mathbf{n} - (\nabla \cdot \mathbf{n})). \end{aligned} \quad (2.24)$$

The Frank elastic constants follow the convention of being named after the particular deformation they have the effect on. Hence,  $K_1$  is the splay constant,  $K_2$  is the twist constant, and  $K_3$  is the bend constant [8, 36]. The remaining combination of  $K_2 + K_4$  from Eq. (2.24) is called the saddle-splay constant. It is usually omitted from the bulk energy, as it can be modified into a surface term through the divergence theorem. These

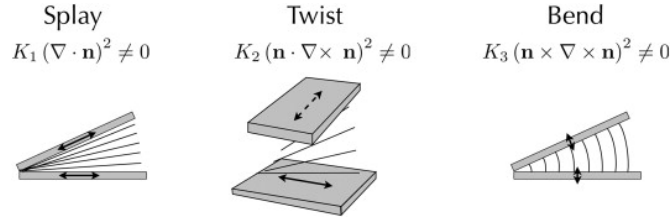


Figure 2.3: Types of elastic deformations in liquid crystals. From left to right, they include splay, twist, and bend. Reprinted from [10] with permission from Elsevier.

deformations of splay, twist, and bend are shown graphically in Fig. 2.3, together with their related elastic constants. Those elastic constants obey the Ericksen inequalities [50]

$$K_1 \geq 0, \quad K_2 \geq 0, \quad K_3 \geq 0, \quad K_2 \geq |K_4|, \quad K_1 \geq \frac{1}{2}(K_2 + K_4) \geq 0. \quad (2.25)$$

Typical values for the elastic constants are in the  $10^{-11}N$  range [51], however they are temperature and material dependant. When working with the bulk elastic energy density it is common to use the one constant approximation, which we elect to do as well. This approximation assumes that the splay, twist, and bend elastic constants are equal, i.e.  $K = K_1 = K_2 = K_3$ , and that  $K_4 = 0$ . This assumption simplifies the material properties of a standard nematic, however the ratio of the elastic constants is usually not significantly greater than unity and it is not expected that there would

be a large qualitative difference in behaviour under this approximation [52]. Experimentally, it is difficult to measure all the elastic constants of a particular material as they are temperature dependent but it has been done for many well known liquid crystal compounds [53]. One of those compounds, easily the most commonly used in many studies, is 4-Cyano-4'-pentylbiphenyl universally referred to as 5CB. The values for 5CB at 24°C under one-constant approximation are  $K \approx 6$  pN [54]. Under the one constant approximation Eq. (2.24) is transformed into

$$\omega = \frac{K}{2} [(\nabla \cdot \mathbf{n})^2 + (\nabla \times \mathbf{n})^2 + \nabla \cdot ((\mathbf{n} \cdot \nabla)\mathbf{n} - (\nabla \cdot \mathbf{n}))] \quad (2.26)$$

which is the one constant approximation Frank-Oseen free energy.

## 2.6 Landau de Gennes theory

As previously mentioned, the molecular order within a nematic mesophase can be altered by changing the temperature. For significant variations in temperature the phase transition, that is the transformation from one state to another, changes the structure and the symmetry of the mesophase. This change affects the physical properties such as density or viscosity. In thermodynamics terms, this means that the entropy of the system  $S_e$  changes:

$$S_e = - \left( \frac{\partial \mathcal{F}}{\partial T} \right)_V \quad (2.27)$$

where  $\mathcal{F}$  is the free energy at a given temperature  $T$  and volume  $V$ . The order of the phase transition is determined by  $S_e$ , such that a discontinuous variation of  $S_e$  with temperature gives a first order transition and a continuous variation of  $S_e$  is a second order phase transition. The discontinuity in the first order transition leads to the exchange of latent heat  $Q_l = T_{NI} \delta S_e$  at some phase transition temperature  $T_{NI}$ . Phase transitions in thermotropic mesophases lie within the Landau de Gennes theory, which is built around the order parameter of a specific phase transition [8]. In general terms, the order parameter is a spatially inhomogeneous tensorial field with a free energy that is a functional of that field [55]. Landau theory writes the bulk free energy as a power

series in terms of the order parameter, which vanishes above a certain temperature. Following this Landau formalism, the argument can be presented in terms of the bulk energy density  $f_b$  expanded by using the powers of the order parameter [8]:

$$f_b = \frac{1}{2}A(T) \text{tr} \mathbf{Q}^2 + \frac{1}{3}B(T) \text{tr} \mathbf{Q}^3 + \frac{1}{4}C(T)(\text{tr} \mathbf{Q}^2)^2 \quad (2.28)$$

$$= \frac{1}{2}A(T)Q_{\alpha\beta}Q_{\beta\alpha} + \frac{1}{3}B(T)Q_{\alpha\beta}Q_{\beta\gamma}Q_{\gamma\alpha} + \frac{1}{4}C(T)(Q_{\alpha\beta}Q_{\alpha\beta}Q_{\gamma\delta}Q_{\gamma\delta}). \quad (2.29)$$

with summation over repeated indices being implied, and where  $A, B, C$  are temperature and pressure dependent material coefficients. Usually,  $A$  tends to be written in the form  $A = a(T - T^*)$ , with  $T^*$  being the super-cooling temperature while  $B, C$  are assumed to be constants such that  $B < 0$  and  $C > 0$ . The lack of linear term ensures that the state minimum occurs when  $Q$  is zero (for  $T > T^*$ ) i.e. the material is in an isotropic phase. What is important to note is that there is no symmetry relation between states  $Q_{\beta\alpha}$  and  $-Q_{\beta\alpha}$ . This means that there is a non-vanishing term of order  $\mathcal{O}(3)$ . Because of this non zero term of third order the phase transition must be a first order one. The nematic-isotropic transition is of first order, however it is in ‘weakly first order’ [8] with the  $B$  coefficient being relatively small.

### 2.6.1 Nematic to isotropic phase transition

The nematic to isotropic transition is a first order transition, where the order parameter  $S$  vanishes at the transition temperature  $T_{NI}$  [56]. Following the bulk free energy in Eq. (2.29), we can now relate this bulk free energy with the scalar order parameter  $S$  [8]. Following the previous assumptions for the material constants  $A, B$  and  $C$  Eq. (2.29) becomes

$$f_b = \frac{1}{2}a(T - T^*) \text{tr} \mathbf{Q}^2 + \frac{1}{3}B \text{tr} \mathbf{Q}^3 + \frac{1}{4}C(\text{tr} \mathbf{Q}^2)^2 \quad (2.30)$$

where  $T^*$  is the super-cooling temperature. The nematic to isotropic transition is driven by the factor  $\frac{1}{2}a(T - T^*)$ . By considering the uniaxial order parameter, we can use the

expression for the Q-tensor from Eq. (2.14) and the relations

$$\text{tr } \mathbf{Q}^2 = \frac{3}{2}S^2 \quad \text{and} \quad \text{tr } \mathbf{Q}^3 = \frac{3}{4}S^3$$

to rewrite the bulk free energy as

$$f_b = \frac{3}{4}a(T - T^*)S^2 + \frac{1}{4}BS^3 + \frac{9}{16}CS^4. \quad (2.31)$$

This equation then relates the bulk free energy functional with the scalar order parameter  $S$ . The first term is responsible for the transition, the second is a result of  $S \neq -S$ . The remaining term comes from a fourth order that is the lowest suitable term for the description of a phase transition, as it allows the free-energy density to have two distinct minima. The equilibrium of the system can therefore be found by minimising the free energy for the entire volume at a given temperature. This is done by finding relevant solutions to

$$\frac{3}{2}AS + \frac{3}{4}BS^2 + \frac{9}{4}CS^3 = 0, \quad (2.32)$$

where  $A = a(T - T^*)$ . The solutions are given by

$$S_I = 0, \\ S_N = -\frac{B}{6C} \left( 1 + \sqrt{B^2 - 24AC} \right),$$

and they correspond to the values of the scalar order parameter in the isotropic and the nematic phase respectively. From these solutions, we can make the following observations. Above the superheating temperature  $S^+$ , the material is isotropic and there is no nematic phase. Below the transition temperature  $T_{NI}$  the nematic state is in the global minimum energy state. The limit of the metastability for a nematic is some temperature  $T^+$ , such that

$$T^+ = T^* + \frac{B^2}{24AC}. \quad (2.33)$$

At the transition temperature, the free energies of the nematic and isotropic are equal. This occurs for  $a = \frac{B^2}{27C}$ , resulting in

$$T_{NI} = T^* + \frac{B^2}{27AC} \quad (2.34)$$

where  $T^*$  is the super cooling temperature that corresponds to the metastability limit of the isotropic phase. Theoretically, it should be possible to be able to supercool an isotropic fluid to this temperature. This temperature for  $A = 0$ , is where the isotropic phase loses stability. Once the  $A$  coefficient changes sign,  $S = 0$  is no longer the local minimum of the free energy.

Following this analysis we can see that the Landau-de Gennes theory predicts a discontinuous phase transition [8]. This happens at the transition temperature  $T_{NI}$  that is slightly above  $T^*$ , as a result of the odd-order powers of  $S$  in the expansion of the bulk free energy. The bulk free energy  $f$  and its dependence on  $S$  is shown in Fig. 2.4 for the three different temperatures: the supercooling  $T^*$ , nematic-isotropic transition  $T_{NI}$ , and metastability limit  $T^+$ .

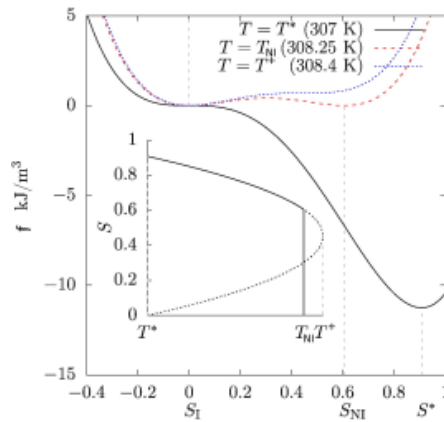


Figure 2.4: Free energy of 5CB nematic mesophase as a function of the scalar order parameter for three different temperatures:  $T^*$ ,  $T_{NI}$ , and  $T^+$ . The inset shows the change of order parameter with temperature. This figure is adapted (temperature labels change only) from [57] licensed under CC BY 4.0.

## 2.6.2 Landau de Gennes free energy

The Landau de Gennes model for nematic liquid crystals consists of a free energy that incorporates the free energy contributions from the nematic order and from the elasticity into one functional, expressed as an integral over a function of a tensor field  $Q$ , which is also an integral over volume.

$$\mathcal{F}(Q) = \int_{\Omega} (\omega + f_b) dV, \quad (2.35)$$

where  $\mathcal{F}$  gives the free energy over some region of the material  $\Omega$ , and in other words is referred to as the Landau free energy density,  $\omega$  is the elastic free energy density, and  $f_b$  is the bulk free energy density. As a consequence of using two contributing terms in the Landau de Gennes theory, a characteristic length of the nematic order variation is introduced. This length is known as the nematic correlation length  $\xi_N$  and it can be found by minimising the  $\mathcal{F}$  functional by using the Euler-Lagrange equation. The correlation length increases when approaching the phase transition temperature  $T_{NI}$ . Usually the  $\xi_N$  is in the order of few nanometers, commonly also expressed in angstroms. The Landau de Gennes model is one of the most general models for describing liquid crystal phenomena, as it is relevant for different length-scales, boundary conditions, and can be reasonably easily extended to include external fields.

## 2.7 Boundary conditions

Another facet of the system that needs to be considered is what happens at the solid-fluid boundaries. In the case of colloidal particles placed in a channel with a nematic fluid, those boundaries are between the colloid and the liquid crystal, and between the liquid crystal and the channel walls.

### 2.7.1 Surface anchoring

The nematic director field is uniform and determined by the internal ordering of the liquid crystal phase in the absence of any external fields or interacting surfaces. In a



system with surface interaction, be it from a solid, liquid, or gas, the inherent ordering is affected, modifying the equilibrium state. The liquid crystal molecules tend to locally orient themselves in some direction at the interface between liquid and solid. The axis of this orientation is called the easy axis. This phenomenon, i.e. the change in orientation of liquid crystals by surfaces, is called surface anchoring [58]. In  $Q$ -tensor terms, we can represent this surface induced ordering by using the tensor order parameter

$$Q_{\alpha\beta}^0 = \frac{S^0}{2}(3n_\alpha^0 n_\beta^0 - \delta_{\alpha\beta}) \quad (2.36)$$

where  $n_\alpha^0$  is the direction of the easy axis and  $S^0$  is the surface induced order. The two most common orientation types are homeotropic and planar anchoring, as shown in Fig. 2.5. For planar anchoring, as in Fig. 2.5 a), the director is oriented parallel to the surface, while in Fig. 2.5 b) the director is perpendicular to the surface, resulting in homeotropic anchoring. The final part c) of Fig. 2.5 shows tilted anchoring, for some orientation between parallel and perpendicular to the surface. These are the

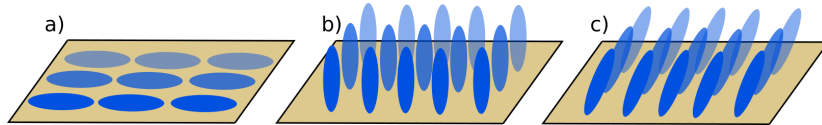


Figure 2.5: Different anchoring types of a nematic liquid crystal, where a) is planar anchoring, b) is homeotropic (normal) anchoring, and c) tilted anchoring.

most common uniform surface anchoring patterns. In experiments, surface anchoring is obtained by fabricating cells with appropriate substrates using methods such as surface rubbing, photo-alignment [59], or microtexturing [60]. The corrugations in the substrate can be achieved with good control, meaning that there are many different combinations of surface anchoring patterns that can be achieved. The modifications to the basic uniform anchoring can be useful to tailor the substrate characteristics for liquid crystal alignment, as the increase in the surface anchoring energy can lead to a lowering of the elastic energy due to the spatial variations [60]. In our simulations however, we maintain uniform anchoring conditions. The strength of the anchoring will influence how much the director field will tend to align, with greater strength increasing

the alignment, although the effect fades with distance away from the boundary.

To achieve a general boundary condition for a solid-fluid interface, we look at the gradient terms in the free energy and at a surface free energy. The latter, which can be thought of as an area density, is dependent on the particular type of anchoring to be used. It is dependent on the order parameter, but not on its gradients, and can be generally be written as

$$f_s = f_s(Q_{\alpha\beta}, Q_{\alpha\beta}^0) \quad (2.37)$$

with  $Q_{\alpha\beta}^0$  being some decided upon configuration which we will expand upon later. For the boundary conditions we use the Euler-Lagrange equations which will result in a relation

$$n_\gamma \frac{\partial f}{\partial Q_{\alpha\beta,\gamma}} + \frac{\partial f_s}{\partial Q_{\alpha\beta}} = 0, \quad (2.38)$$

where  $n_\gamma$  is the unit normal at the surface that points into the fluid and the volume contribution  $f = f_b + \omega$ . The first term in the derivative of that fluid free energy term, with respect to  $Q_{\alpha\beta,\gamma}$ , can be expanded into

$$\kappa_0 n_\beta \partial_\gamma Q_{\alpha\gamma} + \kappa_1 n_\gamma (\partial_\gamma Q_{\alpha\beta} - \partial_\alpha Q_{\gamma\beta}) - 2\kappa_1 q_0 n_\gamma \epsilon_{\alpha\gamma\sigma} Q_{\sigma\beta}.$$

where  $K_0$  and  $K_1$  are elastic constant. The expression above can be rewritten into its symmetric form as

$$\begin{aligned} & \frac{1}{2}\kappa_0 (n_\alpha \partial_\gamma Q_{\beta\gamma} + n_\beta \partial_\gamma Q_{\alpha\gamma}) + \kappa_1 n_\gamma \partial_\gamma Q_{\alpha\beta} - \frac{1}{2}\kappa_1 n_\gamma (\partial_\alpha Q_{\gamma\beta} + \partial_\beta Q_{\gamma\alpha}) \\ & - \kappa_1 q_0 n_\gamma (\epsilon_{\alpha\gamma\sigma} Q_{\sigma\beta} + \epsilon_{\beta\gamma\sigma} Q_{\sigma\alpha}). \end{aligned}$$

The full boundary condition will include the above term together with a surface anchoring condition, from Eq. (2.38). Returning to the choices for the imposed anchoring, we can use normal (homeotropic) and planar anchoring. For normal anchoring the preferred orientation of the order at the surface is normal to it. The normal anchoring is thus given by

$$f_s = \frac{1}{2}w(Q_{\alpha\beta} - Q_{\alpha\beta}^0)^2 \quad (2.39)$$

where  $w$  is the surface anchoring strength (not to be confused with the elastic free energy density  $\omega$ ), with values of  $w_{wall}$  and  $w_{part}$  at the wall and particle surfaces respectively. By setting the director to be equal to the unit normal at the surface  $n_\gamma$ , we find the preferred orientation  $Q_{\alpha\beta}^0$  to be

$$Q_{\alpha\beta}^0 = \frac{1}{2}A_0(3n_\alpha n_\beta - \delta_{\alpha\beta}), \quad (2.40)$$

where the amplitude  $A_0$  is given by

$$A_0 = \frac{2}{3} \left( \frac{1}{4} + \frac{3}{4} \sqrt{1 - \frac{8}{3\gamma}} \right). \quad (2.41)$$

The  $\gamma$  parameter controls the temperature difference from the isotropic-nematic transition and is related to the reduced temperature  $\tau$  by

$$\tau = \frac{27}{\gamma} \left( 1 - \frac{\gamma}{3} \right). \quad (2.42)$$

For  $\gamma > 3$  or  $\tau < 0$  the ordered nematic state is the equilibrium phase. For  $2.7 \leq \gamma \leq 3$  or  $0 \leq \tau \leq 1$  the nematic state is metastable, while for  $\gamma < 2.7$  or  $\tau > 1$  we get the isotropic state. Writing out the full expression for the boundary condition with normal anchoring we obtain

$$\begin{aligned} \frac{1}{2}\kappa_0(n_\alpha \partial_\gamma Q_{\beta\gamma} + n_\beta \partial_\gamma Q_{\alpha\gamma}) + \kappa_1 n_\gamma \partial_\gamma Q_{\alpha\beta} - \frac{1}{2}\kappa_1 n_\gamma (\partial_\alpha Q_{\gamma\beta} + \partial_\beta Q_{\gamma\alpha}) \\ - \kappa_1 q_0 n_\gamma (\epsilon_{\alpha\gamma\sigma} Q_{\sigma\beta} + \epsilon_{\beta\gamma\sigma} Q_{\sigma\alpha}) - w(Q_{\alpha\beta} - Q_{\alpha\beta}^0) = 0. \end{aligned} \quad (2.43)$$

In planar anchoring, the preferred orientation is actually in the tangent plane to the surface. Since it is energetically equivalent in any orientation, it is also referred to as a degenerate case. The computation of this is more complex than the homeotropic case, and following the examples in literature [61] we express the appropriate surface energy density as

$$f_s = \frac{1}{2}w_1(\tilde{Q}_{\alpha\beta} - \tilde{Q}_{\alpha\beta}^\perp)^2 + \frac{1}{2}w_2(\tilde{Q}_{\alpha\beta}^2 - A^2)^2, \quad (2.44)$$

with the amplitude defined before by Eq. (2.41). The quantity  $\tilde{Q}_{\alpha\beta}^\perp$  comes from the appropriate combination of the local fluid order parameter  $Q_{\alpha\beta}$  such that  $\tilde{Q}_{\alpha\beta} = Q_{\alpha\beta} + \frac{1}{2}A\delta_{\alpha\beta}$ . It can now be related to the tangent plane via  $\tilde{Q}_{\alpha\beta}^\perp = P_{\alpha\gamma}\tilde{Q}_{\gamma\sigma}P_{\sigma\beta}$  with the local surface normal being introduced through  $P_{\alpha\beta} = \delta_{\alpha\beta} - n_\alpha n_\beta$ . We can again explicitly write out the full boundary condition for planar anchoring

$$\begin{aligned} & \frac{1}{2}\kappa_0(n_\alpha\partial_\gamma Q_{\beta\gamma} + n_\beta\partial_\gamma Q_{\alpha\gamma}) + \kappa_1 n_\gamma\partial_\gamma Q_{\alpha\beta} - \frac{1}{2}\kappa_1 n_\gamma(\partial_\alpha Q_{\gamma\beta} + \partial_\beta Q_{\gamma\alpha}) \\ & - \kappa_1 q_0 n_\gamma(\epsilon_{\alpha\gamma\sigma}Q_{\sigma\beta} + \epsilon_{\beta\gamma\sigma}Q_{\sigma\alpha}) - w_1(\tilde{Q}_{\alpha\beta} - \tilde{Q}_{\alpha\beta}^\perp) - 2w_2(\tilde{Q}_{\alpha\beta}^2 - A^2)\tilde{Q}_{\alpha\beta} = 0. \end{aligned} \quad (2.45)$$

## 2.8 Topological defects

Topological defects [62, 63] are ever present in materials with changing symmetries, examples of which include ordered media like magnetic or crystalline materials [64, 65] or quantum Hall fluids [66]. The underpinnings of modern dislocation theory come from the early studies done by Lehmann, Friedel, and Grandjean [67]. In liquid crystal theory terms, defects are regions where the director is ill-defined. Although the name suggests irregularity in the material they are very common in phase systems and are a natural consequence of symmetry breaking. In nematic liquid crystals topological defects exhibit as point defects or as disclination lines. Due to the optical properties of liquid crystals, including birefringence, these topological defects are easy to observe under a microscope. While defects change the physical properties of liquid crystal in their surrounding region, they also increase the overall free energy of the system. As materials find their equilibrium, in a perfectly ordered medium there would be no defects present. In reality, factors such as external fields, surfaces, phase transitions can create and stabilise defects, spontaneously, in a controlled way or both.

When the liquid crystal is confined to two dimensions, the defects occur as points, examples of which are shown in Fig. 2.6. Their classification is done by using the winding number and topological rank. As seen in Fig. 2.6, we can focus on a defect to calculate the individual winding numbers in each case as follows. In a clockwise direction, we look at the orientation of the director as we go around the point until

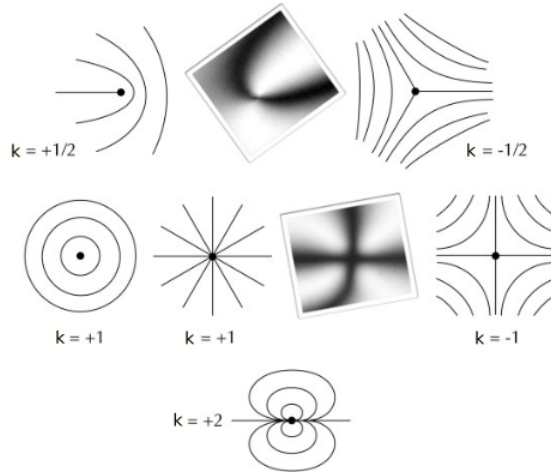


Figure 2.6: Topological defects in two dimensions. Black dots indicate the point defects, with the lines showing a representation of the director field close to the core of the defect. First row shows semi-integer defects of rank  $1/2$ . Second row shows defects with rank 1, and third row shows defect of rank 2. The black and white images are examples of defects under a polarising microscope Reprinted from [10] with permission from Elsevier.

we reach a full circle. Then the resulting total angle  $\alpha$  of that director rotation is a multiple of  $\pi$ , and can be used to find the winding number  $k$  through the relation:

$$k = \frac{\alpha}{2\pi}, \quad (2.46)$$

Depending on the rotation, the angle can be positive or negative thus giving the topological charge associated with the winding number. Many cases of such defects are of topological rank  $1/2$  or a  $-1/2$ , a result of  $\pi$  and  $-\pi$  angles, as shown in the first row of Fig. 2.6. A disclination line is commonly found in liquid crystals and it can be thought of as an extension of the 0-dimensional point defect into a 1-dimensional line defect. It is easily created by perturbation in the structure of the mesophase, including anything from the isotropic to nematic transition, applying flow or simply mixing the liquid crystal with a stirring rod. For  $k = 1$  or  $-1$ , we get three configurations called the circular, radial, and hyperbolic, shown in that order in the second row of Fig. 2.6. They are also relatively common in nematics. While higher winding numbers are possible, the larger elastic deformation increases the total free energy of the system which makes

them unfavourable and much less likely to be observed in the real world. Nonetheless, an example of such a configuration is shown in the third row of Fig. 2.6. The cases outlined above are standard in liquid crystals, mathematically for their simplicity and experimentally in cells or confined channels. When there are several topological defects in a sample, their combined charge is a sum of all the individual charges. For the purposes of estimating their total energy, both the distance between the defects and their charge are factors. The defects can be created and annihilated, but the sum of total charges is conserved. The disclinations can be stable, however they normally do not correspond to the lowest free energy state [68]. With the assumption of the one constant approximation, the energy of a single disclination line per unit length is

$$E = \int_{r_c}^D \omega(2\pi r) dr = \pi K k^2 \ln \left( \frac{D}{r_c} \right), \quad (2.47)$$

with  $D$  being the sample size,  $r_c$  being the core radius,  $K$  being the elastic constant, and  $k$  being the winding number, and as before  $\omega$  being the elastic free energy density. The order parameter within the core reduces to zero [53]. From this equation, we can note that the average energy of the disclination varies with the squared topological rank  $k$ . Thus, higher rank integer defects tend to transform to lower energy semi-integer defects [69]. Annihilation of defect pairs can happen as defects with opposite signs attract each other, which can lead to states free of defects [70]. In the results chapters we will observe how the flow, director field, and topological defects interact with one another. The overall dynamics of the system is ultimately affected and linked to the coupling between the director and the flow.

## 2.9 Viscosity

Nematic liquid crystals, as mentioned before, are non-Newtonian. They are chiefly shear thinning, meaning that their viscosity is reduced under strain [7]. In general, the behaviour of a fluid under flow is influenced by its viscosity with an average bulk viscosity coefficient used to characterise such behaviour. In an anisotropic fluid, flow

influences the orientation of the molecules. However, the viscosity coefficient depends on the orientation of the molecules. Thus for anisotropic fluids, such as nematic liquid crystals, the coefficient is a function of the velocity gradient [71]. A set of viscosity coefficients is to be found with three principal values depending on three directions of orientation. These three directions are:

$$\eta_1 \text{ for } \mathbf{n} \parallel \mathbf{v}, \quad \eta_2 \text{ for } \mathbf{n} \parallel \nabla \mathbf{v}, \quad \eta_3 \text{ for } \mathbf{n} \perp \mathbf{v} \text{ and } \mathbf{n} \perp \nabla \mathbf{v}, \quad (2.48)$$

meaning parallel to the direction of flow, parallel to the direction of the velocity gradient, and perpendicular to both of them respectively. This was first observed experimentally by Miesowicz [71] by stabilising the director field using a strong magnetic field for the respective viscosity coefficients for two different liquid crystals: PAA (p-Azoxyanisole) and PAP (p-Azoxyphenetole). Further experiments by other scientists confirmed the observation of Miesowicz, now including the effects of temperature on the anisotropy of viscosity [72] for another set of nematic liquid crystals: HBAB (P-n-hexyloxybenzylidene-P'-aminobenzonitrile) and MBBA (P'-methoxybenzylidene-P-n-butylaniline). Together with the compounds used by Miesowicz, the inequality of  $\eta_1 < \eta_3 < \eta_2$  was observed [73].

In a similar time frame, there was also formulations for the description of the dynamics of liquid crystal materials, which includes a mathematical perspective on the viscosity factors. Theoretically, the stress tensor formulated by Ericksen [74] and Leslie [40] was found to have six coefficients ( $\alpha_n$  with  $n = 1, \dots, 6$ ) usually referred to as Leslie viscosity coefficients, or simply Leslie viscosities. Further work by Parodi [75] used the Onsager relation to reduce the number of the Leslie coefficients through showing that  $\alpha_2 + \alpha_3 = \alpha_6 - \alpha_5$ . Those five independent coefficients were able to be directly evaluated experimentally by the work of Gähwiler [72].

Under rotational motion, there is also an effective viscosity coefficient that can be found [36], the rotational viscosity  $\gamma_1$ . In fact, the Miesowicz viscosities and rotational viscosity  $\gamma_1$  are related to the Leslie coefficients, such that they can be found through

the following relations:

$$\eta_1 = \frac{1}{2}(\alpha_3 + \alpha_4 + \alpha_6), \quad (2.49)$$

$$\eta_2 = \frac{1}{2}(-\alpha_2 + \alpha_4 + \alpha_5), \quad (2.50)$$

$$\eta_3 = \frac{1}{2}\alpha_4, \quad (2.51)$$

$$\gamma_1 = \alpha_3 - \alpha_2. \quad (2.52)$$

## 2.10 Fluid dynamics

### 2.10.1 Basic theory of fluid dynamics

Before introducing the chosen methods that will be used to obtain our results, it is important to explain the background and give an overview of fluid dynamics. A fluid, in physical terms, is a substance that continually deforms under shear stress. Fluid dynamics, in most basic terms, is a discipline of science that describes the flow of liquids and gases. Historically, it was synonymous with hydrodynamics, however the latter is now a subset that specifically focuses on liquids in motion. The study of fluid mechanics is divided into fluid dynamics and statics, with the former focused on the motion of fluid and the latter, as the name suggests, fluid at rest. Fundamentally, all fluids are assumed to obey the laws of conservation of mass, momentum, and energy. It is possible to mathematically describe the behaviour of a fluid using various representations using those assumptions. For example, a microscopic approach would be one where the focus is on individual molecules and their interactions over some volume. However, that is not the only way to describe a fluid, and this is where length scales are relevant. In most cases the conservation laws are combined with the continuum approach - the fluid can be thought of as a continuous volume of matter and the molecular nature of it is effectively ignored as the particles making up the fluid are sufficiently small in comparison to the system size. This is a very robust approximation for most applications. The fully continuous assumption, with tangible qualities of velocity and density, can be thought of as the macroscopic description.



To introduce the continuity equation, we shall consider some small fluid element with density  $\rho$ , occupying a volume  $V$ . As such, the mass is given by  $\int_V \rho dV$ . Mass cannot be created or destroyed, so when change over time is considered, that can only be achieved by flow into or out of the volume. This can be written as follows, after using the divergence theorem,

$$\frac{\partial}{\partial t} \int_V \rho dV = - \oint_{\partial V} \rho \mathbf{u} \cdot d\mathbf{A}, \quad (2.53)$$

where  $\partial V$  is the surface and  $\mathbf{u}$  is the fluid velocity. Taking everything to the left hand side and knowing that the volume chosen is stationary, we get the continuity equation

$$\frac{\partial \rho}{\partial t} + \nabla \cdot (\rho \mathbf{u}) = 0 \quad (2.54)$$

that reflects the conservation of mass. It is a partial differential equation (PDE), where  $\rho \mathbf{u}$  is the momentum density, and can be written in various ways. For example, it is common to express the continuity equation by using the material derivative

$$\frac{D}{Dt} = \frac{\partial}{\partial t} + \mathbf{u} \cdot \nabla \quad (2.55)$$

such that Eq. (2.54) would be expressed as follows:

$$\frac{D\rho}{Dt} + \rho \nabla \cdot \mathbf{u} = 0. \quad (2.56)$$

The material derivative gives the rate of change of the fluid as it moves through space rather than at a fixed point.

The same logic can be applied to consider what happens when looking at the change of momentum of some small fluid element with density  $\rho$  and velocity  $\mathbf{u}$  occupying a volume  $V$ . For simplicity, in an ideal fluid the changes in the net momentum are due to: the flow of momentum in or out, the differences in pressure  $p$ , and the external body forces  $F$ . Writing all the possible contributions out on the right hand side, we

get a momentum balance equation

$$\frac{d}{dt} \int_V \rho \mathbf{u} dV = - \oint_{\partial V} \rho \mathbf{u} \mathbf{u} \cdot d\mathbf{A} - \oint_{\partial V} p d\mathbf{A} + \int_V \mathbf{F} dV \quad (2.57)$$

where  $\mathbf{u} \mathbf{u}$  is the outer product with components  $u_\alpha u_\beta$ . As before, using the divergence theorem to transfer the surface integrals to volume integrals the previous equation now becomes

$$\int_V \frac{\partial(\rho \mathbf{u})}{\partial t} dV = - \int_V \nabla \cdot (\rho \mathbf{u} \mathbf{u}) dV - \int_V \nabla p dV + \int_V \mathbf{F} dV. \quad (2.58)$$

This leads to a PDE describing the momentum conservation for an ideal fluid, called the Euler equation:

$$\frac{\partial(\rho \mathbf{u})}{\partial t} + \nabla \cdot (\rho \mathbf{u} \mathbf{u}) = -\nabla p + \mathbf{F}. \quad (2.59)$$

More generally, this can be written in a universal form as the Cauchy momentum equation,

$$\frac{\partial(\rho \mathbf{u})}{\partial t} + \nabla \cdot \mathbf{\Pi} = \mathbf{F}, \quad (2.60)$$

where the momentum flux density tensor is used such that

$$\Pi_{\alpha\beta} = \rho u_\alpha u_\beta - \sigma_{\alpha\beta}$$

with the term  $\sigma_{\alpha\beta}$  being the stress tensor. For simple fluids described by the Euler equation the stress tensor is isotropic, of the form  $\sigma_{\alpha\beta} = -p\delta_{\alpha\beta}$ . This stress tensor describes the non-direct transfer of momentum of the moving fluid. The momentum flux transfer in Eq. (2.59) includes only reversible momentum transfer or conservative pressure forces. In case of real fluids, additional terms of internal friction and viscosity need to be included, which leads to irreversible transfer of momentum of neighbouring fluid elements.

Now, to consider a viscous stress tensor  $\sigma'$  we assume that the viscous contribution is zero for uniform flow, regardless of rigid body rotation and translation. We also assume that for small velocity gradients the momentum transfer due to viscosity is proportional to the first derivative of the velocity [56]. In general, a tensor that fulfils

both conditions can be described by

$$\sigma'_{\alpha\beta} = \eta \left( \frac{\partial u_\alpha}{\partial x_\beta} + \frac{\partial u_\beta}{\partial x_\alpha} \right) + \zeta \delta_{\alpha\beta} \frac{\partial u_\gamma}{\partial x_\gamma} \quad (2.61)$$

where  $\eta$  and  $\zeta$  are viscosity coefficients. These coefficients are usually assumed to be uniform and isotropic.

Often-time, the above defined viscous stress tensor is divided into a traceless shear stress and a normal stress

$$\sigma'_{\alpha\beta} = \eta \left( \frac{\partial u_\alpha}{\partial x_\beta} + \frac{\partial u_\beta}{\partial x_\alpha} - \frac{2}{3} \delta_{\alpha\beta} \frac{\partial u_\gamma}{\partial x_\gamma} \right) + \eta_B \delta_{\alpha\beta} \frac{\partial u_\gamma}{\partial x_\gamma} \quad (2.62)$$

with  $\eta$  being the shear viscosity and the  $\eta_B$  being the bulk viscosity, the latter also described as  $\eta_B = 2\eta/3 + \zeta$ .

The total stress tensor is hence given by the sum of viscosity and pressure contributions

$$\sigma_{\alpha\beta} = \sigma'_{\alpha\beta} - p\delta_{\alpha\beta} \quad (2.63)$$

and can be used to obtain the full momentum equation, also called the Navier-Stokes equation (NSE). Operating under the assumption that the viscosities are constant, it is given by the following:

$$\rho \frac{Du_\alpha}{Dt} = -\frac{\partial p}{\partial x_\alpha} + \eta \frac{\partial^2 u_\alpha}{\partial x_\beta \partial x_\beta} + \left( \eta_B + \frac{\eta}{3} \right) \frac{\partial^2 u_\beta}{\partial x_\alpha \partial x_\beta} + F_\alpha. \quad (2.64)$$

For an incompressible flow the NSE can be greatly simplified using  $\rho = \text{const}$ , such that the continuity equation, Eq. (2.54), reduces to  $\nabla \cdot \mathbf{u}$ . This gives the incompressible Navier-Stokes equation

$$\rho \frac{D\mathbf{u}}{Dt} = -\nabla p + \eta \Delta \mathbf{u} + \mathbf{F} \quad (2.65)$$

where  $\Delta = \nabla \cdot \nabla$  is the Laplace operator.

Continuing with the incompressible fluid description we can now introduce examples of some fundamental flows between two plates. The velocity profiles of those are included in Fig. 2.7. The first example in Fig. 2.7 is that of Couette flow. It describes

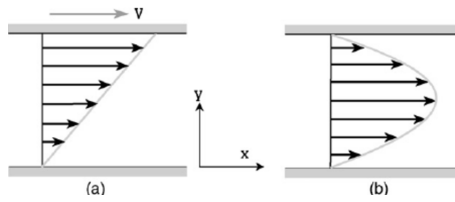


Figure 2.7: Couette and Poiseuille velocity flow profiles, where (a) shows Couette flow and (b) shows the Poiseuille flow. Reprinted from [76], with permission from Elsevier.

a steady shear flow where an incompressible fluid is placed between two parallel plates. The bottom wall is fixed, while the top plate moves with some velocity  $\mathbf{u}$  in the  $x$ -direction. The walls have no slip boundary conditions, which means that the fluid velocity at the wall is equal to that of the wall. The second standard incompressible flow is called the Poiseuille flow and its velocity profile is shown in Fig. 2.7 part (b). In this case, the fluid moves in the  $x$ -direction between two fixed parallel plates. The flow is driven by a constant pressure gradient or an external body force in the  $x$ -direction. It is standard to assume no-slip boundary conditions.

Bringing the above descriptions together, the fluid behaviour can be described by four equations. Namely conservation of mass through the continuity equation, and the conservation of momentum described by the Navier-Stokes equation (which contains a set of three equations, one for each spatial direction). What makes fluid dynamics difficult is that this system of equations is not closed and therefore it is unsolvable. This is because while there are four equations, the fluid actually has five unknowns: density  $\rho$ , pressure  $p$ , and three velocity components  $u_x, u_y, u_z$ . There are different ways of closing the system. An easy one is to fix some variable, for example by assuming constant density as in previously mentioned incompressible flows in Fig. 2.7. Another way is to use the state principle of equilibrium dynamics, which states that any two of the state variables can be related to another state variable through an equation of state [77]. State variables for a local thermodynamic state include: density  $\rho$ , pressure  $p$ , temperature  $T$ , internal energy  $e$ , and entropy  $s$ . Simply introducing an equation of state does not close the system, as it introduces another variable, so the equation must be such that the third state variable can also be derived from the energy equation.

This method is rather cumbersome, and instead it is more prudent to introduce an equation of state with the additional assumption that one of the introduced variables has a suitable approximation. As an example of this, most of acoustics is based on the approximation that the entropy  $s$  is constant [78]. A different way of approximation, that can be used for small deviations, is to linearise the equation of state by using the total differentials and evaluate the resulting derivatives around those small deviations.

### 2.10.2 Beris-Edwards model

Hydrodynamics of liquid crystals is distinct from that of simple liquids. The two important differences between simple fluids and liquid crystals come from the characteristic of symmetry and free energy. As mentioned above, the symmetry of liquid crystals is such that the molecules comprising the mesophase are rotated by the gradients in the velocity field. Additionally, the free energy of liquid crystals is intrinsically more complicated than in a Newtonian fluid, meaning that the complexity of the stress tensor in the Navier-Stokes equations is increased. Additionally, any good numerical method used for modelling of the mesophase must be able to explore both the isotropic and the nematic regions. The equations of motion for liquid crystal dynamics are complex and there are several approaches developed to tackle the problem of dynamics. They include but are not limited to continuum theory based Landau de Gennes [8] or Ericksen–Leslie [79],[41] models, Q-tensor based variational methods such as Beris–Edwards [48] or Qian–Sheng methods[80], and the energetic variational approach of Liu et al. [81],[82]. All the models are broadly in agreement with differences coming from their individual underlying assumptions. Here we shall follow the Beris-Edwards approach[48]. The advantage of using this method is that hydrodynamics of the isotropic, hydrodynamics of the nematics and topological defects are included in the same formalism through the tensor order parameter that can be connected to the second moment of the orientational distribution function of the molecules.

With the Q-tensor formalism, the equations of motion of the mesophase can be

described by using the Beris-Edwards equation [48]

$$\frac{\partial}{\partial t} Q_{\alpha\beta} + \partial_\gamma (u_\gamma Q_{\alpha\beta}) + S_{\alpha\beta}(W_{\alpha\beta}, Q_{\alpha\beta}) = -\Gamma H_{\alpha\beta}. \quad (2.66)$$

This equation relates the rate of change with respect to time of the order parameter to the terms that involve advection, the response to shear  $S_{\alpha\beta}(W_{\alpha\beta}, Q_{\alpha\beta})$ , and the molecular field  $H_{\alpha\beta}$ . The advection term includes the fluid velocity  $u_\gamma$ , while the shear term includes the velocity gradient tensor  $W_{\alpha\beta} = \partial_\beta u_\alpha$ . The full shear term can be defined as

$$\begin{aligned} S_{\alpha\beta}(W_{\alpha\beta}, Q_{\alpha\beta}) = & (\xi D_{\alpha\pi} + \Omega_{\alpha\pi})(Q_{\pi\beta} + \frac{1}{3}\delta_{\pi\beta}) + (Q_{\alpha\pi} + \frac{1}{3}\delta_{\alpha\pi})(\xi D_{\pi\beta} - \Omega_{\pi\beta}) \\ & - 2\xi(Q_{\alpha\beta} + \frac{1}{3}\delta_{\alpha\beta})Q_{\pi\sigma}W_{\sigma\pi}, \end{aligned} \quad (2.67)$$

with  $D_{\alpha\beta} = \frac{1}{2}(W_{\alpha\beta} + W_{\beta\alpha})$  being the symmetric contribution and  $\Omega_{\alpha\beta} = \frac{1}{2}(W_{\alpha\beta} - W_{\beta\alpha})$  being the antisymmetric contribution to the velocity gradient tensor. The shear term appears in the equation of motion because the order-parameter distribution can be both rotated and stretched by flow gradients [83]. Additionally,  $\xi$  is the so-called flow-alignment parameter, a material constant representing an effective molecular aspect ratio which determines whether the liquid crystal molecules are in a flow-aligned state at the Leslie angle or tumbling state.

The right hand side of Eq. (2.66) shows the relaxation of the order parameter towards the minimum of the free energy. It includes the molecular field  $H_{\alpha\beta}$  and the collective rotational diffusion constant  $\Gamma$ . The molecular field  $H_{\alpha\beta}$  is defined as a functional derivative of the free energy functional with respect to the order parameter,

$$H_{\alpha\beta} = -\frac{\delta\mathcal{F}}{\delta Q_{\alpha\beta}} + \frac{\delta_{\alpha\beta}}{3} \text{Tr} \frac{\delta\mathcal{F}}{\delta Q_{\alpha\beta}}, \quad (2.68)$$

where  $\mathcal{F}$  is the Landau de Gennes free energy functional from Eq. (2.35). The second term in Eq. (2.68), involving the trace, ensures tracelessness of the tensor order parameter as it evolves while obeying the Beris-Edwards Eq. (2.66). This leads to the

following molecular field:

$$\begin{aligned}
H_{\alpha\beta} = & -A_0(1 - \gamma/3)Q_{\alpha\beta} + A_0\gamma(Q_{\alpha\mu}Q_{\mu\beta} - \frac{1}{3}Q_{\mu\nu}^2\delta_{\alpha\beta}) \\
& -A_0\gamma Q_{\mu\nu}^2 Q_{\alpha\beta} + \kappa_0\partial_\alpha\partial_\mu Q_{\mu\beta} + \kappa_1\partial_\mu(\partial_\mu Q_{\alpha\beta} - \partial_\alpha Q_{\mu\beta})
\end{aligned} \tag{2.69}$$

The governing equations of hydrodynamic motion are the equation of mass conservation, also known as the continuity equation, and the Navier-Stokes equation that describes the conservation of linear momentum, as discussed at the beginning of this section. Now however, we have some differences in the form of those equations. In tensor notation they read

$$\partial_t\rho + \partial_\alpha(\rho u_\alpha) = 0 \tag{2.70}$$

and

$$\begin{aligned}
\partial_t(\rho u_\alpha) + \partial_\beta(\rho u_\alpha u_\beta) = & \partial_\beta\Pi_{\alpha\beta}^{(LC)} + \partial_\beta\Pi_{\alpha\beta}^{(HD)} \\
& + \eta\partial_\beta(\partial_\beta u_\alpha + \partial_\alpha u_\beta) + \zeta\partial_\alpha(\partial_\gamma u_\gamma),
\end{aligned} \tag{2.71}$$

respectively. In Eq. (2.71),  $\eta$  is the dynamic viscosity and  $\zeta$  is the bulk viscosity. In incompressible fluids, Eq. (2.70) becomes  $\partial_\alpha u_\alpha = 0$  as density is constant. Eq. (2.70) relates the local rate of change of the density  $\rho$  to the advection of mass by the fluid velocity  $u_\alpha$ , while Eq. (2.71) is Newton's second law of momentum change for the fluid, involving the stress tensor  $\Pi_{\alpha\beta}$ . The stress tensor is an important quantity and in its full form combines the dissipative and thermodynamic fluctuations within a liquid crystal. This comes from the Ericksen and Leslie formalism that extends the static equilibrium theory into dynamics for nematic liquid crystals. It reflects the additional complexities of liquid crystal hydrodynamics. It includes the thermotropic stress tensor  $\Pi_{\alpha\beta}^{(LC)}$  and the hydrodynamic stress tensor  $\Pi_{\alpha\beta}^{(HD)}$ . This thermodynamic addition to the stress on

the fluid can be described by a sum of the following form:

$$\Pi_{\alpha\beta}^{(LC)} = \sigma_{\alpha\beta} + \tau_{\alpha\beta} - \partial_\alpha Q_{\pi\nu} \frac{\delta\mathcal{F}}{\delta\partial_\beta Q_{\pi\nu}} \quad (2.72)$$

where  $\sigma_{\alpha\beta}$  and  $\tau_{\alpha\beta}$  are the symmetric and antisymmetric stress contributions respectively. The symmetric contribution  $\sigma_{\alpha\beta}$  is given by

$$\sigma_{\alpha\beta} = -p_0\delta_{\alpha\beta} - \xi H_{\alpha\pi} (Q_{\pi\beta} + \frac{1}{3}\delta_{\pi\beta}) - \xi (Q_{\alpha\pi} + \frac{1}{3}\delta_{\alpha\pi}) H_{\pi\beta} \quad (2.73)$$

$$+ 2\xi (Q_{\alpha\beta} + \frac{1}{3}\delta_{\alpha\beta}) Q_{\pi\nu} H_{\pi\nu}, \quad (2.74)$$

where  $p_0$  is the isotropic pressure taken to be

$$p_0 = \rho T - \frac{\kappa}{2} (\partial_\alpha Q_{\beta\gamma})^2. \quad (2.75)$$

The antisymmetric contribution to the stress tensor is

$$\tau_{\alpha\beta} = Q_{\alpha\pi} H_{\pi\beta} - H_{\alpha\pi} Q_{\pi\beta}. \quad (2.76)$$

The final term in Eq. (2.72) is expanded as

$$\begin{aligned} \partial_\alpha Q_{\pi\nu} \frac{\delta\mathcal{F}}{\delta\partial_\beta Q_{\pi\nu}} &= -\kappa_0 \partial_\alpha Q_{\pi\beta} \partial_\nu Q_{\pi\nu} \\ &\quad - \kappa_1 \partial_\alpha Q_{\pi\nu} (\partial_\beta Q_{\pi\nu} - \partial_\pi Q_{\nu\beta}). \end{aligned} \quad (2.77)$$

The hydrodynamic stress tensor is defined as

$$\Pi_{\alpha\beta}^{(HD)} = -p\delta_{\alpha\beta} - \rho u_\alpha u_\beta + \eta(\partial_\beta u_\alpha + \partial_\alpha u_\beta) + \zeta \partial_\mu u_\mu \delta_{\alpha\beta}. \quad (2.78)$$

The pressure  $p$  is related to the density via an ideal gas equation of state as  $p = c_s^2 \rho$  with  $c_s$  as lattice speed of sound.

An early form of solving the hydrodynamic equations for the nematic phase was formulated by Ericksen and Leslie [8],[50],[41], and used the Leslie coefficients as a measure of the viscous properties of the liquid crystal. The Beris-Edwards equations



reduce to that of Ericksen-Leslie in the uniaxial nematic approximation with a constant value of the magnitude of the order parameter. That is a limiting factor of the Ericksen-Leslie model, as it is not able to include the hydrodynamics of the topological defects. It is possible to map between the Beris-Edwards and the Ericksen-Leslie-Parodi equations which leads to the relationship between the Leslie coefficients and parameters used in the Beris-Edwards approach. Specifically, the Leslie coefficients can be implicitly described through the isotropic dynamic shear viscosities  $\eta$ , the rotational diffusion constant  $\Gamma$ , the flow alignment parameter  $\xi$  and the scalar order parameter  $S_0$ . For the explicit form of the coefficients and the details of that mapping, the reader is guided to [83]. It is worth mentioning that while the Ericksen-Leslie viscosities can be directly related to the Beris-Edwards viscosities, the latter parameterise only a subset of possible values.

### 2.10.3 Dimensionless numbers

We shall now discuss some of the dimensionless quantities relevant in our simulations. In fluid dynamics analysing the relationships between inertial, viscous, thermal, and mass values gives rise to ratios between different types of diffusivity that lead to characteristic dimensionless numbers. Those numbers are particularly useful when comparing different systems, as their strength and characteristics vary across scales. Within transport phenomena, they include the Reynolds and the Prandtl numbers. Since we want to discuss compressible flow, the other dimensionless quantities that require mentioning include the Knudsen and the Mach numbers. Finally, as we focus on nematics, we also need to introduce the Ericksen number, which is a dimensionless number commonly used when discussing liquid crystals.

The Ericksen number is common in the liquid crystal field. It is a dimensionless quantity used to describe the effect of flow on the director field, defined as the ratio of viscous and elastic forces:

$$\text{Er} = \frac{\text{viscous effects}}{\text{elastic effects}} = \frac{\eta u \Lambda}{\kappa},$$

where  $\eta$  is the dynamic viscosity,  $u$  is the characteristic flow velocity,  $\Lambda$  is the characteristic length scale and  $\kappa$  is the elastic constant. For low Ericksen numbers, the elastic forces are larger than the viscous forces, meaning that the flow will have a smaller effect on the director field. At high Ericksen numbers the flow has much higher impact on the overall characteristics.

The Knudsen number defines the ratio between mean free path length and a representative physical length-scale. The latter can be any representative length, such as the size of a channel or a radius of a particle in a fluid:

$$\text{Kn} = \frac{\text{mean free path}}{\text{representative physical length-scale}} = \frac{\lambda}{\Lambda}. \quad (2.79)$$

This number is particularly relevant for choosing an appropriate modelling method. For Knudsen number greater than one (or close to one), that means that the mean free path is very close to the length-scale of the problem, meaning that a continuum approach ceases to be a good approximation. For such systems, statistical methods are a better approach.

The Mach number, sometimes called just Mach, is the ratio between the flow velocity and the speed of sound. Velocities lower than the speed of sound are referred to as subsonic, and velocities faster than the speed of sound are called supersonic:

$$\text{Ma} = \frac{u}{c}, \quad (2.80)$$

where  $c$  is the medium dependent speed of sound and  $u$  is a local velocity, relative to each other. In some cases the Mach number is used as a deciding factor in treating the flow as incompressible (for Mach numbers  $< 0.2 - 0.3$ ) [84].

The Reynolds number is a dimensionless quantity relating the inertial to viscous forces in a fluid. It is defined as

$$\text{Re} = \frac{uL\rho}{\eta},$$

where  $u$  is the flow speed,  $L$  is the characteristic length-scale,  $\rho$  is the fluid density, and  $\eta$  is the dynamic viscosity. In general Reynolds numbers are commonly used in

describing characteristics of fluid flows. The Reynolds number has been used to predict the beginning of turbulent flow due to the chaotic nature of flow, which is a very complicated topic. In liquid crystals, the behaviour usually differs at low and high values of Reynolds numbers.

The Prandtl number is a dimensionless number, defined as the ratio between the momentum diffusivity (in other words, kinematic viscosity) and thermal diffusivity:

$$\text{Pr} = \frac{\text{kinematic viscosity}}{\text{thermal diffusivity}}. \quad (2.81)$$

In contrast to the Reynolds number, there is no length scale variable, with the Prandtl number dependent on the fluid and its state only. To understand the interpretation of this number; for values such that  $Pr \ll 1$ , thermal diffusivity dominates and heat diffuses quickly compared to the momentum, while for  $Pr \gg 1$ , the kinematic viscosity dominates meaning that heat diffuses slowly. For values close to 1, both momentum and heat dissipate at about the same rate.

Nematic liquid crystals in flow usually have three different contributions coming from inertial, viscous, and elastic effects. The flow stability of the dynamics of nematics is for the most part governed by the elastic effects, with the Ericksen number used to estimate the ratio between the viscous and elastic effects. However in isotropic fluids the hydrodynamic instability can be evaluated through the Reynolds number, as isotropic fluids are characterised by competing inertial and viscous effects. This instability occurs when inertial effects dominate the viscous effects, that is at high Reynolds numbers that typically occur at high flow speeds. While the Ericksen and Reynolds numbers are the two most important numbers in relation to liquid crystal analysis, the Knudsen, Mach, and Prandtl numbers are important for the simulation method which we will discuss later on.

## 2.11 Nematic liquid crystal colloids

A colloid is a general term for a mixture consisting of a dispersion medium and a dispersed phase, with the dispersed phase particles having a diameter of approximately 1 nanometre to 1 micrometre [85]. Depending on the type of phase and medium used, these two-phase systems of matter can be classified further as seen in Table 2.1. Col-

		Dispersed phase		
Medium		Gas	Liquid	Solid
	Gas	None	Liquid aerosol	Solid aerosol
	Liquid	Foam	Emulsion or liquid crystal	Sol
	Solid	Solid foam	Gel	Solid sol

Table 2.1: Classification of colloidal suspensions on the basis of the dispersed phase and the dispersion medium.

loidal suspensions fall under the subject of interface and colloid science, a multidisciplinary field with interest from scientists working in the areas of physics, chemistry, and nanoscience. As such, the definitions and nomenclature about what is, and is not, a colloid or a colloidal suspension can vary [86]. In our research, we shall focus on a new state of colloidal matter referred to as nematic liquid-crystal colloids, or nematic colloids in short [87]. They are broadly defined as a dispersion of microparticles (colloidal particles) in a nematic liquid crystal phase that acts as a solvent. These colloidal particles deform the liquid crystal locally resulting in topological defects and long-range orientational ordering. Contrary to the colloidal interactions in an isotropic fluid (usually of van der Waals type), the forces in nematic colloids are much stronger, around the order of  $1000k_bT$  per micrometer particle [19]. The differences in boundary conditions at the colloid-nematic surface lead to different director orientations at the surface, leading to a wide array of phenomena to be explored [88].

The work published by Brochard and de Gennes in 1970 showed the interaction between particles and the mesophase through their calculations of the deformation of the director orientation by the particles and defects bound to them [89]. Further investigations into the topological defects in a nematic were then done by Poulin et al. [90]. In their research they created a dispersion of micrometer diameter water droplets in

a nematic liquid crystal (5CB). These droplets formed chains, their Brownian motion ceased entirely, and they did not coalesce despite being a fluid [90]. The last behaviour, that is the separation between water droplets, occurred due to spontaneously created defects near each droplet. There are limitations in the experimental methods at that time, however in the decades after the progress in the field was enabled by two important techniques that were particularly useful for the investigations into nematic liquid crystal colloids. Those include applications of laser tweezers [91] [92] [93] [94] [95] and fluorescent confocal polarizing microscopy (FCPM) [96] [97] [98].

When describing topological defects, there is more to consider when introducing shaped objects into the director field. Here, we focus on including spherical micro- and nano-particles in the liquid crystal structures. Spherical particles have simple topology which makes it easy to see what happens when they are inserted into a nematic liquid crystal.

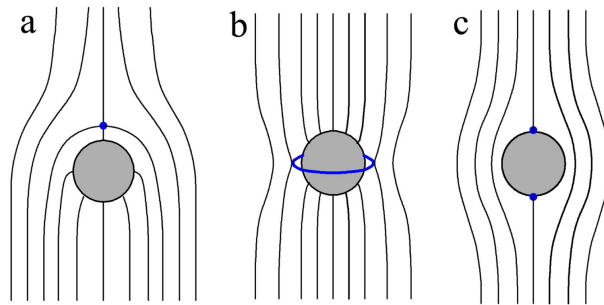


Figure 2.8: Different types of defects (here marked in blue) around a colloidal particle, where: a) shows a point ( $k = -1$ ) hedgehog defect, b) shows a Saturn ring defect, c) shows a pair of boojum defects. Reprinted from [99] with permission from Taylor & Francis.

Fig. 2.8 shows different types of defects around a colloidal particle. The defect type is determined by factors including but not limited to: the anchoring strength, type of anchoring orientation on the particle surface, and the diameter of the particle. For very weak anchoring, there is no defect. For strong normal and normal anchoring, there exists a hedgehog and Saturn ring defect respectively, as shown in Fig. 2.8a and Fig. 2.8b. For planar anchoring on the particle surface, there is a pair of boojum defects, as seen in Fig. 2.8c. In all cases, the orientation of the director is uniform when far away

from the particle. The configuration of the director is dipolar in  $a$ , and quadrupolar in  $b$  and  $c$ . Small particles, i.e. with a strongly curved spherical surface, tend to have Saturn rings around them while larger particles, i.e. with a lower Gaussian curvature, tend to be accompanied by a hyperbolic point hedgehog. The dipolar or quadrupolar characteristics are also dependent on external fields, confinement, and flow. For very thin nematic layers, a quadrupolar structure with a Saturn ring is more likely to occur.

Expressing the inclusion of the particle in the Beris-Edwards model formalism, the total force on the particle consists of a thermotropic contribution  $\mathbf{F}^{(LC)}$  and a hydrodynamic contribution  $\mathbf{F}^{(HD)}$ . The thermotropic contribution is the integral of the gradient of the stress tensor  $\mathbf{\Pi}^{(LC)}$  in Eq. (2.72) over the surface  $S$  of the particle. This can be separated into contributions from the bulk and gradient free energy:

$$\begin{aligned}
F_\alpha^{(LC)} &= \int_S \partial_\beta \Pi_{\alpha\beta}^{(LC)} dS \\
&= \int_S \partial_\beta \left( \Pi_{\alpha\beta}^{(b)} + \Pi_{\alpha\beta}^{(g)} \right) dS \\
&= F_\alpha^{(b)} + F_\alpha^{(g)}.
\end{aligned} \tag{2.82}$$

Splitting the molecular field  $\mathbf{H}$  in Eq. (2.69) into terms that contain only bulk and gradient contributions,

$$\begin{aligned}
H_{\alpha\beta}^{(b)} &= -A_0(1 - \gamma/3)Q_{\alpha\beta} + A_0\gamma(Q_{\alpha\mu}Q_{\mu\beta} - \frac{1}{3}Q_{\mu\nu}^2\delta_{\alpha\beta}), \\
&\quad -A_0\gamma Q_{\mu\nu}^2 Q_{\alpha\beta}
\end{aligned} \tag{2.83}$$

$$H_{\alpha\beta}^{(g)} = \kappa_0\partial_\alpha\partial_\mu Q_{\mu\beta} + \kappa_1\partial_\mu(\partial_\mu Q_{\alpha\beta} - \partial_\alpha Q_{\mu\beta}), \tag{2.84}$$

we obtain together with Eqs. 2.74, 2.76 and 2.77 for the bulk contribution

$$\begin{aligned}
\Pi_{\alpha\beta}^{(b)} &= f_b - \xi H_{\alpha\mu}^{(b)}(Q_{\mu\beta} + \frac{1}{3}\delta_{\mu\beta}) - \xi(Q_{\alpha\mu} + \frac{1}{3}\delta_{\alpha\mu})H_{\mu\beta}^{(b)} \\
&\quad + 2\xi(Q_{\alpha\beta} + \frac{1}{3}\delta_{\alpha\beta})Q_{\mu\nu}H_{\mu\nu}^{(b)} + Q_{\alpha\mu}H_{\mu\beta}^{(b)} - H_{\alpha\mu}^{(b)}Q_{\mu\beta}
\end{aligned} \tag{2.85}$$

and for the gradient contribution

$$\begin{aligned}
\Pi_{\alpha\beta}^{(g)} &= \omega - \xi H_{\alpha\mu}^{(g)} (Q_{\mu\beta} + \frac{1}{3}\delta_{\mu\beta}) - \xi (Q_{\alpha\mu} + \frac{1}{3}\delta_{\alpha\mu}) H_{\mu\beta}^{(g)} \\
&\quad + 2\xi (Q_{\alpha\beta} + \frac{1}{3}\delta_{\alpha\beta}) Q_{\mu\nu} H_{\mu\nu}^{(g)} + Q_{\alpha\mu} H_{\mu\beta}^{(g)} - H_{\alpha\mu}^{(g)} Q_{\mu\beta} \\
&\quad + \kappa_0 \partial_\alpha Q_{\mu\beta} \partial_\nu Q_{\mu\nu} + \kappa_1 \partial_\alpha Q_{\mu\nu} (\partial_\beta Q_{\mu\nu} - \partial_\mu Q_{\nu\beta}).
\end{aligned} \tag{2.86}$$

The hydrodynamic contribution to the force on the particle is also given through the surface integral of the gradient of the hydrodynamic stress tensor  $\mathbf{\Pi}^{(HD)}$ , seen in Eq. (2.78) over the particle surface  $S$  as

$$F_\alpha^{(HD)} = \int_S \partial_\beta \Pi_{\alpha\beta}^{(HD)} dS. \tag{2.87}$$

## 2.12 Experimental background of liquid crystal microfluidics

Liquid crystal microfluidics, sometimes referred to as topological microfluidics [100], involves the investigations of liquid crystals in microchannel environments. The constraints of such channels result in an interplay of surface anchoring conditions, confinement and flow parameters leading to new phenomena. Some examples of experimental research done that in the area of topological microfluidics are shown in Fig. 2.9. The experimental investigations into nematic liquid crystals in microchannels developed through advancements in photo-aligning techniques [105] [106]. This lead way into answering some fundamental questions about the flow behaviour of anisotropic fluids, although such research is still more of a novelty. We can expand more on the research presented in Fig. 2.9. In the first instance, we note that the creation of a disclination line in a microfluidic channel is possible through hybrid anchoring conditions such that in the presence of the flow the line is stabilised in the center of the channel and in the absence of flow it collapses towards one of the channel walls [67]. Additionally, by using planar anchoring on the walls and varying the Ericksen numbers, further flow and confinement induces the formation of disclination lines in the vertical direction,

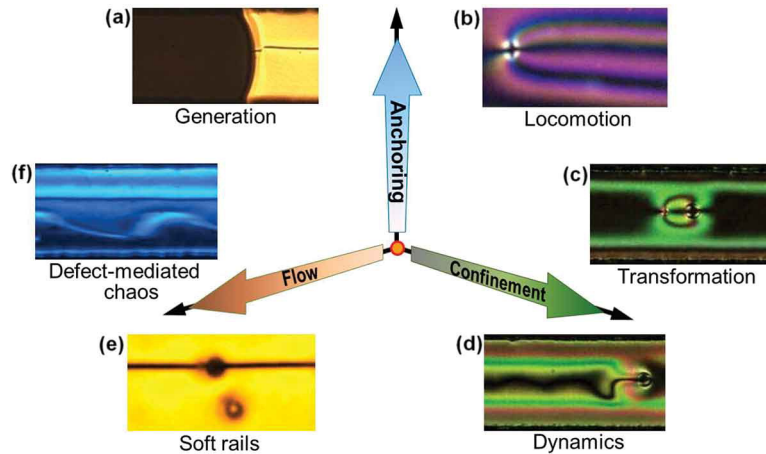


Figure 2.9: Many phenomena can be observed by tuning the flow, anchoring, and confinement conditions in topological microfluidics. Some examples are shown here in the polarisation optical micrographs. (a) Topological defect line generated at the air-NLC meniscus during the filling up of a microchannel by 5CB [67]; (b) flow-induced locomotion of an integer defect leads to imprinted director pattern within a microchannel [101]; snapshots of a defect structure due to flow past at a micropillar undergoing (c) topological transformation and (d) director field reorientation, respectively [102]; (e) topological defect line used as a soft rail to transport colloidal microcargo [103]; and (f) defect-mediated chaotic flow of nematic 5CB at very low Reynolds numbers [104]. Reprinted from [100] with permission from Taylor & Francis.

reorientation to a horizontal direction, pinning in a single direction and eventually chaotic free flowing disclinations as the Ericksen numbers are increased [101]. The observations of those disclination lines were then used to show that guided transport of microscopic cargo in microfluidic devices is possible experimentally through those lines [103]. Confinement is also a potential avenue towards self-assembly and steering organisation, however it presents unique challenges as the methods and techniques are often system-specific and would require interdisciplinary collaboration as well as conceptual and technological advancements [107].

The experimental results discussed above relied on the anchoring conditions, confinement or a combination of the two to create the topological defects, however introducing colloids can also lead to the creation of such defects and changes in overall system behaviours as a result. When thinking of the simplest case, that is introducing a static fixed colloid subject to flow, it turns out it becomes more difficult. In simulations



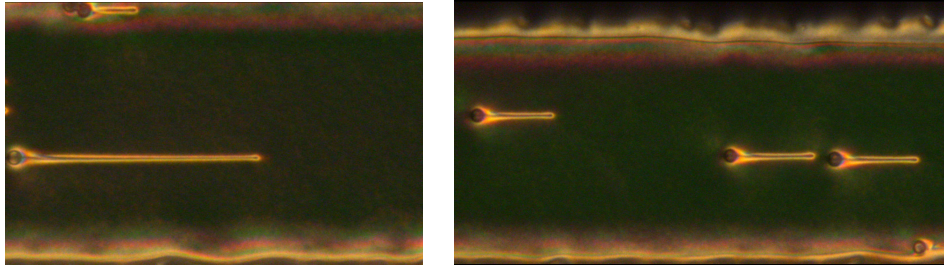


Figure 2.10: Colloidal particles in 5CB in a microfluidic channel with flow. The image on the left shows extensive elongation of the defect, while the image on the right shows shorter elongation of the defects. Image courtesy of Rok Stanc.

the particle can be fixed at a chosen position in a straightforward manner. Experimentally however, that is not the case. The current methods used to keep particles in place when in flow rely on optical tweezers. While it is an important technique with many applications, it increases the temperature of the fluid enough that when applied to a common liquid crystal material such as 5CB it locally changes the mesophase into the isotropic region. The defect behaviour around a fixed particle can not be directly compared to experiments due to the difficulty of creating such a set up without losing either liquid crystal behaviour or fixing the position. As an alternative, an experimental study was done by Sengupta et al., where a cylindrical micro-pillar was introduced that allowed to explore the morphology of the topological defect around a fixed obstacle [102]. The observed elongation of the defect is a particularly relevant result to note here. Additionally, it is possible to observe the defects around unfixed colloidal particles in flow. The elongation of the defect structure has been obtained experimentally during a research collaboration with Prof Uroš Tkalec at the University of Ljubljana in Slovenia. This is shown in Fig. 2.10. This was a promising result, as this defect elongation has now been observed in simulations and in experiments. However, the defect types are different in the two case scenarios. In simulation, in our static case we use small particles that have Saturn ring defects around them which then elongate with higher fluid velocities. As the particles are small, we do not have any hyperbolic hedgehog defects. In the experimental case, the particles are much larger and highly confined, with hyperbolic hedgehog defect. Those hyperbolic hedgehog defects can

elongate in flow, and when the flow is switched off they return to the hedgehog defect. In order to be able to directly compare the results of the simulations and the experiments there are different options available. One option would be to obtain hedgehog defects in simulations. To achieve that, one can either drastically increase the size of the particle, and in turn the size of the system and computational resources, or increase the anchoring strength on the particle. The needed increase in the anchoring strength for our particles was too high to obtain stable simulations. The massive increase in particle and system size was beyond the scope of the project in terms of computational resources and time constraints. A second option would be to obtain Saturn ring defects around the colloids in experiments. In order to do that, either the channel size needs to be increased, or the particles size would need to be much smaller. There is a limit of how small the particles can be to maintain resolution under cross-polarisers. The manufacture of different channels was not feasible at the time of the collaboration due to the experimental lab undergoing restructuring. As such, there is scope for further research into the highly confined hyperbolic hedgehogs and Saturn rings in simulation and in experiments respectively.

A lot of the work done in the field of liquid crystal colloids is focused on effective particle dispersion techniques or on topological defect configurations around a small number of particles that are explored through simulations [108]. A recent experimental study [108] however has demonstrated how large-scale colloidal aggregation in liquid crystal produces significantly different morphologies to aggregates formed in ordinary isotropic solvents. The usual difficulties of achieving a well dispersed initial colloid distribution under good imaging conditions were overcome in this study. This is a promising result in terms of methods used for imaging. However so far we could not find experimental research on flow induced nematic colloid aggregation within microfluid channels. We hope that our investigation of individual particle migration and advection behaviours, which is then extended to large scale simulations with much higher concentration of the colloids (many particle systems), can lead to further experimental activity into this unexplored area of research. As we focus on simulations, we will discuss the simulation methods used in depth in the next chapter.

## Chapter 3

# Simulation methods

### 3.1 Fluid dynamics and simulation approaches

Fluid dynamics is a discipline that is infamous for its complexity, with only a few basic examples of flow regimes that can be solved analytically. Those simple cases include the Couette and Poiseuille flow explained before (see Fig. 2.7). Complex geometries and non-trivial boundary conditions are therefore solved by using numerical methods, which can be just as difficult to resolve requiring large computational resources, narrow scope of application or a combination of both. A typical fluid flow problem will use a simulation method that has a relevant length and timescale. The order of the length and time scales is illustrated in Fig. 3.1, showing where particular models fit within that scope. In the classical mechanics description, the following values are notable:  $l_a$  which is the size of an atom or molecule of the fluid;  $l_{mfp}$  the mean distance travelled between two collisions;  $l$  which is the typical scale for gradients of some macroscopic properties; and  $l_s$  the system size. They are shown in Fig. 3.1, ordered by their size. On the opposite axis is the timescale, which also contains notable times. At shortest timescale the collision time  $t_c$  is given by  $t_c \approx l_a/v_T$ , where  $v_T$  is the average thermal velocity of the molecules. This thermal velocity  $v_T$  is not the same as the macroscopic fluid velocity  $u$ , and in fact  $u \ll v_T$ . In the standard kinetic theory approach, it is usually assumed that the collisions happen instantaneously, that is,  $t_c \rightarrow 0$ . The next

slightly longer time of interest is the mean flight time between two successive collisions  $t_{mfp}$  found by  $l_{mfp}/v_T$ . This timescale is where the bulk of the kinetic theory is applied to, with the collision events moving the system into a local equilibrium.

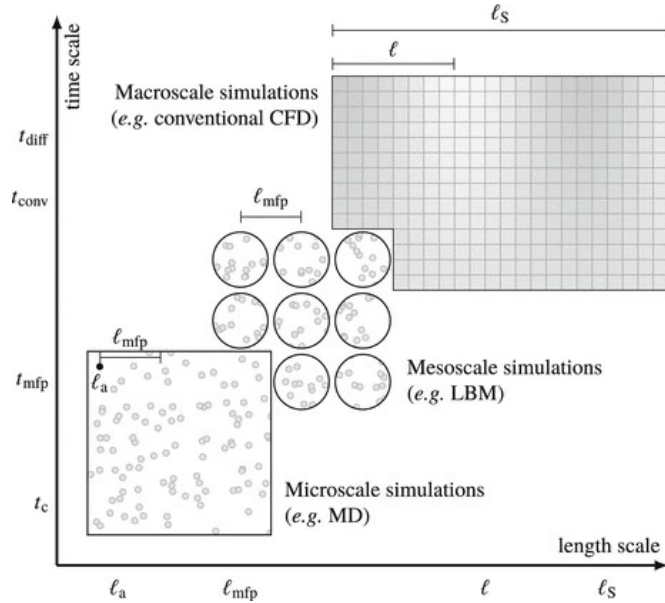


Figure 3.1: Length and time scales of common fluid dynamics problems. Simulation techniques can be chosen depending on the level of detail and computational cost. CFD stands for computational fluid dynamics, LBM stands for lattice Boltzmann method and MD stands for molecular dynamics. Figure from [109]. Reproduced with permission from Springer Nature.

It is common to refer to three particular descriptions: the microscopic, mesoscopic, and macroscopic, in the context of fluid simulations. Here, the microscopic approach means treating the fluid as one composed of individual molecules, whereas the macroscopic description is a fully continuous method in which the fluid has properties such as density and momentum. Due to these differences, a microscopic system is governed by Newton's laws of motion while the macroscopic system uses the Navier Stokes equations. The mesoscopic method is nestled in between the aforementioned descriptions - it does not follow individual atoms, but tracks the representative collections of molecules. It is based on the kinetic theory and its particle distribution function, and it forms the underlying theory behind the lattice Boltzmann method [109].

### 3.1.1 Boltzmann equation

As a quick introduction about this underlying theory we will only briefly touch on the Boltzmann equation and what it does, before moving to the explanation of the lattice Boltzmann method. The Boltzmann equation describes the dynamics of a gas on a mesoscopic scale. It uses the distribution function  $f(\mathbf{x}, \boldsymbol{\xi}, t)$  and its evolution in time. For brevity, we drop the explicit notation of the dependence of the distribution function on the position  $\mathbf{x}$ , particle velocity  $\boldsymbol{\xi}$ , and time  $t$ . Taking the total differential with respect to time and using the Newton's second law which gives the body force such that  $\frac{d\xi_\beta}{dt} = \frac{F_\beta}{\rho}$ , we get the Boltzmann equation:

$$\frac{df}{dt} = \frac{\partial f}{\partial t} + \xi_\beta \frac{\partial f}{\partial x_\beta} + \frac{F_\beta}{\rho} \frac{\partial f}{\partial \xi_\beta}. \quad (3.1)$$

A different commonly used notation for the total differential is  $\Omega(f) = \frac{df}{dt}$ . This equation, Eq. (3.1), can be thought of as an advection equation, with the first two terms on the right-hand side exemplifying the distribution function being advected with the velocity  $\boldsymbol{\xi}$  of its particles. The remaining term illustrates the forces affecting that velocity. On the left hand side the total differential represents the local redistribution of  $f$  due to collisions. Because of that, the term  $\Omega(f)$  is also referred to as the collision operator. The Boltzmann equation leads into the fluid dynamic equations on the macroscopic level from the mesoscale. By solving the Boltzmann equation, that solution can often be used to find the solution of the Navier-Stokes equations for the same given case. Not all solutions of the Boltzmann equation will result in a solution to the Navier-Stokes, as the former equation is more general, however it is a sound method of solving the problem at hand. However, analytically it is even more complex to attempt to solve the Boltzmann equation, as it is a function of seven parameters:  $x, y, z, \xi_x, \xi_y, \xi_z, t$  that is position in three dimensions, particle velocity in three dimensions, and time respectively. This is two more than the Navier-Stokes, which include density  $\rho$ , pressure  $p$ , and the three velocity components  $u_x, u_y, u_z$ . Nonetheless, if we choose to solve it numerically, then we may indirectly find the solution to the Navier Stokes. In fact, the

numerical approach to solving the Boltzmann equation is much simpler to implement and parallelise. This is because the force-free Boltzmann equation in essence describes the advection of the distribution function  $f$  with the particle velocity  $\xi$ , with the source term  $\Omega(f)$  depending only on the local values of  $f$  and not on gradients of it.

Conventional methods, such as finite difference or finite volume, directly discretise the fluid dynamics equations. The complication with those finite difference or volume methods is that to discretise the advection term  $(\mathbf{u} \cdot \nabla)\mathbf{u}$  complex iterative numerical schemes with approximation errors have to be used. On the other hand, the discretised Boltzmann equation results in an exact advection as it takes a differing approach. As all models, it is not well suited for all conceivable applications. For example in its simplest form it is only appropriate for low Mach numbers.

### 3.2 Lattice Boltzmann method: an outline

Before focusing on the more involved derivation of the lattice Boltzmann method, we will first provide a brief outline of the method as an initial introduction that we will then expand upon as appropriate in the later sections of the chapter.

The lattice Boltzmann method uses a fully discretised version of the Boltzmann equation and focuses on the discrete-velocity distribution function  $f_i(\mathbf{x}, t)$ , which is also commonly referred to as the particle populations. This function represents the density of particles with velocity  $\mathbf{c}_i = (c_{ix}, c_{iy}, c_{iz})$  at a position  $\mathbf{x}$  and some time  $t$ . Thus the mass density  $\rho$  momentum density  $\rho\mathbf{u}$  can be obtained through weighted sums known as the moments of  $f_i$ :

$$\rho(\mathbf{x}, t) = \sum f_i(\mathbf{x}, t), \quad \rho\mathbf{u}(\mathbf{x}, t) = \sum \mathbf{c}_i f_i(\mathbf{x}, t). \quad (3.2)$$

What distinguishes the discrete  $f_i$  and continuous  $f$  distribution function, is that all the argument variables of  $f_i$  (i.e. position in three dimensions and time) are discrete, as the name suggests. The  $f_i$  is defined at certain times  $t$ , separated by a time step  $\Delta t$ , at the points  $\mathbf{x}$  in a square lattice with spacing  $\Delta x$ . The subscript  $i$  in  $f_i$  refers to

$\mathbf{c}_i$ , which is a discrete set of velocities  $\mathbf{c}_i$ .

The time step  $\Delta t$  represents a time resolution and the lattice spacing  $\Delta x$  represents a space resolution, in any set of units. Hence, any system could be chosen, for example metric or Imperial units, however the most common choice is the lattice units. This is a simple set of artificially scaled units such that  $\Delta t = 1$  and  $\Delta x = 1$ . It is done that way as the numerical schemes work well with quantities close to 1. As with any measurement system, the lattice units can be converted to the more standard SI unit when needed. Another way to make sure that the underlying behaviour is realistic in two different systems of measurement is to use the similarity argument. This comes from the reasoning that fluid flows that share the same dimensionless numbers determine the same physics when scaled by the typical length and velocity scales in the problem at hand. The dimensionless numbers include for example Reynolds, Knudsen, and Mach numbers.

The set of discrete velocities  $\mathbf{c}_i$  is joined together with a set of weighting coefficients  $w_i$  to create a velocity set  $\{\mathbf{c}_i, w_i\}$ . These velocity sets are commonly denoted in the format  $DdQq$ , where  $d$  is the number of spatial dimensions of the velocity set, and  $q$  is the number of velocities within the set. Some standard sets used to solve the Navier-Stokes equations are D1Q3, D2Q9, D3Q19, and D3Q27, with more detailed overview shown in Section 3.3.1. The explicit form of the relevant velocity sets is included in Tab. 3.1. As is the case in many choices when it comes to simulations, there is a trade-off between factors that minimise memory and computational resource requirements, such as smaller velocity sets e.g. D315, and higher degree of accuracy, given by larger sets such as D3Q27. In 3 dimensions the most common choice is the D3Q19 set, and it is the set chosen for this work.

Through discretising the Boltzmann equation in velocity space (see Section 3.3), and physical space and time (see Section 3.4) we obtain the lattice Boltzmann equation

$$f_i(\mathbf{x} + \mathbf{c}_i \Delta t, t + \Delta t) = f_i(\mathbf{x}, t) + \Delta t \Omega_i(\mathbf{x}, t). \quad (3.3)$$

This expression shows that the particles  $f_i(\mathbf{x}, t)$  move with a velocity  $\mathbf{c}_i$  to an adjoining

point  $\mathbf{x} + \mathbf{c}_i \Delta t$  at the consequent time step  $t + \Delta t$ . Simultaneously, the particles are affected by a collision operator  $\Omega_i$ , which models particle collisions by redistributing particles among the populations  $f_i$  at every site. This is illustrated in Fig. 3.2. Gen-

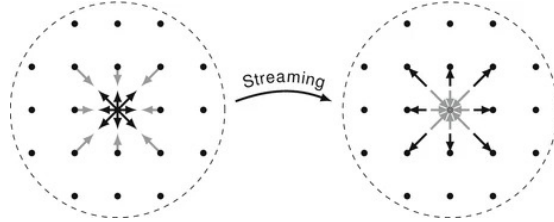


Figure 3.2: Particles streaming from the center node to the adjoining nodes. The left side shows the post-collision distributions  $f_i^*$  before streaming, and the right side shows the pre-collision distributions  $f_i$  after streaming. Figure from [109]. Reproduced with permission from Springer Nature.

erally, the velocity sets  $\{\mathbf{c}_i, w_i\}$  are selected such that any vector  $\mathbf{c}_i \Delta t$  points from a lattice site to a neighbouring lattice site. This avoids a situation where the populations  $f_i$  are trapped between lattice sites, guaranteeing that they will reach another site during the time step  $\Delta t$ .

Expanding on the collision operators, the collisions must conserve the quantities of mass, momentum, and in a monoatomic case, translational energy. Those can be expressed as moments of the collision operator, and are the mass conservation:

$$\int \Omega(f) d^3 \xi = 0, \quad (3.4)$$

and momentum conservation,

$$\int \boldsymbol{\xi} \Omega(f) d^3 \xi = \mathbf{0}. \quad (3.5)$$

The original collision operator considers all possible outcomes of two-particle collisions for any choice of inter molecular forces, resulting in a cumbersome double integral over velocity space. For a collision operator to be practical it needs to obey the conservation laws, and it must ensure that the distribution function  $f$  locally evolves towards the equilibrium  $f_{eq}$ . The BGK operator, named after its inventors Bhatnagar, Gross, and Krook, is the simplest operator that follows both rules, although it is not as exact as



the original Boltzmann operator:

$$\Omega_i(f) = -\frac{f_i - f_i^{eq}}{\tau}. \quad (3.6)$$

This is the simplest suitable operator for the Navier-Stokes simulations. It relaxes the populations  $f_i$  towards equilibrium  $f_i^{eq}$  at a rate given by the relaxation time  $\tau$ . The value of  $\tau$  dictates the transport coefficients, such as heat diffusivity and viscosity. There are however other options available. They include the two-relaxation time (TRT) or multiple relaxation time (MRT). Those other possible collision operators use additional relaxation times for increased accuracy (especially for large viscosities) and stability (particularly for small viscosities). In many cases the BGK model is elegant and efficient, despite its aforementioned limitations. The main difference between the BGK and the original lattice Boltzmann operator is in the prediction of the Prandtl number, introduced earlier, where the BGK operator anticipates  $Pr = 1$ , while the Boltzmann's original operator correctly predicts  $Pr \approx 2/3$  for monoatomic gases [110]. The code used in this thesis uses the MRT collision operator for increased stability and accuracy [111].

The equilibrium in Eq. (3.6) expands to

$$f_i^{eq}(\mathbf{x}, t) = w_i \rho \left( 1 + \frac{\mathbf{u} \cdot \mathbf{c}_i}{c_s^2} + \frac{(\mathbf{u} \cdot \mathbf{c}_i)^2}{2c_s^4} - \frac{\mathbf{u} \cdot \mathbf{u}}{2c_s^2} \right) \quad (3.7)$$

with the weights  $w_i$  determined by the preferred velocity set. The equilibrium  $f_i^{eq}$  depends on the local quantities of density and fluid velocity only, and is such that its moments are equivalent to the moments of  $f_i$ . The latter means that  $\sum_i f_i^{eq} = \sum_i f_i = \rho$  and  $\sum_i \mathbf{c}_i f_i^{eq} = \sum_i \mathbf{c}_i f_i = \rho \mathbf{u}$ . Consequently, mass and momentum are conserved in collisions. Mathematically, this means that  $\sum_i \Omega_i = 0$  and  $\sum_i \mathbf{c}_i \Omega_i = \mathbf{0}$ . Additionally, by using the  $f_i$  moments, the fluid velocity is found to be  $\mathbf{u}(\mathbf{x}, t) = \rho \mathbf{u}(\mathbf{x}, t) / \rho(\mathbf{x}, t)$ .

Comprehensively, the fully discretised lattice Boltzmann equation with the BGK

collision operator is given by

$$f_i(\mathbf{x} + \mathbf{c}_i \Delta t, t + \Delta t) = f_i(\mathbf{x}, t) - \frac{\Delta t}{\tau} (f_i(\mathbf{x}, t) - f_i^{eq}(\mathbf{x}, t)). \quad (3.8)$$

For clarity, we can separate this formula into two unique parts performed consecutively. The initial step is collision (or relaxation)

$$f_i^*(\mathbf{x}, t) = f_i(\mathbf{x}, t) - \frac{\Delta t}{\tau} (f_i(\mathbf{x}, t) - f_i^{eq}(\mathbf{x}, t)), \quad (3.9)$$

where  $f_i^*$  tracks the distribution function after collisions and  $f_i^{eq}$  is found from Eq. (3.7). In terms of implementation of this collision step, it is more convenient to adjust the form of the expression for higher efficiency like so:

$$f_i^*(\mathbf{x}, t) = f_i(\mathbf{x}, t) \left(1 - \frac{\Delta t}{\tau}\right) + f_i^{eq}(\mathbf{x}, t) \frac{\Delta t}{\tau}, \quad (3.10)$$

which simplifies particularly for  $\tau/\Delta t = 1$ , resulting in  $f_i^*(\mathbf{x}, t) = f_i^{eq}(\mathbf{x}, t)$ . The second step is streaming (or propagation)

$$f_i(\mathbf{x} + \mathbf{c}_i \Delta t, t + \Delta t) = f_i^*(\mathbf{x}, t) \quad (3.11)$$

shown and explained visually in Fig. 3.2, streaming the particles to adjoining nodes.

In summary, the lattice Boltzmann method is a two step process consisting of collision and streaming. The collision is a local algebraic operation by using the density  $\rho$  and macroscopic velocity  $\mathbf{u}$  to find the equilibrium distributions  $f_i^{eq}$  and post-collision distribution  $f_i^*$ . After that step is completed, the resulting distribution  $f_i^*$  is streamed to neighbouring nodes. Those two operations correspond to a single time step that elapses once they complete, and the cycle can start again. Having established the idea behind the procedure, it is not necessarily immediately clear how it relates back to the Navier-Stokes equations.

### 3.2.1 Connecting the lattice Boltzmann equation to the Navier Stokes equations

We have shown how the macroscopic behaviour of the undiscretised Boltzmann equation behaves in accordance to the continuity equation and the general Cauchy momentum equation with an unknown stress tensor, without specifically proving that they are in fact linked. Here we use the classical multiscale tool of the Chapman-Enskog analysis. However, there are alternative methods to show that the lattice Boltzmann equation is connected to the macroscopic equations [112], such as asymptotic expansion developed by Sone [113] or Maxwellian iteration described by Ikenberry and Truesdell [114].

As a historical note, this approach is named after two mathematical physicists, Sydney Chapman and David Enskog, who both independently developed similar methods of finding macroscopic equations from the Boltzmann equation with the original collision operator. Chapman later combined those two approaches in his book on the mathematical theory of non uniform gases into what is now known as the Chapman-Enskog analysis [112]. With more methods developed over the years, discussions about the equivalence of them were inevitable [115]. As a general conclusion, the work by Caiazzo et.al. [116] showed that the Chapman-Enskog analysis is a general expansion procedure that encompasses many multi-scale methods. This study makes the case that all expansions are equivalent, as long as the algorithm is stable, and the residues are of the same order therefore meaning that two expansion methods can therefore only differ in their range of applicability [116].

The details of the Chapman-Enskog analysis are given in Appendix A, showing how the link between the Boltzmann equation and the Navier Stokes equations. We can now be confident that the method is a sound approach for solving fluid dynamics problems that follow certain assumptions. Through the Chapman-Enskog analysis, we get the kinematic shear viscosity given by the relaxation time  $\tau$

$$\nu = c_s^2 \left( \tau - \frac{\Delta t}{2} \right) \quad (3.12)$$

with the kinematic bulk viscosity being  $\nu = 2\nu/3$ . Further more, the viscous stress

tensor can be obtained from  $f_i$  as

$$\sigma_{\alpha\beta} \approx - \left(1 - \frac{\Delta t}{2\tau}\right) \sum_i c_{i\alpha} c_{i\beta} f_i^{neq} \quad (3.13)$$

where the non-equilibrium distribution  $f_i^{neq} = f_i - f_i^{eq}$  gives the  $f_i$  deviation from equilibrium. It is usually not needed to explicitly state the form of this viscous stress tensor while running the simulations.

### 3.2.2 A simple lattice Boltzmann algorithm

After introducing an outline of the theory, now we can now give an example of a lattice Boltzmann algorithm one could use to use the method. Let us introduce a simple algorithm with no imposed boundary conditions or forces. To initialise the populations at the simulation start, we set the equilibrium such that  $f_i^{eq}(\mathbf{x}, t = 0) = f_i^{eq}(\rho(\mathbf{x}, t = 0), \mathbf{u}(\mathbf{x}, t = 0))$ . In many cases,  $\rho(\mathbf{x}, t = 0) = 1$  and  $\mathbf{u}(\mathbf{x}, t = 0) = \mathbf{0}$  are used. On

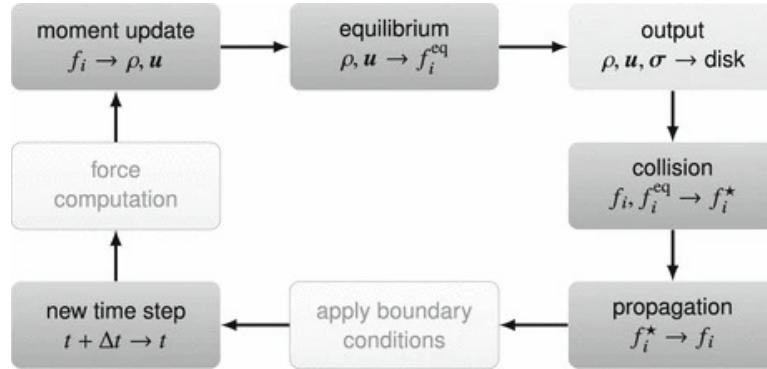


Figure 3.3: A flowchart depicting one cycle of the lattice Boltzmann algorithm. The dark grey boxes show the essential steps for the evolution of the solution. The output step shown in the top right corner is optional, saving the output data. The reduced opacity boxes show additional steps that can be included. Figure from [109]. Reproduced with permission from Springer Nature.

the whole, the essence of the LBM algorithm is a cyclical sequence of sub-steps, with a singular cycle corresponding to one time step, as visualised in the flowchart in Fig.

3.3. Writing it out, we get the following procedure:

1. Compute the macroscopic moments  $\rho(\mathbf{x}, t)$  and  $\mathbf{u}(\mathbf{x}, t)$  from  $f_i(\mathbf{x}, t)$  using Eq.

(3.2).

2. Find the equilibrium distribution function  $f_i^{\text{eq}}(\mathbf{x}, t)$  from Eq. (3.7).
3. (Optional) Write the  $\rho(\mathbf{x}, t)$ ,  $\mathbf{u}(\mathbf{x}, t)$ , and  $\boldsymbol{\sigma}(\mathbf{x}, t)$  to the hard disk for post-processing. The stress tensor can be found using Eq. (3.13).
4. Perform collision via Eq. (3.9).
5. Perform streaming using Eq. (3.11).
6. Increment the time step, by setting  $t$  to  $t + \Delta t$ , go back to step one, repeat until the last time step is reached.

The order of the sub-steps is necessary, as further steps are dependent on the results of earlier steps. This concludes the simplest example of a basic lattice Boltzmann method algorithm implementation.

Now that we have an outline of the lattice Boltzmann method in its simplest form, and what steps need to be taken, we can now focus on the derivations of the discretisation in the next two sections.

### 3.3 Discretisation in velocity

Since introducing the outline of the lattice Boltzmann method, we can now focus on some important derivations. Here, we will go from the Boltzmann equation to the lattice Boltzmann equation. To do that we will begin by deriving the velocity discretisation of the lattice Boltzmann equation. The complication of doing just that, is that the particle distribution function  $f(\mathbf{x}, \boldsymbol{\xi}, t)$  has a seven-dimensional space. Solving such a high-dimensional space is usually computationally expensive, requiring large-scale computing. However, this is often not needed, as we have found that the moments of the Boltzmann equation give the correct equations for mass, momentum and energy conservation. As a result, the underlying physics is not fully relevant if we are only interested in making sure we obtain the correct macroscopic behaviour.

The moments are the weighted integrals of  $f$  in velocity space. In actuality, there is a vast number of functions whose integrals are identical to that of  $f$ , and there are approaches to simplify the continuous Boltzmann equation without getting rid of the moment-based macroscopic behaviour. By discretising the continuous 3D velocity space we reduce the number of velocities to a smaller number of discrete velocities in a way that does not compromise the macroscopic equations. This can be performed using either the Hermite series expansion [117] or the Mach number expansion [118]. Both of the approaches will result in the same equilibrium form on the Navier-Stokes level. While the Mach number expansion is easier to follow, for a strong mathematical foundation we shall adhere to the Hermite series method. The other advantage of using the Hermite series is that in addition to obtaining suitable discrete velocity sets it can also be used to go beyond the conventional Navier-Stokes-Fourier equations and their limitations [117].

The Hermite approach relies on the observation that the equilibrium distribution function  $f_{\text{eq}}$  has a known exponential form such that the  $f_{\text{eq}}$  can be defined by the exponential weight function of Hermite polynomials, unlike the unknown distribution function  $f$ . Furthermore mass and momentum moments may be described by integrals of  $f_{\text{eq}}$  multiplied with Hermite polynomials. This is achieved by a two pronged approach, by firstly expressing  $f_{\text{eq}}$  in a reduced form through a truncated sum of Hermite polynomials. The second part is to then evaluate the integrals of the moments exactly as a discrete sum over the polynomial integrand evaluated at specific points  $\xi_i$  parallel to the  $x$ -axis. Hence, the equilibrium distribution function is converted from continuous to discrete in the velocity space. Having outlined our objective, we can now delve into the details of how to achieve it. We begin by non-dimensionalising the governing equations for simplicity reasons. Let's evoke the Boltzmann equation in a continuous velocity space

$$\frac{\partial f}{\partial t} + \xi_\alpha \frac{\partial f}{\partial x_\alpha} + \frac{f_\alpha}{\rho} \frac{\partial f}{\partial \xi_\alpha} = \Omega(f) \quad (3.14)$$

where  $\Omega(f)$  is the collision operator. As a reminder, the Boltzmann equation describes the evolution of the density of particles with velocity  $\xi$  at a position  $\mathbf{x}$  and time  $t$ . In

a homogeneous, steady, and force free situation, the solution is purely the equilibrium distribution function  $f_{\text{eq}}$ . It can be expressed by

$$f^{\text{eq}}(\rho, \mathbf{u}, T, \boldsymbol{\xi}) = \frac{\rho}{(2\pi RT)^{d/2}} e^{-(\boldsymbol{\xi}-\mathbf{u})^2/(2RT)} \quad (3.15)$$

where  $\rho$  is the density,  $\mathbf{u}$  is the fluid velocity,  $T$  is the temperature,  $d$  is the number of spatial dimensions, and  $R = k_B/m$  is gas constant given by the Boltzmann constant  $k_B$  and particle mass  $m$ .

In general terms, physical phenomena occur at relevant space and time scales. As an example, the average velocity of an unladen swallow is in the order of tens of metres per second [119]. It is useful to classify phenomena by their characteristic scales. To achieve that for fluid properties we can use the characteristic length  $l$ , velocity  $V$  and density  $\rho_0$ , with a resulting characteristic time scale being given by  $t_0 = l/V$ .

Following the convention of using stars to symbolise the non-dimensionalised variables, we can write the following non-dimensionalised derivatives

$$\frac{\partial}{\partial t^*} = \frac{l}{V} \frac{\partial}{\partial t}, \quad \frac{\partial}{\partial x^*} = l \frac{\partial}{\partial x}, \quad \frac{\partial}{\partial \xi^*} = V \frac{\partial}{\partial \xi}. \quad (3.16)$$

We then use that to rewrite the continuous Boltzmann to its non-dimensionalised form

$$\frac{\partial f^*}{\partial t^*} + \xi_\alpha^* \frac{\partial f^*}{\partial x_\alpha^*} + \frac{\mathbf{F}_\alpha^*}{\rho^*} \frac{\partial f^*}{\partial \xi_\alpha^*} = \Omega^*(f^*) \quad (3.17)$$

where  $f^* = fV^d/\rho_0$ ,  $\mathbf{F}^* = \mathbf{F}l/(\rho_0V^2)$ ,  $\rho^* = \rho/\rho_0$ , and  $\Omega^* = \Omega lV^2/\rho_0$ . Doing the same for the equilibrium distribution function, we obtain

$$f^{\text{eq}*} = \frac{\rho^*}{(2\pi\theta^*)^{d/2}} e^{-(\boldsymbol{\xi}^*-\mathbf{u}^*)^2/(2\theta^*)} \quad (3.18)$$

with the non-dimensionalised temperature  $\theta^* = RT/V^2$ . For notational brevity, we omit the  $*$  symbol, henceforth implying non-dimensionalised version of the lattice Boltzmann equations in this section unless specified otherwise. For simplicity, we follow an example of the Hermite series expansion in the force-free ( $\mathbf{f} = \mathbf{0}$ ) instance.

The conservation laws imply that the equilibrium distribution function and the particle distribution function coincide like so:

$$\int f(\mathbf{x}, \boldsymbol{\xi}, t) d^3\xi = \int f^{\text{eq}}(\rho, \mathbf{u}, \theta, \boldsymbol{\xi}) d^3\xi = \rho(\mathbf{x}, t), \quad (3.19)$$

$$\int f(\mathbf{x}, \boldsymbol{\xi}, t) \boldsymbol{\xi} d^3\xi = \int f^{\text{eq}}(\rho, \mathbf{u}, \theta, \boldsymbol{\xi}) \boldsymbol{\xi} d^3\xi = \rho \mathbf{u}(\mathbf{x}, t), \quad (3.20)$$

$$\int f(\mathbf{x}, \boldsymbol{\xi}, t) \frac{|\boldsymbol{\xi}|^2}{2} d^3\xi = \int f^{\text{eq}}(\rho, \mathbf{u}, \theta, \boldsymbol{\xi}) \frac{|\boldsymbol{\xi}|^2}{2} d^3\xi = \rho E(\mathbf{x}, t), \quad (3.21)$$

$$\int f(\mathbf{x}, \boldsymbol{\xi}, t) \frac{|\boldsymbol{\xi} - \mathbf{u}|^2}{2} d^3\xi = \int f^{\text{eq}}(\rho, \mathbf{u}, \theta, \boldsymbol{\xi}) \frac{|\boldsymbol{\xi} - \mathbf{u}|^2}{2} d^3\xi = \rho e(\mathbf{x}, t). \quad (3.22)$$

where  $\rho(\mathbf{x}, t)$  is the mass density,  $\rho \mathbf{u}(\mathbf{x}, t)$  is the momentum density,  $\rho E(\mathbf{x}, t)$  is the total energy density, and  $\rho e(\mathbf{x}, t)$  is the internal energy density.

The space and time dependence in  $f^{\text{eq}}$  only enters through  $\rho(\mathbf{x}, t)$ ,  $\mathbf{u}(\mathbf{x}, t)$ , and  $\theta(\mathbf{x}, t)$ . The conserved quantities on the right hand side of Eq. (3.22) may be expressed as integrals of the distribution functions in velocity space.

In order to discretise the velocity space using the Hermite polynomials we need to first introduce what they are, their properties, and how to apply them to the equations of interest. The details of that are expanded upon in Appendix B. There, we show how the coefficients in a Hermite series expansion of the equilibrium distribution function  $f^{\text{eq}}$  are related to the conserved moments of density, momentum, and energy. The Hermite series expansion can also be applied to the particle distribution function  $f$  such that the conserved quantities are given by the expansion coefficients. The approximation of the equilibrium distribution function up to the third moment can be explicitly written as

$$\begin{aligned} f^{\text{eq}}(\rho, \mathbf{u}, \theta, \boldsymbol{\xi}) &\approx \omega(\boldsymbol{\xi}) \rho [1 + \xi_\alpha u_\alpha + (u_\alpha u_\beta + (\theta - 1) \delta_{\alpha\beta}) (\xi_\alpha \xi_\beta - \delta_{\alpha\beta})] \\ &= \omega(\boldsymbol{\xi}) \rho Q(\mathbf{u}, \theta, \boldsymbol{\xi}) \end{aligned} \quad (3.23)$$

After the Hermite series expansion there are still some tasks remaining to complete the discretisation of velocity. We begin by defining the  $n$  quantities  $f_i^{\text{eq}}(\mathbf{x}, t) = w_i \rho(\mathbf{x}, t) Q(\mathbf{u}(\mathbf{x}, t), \theta(\mathbf{x}, t), \boldsymbol{\xi}_i)$  as the equilibrium distribution function that is related to



the velocity  $\boldsymbol{\xi}$ . However rather than looking at a continuous function  $f^{\text{eq}}(\boldsymbol{\xi})$ , we shall only focus on a finite set of quantities such that  $f_i^{\text{eq}} = f^{\text{eq}}(\boldsymbol{\xi})$

$$f_i^{\text{eq}} = w_i \rho \left[ 1 + \xi_{i\alpha} u_\alpha + \frac{1}{2} (u_\alpha u_\beta + (\theta - 1) \delta_{\alpha\beta}) (\xi_{i\alpha} \xi_{i\beta} - \delta_{\alpha\beta}) \right]. \quad (3.24)$$

This equation can be further simplified by using the isothermal assumption, which implies  $\theta = 1$ , thus removing the temperature from the equilibrium distribution function. Finally, we have obtained the ultimate discrete equilibrium distribution

$$f_i^{\text{eq}} = w_i \rho \left( 1 + \frac{c_{i\alpha} u_\alpha}{c_s^2} + \frac{u_\alpha u_\beta (c_{i\alpha} c_{i\beta} - c_s^2 \delta_{\alpha\beta})}{2c_s^4} \right) \quad (3.25)$$

where  $c_s$  is the speed of sound. It is one of the most important equations for the lattice Boltzmann method. However we have to keep in mind that so far, only velocity has been discretised, meaning that the space and time variables are still continuous and enter the equilibrium distribution function as continuous moments of  $\rho(\mathbf{x}, t)$ ,  $\mathbf{u}(\mathbf{x}, t)$ , and  $\theta(\mathbf{x}, t)$ . The space and time discretisation will be discussed later on to obtain the eventual form of the lattice Boltzmann equations satisfactory for computational simulations.

Having discretised the equilibrium distribution function, we now do the same to the particle distribution function. The Hermite series expansion of it is given by

$$f(\mathbf{x}, \boldsymbol{\xi}, t) \approx \omega(\boldsymbol{\xi}) \sum_{n=0}^N \frac{1}{n!} \mathbf{a}^{(n)}(\mathbf{x}, t) \cdot \mathbf{H}^{(n)}(\boldsymbol{\xi}). \quad (3.26)$$

The first two of the coefficients of this expansion follow the conservation laws and as such are the same as the equilibrium distribution ones (in the case of the isothermal approximation, only density and momentum are considered). The discrete velocities  $\{\mathbf{c}_i\}$  are created such that the moments are conserved, hence following the same method to discretise the distribution function  $f$  will also ensure that the conservation laws are obeyed. For brevity it is unnecessary to repeat all the calculations done before. Using

the same approach as before, the discretised distribution function is

$$f_i(\mathbf{x}, t) = \frac{w_i}{\omega(\mathbf{c}_i)} f(\mathbf{x}, \mathbf{c}_i, t), \quad (3.27)$$

where  $w(\mathbf{c}_i)$  is added to comply with the Gauss-Hermite rule

$$\begin{aligned} \mathbf{a}^{(n)}(\mathbf{x}, t) &= \int f(\mathbf{x}, \mathbf{c}, t) \mathbf{H}^{(n)}(\mathbf{c}) d^d c = \int \frac{\omega(\mathbf{c})}{\omega(\mathbf{c})} f(\mathbf{x}, \mathbf{c}, t) \mathbf{H}^{(n)}(\mathbf{c}) d^d c \\ &\approx \sum_{i=1}^q \frac{w_i}{\omega(\mathbf{c})} f(\mathbf{x}, \mathbf{c}_i, t) \mathbf{H}^{(n)}(\mathbf{c}_i) = \sum_{i=1}^q f_i(\mathbf{x}, t) \mathbf{H}^{(n)}(\mathbf{c}_i). \end{aligned} \quad (3.28)$$

This means that there are now  $q$  functions  $f_i(\mathbf{c}_i)$ , each related to one discrete velocity  $\mathbf{c}_i$ . As before, they remain continuous in space and time. Now we can compose the discrete-velocity Boltzmann equation (not the lattice Boltzmann equation, as it is not fully explicit)

$$\partial_t f_i + c_{i\alpha} \partial_\alpha f_i = \Omega(f_i), \quad i = 1, \dots, q. \quad (3.29)$$

The macroscopic moments, that is density and momentum, are then found using the finite sums

$$\begin{aligned} \rho &= \sum_i f_i = \sum_i f_i^{\text{eq}}, \\ \rho \mathbf{u} &= \sum_i f_i \mathbf{c}_i = \sum_i f_i^{\text{eq}} \mathbf{c}_i \end{aligned} \quad (3.30)$$

instead of computing the integrals of the particle  $f(\boldsymbol{\xi})$  and equilibrium  $f^{\text{eq}}(\boldsymbol{\xi})$  distribution functions. The final matter that is left to discuss to conclude the discretisation of the velocity space is the details of the velocity sets and their properties.

### 3.3.1 Velocity Sets

The question about the choice of the velocity set is of import. As with many things in life, it is a balancing act. The chosen set needs to be sufficiently well-resolved to obtain consistent and accurate solutions to the Navier-Stokes or Navier-Stokes-Fourier equations. Yet, with an increase in the number of velocities, so do the computational

resources required to solve them. It is therefore crucial to choose a satisfactory set of velocities that is able to capture the underlying physics at an optimal numerical cost. For a comprehensive perspective of the historical choice of the velocity sets an interested reader is referred to the Chapters 3 and 5 of [120].

The accepted general notation for velocity sets uses their number of spatial dimensions  $d$  and discrete velocities  $q$  in the form  $DdQq$  [121]. Some common examples include D2Q9 and D3Q19 meaning 9 discrete velocities in two dimensions and 19 discrete velocities in three dimensions. A velocity set in the lattice Boltzmann algorithm is fully described by two sets of quantities: the velocities  $\{\mathbf{c}_i\}$  and their corresponding weights  $\{w_i\}$ . A third quantity can be derived from those sets: the speed of sound  $c_s$ .

It is relevant to note that the velocities in a set are not consistently numbered or ordered in the same way in literature. In some cases the indices go from 0 to  $q - 1$ , while others are counted from 1 to  $q$ , orders are seemingly random. For this reason the most common velocity sets are usually included in an illustrated form with numbered velocity vectors.

A velocity set generally will include one rest velocity with zero magnitude that corresponds to stationary particles. If the set includes the rest velocity, we will assign the index  $i = 0 : \mathbf{c}_0 = \mathbf{0}$  to it using the numbering system going from 0 to  $q - 1$ . If a set has no rest velocity, it will be counted from 1 to  $q$ .

There is more than one method of assembling the lattice Boltzmann velocity sets. From the Gauss-Hermite quadrature rule from before, we obtain the following sets: D1Q3, D2Q7, D2Q9, D3Q15, D3Q19, D3Q27. A different method would be to use lattice projection to obtain a  $(d - 1)$ -dimensional velocity set from an already known velocity set in  $d$  dimensions. Another possibility to consider is to find the general conditions that need to be satisfied by the velocity set. As usual, they need to conserve mass and momentum, but in addition to that they also need to conserve the rotational isotropy of the lattice [122]. What sufficiently isotropic means depends on the underlying physics, here we can assume that means all lattice Boltzmann method moments of the weight  $w_i$  used to solve the Navier-Stokes equations are solved up to the fifth

order. This suggests the subsequent conditions [123, 124]:

$$\begin{aligned}
\sum_i w_i &= 1, \\
\sum_i w_i c_{i\alpha} &= 0, \\
\sum_i w_i c_{i\alpha} c_{i\beta} &= c_s^2 \delta_{\alpha\beta}, \\
\sum_i w_i c_{i\alpha} c_{i\beta} c_{i\gamma} &= 0, \\
\sum_i w_i c_{i\alpha} c_{i\beta} c_{i\gamma} c_{i\mu} &= c_s^4 (\delta_{\alpha\beta} \delta_{\gamma\mu} + \delta_{\alpha\gamma} \delta_{\beta\mu} + \delta_{\alpha\mu} \delta_{\beta\gamma}), \\
\sum_i w_i c_{i\alpha} c_{i\beta} c_{i\gamma} c_{i\mu} c_{i\nu} &= 0,
\end{aligned} \tag{3.31}$$

where all the weights  $w_i$  are non-negative. A velocity set that does not satisfy these conditions is unsuitable for the lattice Boltzmann method as a Navier-Stokes solver.

As a straightforward approach, we can start with a brand new velocity set  $\{c_i\}$  and use Eq. (3.31) as a conditional factor to obtain the unknown weights  $w_i$  and the speed of sound  $c_s$ . If only a few velocities are chosen not all conditions of Eq. (3.31) will be satisfied at the same time, as is the case for the D2Q5 lattice (which only satisfies the first four equations). Choosing more velocities however, will lead to over-determination. This is the case for D3Q27, where the weights  $w_i$  and the speed of sound  $c_s$  are not unique and can vary [125]. This actually results in more versatility, as the free parameters can be used for optimisation of other properties, like for example stability.

The lattice Boltzmann method may be used to simulate advection-diffusion problems that have a lower level of isotropy, meaning that simply solving the first four equations of Eq. (3.31) is sufficient for this purpose. Larger velocity sets will be required for the solving of the Navier-Stokes-Fourier systems, as they include the energy equation and hence having higher moments that will need to be solved. Thus, the so self-styled extended lattices will need to be deployed to accommodate that.

A final note, before going over some common velocity sets for the hydrodynamics, is

that it is extraordinarily advantageous to specifically choose certain velocity sets. They should be constructed in such a way that all velocities directly connect the spatially and temporary discretised lattice sites, without off-lattice positions somewhere in between. This is achieved by using vectors  $\mathbf{c}_i$  such that all of their components are integer multiples of  $\Delta x/\Delta t$ . The prevailing choice in the literature is to set  $\Delta x$  and  $\Delta t$  to be equal to 1, and so the velocity vector components  $c_{i\alpha}$  are integers. It is entirely possible to not follow this condition in constructing the velocity sets [117, 126]. The velocity

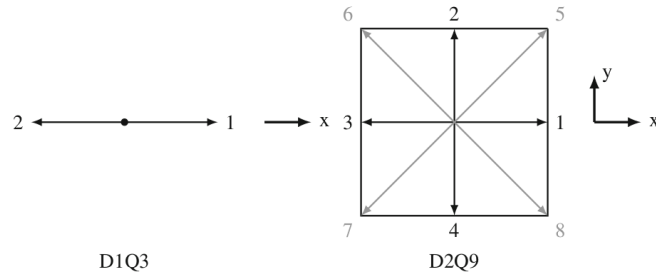


Figure 3.4: Visual representation of the D1Q3 and D2Q9 velocity sets. The edge length of the solid square is  $2\nabla x$ . Rest velocity vectors  $|\mathbf{c}_i| = 1$  and  $\sqrt{2}$  are shown in black and grey respectively. Figure from [109]. Reproduced with permission from Springer Nature.

sets of D1Q3 and D2Q9 are shown in Fig. 3.4, commonly used in the one and two dimensional simulations. For three dimensional simulations, the prevailing choices are the D3Q15, D3Q19, and less used D3Q27. Each of these schemes has different benefits and drawbacks. All recover the hydrodynamics to leading order, where most of the commonalities end. The most efficient computationally set is D3Q15 followed by less efficient D3Q19, that is consecutively less efficient than D3Q27. The truncation errors differ for all three, with the numerical errors usually being less significant for larger velocity sets. The larger velocity sets tend to have higher stability. The longstanding agreement disregarded D3Q27 as a viable choice, as it requires 40 % more memory and computing power than D3Q19. In more recent years, it was discovered [124] that a few truncation terms and non-linear momentum advection corrections are not actually rotationally invariant in D3Q15 and D3Q19, but they are isotropic in D3Q27. As a result of this, the lack of the isotropy in the lower sets may lead to issues for non-

linear phenomena questions. This becomes particularly important for simulations of, for example, high Reynolds number flows [127, 128]. As such, the D3Q27 is the best choice for modelling that includes turbulence, with D3Q19 continuing to be a good choice for laminar flow.

The velocity sets described in the sections above are written out in Tab. 3.1, including their properties of length and weight, with the speed of sounds for all given by  $c_s = 1/\sqrt{3}$ .

Notation	Velocities $\mathbf{c}_i$	Number	Length $ \mathbf{c}_i $	Weight $w_i$
D1Q3	(0)	1	0	2/3
	( $\pm 1$ )	2	1	1/6
D2Q9	(0,0)	1	0	4/9
	( $\pm 1,0$ ), (0, $\pm 1$ )	4	1	1/9
	( $\pm 1, \pm 1$ )	4	$\sqrt{2}$	1/36
D3Q15	(0,0,0)	1	0	2/9
	( $\pm 1,0,0$ ), (0, $\pm 1,0$ ), (0,0, $\pm 1$ )	6	1	1/9
	( $\pm 1, \pm 1, \pm 1$ )	8	$\sqrt{3}$	1/72
D3Q19	(0,0,0)	1	0	1/3
	( $\pm 1,0,0$ ), (0, $\pm 1,0$ ), (0,0, $\pm 1$ )	6	1	1/18
	( $\pm 1, \pm 1,0$ ), ( $\pm 1,0, \pm 1$ ), (0, $\pm 1, \pm 1$ )	12	$\sqrt{2}$	1/36
D3Q27	(0,0,0)	1	0	8/27
	( $\pm 1,0,0$ ), (0, $\pm 1,0$ ), (0,0, $\pm 1$ )	6	1	2/27
	( $\pm 1, \pm 1,0$ ), ( $\pm 1,0, \pm 1$ ), (0, $\pm 1, \pm 1$ )	12	$\sqrt{2}$	1/54
	( $\pm 1, \pm 1, \pm 1$ )	8	$\sqrt{3}$	1/216

Table 3.1: Most commonly used velocity sets appropriate for the Navier-Stokes simulation. Reproduced from [109].

### 3.4 Discretisation in space and time

Up to this point, the velocity is the only quantity that has been discretised. To finalise the formulation of the fully discretised lattice Boltzmann equation, the space and time

remain to be discretised.

In conventional computational fluid dynamics methods, such as finite volume or finite elements, the space discretisation is somewhat arbitrary. This is because each volume or element has many possible shapes that can be chosen, including options such as triangles, pyramids, tetrahedra or hexagons. The classical lattice Boltzmann method is in comparison less flexible, built on uniform and structured grids. In modern day, new approaches are achievable, relying on either discretisation on unstructured grids [129, 130] or by local grid refinement on structured grids, where [131] gives an overview of it. While the other methods are possible, it is standard to use a structured grid that also implies a strong coupling between the spatial and temporal discretisation in the lattice Boltzmann method.

Historically, the original lattice Boltzmann algorithm assumes that the populations  $f_i$  move with a velocity  $\mathbf{c}_i$  from one lattice site to another. After a single time step  $\Delta t$ , each population should completely reach a neighbouring site. For that to be the case, two conditions must be met. Firstly, the underlying spatial lattice is uniform and regular with some lattice constant  $\nabla x$ , and secondly, the velocity components must be integer multiples of  $\nabla x/\Delta t$ , that is  $c_{i\alpha} = n\Delta x/\Delta t$ . Due to the appropriate formulation of the velocity sets mentioned before, we ensure that these conditions are met, meaning that no populations should ‘get stuck’ in between lattice sites.

Let’s reestablish the non-dimensional force-free discrete-velocity Boltzmann equation with a general collision operator  $\Omega_i$ , that conserves density and momentum

$$\partial_t f_i + c_{i\alpha} \partial_\alpha f_i = \Omega_i, \quad (3.32)$$

where  $f_i(\mathbf{x}, t) = f(\mathbf{x}, \mathbf{c}_i, t)$  is the particle distribution function discretised in velocity space. We will refer to  $f_i$  as the population of particles moving in the direction  $\mathbf{c}_i$ , but at this point the form of the collision operator is not specified. We will operate under the assumption that this collision operator depends on the discretised populations  $\{f_i\}$  and the equilibrium populations  $\{f_i^{\text{eq}}\}$ . Those equilibrium populations depend on the macroscopic quantities (such as density and velocity) that can be found through the

moments of the populations explicitly. Hence, it is safe to assume that the collision operator  $\Omega_i$  can be completely expressed through the discretised populations. Eq. (3.32) is a first-order partial differential equation (PDE), where each velocity  $\mathbf{c}_i$  is a known constant. There are a number of techniques that can be used to solve such PDEs including analytical solutions through separation of variables, method of characteristics or integral transforms and numerical ways such as finite element, finite difference or finite volume methods.

Here, we shall use the method of characteristics, also known as the method of trajectories, to simplify Eq(3.32), by finding characteristic curves along which the first-order PDE becomes an ordinary differential equation (ODE). Thus, we could write the solution to Eq. (3.32) as  $f_i = f_i(\mathbf{x}(\zeta), t(\zeta))$ , where  $\zeta$  parameterises a trajectory in space. Then, we covert the left-hand side of Eq. (3.32) into a total derivative with respect to  $\zeta$  so that the PDE is now an ODE:

$$\frac{df_i}{d\zeta} = \left( \frac{\partial f_i}{\partial t} \right) \frac{dt}{d\zeta} + \left( \frac{\partial f_i}{\partial x_\alpha} \right) \frac{dx_\alpha}{d\zeta} = \Omega_i(\mathbf{x}(\zeta), t(\zeta)). \quad (3.33)$$

For Eq. (3.33) to be consistent with Eq. (3.32), the following must be true:

$$\frac{dt}{d\zeta} = 1, \quad \frac{dx_\alpha}{d\zeta} = c_{i\alpha}. \quad (3.34)$$

Now to solve Eq. (3.33), we start with some initial conditions. Let's choose a trajectory that goes through some point  $(\mathbf{x}_0, t_0)$  such that  $t(\zeta = 0) = t_0$  and  $\mathbf{x}(\zeta = 0) = \mathbf{x}_0$ . Integrating Eq. (3.33) from  $\zeta = 0$  to  $\zeta = \delta t$  results in

$$f_i(\mathbf{x}_0 + \mathbf{c}_i \Delta t, t_0 + \Delta t) - f_i(\mathbf{x}_0, t_0) = \int_0^{\Delta t} \Omega_i(\mathbf{x}_0 + \mathbf{c}_i \zeta, t_0 + \zeta) d\zeta. \quad (3.35)$$

Through the fundamental theorem of calculus, the integration of the left-hand side is exact. Since the chosen point  $(\mathbf{x}_0, t_0)$  is arbitrary, we can more broadly write

$$f_i(\mathbf{x} + \mathbf{c}_i \Delta t, t + \Delta t) - f_i(\mathbf{x}, t) = \int_0^{\Delta t} \Omega_i(\mathbf{x} + \mathbf{c}_i \zeta, t + \zeta) d\zeta. \quad (3.36)$$



The right-hand side of Eq. (3.36) is not as simple to determine in comparison with the left-hand side. The integral on the right-hand side can indeed be approximated by a number of suitable methods, such as the Crank-Nicolson [132] or the Runge-Kutta [133] schemes. These methods tend to obtain a more accurate result of the integration, yet the classical lattice Boltzmann equation uses a comparatively simpler forward Euler scheme. The reasons for this are practical, with the Runge-Kutta type of scheme requiring tracking the populations  $f_i$  at various points in time. This turns out to be memory intensive, especially for high discrete velocity set D3Q27. The Crank-Nicolson time-space discretisation of the lattice Boltzmann equation [132, 134] introduces new variables while leading back to the original lattice Boltzmann equation. Implicit discretisation of Eq. (3.36) lead to a linear systems of equations to be solved, which is computationally very demanding. For example for D3Q27 has 27 populations per each node, while the incompressible Navier-Stokes equation has four variables that can be found by using a finite volume solver in a less resource intensive way. The biggest strength of the lattice Boltzmann method is also its biggest weakness, its explicitness with a uniform grid. The advantage of the explicit discretisation of the velocities, space, and time means that it is easy to set up complex boundary conditions, for example for multiphase flows in porous media, while the use of uniform grid allows effective parallelisation [135]. The drawback of that is that there are stability restrictions on the lattice constant  $\Delta x$  and the timestep  $\Delta t$ .

We can now expand upon the first and second order discretisation of the right-hand side of Eq. (3.36). The first order discretisation, also called the rectangular discretisation, approximates the integral of the collision operator by a single point:

$$f_i(\mathbf{x} + \mathbf{c}_i \Delta t, t + \Delta t) - f_i(\mathbf{x}, t) = \Delta t \Omega_i(\mathbf{x}, t). \quad (3.37)$$

It is a fully explicit scheme, although  $\Omega_i$  has not yet been specified in the right form. A general expectation is that it would be of first order accuracy in time, as we used a first-order approximation. Nonetheless, we will investigate what happens while using the second-order discretisation. We again approximate the right-hand side of Eq. (3.36)

this time by using the trapezoidal rule

$$f_i(\mathbf{x} + \mathbf{c}_i \Delta t, t + \Delta t) - f_i(\mathbf{x}, t) = \Delta t \frac{\Omega_i(\mathbf{x}, t) + \Omega_i(\mathbf{x} + \mathbf{c}_i \Delta t, t + \Delta t)}{2} \quad (3.38)$$

which is a second-order approximation. This equation is implicit, as  $\Omega_i(\mathbf{x} + \mathbf{c}_i \Delta t, t + \Delta t)$  depends on  $f_i$  at  $t + \Delta t$ . It is possible to transform this equation into an explicit form, with the transformation including a change of variables from  $f_i$  to  $\bar{f}_i$

$$\bar{f}_i(\mathbf{x} + \mathbf{c}_i \Delta t, t + \Delta t) = \bar{f}_i(\mathbf{x}, t) + \Delta t \Omega_i(\mathbf{x}, t) \quad (3.39)$$

with a redefined collision operator. It would be useful to eliminate the untransformed variable  $f_i$  from Eq. (3.39), in order to be able to solve the equation for  $\bar{f}_i$  without determining  $f_i$ . Most common collision operators can be re-expressed with  $\bar{f}_i$  instead of  $f_i$ . This showed an unusual result where the second order discretisation and the first order discretisation are of the same form, demonstrating that both are second-order accurate [136] [137]. This second order accuracy of the lattice Boltzmann equation can be proven by other methods [132].

The methods above did not use a rigorously defined collision operator, which we will now rectify by examining the details of using the BKG operator. As mentioned before, the original collision operator in the Boltzmann equation considers all outcomes of binary collisions and as such is described in a complicated mathematical form. The BGK is usually normally only suitable for gas simulations, due to only accounting for binary collisions of molecules. As liquids have higher density, more complicated three or more particle interactions occur more frequently. It is reasonable to assume that the integrals used to describe the latter case would be more complicated, however that is fortunately not a limitation. This is because we do not focus on the intricate underlying microscopic interactions to recover the macroscopic approach, allowing to significantly simplify the collision operator. To that effect, we begin by approximating the collision operator and rework it in terms of the known variables - the populations  $f_i$  and the equilibrium populations  $f_i^{\text{eq}}$ . The most straightforward functional form is simply a

linear relation, which gives the assumption that  $\Omega_i \propto (f_i - f_i^{\text{eq}})$ . This assumption in its linear form does lead to the conservation of mass and momentum, which is required for the Navier-Stokes description

$$\begin{aligned}\sum_i \Omega_i &\propto \sum_i (f_i - f_i^{\text{eq}}) = 0 \\ \sum_i \Omega_i \mathbf{c}_i &\propto \sum_i (f_i \mathbf{c}_i - f_i^{\text{eq}} \mathbf{c}_i) = \mathbf{0}\end{aligned}\tag{3.40}$$

which is the most vital property of any collision operator. The BGK operator introduced earlier in Eq. (3.6) is now modified [138] as

$$\Omega_i = -\frac{f_i - f_i^{\text{eq}}}{\tau}.\tag{3.41}$$

Physically, this can be thought of as the tendency of the populations  $f_i$  to approach the equilibrium state  $f_i^{\text{eq}}$  after a time  $\tau$ . Another way to describe this process is the relaxation towards the equilibrium, and so  $\tau$  is generally called the relaxation time. Having presented a general way of using the method of characteristics for an unspecified collision operator, it is appropriate to have a closer look at doing so for a particular operator, for example, the BGK operator. Once again, we aim to solve the continuous Boltzmann equation of the form

$$\frac{\partial f_i}{\partial t} + c_{i\alpha} \frac{\partial f_i}{\partial x_\alpha} = -\frac{f_i - f_i^{\text{eq}}}{\tau}.\tag{3.42}$$

By the method of characteristics, we introduce a new variable  $\zeta$ , rewriting the equation to be solved to be

$$\frac{\partial f_i}{\partial \zeta} = \frac{\partial f_i}{\partial t} \frac{dt}{d\zeta} + \frac{\partial f_i}{\partial x_\alpha} \frac{dx_\alpha}{d\zeta} = -\frac{f_i(\zeta) - f_i^{\text{eq}}(\zeta)}{\tau}\tag{3.43}$$

where

$$\frac{dt}{d\zeta} = 1, \quad \frac{dx_\alpha}{d\zeta} = c_{i\alpha}.\tag{3.44}$$

The parametrisations  $\rho(\zeta) = \rho(\mathbf{x}(\zeta), t(\zeta))$  and  $\mathbf{u}(\zeta) = \mathbf{u}(\mathbf{x}(\zeta), t(\zeta))$  lead to the depen-

dence of  $f_i^{\text{eq}}$  on  $\zeta$  through  $f_i^{\text{eq}}(\rho(\zeta), \mathbf{u}(\zeta))$ . By integrating Eq. (3.44) it is trivial to retrieve the characteristic equation

$$t = \zeta + t_0, \quad \mathbf{x} = \mathbf{c}_i \zeta + \mathbf{x}_0 \quad (3.45)$$

with  $t_0 = t(\zeta = 0)$  and  $\mathbf{x}_0 = \mathbf{x}(\zeta = 0)$ . Now to integrate Eq. (3.43), we consider an ODE

$$\frac{dy(\zeta)}{d\zeta} = g(\zeta)y(\zeta) + h(\zeta) \quad (3.46)$$

of  $y(\zeta)$  with some given coefficient functions  $g(\zeta)$  and  $h(\zeta)$ . To get the solution to this, we can use the recognisable variation of constants:

$$y(\zeta) = e^{G(\zeta)} \left[ C + \int_{\zeta_0}^{\zeta} e^{-G(\zeta')} h(\zeta') d\zeta' \right] \quad (3.47)$$

where

$$G(\zeta) = \int_{\zeta_0}^{\zeta} g(\zeta') d\zeta' \quad (3.48)$$

with integration constants  $C$  and  $\zeta_0$ . We can rework the original equation we are looking to solve (Eq. (3.43)) into the expression of the ordinary differential Eq. (3.46) such that

$$\frac{df_i(\zeta)}{d\zeta} = -\frac{1}{\tau} f_i(\zeta) + \frac{f_i^{\text{eq}}}{\tau}. \quad (3.49)$$

Therefore we can match  $f_i(\zeta)$  with  $y(\zeta)$ ,  $-1/\tau$  with  $g(\zeta)$ , and  $f_i^{\text{eq}}/\tau$  with  $h(\zeta)$ , leading to  $G(\zeta) = -(\zeta - \zeta_0)/\tau$ . Integrating over one time step, that is using our integration limits  $\zeta_0$  and  $\zeta = \zeta_0 + \Delta t$ , we initially obtain

$$f_i(\zeta_0 + \Delta t) = e^{-\Delta t/\tau} \left[ C + \frac{1}{\tau} \int_{\zeta_0}^{\zeta_0 + \Delta t} e^{\zeta'/\tau} f_i^{\text{eq}}(\zeta') d\zeta' \right]. \quad (3.50)$$

From here the constant  $C$  can be equated to  $f_i(\zeta_0)$ , and we drop the dependence on  $\zeta$  by reintroducing  $\mathbf{x}$  and  $t$ . Also, as the integration constant can be chosen arbitrarily,

we can drop the 0 index from  $\mathbf{x}$  and  $t_0$ . Putting it all together we get

$$f_i(\mathbf{x} + \mathbf{c}_i \Delta t, t + \Delta t) = e^{-\Delta t/\tau} \left[ f_i(\mathbf{x}, t) + \frac{1}{\tau} \int_t^{t+\Delta t} e^{(t'-t)/\tau} f_i^{\text{eq}}(\zeta') d\zeta' \right], \quad (3.51)$$

which is the integral form solution of the lattice BGK equation. To make this equation usable for computer simulations we want to discretise it. Some of the ways of achieving that include first-order accurate forward Euler or second-order accurate trapezoidal rule methods.

For the first-order approximation in  $\Delta t$ , the integral of the form  $\int_t^{t+\Delta t} g(t') dt'$  is replaced by  $g(t)\Delta t$ , resulting in

$$f_i(\mathbf{x} + \mathbf{c}_i \Delta t, t + \Delta t) = e^{-\Delta t/\tau} f_i(\mathbf{x}, t) + \frac{e^{-\Delta t/\tau}}{\tau} f_i^{\text{eq}}(\mathbf{x}, t) \Delta t. \quad (3.52)$$

Then, we expand the exponentials and keep first order terms only,

$$f_i(\mathbf{x} + \mathbf{c}_i \Delta t, t + \Delta t) = \left( 1 - \frac{\Delta t}{\tau} \right) f_i(\mathbf{x}, t) + \frac{\Delta t/\tau}{\tau} f_i^{\text{eq}}(\mathbf{x}, t) + \mathcal{O}(\Delta t^2), \quad (3.53)$$

obtaining the standard discretised lattice BGK equation, bearing in mind it is first-order accurate only.

A second order approximation using the trapezoid rule of  $\int_t^{t+\Delta t} g(t') dt' \approx [g(t) + g(t + \Delta t)]\Delta t/2$  gives

$$\begin{aligned} f_i(\mathbf{x} + \mathbf{c}_i \Delta t, t + \Delta t) &= e^{-\Delta t/\tau} f_i(\mathbf{x}, t) \\ &+ \frac{e^{-\Delta t/\tau} \Delta t}{2\tau} \left( e^{-\Delta t/\tau} f_i^{\text{eq}}(\mathbf{x} + \mathbf{c}_i \Delta t, t + \Delta t) + f_i^{\text{eq}}(\mathbf{x}, t) \right). \end{aligned} \quad (3.54)$$

As before, we expand the exponentials, this time up to the second order in  $\Delta t$

$$\begin{aligned} f_i(\mathbf{x} + \mathbf{c}_i \Delta t, t + \Delta t) &= \left( 1 - \frac{\Delta t}{\tau} + \frac{\Delta t^2}{2\tau^2} \right) f_i(\mathbf{x}, t) \\ &+ \frac{\Delta t}{2\tau} \left[ f_i^{\text{eq}}(\mathbf{x} + \mathbf{c}_i \Delta t, t + \Delta t) + \left( 1 - \frac{\Delta t}{\tau} \right) f_i^{\text{eq}}(\mathbf{x}, t) \right] + \mathcal{O}(\Delta t^3). \end{aligned} \quad (3.55)$$

The aim now is to look for a transformation  $f_i \rightarrow \bar{f}_i$  to convert Eq. (3.55) so that it resembles Eq. (3.39), with the BGK collision operator  $\Omega_i = -(f_i - f_i^{\text{eq}}/\tau)$ . This can be done by establishing a new population

$$\bar{f}_i = f_i - \frac{\Omega_i \Delta t}{2} = f_i + \frac{(f_i - f_i^{\text{eq}}) \Delta t}{2\tau}. \quad (3.56)$$

The collision operator  $\Omega_i$  conserves mass and momentum, and hence the new population  $\bar{f}_i$  has the same mass and momentum as  $f_i$

$$\begin{aligned} \sum_i \bar{f}_i &= \sum_i f_i - \sum_i \frac{\Omega_i \Delta t}{2} = \sum_i f_i = \rho, \\ \sum_i \bar{f}_i \mathbf{c}_i &= \sum_i f_i \mathbf{c}_i - \sum_i \frac{\Omega_i \mathbf{c}_i \Delta t}{2} = \sum_i f_i \mathbf{c}_i = \rho \mathbf{u}. \end{aligned} \quad (3.57)$$

Following some algebraic manipulation [132], we finally obtain

$$\bar{f}_i(\mathbf{x} + \mathbf{c}_i \Delta t, t + \Delta t) = \bar{f}_i(\mathbf{x}, t) + \frac{(\bar{f}_i(\mathbf{x}, t) - f_i^{\text{eq}}(\mathbf{x}, t))}{\bar{\tau}} + \mathcal{O}(\Delta t^3) \quad (3.58)$$

with a modified relaxation time of

$$\bar{\tau} = \tau + \frac{\Delta t}{2}. \quad (3.59)$$

Hence both the first and second order approximations of the collision integrals give a result that is virtually the same. This is a specific feature of the lattice Boltzmann method, and simultaneously one of the ways of proving the second-order time accuracy of this method [132]. The rudimentary approximation of the original Boltzmann operator by the BGK operator works well in most cases, with the BGK operator combined with the lattice Boltzmann equation reproducing the continuity and Navier-Stokes equations. It is one of the reasons for the popularity of this approach, however there are also two-relaxation-times (TRT) and multi-relaxation-times (MRT) utilising, as their name suggest, more than one relaxation times. The extended collision operators mitigate some of the stability and accuracy limitations of the BGK operator.

$$\bar{f}_i(\mathbf{x} + \mathbf{c}_i \Delta t, t + \Delta t) = \bar{f}_i(\mathbf{x}, t) - \frac{\Delta t}{\bar{\tau}} (\bar{f}_i(\mathbf{x}, t) - f_i^{\text{eq}}(\mathbf{x}, t)). \quad (3.60)$$

The discretised in time and space lattice BGK equation is different from the continuous BGK in a major way; it can evolve  $f_i$  towards, immediately or past  $f_i^{\text{eq}}$ , while the latter always evolves  $f_i$  towards  $f_i^{\text{eq}}$ . In order to see why, we focus on the discrete analogue of the spatially homogenous continuous BGK equation in the form

$$f_i(t + \Delta t) = \left(1 - \frac{\Delta t}{\tau}\right) f_i(t) + \frac{\Delta t}{\tau} f_i^{\text{eq}}. \quad (3.61)$$

The choice of  $\tau/\Delta t$  influences the way that the populations  $f_i$  relax. Those ways are

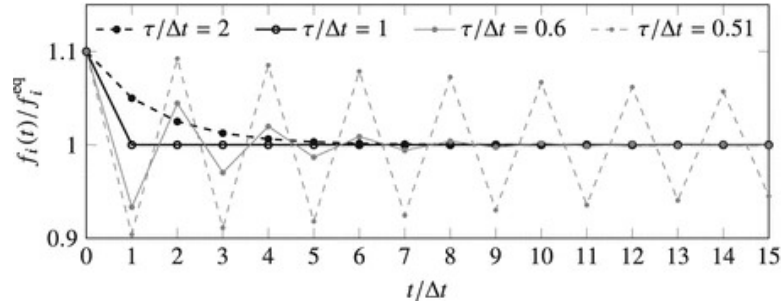


Figure 3.5: Relaxation of the BGK operator, including under, full, and over relaxation with an initial condition of  $f_i(0)/f_i^{\text{eq}} = 1.1$  and constant  $f_i^{\text{eq}}$ . Figure from [109]. Reproduced with permission from Springer Nature.

- Under relaxation, for  $\tau/\Delta t > 1$ , where  $f_i$  decays exponentially towards  $f_i^{\text{eq}}$ , the same as in the continuous-time BGK equation,
- Full relaxation for  $\tau/\Delta t = 1$ , where  $f_i$  decays directly to  $f_i^{\text{eq}}$ ,
- Over relaxation for  $1/2 < \tau/\Delta t < 1$ , where  $f_i$  oscillates around  $f_i^{\text{eq}}$  with an exponentially decreasing amplitude,
- Instability for  $\tau/\Delta t < 1/2$ , where  $f_i$  oscillates around  $f_i^{\text{eq}}$  with an exponentially increasing amplitude. This makes  $\tau/\Delta t \geq 1/2$  a necessary stability condition,

as shown in Fig. 3.5. This ultimately means that we have fully discretised the Boltzmann equation in the velocity space, physical space, and time. The intricate collision

operator was replaced with a simpler BGK collision operator. Before fully getting into the written lattice Boltzmann code, another concept that bears repeating is the separation of Eq. (3.60) into the streaming and collision sub steps. Looking closely at the equation, there are two distinct parts, one coming from the integration along the characteristics  $f_i(\mathbf{x} + \mathbf{c}_i\Delta t, t + \Delta t) - f_i(\mathbf{x}, t)$ , and the other from the local collision operator  $-\Delta t[f_i(\mathbf{x}, t) - f_i^{\text{eq}}(\mathbf{x}, t)]/\tau$ . As a reminder, each lattice site at a point  $\mathbf{x}$  and a time  $t$  stores  $q$  populations  $f_i$ . In the collision step, each population  $f_i(\mathbf{x}, t)$  receives a contribution from the collision to become

$$f_i^* = f_i(\mathbf{x}, t) - \frac{\Delta t}{\tau}[f_i(\mathbf{x}, t) - f_i^{\text{eq}}(\mathbf{x}, t)]. \quad (3.62)$$

The collision is a purely local algebraic operation, where  $f_i^*$  is the state of the population after the collision. In the streaming step, the post-collision populations  $f_i^*(\mathbf{x}, t)$  stream along their associated direction  $\mathbf{c}_i$  until they reach the neighbouring lattice site, where they become:

$$f_i(\mathbf{x} + \mathbf{c}_i\Delta t, t + \Delta t) = f_i^*(\mathbf{x}, t). \quad (3.63)$$

This operation is non-local, where the memory content of  $f_i^*(\mathbf{x}, t)$  has to be copied to the lattice site occupying  $\mathbf{x} + \mathbf{c}_i\Delta t$  and overwrite the old information. Vigilance is required to not overwrite the populations that are still needed. A common method of avoiding this pitfall is to use two sets of populations, one for reading data and one for writing data.

As a summary, the lattice BGK equation has two sub steps of collision Eq. (3.62) and streaming Eq. (3.63). We have derived all that is needed for writing a simple lattice Boltzmann code, currently with no boundary conditions or forces. Hence, we will now move to the discussion of the boundary and initial conditions.

### 3.5 Boundary conditions

In conventional hydrodynamics, the conservation of mass and momentum is described using a set of partial differential equations[139], which fundamentally cannot be uniquely



determined without proper initial and boundary conditions. Those conditions allow us to find the specific solution to the fluid flow problem that is being considered, making it both a mathematical and physical necessity. As the theoretical framework of modelling fluid flows is reliant on the same set of equations, namely Navier-Stokes equations, this additional information is required and contained in the boundary and initial conditions, remaining incomplete without them. In a way, the most important assignment in simulating a fluid flow problem is to specify the right starting point and boundaries.

Let's focus on straight boundaries that align with the lattice nodes, which is a non-complex geometry. In the lattice Boltzmann method, the boundary conditions apply at boundary nodes  $\mathbf{x}_b$  which are sites that have at least one link to a solid and a fluid node. The boundary conditions apply to the mesoscopic populations  $f_i$  rather than specifying the macroscopic variables such as  $\rho$  and  $\mathbf{u}$ , typically resulting in a non-trivial task. This is a result of the populations having more degrees of freedom, giving rise to a non-uniqueness problem that manifests in a 'zoo' of different lattice Boltzmann boundary schemes available. In contrast to conventional numerical methods, the lattice Boltzmann boundary schemes possess a distinguishing feature: the order of accuracy and exactness does not match. As an example of this, a second-order accurate scheme does not exactly accommodate a parabolic solution. In general, these schemes can be divided into two main categories, the link-wise and the wet-node. In our research we use and focus on the former.

An example of this approach, as presented by Ladd [140] [141], is also referred to as the bounce-back on links method. The solid objects are defined by some boundary surface which intersects some of the velocity vectors  $\mathbf{c}_i$  joining lattice nodes. The sites inside are designated to be solid, while the sites outside are the fluid. Hence, the correct boundary condition is taken by identifying the links between the fluid and solid sites such that if a particle meets a rigid boundary during propagation, it will reflect back to its original location with its velocity being reversed. In our research we use a later approach introduced by Nguyen and Ladd [142], that improves the original Ladd approach (where the fluid occupied nodes both inside and outside the particle for short timescales) to fully solid particles.

Let us assume that the colloidal particles are spherical with a geometrical centre, functioning also as the center of mass, of  $\mathbf{r}_c$ . This center can move continuously across the lattice with a velocity  $\mathbf{U}$ , where the angular velocity of the particle is  $\mathbf{\Omega}$ . The surface of the colloid will be given by a chosen radius which determines which lattice nodes are inside or outside the colloid, with a lattice node exactly at the solid-fluid interface chosen to be defined as outside of the colloid.. The boundary links are then the set of vectors joining lattice nodes which intersect the spherical surface  $\{\mathbf{c}_b\}$ .

A boundary link is hence defined as joining a node  $\mathbf{r}$  inside the particle to one outside at  $\mathbf{r} + \mathbf{c}_b\Delta t$ . If the post-collision distributions are denoted by  $f^*$ , then the distributions must be reflected at the solid surface so that

$$f_{b'}(\mathbf{r}; t + \Delta t) = f_b^*(\mathbf{r}; t) - \frac{2w_{c_b}\rho_0\mathbf{u}_b\cdot\mathbf{c}_b}{c_s^2} \quad (3.64)$$

where the boundary link is such that  $\mathbf{c}_{b'} = -\mathbf{c}_b$ . For clarity, the terms in Eq. (3.64) are outlined as follows. The  $w_{c_b}$  are the weights of  $c_b$  appearing in the distribution function,  $\rho_0$  is the mean fluid density, and  $\mathbf{u}_b$  is the velocity at the boundary. The  $c_s$  corresponds to the speed of sound, and as before, is given by  $c_s = \frac{1}{\sqrt{3}}$ . Importantly, the local density at the fluid site  $\rho(\mathbf{r}; t)$  in Eq. (3.64) is replaced by the mean fluid density  $\rho_0$  in the second term on the right-hand side. And finally, the velocity at the boundary is

$$\mathbf{u}_b = \mathbf{U} + \mathbf{\Omega} \times \mathbf{r}_b. \quad (3.65)$$

The force exerted on a single link is given by

$$\mathbf{F}_b(\mathbf{r} + \frac{1}{2}\mathbf{c}_b\Delta t; t + \frac{1}{2}\Delta t) = \frac{\Delta x^3}{\Delta t} \left[ 2f_b^*(\mathbf{r}; t) - \frac{2w_{c_b}\rho_0\mathbf{u}_b\cdot\mathbf{c}_b}{c_s^2} \right] \mathbf{c}_b, \quad (3.66)$$

with corresponding torque  $\mathbf{T}_b = \mathbf{r}_b \times \mathbf{F}_b$ . The total hydrodynamic force on the particle is then found by taking the sum of  $\mathbf{F}_b$  over all the boundary links defining the particle. There is an associated torque on each link of  $\mathbf{r}_b \times \mathbf{F}_b$ , which again is summed over all links to give the total torque on the colloid. By combining Eq. (3.64) and Eq. (3.65) we can eliminate the velocity at the boundary,  $\mathbf{u}_b$ , and hence split the total force and

torque on the colloid into a velocity dependent and a velocity independent part, which then can be used to update the position of the particle for the next time step.

## 3.6 Liquid crystal inclusion

We have discussed the background of the lattice Boltzmann method itself and given context into a number of standard choices available such as collision operators, boundary setting or spatial dimensions. As what we are interested in investigating goes beyond isotropic fluids into the mesophase territory, we use a free energy lattice Boltzmann model. This is realized by adding a free energy to the problem at hand, defined in terms of an appropriate order parameter. The particular coupling of the thermo- and hydro- dynamics is abstracted so that the core of the hydrodynamics does not require alteration regardless of the choice of additional free energy that is introduced. This is implemented by a series of call back functions in the free energy at the beginning of the simulation. Various bulk fluid free energy choices are complemented by an appropriate surface free energy contributions that alter the order parameter gradients at a solid surface. In our case, we include the Landau-de-Gennes liquid crystal free energy with tensor orientational order parameter  $Q_{\alpha\beta}$ , that can be extended to active fluids and is related to the Beris-Edwards equation.

### 3.6.1 Landau de Gennes

Having contextualised the liquid crystal theory in depth earlier, we will now discuss the way it is incorporated into our specific lattice Boltzmann code. The free energy functional whose density  $f(Q_{\alpha\beta}, \partial_\gamma Q_{\alpha\beta})$  has bulk contributions depending on the symmetric traceless tensor  $Q_{\alpha\beta}$  and elastic (distortion) contributions that depend on the gradients of the order parameter  $\partial_\gamma Q_{\alpha\beta}$ . The bulk contributions are included through

$$f(Q_{\alpha\beta}) = \frac{1}{2}A_0(1 - \gamma/3)Q_{\alpha\beta}^2 - \frac{1}{3}A_0\gamma Q_{\alpha\beta}Q_{\beta\pi}Q_{\pi\alpha} + \frac{1}{4}A_0\gamma(Q_{\alpha\beta}^2)^2, \quad (3.67)$$

where  $A_0$  is a constant which sets the overall energy scale and  $\gamma$  is a temperature-like parameter controlling the position in the phase diagram in relation to the isotropic-nematic transition. The gradient or elastic free energy comes from the combination of the bend, splay, and twist, that can be described using two elastic constants  $\kappa_0$  and  $\kappa_1$ .

$$f(\partial_\gamma Q_{\alpha\beta}) = \frac{1}{2}\kappa_0(\partial_\alpha Q_{\alpha\beta})^2 + \frac{1}{2}\kappa_1(\epsilon_{\alpha\mu\nu}\partial_\mu Q_{\nu\beta})^2, \quad (3.68)$$

with  $\epsilon_{\alpha\mu\nu}$  being the permutation tensor. The one-constant approximation can be used here by assuming that  $\kappa_0 = \kappa_1 = \kappa$ . The difference between  $\kappa_0$  and  $\kappa_1$  can be kept for better understanding, although ultimately we do use the one constant approximation in the results section.

### 3.7 *Ludwig code*

For some background into how the fluid dynamics equations are implemented in the code for now we focus on the three different aspects of how the liquid crystal modelling is implemented: fluid, solid, and boundary conditions. For the fluid, the hybrid approach is used to find the time evolution of the order parameter. It is called a hybrid approach, as the lattice Boltzmann method is used for the general hydrodynamics, while the Beris-Edwards equation is solved with a finite difference approach. The hydrodynamic quantities and the order parameter are both solved on the same shared regular lattice. The velocity field found by using the lattice Boltzmann method contributes the advection terms and the velocity gradient tensor through a finite difference stencil. Additionally a body force is computed locally at each lattice site by the divergence of the stress in Eq. (2.72), that is then coupled to the Navier-Stokes equations. The distinction between the way a solid and a fluid is assigned on a fluid lattice node for the order parameter is done by assigning an inside and an outside. This is done by using the radius of the colloid  $a_0$  and its position. Additionally, one can think of a series of control volumes around each lattice node (see Fig. 3.6) such that the faces are aligned with the lattice nodes. A set of these establish the solid-fluid boundary in the hybrid

model. For advective fluxes of the order parameter they are computed at the faces of the control volumes with the zero normal flux at the solid-fluid interface. Assigning of the fluxes is done under the assumption of a stationary colloid. The net hydrodynamic

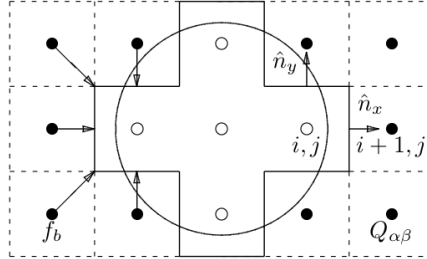


Figure 3.6: The hybrid model. For the lattice Boltzmann part, a surface is defined by using a set of links  $f_b$  that involve discrete vectors  $\mathbf{c}_b\Delta t$  which connect the fluid and solid sites. For the order parameter the colloid is given by the set of faces. An example of one is that between the sites  $i,j$  and  $i+1,j$  with a unit normal  $\hat{n}_x$ . Reproduced from [143].

force is computed by using the bounce back on links. The force on the fluid coming from the order parameter is done through the discrete divergence of the stress  $\Pi_{\alpha\beta}$ . For a fluid, this is achieved by interpolating  $\Pi_{\alpha\beta}$  to the control volume faces and taking the difference of them in each direction. The advantage of doing it through the control solid faces the solid-fluid boundary can be extrapolated, allowing to compute the divergence of the stress at fluid nodes adjacent to the colloid in the usual way. By summing  $\Pi_{\alpha\beta}$  over the relevant solid-fluid control volume faces, the discrete equivalent

$$F_\alpha^{\text{coll}} = \int \Pi_{\alpha\beta} \hat{n}_\beta dS \quad (3.69)$$

is found. This design ensures that the momentum lost by the fluid is gained by the colloid, maintaining the global momentum. At this point we can come back to the motion of such a colloid, that results in changes in its discrete shape. When a fluid site is destroyed, the order parameter information on it is also lost. For new fluid sites, the new order parameter information can be added locally either through interpolation from nearby fluid sites, or from geometrical information from local surface anchoring. A final note on the boundary conditions implementation in three dimension coming

	$Q_{xx,x}$	$Q_{xy,x}$	$Q_{xz,x}$	$Q_{yy,x}$	$Q_{yz,x}$	$Q_{zz,x}$
$Q_{xx}$	$\kappa_0 n_x$	$-\kappa_1 n_y$	$-\kappa_1 n_z$			
$Q_{xy}$	$\kappa_0 n_y$	$\kappa' n_x$		$-\kappa_1 n_y$	$-\kappa_1 n_z$	
$Q_{xz}$	$\kappa_0 n_z$		$\kappa' n_x$		$-\kappa_1 n_y$	$-\kappa_1 n_z$
$Q_{yy}$		$\kappa_0 n_y$		$\kappa_1 n_x$		
$Q_{yz}$		$\kappa_0 n_z$	$\kappa_0 n_y$		$2\kappa_1 n_x$	
$Q_{zz}$			$\kappa_0 n_z$			$\kappa_1 n_x$
	$Q_{xx,y}$	$Q_{xy,y}$	$Q_{xz,y}$	$Q_{yy,y}$	$Q_{yz,y}$	$Q_{zz,y}$
$Q_{xx}$	$\kappa_1 n_y$	$\kappa_0 n_x$				
$Q_{xy}$	$-\kappa_1 n_x$	$\kappa' n_y$	$-\kappa_1 n_z$	$\kappa_0 n_x$		
$Q_{xz}$		$\kappa_0 n_z$	$2\kappa_1 n_y$		$\kappa_0 n_x$	
$Q_{yy}$		$-\kappa_1 n_x$		$\kappa_0 n_y$	$-\kappa_1 n_z$	
$Q_{yz}$			$-\kappa_1 n_x$	$\kappa_0 n_z$	$\kappa' n_y$	$-\kappa_1 n_z$
$Q_{zz}$					$\kappa_0 n_z$	$\kappa_1 n_y$
	$Q_{xx,z}$	$Q_{xy,z}$	$Q_{xz,z}$	$Q_{yy,z}$	$Q_{yz,z}$	$Q_{zz,z}$
$Q_{xx}$	$\kappa_1 n_z$		$\kappa_0 n_x$			
$Q_{xy}$		$2\kappa_1 n_z$	$\kappa_0 n_y$		$\kappa_0 n_x$	
$Q_{xz}$	$-\kappa_1 n_x$	$-\kappa_1 n_y$	$\kappa' n_z$			$\kappa_0 n_x$
$Q_{yy}$				$\kappa_1 n_z$	$\kappa_0 n_y$	
$Q_{yz}$		$-\kappa_1 n_x$		$-\kappa_1 n_y$	$\kappa' n_z$	$\kappa_0 n_y$
$Q_{zz}$			$-\kappa_1 n_x$		$-\kappa_1 n_y$	$\kappa_0 n_z$

Table 3.2: Coefficients of the various derivatives of the order parameter tensor appearing in six equations for the elements of the order parameter (including  $Q_{zz}$ ). Note  $\kappa_0 + \kappa_1 = \kappa'$  and all the coefficients have been multiplied by a factor of 2 in the off-diagonal equations. Reproduced from [143].

from Eq. (2.38) gives six equations with potentially 18 unknown derivatives of  $\partial_\gamma Q_{\alpha\beta}$ , that in turn correspond to the six elements of the order parameter tensor  $Q_{xx}$ ,  $Q_{xy}$ ,  $Q_{xz}$ ,  $Q_{yy}$ ,  $Q_{yz}$ ,  $Q_{zz}$ . The equation corresponding to  $Q_{zz}$  must be present to maintain isotropy, the  $Q_{zz}$  itself (and its derivatives) can be replaced by a restriction on the trace of  $Q_{\alpha\beta}$ . As such, either solving a fully determined system including  $Q_{zz}$ , and then imposing tracelessness on the result, or replacing  $Q_{zz}$  and solving six equations for five unknowns, with the sixth equation acting as the constraint will result in the same answer. Due to the sheer number of the equations and the various coefficients of the derivatives the Eq. (2.38) is rather cumbersome. Those coefficients are portrayed in Tab. 3.2. As an example of this, let us consider a flat surface with normal anchoring. For this surface  $n = (1, 0, 0)$ , and the six unknowns are the gradients  $\partial_x Q_{\alpha\beta}$  at the

boundary. We can also assume that the tangential gradients  $\partial_y Q_{\alpha\beta}$  and  $\partial_z Q_{\alpha\beta}$  can be approximated using a standard method involving only fluid values of  $Q_{\alpha\beta}$ . We thus proceed by computing the constant terms that are relevant for normal anchoring

$$-\kappa_1 q_0 n_\gamma (\epsilon_{\alpha\gamma\sigma} Q_{\sigma\beta} + \epsilon_{\beta\gamma\sigma} Q_{\sigma\alpha}) - w(Q_{\alpha\beta} - Q_{\alpha\beta}^0)$$

by using  $Q_{\alpha\beta}$  from an adjacent fluid site. Then, we can add the tangential gradients to these constant terms. Finally, the gradients at the surface are found by solving a 6x6 linear algebra problem for  $\partial_x Q_{\alpha\beta}$ , allowing the full gradient at the adjacent fluid site to be constructed.

For concave edges or corners a different approach is required, as it is not possible to compute the tangential gradients from the usual stencil. Here, either a  $12 \times 12$  or  $18 \times 18$  system of equations is solved containing the relevant unknown coefficients from Tab. 3.2 and the relevant constant terms computed as before.

### 3.7.1 Parameter Mapping to Physical Units

In order to map our simulation units to physical units we need to calibrate the units of length, time and pressure. To this end, we relate the lattice spacing  $\Delta x$ , the algorithmic time step  $\Delta t$  and the reference pressure  $p^*$ , which are all unity in lattice Boltzmann units (LBU), to their values in SI units.

The calibration of the length scale relies on choosing an appropriate length to consider. In some cases it is better to consider the diameter  $D$  of the colloidal particle, while in others the dimensions of the microfluidic channel are the better choice. Assuming the largest radius particle that we consider corresponds to a relatively small diameter of  $D = 0.2 \mu\text{m}$  in SI units, then a LBU of length  $\Delta x \hat{=} 10^{-8}$  m becomes  $= 10$  nm SI units. This length scale allows for an accurate resolution of the liquid-crystalline order structure and flow field around the particle, while keeping the necessary computational resource relatively low. A different characteristic length scale can be set by considering the dimensions of the microfluidic duct. If, for example, a gap size of  $L_x = 24$  in LBU corresponds to  $L_x \hat{=} 1.2 \times 10^{-6}$  m in SI units, we obtain an LBU length

of  $\Delta x \hat{=} 5 \times 10^{-8} \text{ m} = 50 \text{ nm}$  in SI units.

To obtain a pressure scale, we use the measurements of the Landau-de Gennes parameters [144] (see Appendix D therein), which suggest

$$\frac{27}{2A_0\gamma} \simeq 5 \times 10^{-6} \text{ J}^{-1}\text{m}^3 = 5 \times 10^{-6} \text{ Pa}^{-1}$$

for some liquid crystals. Using an example from one of the results sections, choosing  $A_0 = 0.01$  and  $\gamma = 3.1$  in our simulations leads to a reference pressure of  $p^* = 1 \text{ LBU} \hat{=} 10^8 \text{ Pa}$  in SI units.

For the timescale calibration we use the following formula, which relates the rotational viscosity  $\gamma_1$  of the director, to the equilibrium scalar order parameter  $q$  and the order parameter mobility  $\Gamma$ :

$$\gamma_1 = \frac{2q^2}{\Gamma}$$

For example, if we use  $\Gamma = 0.5$  and bulk energy density parameters that give  $q \approx 0.5$  since it is assumed that the system is well within the nematic phase. Therefore, the rotational viscosity  $\gamma_1 = 1 \text{ LBU}$ . Typical values for liquid crystals in SI units are  $\gamma_1 = 0.1 \text{ Pa s}$  [8]. Together with  $1 \text{ Pa}$  equating to a pressure of  $10^{-8}$  in LBU, we obtain for the algorithmic time step  $\Delta t \hat{=} 10^{-9} \text{ s} = 1 \text{ ns}$ .

### 3.7.2 Using *Ludwig*

Having introduced the lattice Boltzmann method and the hybrid model, we can now make a mention of the existing code that is used to obtain our results. The code is called *Ludwig* [143] and is largely developed at the University of Edinburgh. It is named after the Austrian physicist Ludwig Boltzmann, given that it solves the Navier Stokes hydrodynamic equations using the lattice Boltzmann method. While this parallel code can be used to solve simple Newtonian fluids, it is broadly used for complex fluids such as liquid crystals, colloidal suspensions or mixtures. The free energy approach is used in a framework such that the distinct compositional or orientational order parameters are evolved with the appropriate coarse-grained dynamics that are fully coupled with



the fluid interaction. The code is written in standard C and can be used in serial or in parallel, using the Message Passing Interface (MPI) to achieve distributed memory parallelism.

To use the code an appropriately chosen serial or parallel configuration is picked and compiled, which will build the executable, some unit tests, and a handful of utilities. An input file in the same directory as the executable is needed to successfully run the code. It is a simple ASCII text file where all the required parameters need to be specified. After choosing relevant parameters to model and running the executable on an appropriate computational resource the code will output various data that can be then post-processed, visualised by using relevant software, and analyzed. The specific details, including the *Ludwig* version and an example of a standard input file needed to reproduce the results, are given in Appendix C. For further information relevant to the numerical description the reader is referred to the Ludwig code repository and related literature [145, 146].

### 3.7.3 Technical limitations

Some technical limitations of the model used in *Ludwig* should be noted. While the centre of mass of a particle is integrated off-grid according to Newton's equation, the particle in itself is discretised using a stair-case geometry. This requires continuous remapping of the particle onto the lattice as the particle moves with time. This can lead to spikes in the force at iteration steps, although these average out over a few iteration steps with no detrimental effect on the trajectories. The pressure obeys an ideal gas equation of state and is directly related to the density via  $p = c_s^2 \rho$ , while the effect of the constant pressure gradient is modelled through an additional body force density on the fluid. Both assumptions are not uncommon in the lattice Boltzmann methodology. While this allows for an accurate modelling of a weakly compressible fluids, the constant pressure gradient assumption is simplified over the real situation. Thermal fluctuations have not been included. This is because the simulations were carried out at a point in the phase diagram that is in the ordered state well away from the isotropic-nematic transition, meaning that the elastic forces from the anchoring of

the liquid crystal dominate over thermal forces by orders of magnitude.

## Chapter 4

# Static particle in liquid crystal flow

### 4.1 Simulation set up

In this chapter we investigate a single fixed particle placed in a channel filled with a nematic liquid crystal and subject to flow. This is achieved by using the lattice Boltzmann scheme explained in Chapter 3 to model the liquid crystal through the dynamics of the  $Q$ -tensor using a finite difference scheme and applying the lattice Boltzmann method to the hydrodynamics. The system consists of a three dimensional rectangular channel of size  $L_x \times L_y \times L_z = 64 \times 32 \times 128$  lattice sites, with solid walls at the top and bottom in the  $x$  plane and no slip boundary conditions and the remaining walls in the  $y$ - and  $z$  being periodic. The boundaries in the  $z$ -direction will act as the inlet and outlet of the channel. A pressure gradient  $\Psi = \Delta p/L_z$  is applied in the  $z$ -direction as a body force density acting on all fluid sites. The sketch of the geometry is shown in Fig. 4.1.

A single solid particle is discretised with a radius of  $R = 4.8$  lattice sites. The boundary conditions on the walls and particle surfaces are no-slip and no-penetration, introduced with the bounce-back on links scheme [109, 140] as explained in Chapter 3. The surface free energy on the particle that we investigate will have weak homeotropic

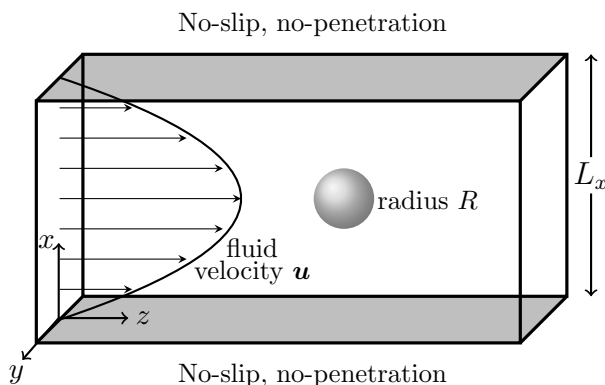


Figure 4.1: Sketch of the computational geometry: We apply no-slip boundary conditions at the walls in  $x$ -direction and periodic boundary conditions at the  $y$ - and  $z$ -boundaries. Not to scale.

anchoring, with the director having a preferred orientation perpendicular to the surface of the particle. The particle is fixed in its position, at the center of  $x$ - and  $y$ -directions and at a position about 3 radii away from the inlet in the  $z$ -direction. The system is initialised and left to equilibrate for 200,000 timesteps reaching a stable position. We explore the effect of changing the elastic constant  $K$ , viscosity  $\eta$ , order parameter mobility  $\Gamma$ , and pressure gradient  $\Psi$ . In the first instance we look at simulations with homeotropic wall anchoring, and separately repeated for planar wall anchoring.

Investigations into inertial flows around three dimensional rigid bodies have been conducted for decades. There has been a lot of focus on the hydrodynamic forces acting on fixed bodies, such as solid particles or liquid drops, subjected to some prescribed flow [147]. Simple Newtonian flows around a rigid body in general are ubiquitous in nature and human activities with one example of many being aerodynamics around buff or streamlined bodies [148]. Such flows have many applications in engineering, for example in optimisation of drag coefficient and aerodynamics of cars, planes, submarines or space shuttles. Returning to the viscous flow past a fixed sphere, it can be considered as a simplified case of solutions for general immersed bluff-body flows [149]. The behaviour of the flow past a sphere at varying Reynolds numbers has been studied by a number of researchers [150–153]. Such studies focused on finding critical values of Reynolds numbers beyond which the wake of a solid bluff body becomes unstable and develops

vortex shedding, dramatically dependent on whether the body is free to move or not [147]. Our Reynolds numbers are small enough that turbulent flow is not a concern.

In this chapter we focus our investigation on the defect structure around the colloidal particle and the influence of changing the values of the elastic constant  $\kappa$  (we operate under the one constant approximation where  $\kappa_0 = \kappa_1 = \kappa$ ), mobility parameter  $\Gamma$ , dynamic  $\eta$  and bulk  $\zeta$  viscosities, and the pressure gradient  $\Psi$ . We will focus on a system with homeotropic wall anchoring at the top and bottom walls in the  $x$ -direction. Relevant simulation parameters are outlined in Tab. 4.1. Simulations ran

Variable		
Elastic constants	$\kappa$	0.01, 0.005
Dynamic viscosity	$\eta$	0.416666, 0.8333333
Bulk viscosity	$\zeta$	0.416666, 0.8333333
Mobility parameter	$\Gamma$	0.25, 0.5
Invariable		
Bulk energy scale	$A_0$	0.01
Inverse temperature	$\gamma$	3.1
Wall anchoring strength	$w_{\text{wall}}$	0.02
Particle anchoring strength	$w_{\text{part}}$	0.02
Flow alignment parameter	$\xi$	0.7
Density	$\rho$	1.0
Particle radius	$R$	4.8

Table 4.1: Overview of simulation parameters

for  $2 \times 10^5$  iteration steps at various pressure gradients. An individual simulation took approximately 10 hours to complete using a hybrid Message Passing Interface/OpenMP parallelisation with 8 MPI- tasks each running on 20 OpenMP threads.

## 4.2 Homeotropic wall anchoring

For a nematic liquid crystal with homeotropic anchoring at the walls the director is forced to be oriented parallel to the wall normals. It is known that the degree of alignment is dependent on anchoring strength and also on the velocity gradient. The latter means that the alignment is dependent on the pressure gradient.

As noted earlier, for a colloidal particle in a static liquid crystal with weak homeotropic anchoring on its surface, we expect either a Saturn ring or a hyperbolic hedgehog. For small particles Saturn rings are more commonly expected. As an example case with  $\Gamma = 0.5, \kappa = 0.01, \eta = \zeta = 0.833333$  and at a very low pressure gradient of  $\Psi = 1 \cdot 10^{-6}$ , we observe the Saturn ring defect, as shown in Fig. 4.2. This is expected as the pressure gradient is low, leading to a small fluid velocity that does not affect the defect around the particle. For a state with no flow, the homeotropic wall anchoring induces

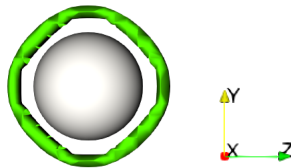


Figure 4.2: Saturn ring defect around a colloidal particle at low pressure gradient  $\Psi = 1 \cdot 10^{-6}$ , such that the fluid velocity is  $v = 2 \cdot 10^{-4}$  LBU. Other simulation parameters include:  $\Gamma = 0.5, \kappa = 0.01, \eta = \zeta = 0.833333$ .

a nematic order with a director orientation parallel to the wall normals ( $z$ -direction in Fig. 4.1). When the flow is applied, the director flow-aligns to the appropriate Leslie angle. The nematic mesophase adopts one of the possible conformations, bend or splay. In both splay and bend the director flow-aligns to a positive Leslie angle in the lower part of the channel (where there is positive shear) and to a negative Leslie angle in the upper part of the channel (where there is negative shear). The difference between the bend state (sometimes called the H-state) and splay state (sometimes called the V-state) at the centre of the channel comes from the way the director rotates between the Leslie angles in the lower and upper halves of the channel. In the bend state the director at the centre is perpendicular to the walls while in the splay state the director at the centre is parallel to the walls.

When comparing the results for the different simulation variables used, we can use the Ericksen and Reynolds numbers and the fluid velocity. Here, we take the diameter of the particle as the characteristic length-scale, and we keep the values of bulk and

dynamic viscosity to be equal for all combinations of parameters such that

$$\text{Er} = \frac{\eta \cdot v \cdot 2R}{\kappa} \quad \text{and} \quad \text{Re} = \frac{\rho \cdot v \cdot 2R}{\eta} \quad (4.1)$$

are the Ericksen and Reynolds numbers, with  $\eta = \zeta$ . Note that the mobility parameter  $\Gamma$  is not present in either of these dimensionless quantities. The applied pressure gradient leads to a Poiseuille flow profile in the  $z$ - direction, as shown in Fig. 4.1. The fluid velocity is measured at a position of half the channel length in the direction of flow away from the particle, meaning the furthest point away from the particle, at the center of the channel in the  $x$ - direction. The size of the system is kept constant,  $L_x \times L_y \times L_z = 64 \times 32 \times 128$ .

#### 4.2.1 Defect structure


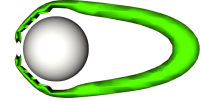


$\Psi = 1 \cdot 10^{-5}$	$\Psi = 1.5 \cdot 10^{-5}$	$\Psi = 2 \cdot 10^{-5}$	$\Psi = 2.5 \cdot 10^{-5}$
			

Table 4.2: Evolution of the defect around a colloidal particle at increasing pressure gradients, where  $\Gamma = 0.5$ ,  $\kappa = 0.01$ ,  $\eta = \zeta = 0.833333$ .

Tab. 4.2 shows the defect structure around the particle at increasing pressure gradients. The perspective is the same as shown in Fig. 4.2, with flow going to the right, as the  $z$ -direction is the direction of flow. This viewing perspective is common in experiments when looking at flow in channels. The bright green region corresponds to the defect where liquid crystalline order is reduced. The parameters used in Fig. 4.2 are  $\Gamma = 0.5$ ,  $\kappa = 0.01$ ,  $\eta = \zeta = 0.833333$ . At low fluid velocity, the Saturn ring remains undistorted, as seen in Fig. 4.2. With increased pressure gradient, the Saturn ring defect becomes elongated in the wake of the stationary particle and thinner on the opposite side, starting at  $1 \cdot 10^{-5}$ . Higher fluid velocities lead to further elongation of the defect that remains unchanging over time for the constant applied pressure gradient. The elongation of the Saturn ring defect around a static obstacle has been observed

experimentally [102]. Eventually after a critical value is reached, the defect is no longer a Saturn ring defect. It now more closely resembles a cap, upstream from the particle. The transition between the elongated Saturn ring defect and the ‘cap’ defect occurs at a pressure gradient roughly between  $2.35 \cdot 10^{-5}$  and  $2.4 \cdot 10^{-5}$ , which results in a velocity between  $v = 0.00802$  and  $v = 0.00905$ . This transition occurs together with the reorientation of the director field such that the director goes from bend to splay. We shall refer to this behaviour as the bend-to-splay transition.

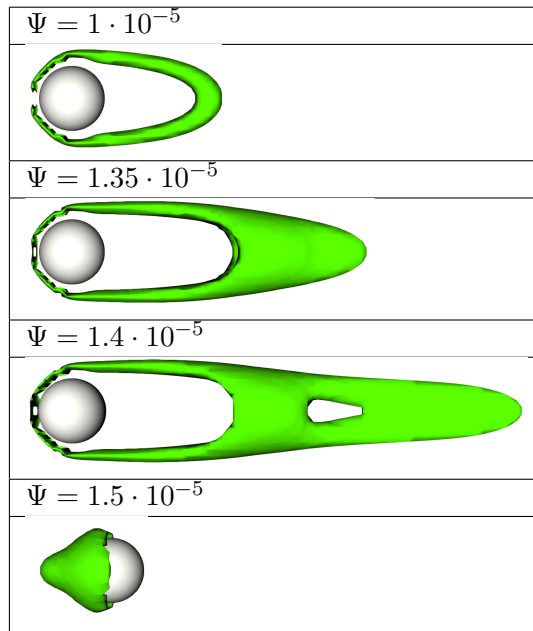


Table 4.3: Evolution of the defect around a static colloidal particle at increasing pressure gradients, where:  $\Gamma = 0.25$ ,  $\kappa = 0.01$ ,  $\eta = \zeta = 0.833333$ .

Tab. 4.3 shows the defect structures at increasing pressure gradient for the parameters  $\Gamma = 0.25$ ,  $\kappa = 0.01$ ,  $\eta = \zeta = 0.833333$ , with the same perspective as Fig. 4.2. The change between this table and Tab. 4.2 is that the mobility parameter  $\Gamma$  is half of what it was in the previous case. As shown, the Saturn ring defect is elongated in the wake of the particle at a pressure gradient of  $\Psi = 1.5 \cdot 10^{-5}$  and thinned upstream of the particle. With increasing flow velocity, the elongated shape now has a section in furthest away from the particle that is changes from an elongated ring into a cap. Increasing the applied pressure even further, leading to a fluid velocity of  $v = 0.00403$



LBU leads to a stable defect that resembles a safety pin with a further flat elongation of the defect the most far away from the particle. Again, there is a critical value of applied pressure gradient, between  $\Psi = 1.4 \cdot 10^{-5}$  and  $\Psi = 1.5 \cdot 10^{-5}$  and as such the velocity (0.00403 – 0.00507 LBU) after which a bend to splay transition occurs. The bend to splay transition again occurs while the defect undergoes the transition from an elongated Saturn ring to an upstream cap. The critical value of the transition here (Tab. 4.3) occurs at roughly half the fluid velocity of the previous case shown in Tab. 4.2. Since the velocity is halved while the elastic and viscosity parameters remain constant, the Ericksen and Reynolds are also halved as shown in Tab. 4.4. As the only variable changed is the mobility parameter  $\Gamma$ , we can conclude that this parameter effects the critical value at which the bend to splay transition occurs. Detailed information about the applied pressure gradients, fluid velocities and dimensionless numbers is compiled in Tab. 4.4.

Table 4.4: Ericksen and Reynolds numbers at different pressure gradients  $\Psi$  and fluid velocity  $v$  for simulations with the elastic constant  $\kappa = 0.01$ . Part a) shows results for  $\Gamma = 0.25, \eta = \zeta = 0.833333$ , while part b) shows the results for  $\Gamma = 0.5, \eta = \zeta = 0.833333$ . The grey line marks the transition point.

(a) $\Gamma = 0.25, \eta = \zeta = 0.833333$				(b) $\Gamma = 0.5, \eta = \zeta = 0.833333$			
$\Psi$	$v$	Er	Re	$\Psi$	$v$	Er	Re
$1 \cdot 10^{-5}$	0.00257	2.06	0.0296	$1 \cdot 10^{-7}$	0.00002	0.0158	0.000228
$1.35 \cdot 10^{-5}$	0.00378	3.03	0.0436	$1 \cdot 10^{-6}$	0.0002	0.160	0.00230
$1.4 \cdot 10^{-5}$	0.00403	3.22	0.0464	$1 \cdot 10^{-5}$	0.00290	2.32	0.0334
$1.5 \cdot 10^{-5}$	0.00507	4.06	0.0584	$1.5 \cdot 10^{-5}$	0.00477	3.81	0.0549
$2 \cdot 10^{-5}$	0.00701	5.61	0.0808	$2 \cdot 10^{-5}$	0.00672	5.38	0.0774
$2.5 \cdot 10^{-5}$	0.00899	7.19	0.104	$2.3 \cdot 10^{-5}$	0.00784	6.28	0.0904
				$2.35 \cdot 10^{-5}$	0.00802	6.41	0.0924
				$2.4 \cdot 10^{-5}$	0.00905	7.24	0.104
				$2.5 \cdot 10^{-5}$	0.00946	7.56	0.109
				$5 \cdot 10^{-5}$	0.0199	15.89	0.229
				$1 \cdot 10^{-4}$	0.0413	33.04	0.476

We now focus on the defect behaviour for varying pressure gradient with the parameters  $\Gamma = 0.5, \kappa = 0.005, \eta = \zeta = 0.833333$ . This is shown in Fig. 4.5. As in the previous cases, the Saturn ring is elongated at lower pressure gradient, here  $\Psi = 1.35 \cdot 10^{-5}$ . This elongated defect with higher fluid velocity reaches a state where

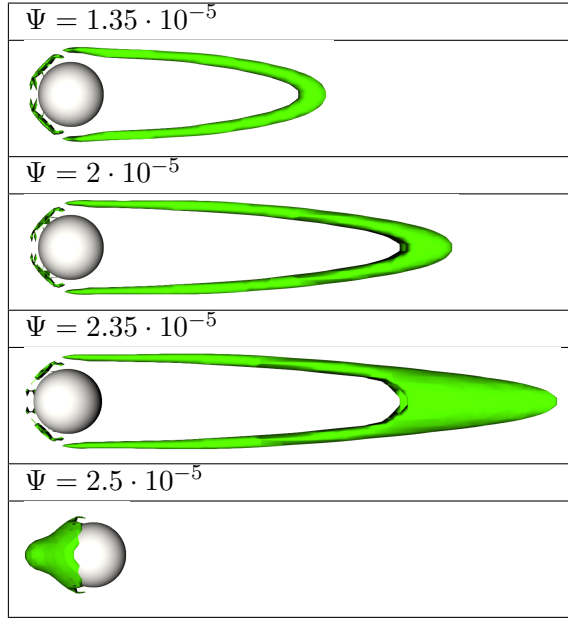


Table 4.5: Evolution of the defect around a static colloidal particle at increasing pressure gradients, where:  $\Gamma = 0.5$ ,  $\kappa = 0.005$ ,  $\eta = \zeta = 0.833333$ .

the ring elongation extends to its maximum stretch, with a cap like defect presenting at the furthest point away from the particle in its wake. Following that, the bend to splay transition and reorientation of the defect, from resembling a safety pin to an upstream cap, occurs for a fluid velocity between  $v = 0.00894$  LBU and  $v = 0.00915$  LBU. This critical value is at occurs at the same applied pressure gradient as in the case with  $\Gamma = 0.5$ ,  $\kappa = 0.01$ ,  $\eta = \zeta = 0.833333$  (shown in Tab. 4.2), where the only parameter difference between those two scenarios is in the elastic constant, here  $\kappa = 0.005$ . As the critical value occurs for the same fluid velocity and there is no changes in the viscosity parameters, the Reynolds numbers are the same. However, the Ericksen number is halved, as the elastic constant value was halved. The elastic constant changes the stretch of the elongated defect, such that the distance between the particle position and the beginning of the cap in the wake of the particle is 1.8 times greater (45 lattice units) than the same distance when the elastic constant is twice as large (25 lattice units).

Moving on to the last case for the dynamic and bulk viscosities equal to  $\eta = \zeta =$

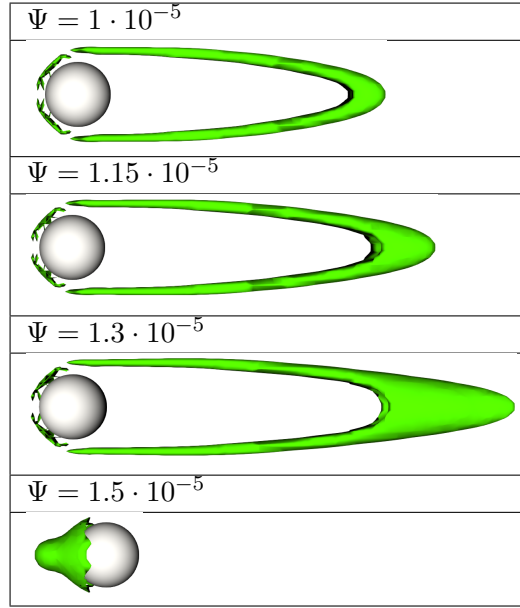


Table 4.6: Evolution of the defect around a static colloidal particle at increasing pressure gradients, where:  $\Gamma = 0.25$ ,  $\kappa = 0.005$ ,  $\eta = \zeta = 0.833333$ .

0.833333, we look at the defect behaviour for the increasing pressure gradients with parameters  $\Gamma = 0.25$  and  $\kappa = 0.005$ . The resulting defect structures for some chosen pressure gradients are shown in Tab. 4.6. The Saturn ring defect is elongated at the lower pressure gradients for a system in the bend state, until reaching a critical value of velocity between  $v = 0.00484$  to  $v = 0.0053$  where the director is in the splay state. As before, the director goes from an elongated ring to a cap in the upstream of the particle. The elongation of the defect is consistent as in the case with the same value of the elastic parameter  $\kappa$  in Tab. 4.5. The values for the critical velocity are in the same range as in the case with the same mobility parameter  $\Gamma$ , which is half of the velocity for the cases where  $\Gamma$  is twice as large. An extended overview for the applied pressure gradient, fluid velocity, Ericksen and Reynolds numbers is given in Tab. 4.7

We have now discovered that the mobility parameter  $\Gamma$  influences the values of fluid velocity at which the director reorients, while the elastic constant  $\kappa$  affects the size and shape of the defect. The exploration of the defect structures for the different parameters lead us to 3 types of defect orientations: the expected Saturn ring defect at very low fluid velocities, the elongated Saturn ring in the wake of the particle, and

Table 4.7: Ericksen and Reynolds numbers at different pressure gradients  $\Psi$  and resulting fluid velocity  $v$  for simulations with the elastic constant  $\kappa = 0.005$ . Part a) gives the results for  $\Gamma = 0.25, \eta = \zeta = 0.833333$ , while part b) gives results for  $\Gamma = 0.5, \eta = \zeta = 0.833333$ . The grey line marks the transition point.

(a) $\Gamma = 0.25, \eta = \zeta = 0.833333$				(b) $\Gamma = 0.5, \eta = \zeta = 0.833333$			
$\Psi$	$v$	Er	Re	$\Psi$	$v$	Er	Re
$1 \cdot 10^{-5}$	0.00301	4.81	0.0346	$1.35 \cdot 10^{-5}$	0.00464	7.431	0.0535
$1.15 \cdot 10^{-5}$	0.00354	5.66	0.0408	$2 \cdot 10^{-5}$	0.00724	11.58	0.0834
$1.3 \cdot 10^{-5}$	0.00409	6.55	0.0472	$2.35 \cdot 10^{-5}$	0.00894	14.30	0.103
$1.35 \cdot 10^{-5}$	0.00450	7.21	0.0519	$2.38 \cdot 10^{-5}$	0.00910	14.56	0.105
$1.4 \cdot 10^{-5}$	0.00484	7.74	0.0557	$2.39 \cdot 10^{-5}$	0.00915	14.63	0.105
$1.5 \cdot 10^{-5}$	0.0053	8.48	0.0611	$2.4 \cdot 10^{-5}$	0.00915	14.63	0.105
$2 \cdot 10^{-5}$	0.00726	11.62	0.0837	$2.5 \cdot 10^{-5}$	0.00970	15.52	0.111
$2.5 \cdot 10^{-5}$	0.00926	14.81	0.107				

a cap like defect upstream of the particle. The elongated Saturn ring can vary in its presentation, through the length of the elongation, the cap like end at the rightmost point in the wake of the particle, or a safety pin like appearance.

The same investigation into the critical values for the transition from splay to bend and the defect structure effects can be repeated for the previously used parameters of  $\Gamma$  and  $\kappa$ , but this time for halved values of the dynamic  $\eta$  and bulk  $\zeta$  viscosities, i.e.  $\eta = \zeta = 0.416666$ . The results of those simulations are presented in Tab. 4.8. Comparing the results between simulations with  $\eta = \zeta = 0.416666$  and  $\eta = \zeta = 0.833333$  we can see that for like to like values of  $\Gamma$  and  $\kappa$ , the critical transition velocity is in the same range of values regardless of the dynamic and bulk viscosity changes. There are differences in the values of pressure gradients that need to be applied to result in the same fluid velocity. Higher viscosity relies on higher values of pressure to obtain the same fluid velocity, while lower pressure is necessary for lower viscosity. This matches the expectations of real world behaviour.

Both the Ericksen and Reynolds numbers are directly proportional to the fluid velocity. Additionally, the Ericksen number is directly proportional to the bulk and dynamic viscosities, while the Reynolds number is inversely proportional to those viscosities. Hence, as the viscosity is halved, for the corresponding values of  $\Gamma$  and  $\kappa$  the Ericksen number is halved, while the Reynolds number is doubled. In all of the consid-

Table 4.8: Applied pressure gradient  $\Psi$ , fluid velocity  $v$ , Ericksen and Reynolds numbers for simulations with  $\eta = \zeta = 0.416666$ . The elastic constant  $\kappa$  and the mobility parameter  $\Gamma$  values are given separately for each sub-table. The grey line marks the transition point.

(a) $\Gamma = 0.25, \kappa = 0.01$				(b) $\Gamma = 0.5, \kappa = 0.01$			
$\Psi$	$v$	Er	Re	$\Psi$	$v$	Er	Re
$6.5 \cdot 10^{-6}$	0.00233	0.932	0.0537	$1 \cdot 10^{-5}$	0.00509	2.04	0.117
$8.5 \cdot 10^{-6}$	0.00353	1.41	0.0813	$1.15 \cdot 10^{-5}$	0.00614	2.46	0.141
$8.8 \cdot 10^{-6}$	0.00366	1.47	0.0844	$1.35 \cdot 10^{-5}$	0.00750	3.00	0.173
$8.9 \cdot 10^{-6}$	0.00378	1.51	0.0870	$1.40 \cdot 10^{-5}$	0.00791	3.16	0.182
$9 \cdot 10^{-6}$	0.00484	1.94	0.112	$1.50 \cdot 10^{-5}$	0.0100	4.01	0.231
$1 \cdot 10^{-5}$	0.00576	2.30	0.133				
(c) $\Gamma = 0.25, \kappa = 0.005$				(d) $\Gamma = 0.5, \kappa = 0.005$			
$\Psi$	$v$	Er	Re	$\Psi$	$v$	Er	Re
$6.5 \cdot 10^{-6}$	0.00303	2.43	0.0699	$1 \cdot 10^{-5}$	0.00596	4.76	0.137
$7.9 \cdot 10^{-6}$	0.00391	3.13	0.0901	$1.15 \cdot 10^{-5}$	0.00702	5.61	0.162
$8 \cdot 10^{-6}$	0.00401	3.21	0.0924	$1.35 \cdot 10^{-5}$	0.00893	7.14	0.206
$8.1 \cdot 10^{-6}$	0.00413	3.30	0.0951	$1.36 \cdot 10^{-5}$	0.00905	7.24	0.209
$8.5 \cdot 10^{-6}$	0.00483	3.86	0.111	$1.40 \cdot 10^{-5}$	0.00973	7.78	0.224
$1 \cdot 10^{-5}$	0.00618	4.94	0.142	$1.50 \cdot 10^{-5}$	0.0105	8.39	0.242

ered cases the Ericksen and Reynolds numbers are small, with  $0.0158 < \text{Er} < 33.04$  and  $0.000228 < \text{Re} < 0.476$ .

#### 4.2.2 Director field

The defects shown earlier are defined through the underlying director around the particle and in the channel. This director can be thought of and presented as a field of uniaxial lines that give the local preferred orientation of the liquid crystal. The orientation of those lines varies at different flow velocities. As an example of the differences in the director field we look at three different pressure gradients of  $\Psi = 1 \cdot 10^{-6}$ ,  $\Psi = 1 \cdot 10^{-5}$ , and  $\Psi = 2.5 \cdot 10^{-5}$  obtained for simulations with parameters  $\Gamma = 0.5$ ,  $\kappa = 0.01$ ,  $\eta = \zeta = 0.833333$ , as shown in Fig. 4.3. The perspective is such that the  $x$ -walls are at the top and bottom, while the direction of flow is to the right. The director is color coded with respect to the  $z$ -component. That is, in the direction of flow, such that values of 1 (red) are parallel to the direction of flow and values of 0 (blue) are

fully perpendicular to the direction of flow. Homeotropic anchoring conditions on the  $x$ - walls can be seen through the dark blue director orientation on the top and bottom of director fields in Fig. 4.3. At a relatively low pressure gradient of  $\Psi = 1 \cdot 10^{-6}$  the

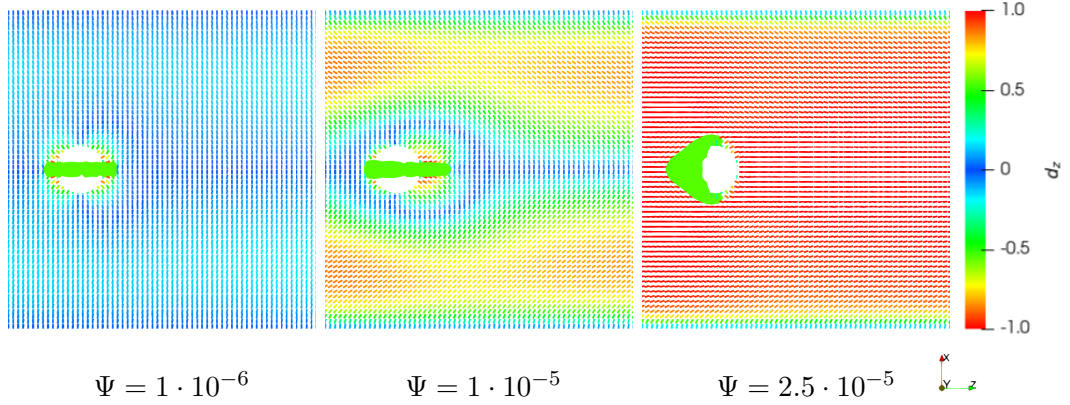


Figure 4.3: Director structure for metastable states at different pressure gradients  $\Psi$  for a simulation with parameters of  $\Gamma = 0.5$ ,  $\kappa = 0.01$ ,  $\eta = \zeta = 0.833333$ . The  $x$ - walls are on the top and bottom with imposed homeotropic anchoring. The flow goes to the right, in the  $z$ - direction.

system is the bend state with some flow alignment, with a Saturn ring defect around the particle, as seen in the leftmost image of Fig. 4.3. At ten times the pressure gradient, the flow alignment is greater, with some minor elongation of the defect in the wake of the particle, shown in the middle of Fig. 4.3. We can see that the region in the wake of the particle between the particle and the elongated ring now has the director aligned parallel to the direction of flow. In the last case, for a higher still flow velocity, the director everywhere but at the walls is fully parallel to the direction of flow. This is after a bend to splay transition has occurred.

As mentioned earlier, we found three different stable defect shapes. The standard Saturn ring, the elongated ring and a cap like defect. The elongated ring is of most interest, which we shall explore it through the director field, in two configurations: elongated ring and a safety pin like defect.

Fig. 4.4 shows a particle with an elongated defect ring for parameters  $\Psi = 2 \cdot 10^{-5}$ ,  $\kappa = 0.01$ ,  $\Gamma = 0.5$ ,  $\eta = \zeta = 0.833333$ , including three slices through the  $xy$ - plane showing the director field. The slices are shown in more detail in Fig. 4.5. The director

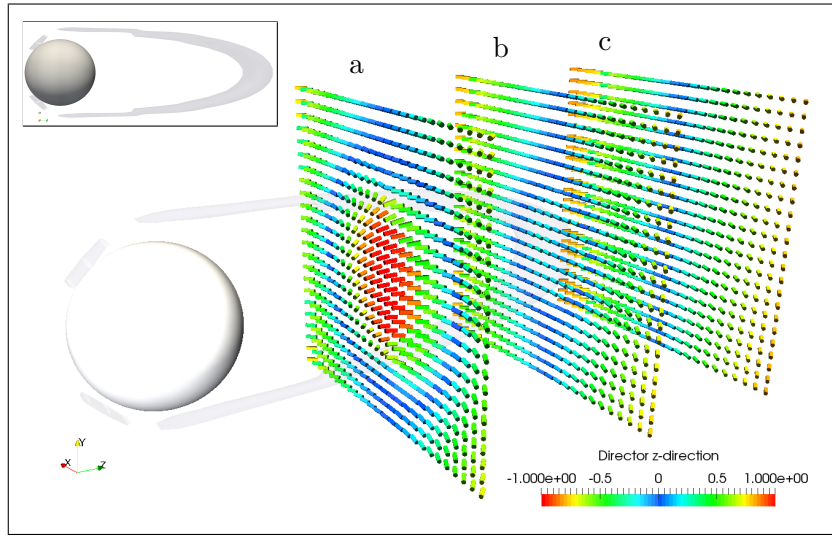


Figure 4.4: Director field structure of a particle and its defect (light grey) in a steady state with  $\Psi = 2 \cdot 10^{-5}$ . The slices showcase the differences in the director field. The inset shows the  $yz$ -viewing angle.

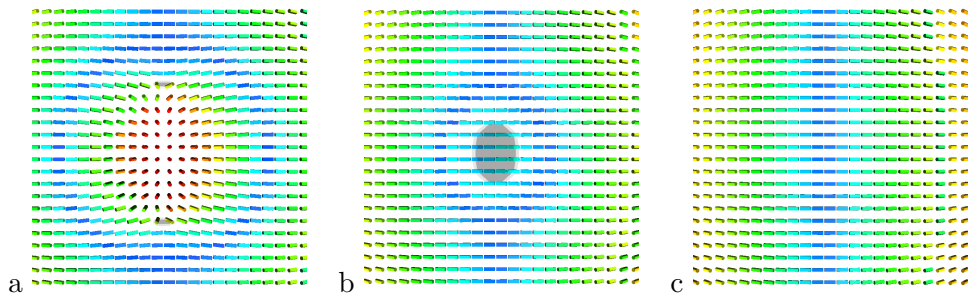


Figure 4.5: Director field in the  $xy$ - plane at points as shown in Fig. 4.4. Slice a is before the 'bulk' of the defect, slice b is through the bulk and slice c is just after the defect.

orientation in the  $xy$ - plane is shown in Fig. 4.5 at three different positions. The  $x$ -walls here are on the right and left hand-sides of the slice, showing only the central region. In part a, the director field is at half distance between the particle position and the end of the defect. There is a region of orientation parallel to the direction of flow, that is in the center shown in red. This region starts from the defect, shown in shaded grey and is locally stable. Eventually with a higher fluid velocity this region will expand until the defect extends so far out that it meets its image resulting in the entire channel being in that splay orientation. The second slice, b, goes through the

defect at a further away point, and it can be seen that there is no region with the director parallel to the flow. Around the defect there is a slight reorientation so that at the very center of the channel through the  $x$ - and  $y$ - directions the director is not fully perpendicular to the flow. Finally, the last slice  $c$  is at a point beyond the defect. It shows that the orientation through the middle of the  $y$ - direction is perpendicular to the flow direction.

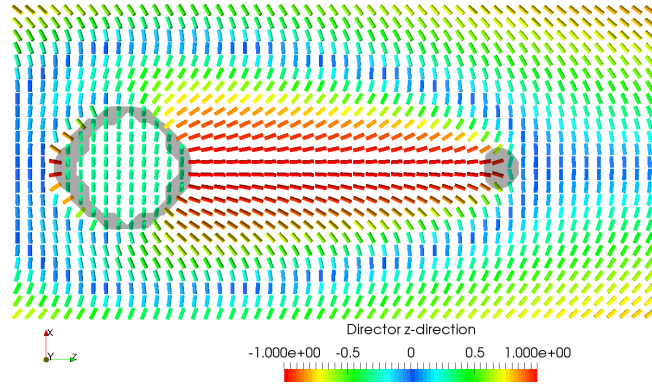


Figure 4.6: Director field in the  $xz$ -plane through the middle of the channel for  $\Psi = 2 \cdot 10^{-5}$ . The particle and defect are represented by the gray shadow on the left and right side of the image respectively.

Fig. 4.6 shows the vital director information around the particle and its defect in the middle of the channel in the  $xz$ - plane. The shaded region on the left is the particle, while the one on the right is the defect. We can see that the director is oriented parallel to the direction of flow in between the particle and its defect at the center of the channel. The overall field is stable, as the defect does not change any further with time under constant pressure gradient. The director flow aligns to the Leslie angle in the top and bottom of the channel, which can be clearly seen far away from the particle. This state is in the bend configuration in the region that does not include the particle and its defect. The presence of both creates a local change in the director orientation where the perpendicularly oriented directors would be in the middle of the channel but is now pushed closer to the top and bottom  $x$ - walls.

Another defect worth describing is the ‘safety pin’ like defect, that exists for a very narrow range of fluid velocities. This region is so narrow in fact, that it is unlikely to



be able to be observed in experiments with currently available methods. An example of this for a system with parameters  $\Gamma = 0.5$ ,  $\kappa = 0.1$ ,  $\eta = \zeta = 0.833333$  at a pressure gradient of  $\Psi = 2.35 \cdot 10^{-5}$  shown in Fig. 4.7. The inlet of the figure shows the safety pin defect in the  $yz$ - plane with the flow going towards the right. We look at six slices in the  $xy$ - plane at different positions marked a-f, going from different positions near through or near the defect. Those slices are shown separately in more detail in Fig. 4.8. Each slice shows a defect region focused nearby the defect, not across the entire channel in the  $xy$ - plane, with the  $x$  walls being to the right and left hand-side of the slices. Part a of Fig. 4.8 shows a slice at a position between the particle and the

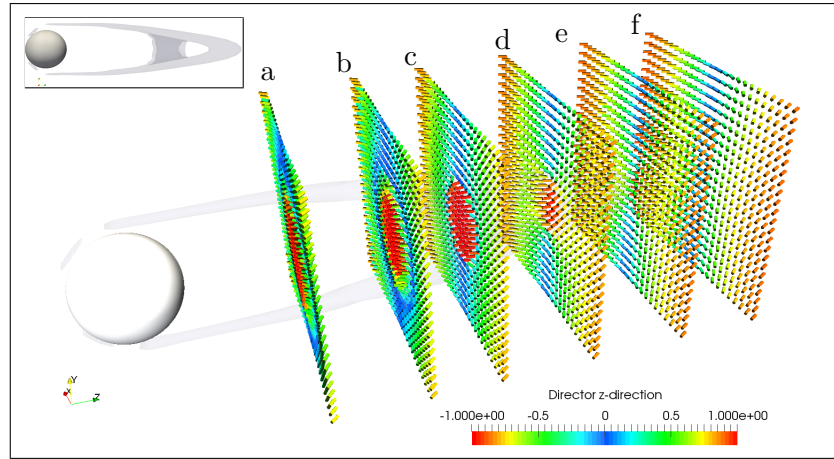


Figure 4.7: Director field structure of a particle and its defect at a metastable state with constant applied pressure gradient of  $\Psi = 2.35 \cdot 10^{-5}$ . The slices showcase the differences in the director field at different positions. The inlet shows that particle and defect in the  $yz$ - plane.

sleeve section, roughly equidistant from each. The grey outline shows the defect. It can be seen that the region between the defect is oriented in parallel to the direction of flow, and perpendicularly to the flow direction between the defect and the wall. This perpendicular orientation (marked in dark blue) continues in a loop around the differently oriented molecular region bounded by the defect. In part b of the same figure, the slice is taken at a position closer to the sleeve defect but not yet through it. The region of the liquid crystal aligned with the direction of flow is now smaller, as before, present in between the defect marked as the grey region. The loop of molecules

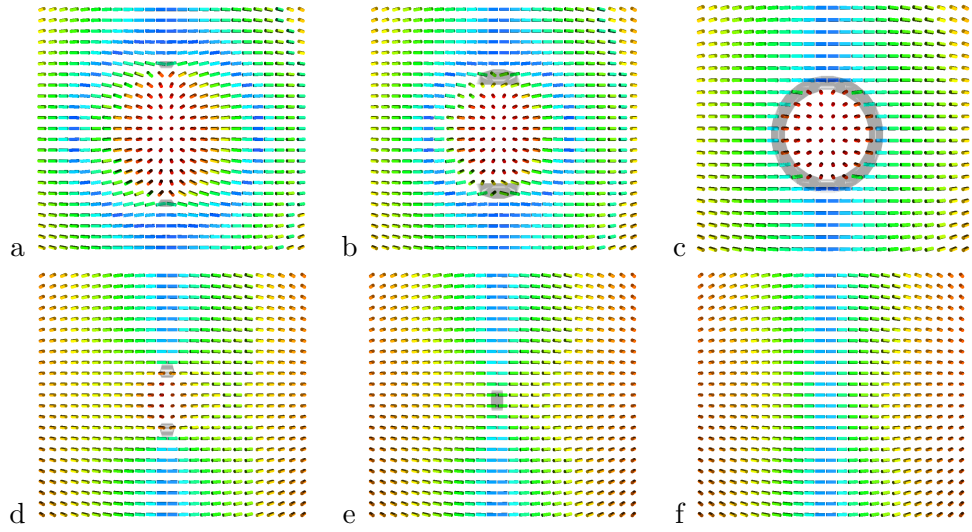


Figure 4.8: These are slices in the  $xy$ -plane through the director field at different points as seen in Fig. 4.7. Sections a) and b) are before the ‘sleeve’, c) is through the sleeve, d) in between the sleeve and the tip of the defect, e) through the tip, and f) away from the tip of the defect.

pointing in the direction perpendicular to the flow direction is now smaller. Outside of that the liquid crystal molecules are pointing in the direction in between parallel and perpendicular to the flow. Slice c goes through the sleeve defect, showing a circular region in dark grey that corresponds to the defect. Within the sleeve, as before, the region can be described by a director that is parallel to the direction of flow. This time however, there is no region of dark blue colour coded molecules, corresponding to orientation that is perpendicular to the flow direction, around the defect. Part d shows a section of molecular arrangement between the sleeve and the tip of the defect. The two gray regions show the defect as expected, with the molecules located between them being oriented parallel to the direction of flow. This region is small, with small changes in the orientation of the molecules around it. The remaining two sections e and f show slices through the tip and through a position after the defect respectively. In part e we see a small change in the defect structure such that the liquid crystal molecules orientation resembles an hourglass shape, with the narrowest point being at the defect. In the final slice f without a defect, we can see an expected standard orientation of the liquid crystal within this region of the channel. This f slice shows the bend state

orientation of the region, as the director at the centre is perpendicular to the walls.

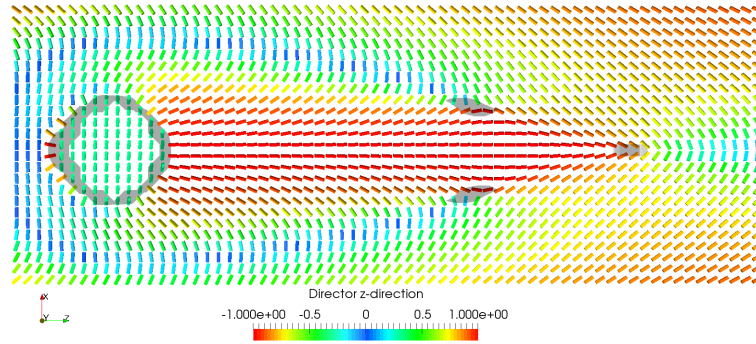


Figure 4.9: Director orientation in a  $xz$ - plane around the particle and its defect for an applied pressure gradient of  $\Psi = 2.35 \cdot 10^{-5}$ .

Fig. 4.9 shows the director orientation in the channel with an applied pressure gradient of  $\Psi = 2.35 \cdot 10^{-5}$ , the same as in Fig. 4.7, with a viewing perspective in the  $xz$ - plane. The director field is shown as a slice near the particle and the defect around it through the middle of the channel with the direction of flow being to the right. The light grey shaded region on the left represents the particle, while the dark grey regions on the right correspond to the defect within this plane. The system reached a locally stable equilibrium as it does not change any further with the constant pressure gradient. What is easily noticed is the region existing between the particle and its defect where the director is parallel to the direction of the flow (shown in red). Otherwise, in the center position the preferred orientation of the liquid crystal molecules is perpendicular to the direction of flow, consistent with the bend orientation before the transition of splay. This transition occurs at higher pressure gradient, causing a reorientation of the defect and changes in the director field. This locally stable elongation of the defect is of note in our simulations. In contrast to experimental methods it is much simpler to observe and analyse the director field viewed in between the top and bottom walls, rather than through them as it is done under cross - polarises.

### 4.3 Summary

In this chapter (Chapter 4) we focus on a fixed particle in a channel undergoing flow of a nematic liquid crystal. Through studying the behaviour of the Saturn ring defect under varying fluid velocities several key findings were unveiled. At low fluid velocities, the elongation of the Saturn ring was observed leading to a bend to splay transition. This transition was found to be linked to the reorientation of the director field within the area between the colloid and the ring. Moreover, the mobility parameter  $\Gamma$  was identified as a significant factor influencing the critical value of the bend to splay transition, indicating its crucial role in the defect behavior under different conditions. Furthermore, our investigation highlighted the impact of the elastic constant  $\kappa$  on the size and shape of the elongated Saturn ring defect. Specifically, variations in  $\kappa$  were shown to affect the length of the elongation as well as the shape, including the distinctive safety pin like defect. This suggests that the elastic properties play a crucial role in determining the structural characteristics of the defects observed. The elongation observed here is similar to previous experimental result [102], which focused on microfluidic flow of a nematic around a fixed cylinder. Interestingly, the simulations revealed that the dynamic  $\eta$  and bulk  $\zeta$  viscosity did not have a significant impact on the critical transition values between bend and splay configurations. This finding suggests that while certain parameters such as  $\Gamma$  and  $\kappa$  play crucial roles in the defect behavior, others like viscosity have a lesser influence. These insights provide valuable information for understanding the complex dynamics of the Saturn ring defects under varying fluid conditions. As such, the key results of defect elongation and influences of the  $\kappa$  and  $\Gamma$  parameters align with the project aim of defining factors of enhancing our understanding of nematic liquid crystal defect behaviour in flow.

Thanks to a collaboration with Professor Uroš Tkalec, we found that the defect elongation was observed both experimentally and in simulation, however due to the differences between the defect types around the colloid those effects are not the same. This creates a clear scope for further research into the highly confined hyperbolic hedgehogs and Saturn rings in simulation and in experiments respectively. This is to match

the simulations to experiments, and experiments to simulations as mentioned in section 2.12.

After focusing on a fixed particle and finding the appropriate simulation parameters we can now move to the investigation into dynamic particles presented in the next chapter, Chapter 5, and published [1]. There we we simulate the behaviour of a free flowing particle in a microfluidic channel, focusing on the changes due to increasing pressure gradient and also on the influence of particle size.

## Chapter 5

# Particle migration in liquid crystal flow

### 5.1 Simulation set up

In this chapter we expand on the dynamics of a single colloidal particle in a nematic liquid crystal environment, as presented in [1]. Through the interplay of the viscous, elastic and inertial effects we observe novel behaviour and positional control of a colloidal particle in a microchannel nematic liquid crystal flow. We explore the presence of multi-stability of particle position and show that its equilibrium is tunable through the applied pressure gradient. Fig. 5.1 shows a sketch of the three dimensional computational geometry, which consists of a channel of dimensions  $L_x \times L_y \times L_z = 128 \times 64 \times 256$  lattice sites. We used a hybrid lattice Boltzmann scheme [154] that treats the dynamics of the  $\mathbf{Q}$ -tensor order parameter with a finite-difference scheme and applies the lattice Boltzmann method to the hydrodynamic variables, as explained in Chapter 3. Parallel, solid walls are positioned at  $x = 0$  and  $x = L_x$ , whereas periodic boundary conditions are applied in  $y$ - and  $z$ -direction with the  $z$ -boundaries acting as inlet and outlet of the microchannel. No-slip and no-penetration boundary conditions are imposed through the bounce-back on links scheme [109], [140] on the walls and particle surfaces. The surface free energy (both at the walls and the particle) leads to weak anchoring condi-

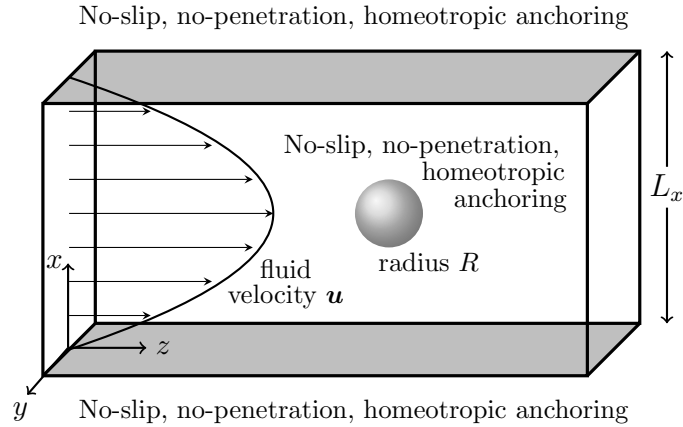


Figure 5.1: Sketch of the computational geometry: We apply no-slip boundary conditions and homeotropic anchoring conditions at the walls in  $x$ -direction and periodic boundary conditions at the  $y$ - and  $z$ -boundaries.

tions with a preferred orientation of the director normal to the surfaces. The pressure gradient  $\Psi = \Delta p/L_z$  is applied in  $z$ -direction as body force density that acts on all fluid sites besides the forces that arise from the thermotropic and hydrodynamic stresses.

The thermotropic force on the particle  $\mathbf{F}^{(LC)}$  is integrated using a finite-difference scheme in  $\mathbf{Q}$  and its gradients. The hydrodynamic force  $\mathbf{F}^{(HD)}$  is integrated in a similar way using the hydrodynamic stress tensor  $\mathbf{\Pi}^{(HD)}$ , which is directly accessible in the lattice Boltzmann method through second order moments of the non-equilibrium distributions. The total force  $\mathbf{F} = \mathbf{F}^{(LC)} + \mathbf{F}^{(HD)}$  is fed into a molecular dynamics algorithm to integrate the motion of the particles.

The values of parameters used in the simulations in this chapter are given in Tab. 5.1. Typical simulations ran for  $8 \times 10^5$  iteration steps at various pressure gradients. An individual simulation took approximately 16 hours to complete using a hybrid Message Passing Interface/OpenMP parallelisation with 4 MPI- tasks each running on 20 OpenMP threads.

Table 5.1: Overview of simulation parameters

Variable		
Particle radius	$R$	7.2, 9.6
Dynamic viscosity	$\eta$	0.166667, 0.8333333
Bulk viscosity	$\zeta$	0.166667, 0.8333333
Invariable		
Bulk energy scale	$A_0$	0.01
Inverse temperature	$\gamma$	3.1
Elastic constants	$\kappa$	0.01
Mobility parameter	$\Gamma$	0.5
Wall anchoring strength	$w_{\text{wall}}$	0.02
Particle anchoring strength	$w_{\text{part}}$	0.01
Flow alignment parameter	$\xi$	0.7
Density	$\rho$	1.0

## 5.2 Particle migration

### 5.2.1 Segré Silberberg effect

Before presenting the results for particle migration in a nematic liquid crystal, we will first introduce additional information for future reference. For a state with no flow, the homeotropic wall anchoring induces a nematic order with a director orientation parallel to the wall normals ( $x$ -direction in Fig. 5.1). When the flow is applied, the director flow-aligns to the appropriate Leslie angle. The nematic mesophase adopts one of the possible conformations, bend or splay, as shown in Fig. 5.2.

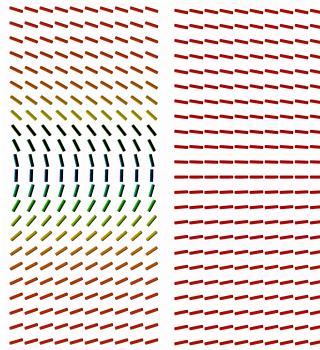


Figure 5.2: Bend or H-state (left) and splay or V-state (right) at the centre of the channel.



In both splay and bend the director flow-aligns to a positive Leslie angle in the lower part of the channel (where there is positive shear) and to a negative Leslie angle in the upper part of the channel (where there is negative shear). The difference between the bend state (sometimes called the H-state) and splay state (sometimes called the V-state) at the centre of the channel comes from the way the director rotates between the Leslie angles in the lower and upper halves of the channel. In the bend state the director at the centre is perpendicular to the walls while in the splay state the director at the centre is parallel to the walls.

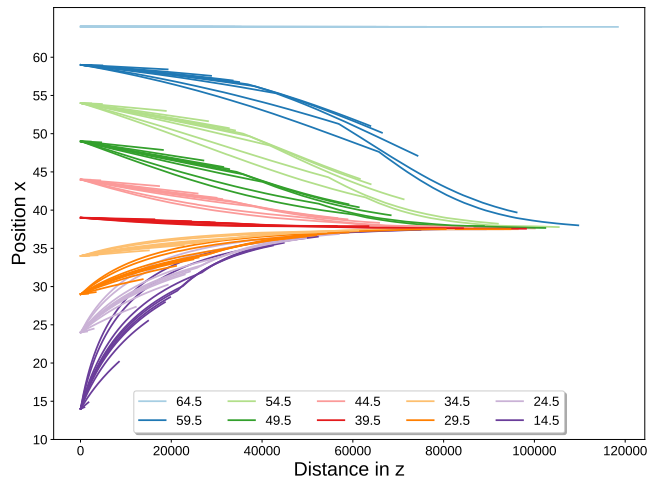


Figure 5.3: Particle migration in an isotropic fluid due to the Segré-Silberberg effect. Shown are particle position  $x$ , across the channel gap, versus the particle position  $z$ , along the channel, for a variety of starting positions (color coded) and pressure gradients in the range  $1.25 \times 10^{-6} \leq \Psi \leq 1.75 \times 10^{-5}$ . The size of the channel is  $L_x \times L_y \times L_z = 128 \times 64 \times 256$ . All quantities are given in LBU.

For a classical Newtonian fluid, or in a liquid crystal above the isotropic-nematic transition point, there is a preferential migration of colloidal particles to an  $x$ -position between the centre and wall of the channel. This is referred to as the Segré-Silberberg effect, first observed by Segré and Silberberg [155]. It is shown in Fig. 5.3 through particle trajectories for all starting positions  $x_s$  at all applied pressure gradients  $\Psi$ . The starting positions are all in the bottom half of the channel, as the other part of the

channel would result in symmetrical behaviour. Two aspects of the Segré-Silberberg effect are important to note for comparison to our results. Firstly, except for particles that start exactly at the centre of the channel, migration occurs to a single equilibrium  $x$ -position over time. Secondly, the value of that equilibrium position  $x$  does not vary significantly at low Reynolds numbers. As seen in Fig. 5.3, our simulations of an isotropic fluid show these aspects of the Segré-Silberberg effect: all particles migrate to an equilibrium at  $x$ -position of approximately 38 regardless of their starting position or applied pressure.

It should be noted that the Segré-Silberberg equilibrium position seen in Fig. 5.3 is not at the well-known 0.6 tube radii (or channel half-widths in the planar case) from the centre line, but at approximately 0.4 channel half-widths. This shift of the equilibrium position towards the channel centre has been observed before in simulations [156, 157]. This can be attributed to our particle confinement ratio of  $2R/L_x = 19.2/128 = 0.15$ . In contrast, the analytical results [158, 159] were obtained for particles that are negligibly small compared to the tube diameter or gap width, corresponding closer to a zero confinement ratio. Our study uses Reynolds numbers that are around two orders of magnitude smaller than those in previous simulation studies [156, 157], which is known to result in equilibrium positions that are closer to the channel centre.

### 5.2.2 Migration in a nematic

Having given additional context to the expected particle behaviour in an isotropic liquid, we can now explore what happens in a nematic liquid crystal. We focus on the migration behaviour of a single particle at different pressure gradients  $\Psi (= \Delta p/L_z)$  and start positions  $x_s$  in the mesophase.

Fig. 5.4 shows particle trajectories  $x(z)$  for starting positions in the lower portion of the channel (the channel centre is at  $x = 64$ ). For low pressure gradients  $\Psi = 7.5 \times 10^{-6}$  (red lines in Fig. 5.4) the particle migrates either to the channel walls (for starting position  $x_s \leq 40$ ) or towards the centre of the channel (for  $x_s \geq 44$ ). Particles that start at the centre stay in that position, while those further away from the centre show a tendency to overshoot and remain in an off-centre position. At slightly larger pressure

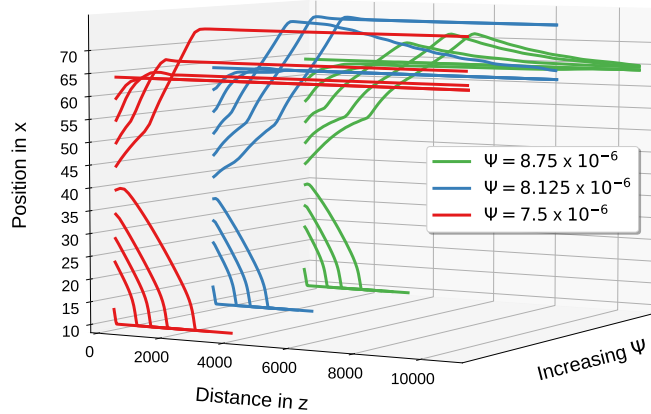


Figure 5.4: Particle trajectories for particle radius  $R = 9.6$  at sub-critical pressure gradients  $\Psi = 7.5 \times 10^{-6}$ ,  $8.125 \times 10^{-6}$ ,  $8.75 \times 10^{-6}$ , showing particle  $x$ -positions across the channel gap versus the  $z$ -distance travelled in the flow direction for various initial positions  $x_s$ . The particle Ericksen numbers  $Er$  (particle Reynolds numbers  $Re$ ) are from front to back  $Er = 25.62$  ( $Re = 0.37$ ),  $Er = 27.91$  ( $Re = 0.40$ ),  $Er = 30.20$  ( $Re = 0.43$ ). All quantities are given in LBU.

gradients  $\Psi = 8.125 \times 10^{-6}$ ,  $8.75 \times 10^{-6}$  (blue and green lines in Fig. 5.4, respectively), this bi-stability remains, but with the division between migration towards the wall or centre now at around  $x_s \simeq 38$ . Some trajectories exhibit the onset of a pull-back behaviour from overshoot off-centre positions towards the centre, in particular for the larger pressure gradient of  $\Psi = 8.75 \times 10^{-6}$ . Additionally for low pressure gradients,  $\Psi \leq 5 \times 10^{-6}$ , we also observe off-centre equilibrium positions in the form of a weak attractor that moves to the channel centre with increasing pressure gradient.

A further increase in the pressure gradient leads to a new type of preferential migration behaviour [1]. In Fig. 5.5 we see that for  $\Psi = 9.125 \times 10^{-6}$  a pronounced trajectory kink emerges at  $x \simeq 50 - 53$ . A precursor of this effect is visible for lower pressure gradients in Fig. 5.4. For the pressure gradients  $\Psi = 9.6 \times 10^{-6}$  (blue lines in Fig. 5.5 this kink transitions into an emergent particle attractor, representing a third preferential position in addition to the channel centre and the wall. At  $\Psi = 9.6 \times 10^{-6}$  this emergent attractor is located at  $x \simeq 48$  and trajectories with initial positions  $40 < x_s < 50$  migrate towards the attractor. Increasing the pressure gradient further leads to a movement of the emergent attractor towards the wall, and for  $\Psi = 1.125 \times 10^{-5}$  the attractor position is  $x \simeq 40$ .

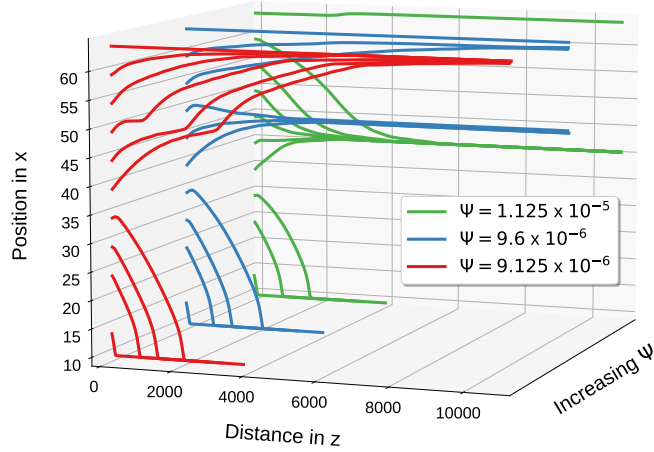


Figure 5.5: Particle trajectories for particle radius  $R = 9.6$  at pressure gradients  $\Psi = 9.125 \times 10^{-6}$ ,  $9.6 \times 10^{-6}$ ,  $1.125 \times 10^{-5}$ , showing particle  $x$ -positions across the channel gap vs. the distance travelled in the flow direction for some initial positions  $x_s$ . The emergence of the particle attractor is shown for  $\Psi = 9.6 \times 10^{-6}$ ,  $1.125 \times 10^{-5}$ . The particle Ericksen numbers  $Er$  (particle Reynolds numbers  $Re$ ) are from front to back  $Er = 31.58$  ( $Re = 0.45$ ),  $Er = 33.33$  ( $Re = 0.48$ ),  $Er = 39.57$  ( $Re = 0.57$ ). All quantities are given in LBU.

Fig. 5.6 shows the complete set of trajectories for a particle with radius  $R = 9.6$  and pressure gradients ranging from  $\Psi = 1.25 \times 10^{-6}$  to  $1.75 \times 10^{-5}$ . The first row of Fig. 5.6 shows results for low pressure gradients  $\Psi = 1.25 \times 10^{-6}$ ,  $2.5 \times 10^{-6}$ ,  $5 \times 10^{-6}$ , indicating typical behaviour at low pressure gradients of migration toward the wall or toward the weak attractor region that moves closer to the channel centre with increasing pressure gradient. In all cases the director remains in the bend state, as indicated by blue lines. The second row of Fig. 5.6 shows trajectories for intermediate pressure gradients  $\Psi = 7.5 \times 10^{-6}$ ,  $8.75 \times 10^{-6}$ ,  $9.125 \times 10^{-6}$ , for which we can observe trajectories with overshooting and pull-back behaviour as well as a transition from the bend (blue lines) to the splay (red lines) state, through an intermediate state (black lines). For the lowest of these intermediate pressure gradients,  $\Psi = 7.5 \times 10^{-6}$ , overshooting can be seen.

Overshooting followed by pull-back to the centre is seen for  $\Psi = 8.75 \times 10^{-6}$ . This overshoot behaviour has disappeared at the higher pressure gradient of  $\Psi = 9.125 \times 10^{-6}$ . In all cases of overshoot and pull-back there is a bend to splay transition. The precursor of the emergent attractor can be seen in the trajectories for the  $9.125 \times 10^{-6}$

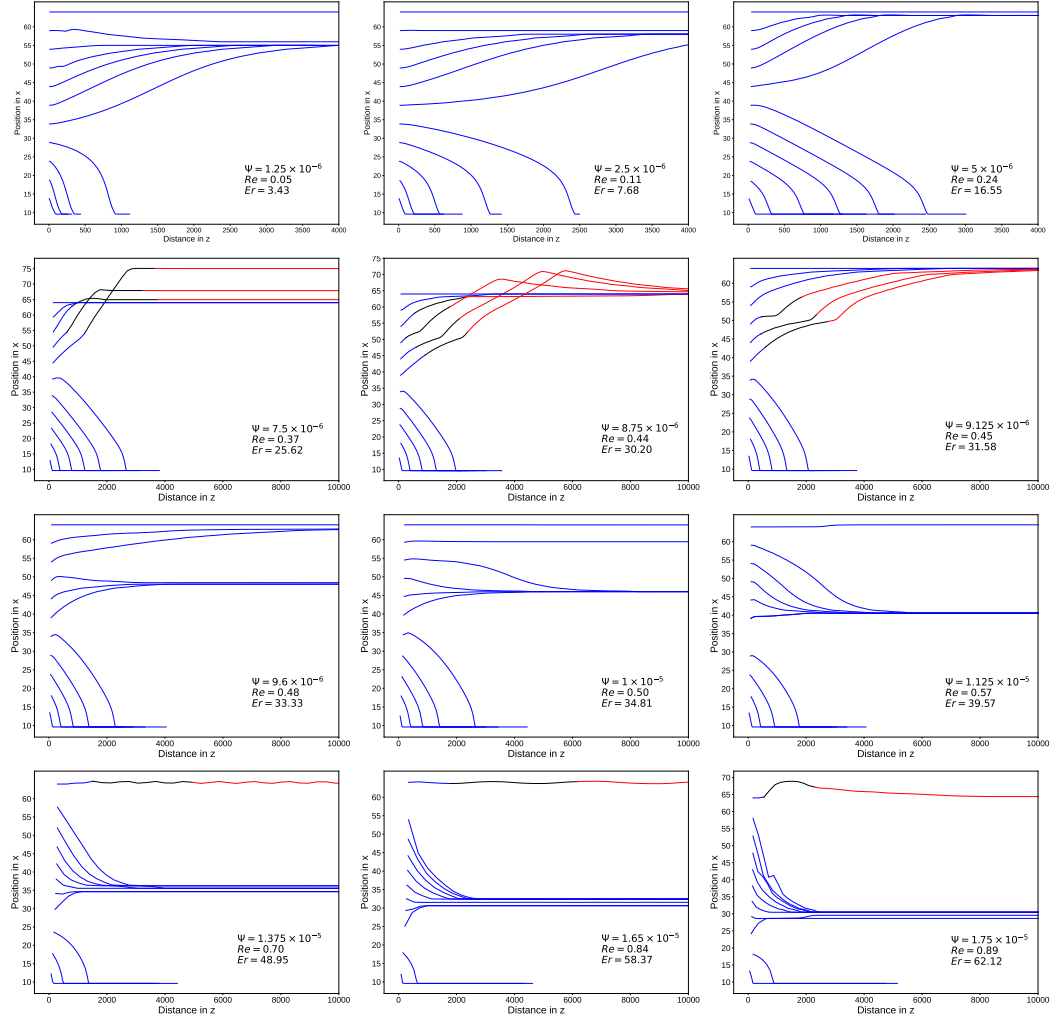


Figure 5.6: Particle trajectories in a nematic liquid crystal host phase for particle size of  $R = 9.6$  and applied pressure gradients ranging from  $\Psi = 1.25 \times 10^{-6}$  to  $1.75 \times 10^{-5}$ . Blue lines indicate that the director structure is in a bend state, whereas red lines indicate that the director has transitioned to the splay state. Black lines mark a transition state between bend and splay. The particle Ericksen numbers  $Er$  and particle Reynolds numbers  $Re$  are given in each sub-plot. All quantities are given in LBU.

case, the right most image of the second row of Fig. 5.6. For the highest intermediate pressure gradient,  $\Psi = 9.6 \times 10^{-6}$ , the third attractor state emerges. The last two rows of Fig. 5.6 cover the higher range of pressure gradients, for which the emergent attractor state is possible, albeit for sufficiently high pressure gradients. It is clear that the position of the emergent attractor state moves towards the wall with increasing pressure gradient. To further check the consistency of our findings, we also ran a number of additional simulations with  $R = 9.6$  at a lower shear and bulk viscosity  $\eta = \zeta = 1/6$ , which led to the same equilibrium position and confirmed these results.

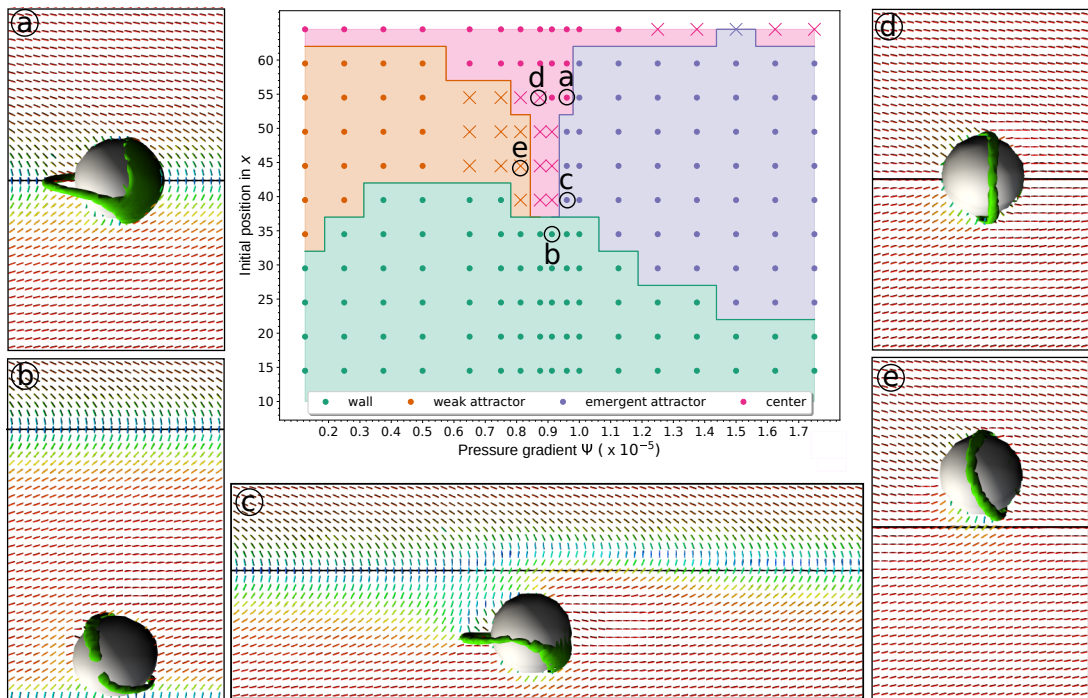


Figure 5.7: Phase diagram of the preferential migration of the colloidal particle in a nematic host phase. Coloured regions show the equilibrium particle position (wall, weak attractor, emergent attractor, centre) as a function of the initial  $x$ -position of the particle and the applied pressure gradient  $\Psi$ . Equilibrium director bend states are marked with dots, whereas equilibrium splay states are shown with crosses. Subplots (a)-(e) show the scalar order parameter (green isosurface showing the low order region) and director field (short coloured lines) around the particle for typical equilibrium states: (a) bend state, centre position; (b) bend state, wall position; (c) bend state, emergent attractor position; (d) splay state, centre position; (e) splay state, weak attractor position. The centre of the channel is marked by the horizontal blue line.

The main plot in Fig. 5.7 summaries the results, showing a phase diagram of the

equilibrium position as a function of the starting position  $x_s$  and the applied pressure gradient  $\Psi$ . This presents an overview of novel migration behaviour observed within the system under investigation [1]. For particles initially close to the walls, migration towards the walls occurs for all pressure gradients. Similarly, particles initially close to the centre of the channel migrate to the centre of the channel. Initial particle positions that are around one or two particle radii away from the centre give rise to significantly more complicated behaviour. At low pressure gradients the particle migrates to an off-centre weak attractor position. For a narrow range of pressure gradients around  $\Psi \simeq 9 \times 10^{-6}$  centre positions are preferred, and above a critical pressure gradient  $\Psi \simeq 9.5 \times 10^{-6}$  the phase diagram is increasingly dominated by the emergent attractor states.

Also shown in Fig. 5.7, through the subplots (a)-(e), are the director and scalar order parameter structures within the channel. Previous theoretical and experimental work has shown that the director structure within channel flow of a nematic can exhibit either predominately bend or splay deformation [160, 161] for low and high flow speeds respectively. Both states are observed in our simulations, and both exhibit flow alignment at the appropriate Leslie angle. That is positive (negative) angles in the lower (upper) half of the channel where the shear gradient is positive (negative). As mentioned above, the states differ in their transition between positive and negative Leslie angle at the centre of the channel, with the bend state exhibiting director alignment along  $x$  at the centre of the channel (for example in Fig. 5.7(a), and the splay state exhibiting director alignment along  $z$  at the centre (Fig. 5.7(d)). For the pressure gradients that are considered, the bend state would normally be maintained. However, we observe a novel particle-induced mechanism for switching from the bend to splay state (see Fig. 5.2) with the migration of the particle to the centre being the initiating event for a range of pressure gradients (see Fig. 5.7), indicated by crosses.

For wall equilibrium positions a bend state occurs with a tilted, but otherwise regular, Saturn ring defect around the particle (see Fig. 5.7(b)). For centre equilibrium positions a bend state occurs for  $\Psi < 1.2 \times 10^{-5}$  and a splay state for  $\Psi > 1.2 \times 10^{-5}$ . For an initial particle position away from the centre, the bend state occurs for the

weak attractor, centre and emergent attractor equilibrium positions, for both low and high pressure gradients. However, at intermediate pressure gradients  $6 \times 10^{-6} \leq \Psi \leq 8.5 \times 10^{-6}$  we observe a transition to the splay state (Fig. 5.7(d),(e)). The transition from the bend to the splay state does not have a determining effect on whether the particles migrate to centre or off-centre positions as we see the same behaviour for initial positions close by and/or at lower pressure gradients. However, it does affect the nature of the Saturn ring defect around the particle: for bend equilibrium states the Saturn ring defect is approximately horizontal see Fig. 5.7(a),(c), and for splay equilibrium states the Saturn ring defect is approximately vertical, see Fig. 5.7(d),(e). For bend equilibrium states, the defect structure also develops a pronounced cap-shaped region of low liquid-crystalline order at the bow of the particle (Fig. 5.7(a),(c)).

In comparison to the Segré-Silberberg effect in isotropic fluids, as seen in Fig. 5.3, we notice several fundamental differences. Firstly, in isotropic fluids, particles migrate to a single equilibrium position. In nematic host phases migration to one of multiple equilibrium positions can happen, depending on particle starting positions and the applied pressure gradient. Secondly, while for the Segré-Silberberg effect the location of the attractor state between the wall and centre depends only weakly on the flow velocity [159, 162]. In fact our simulations with an isotropic host phase, see Fig. 5.3, show no appreciable change in equilibrium position over the entire range of applied pressure gradients. The position of the emergent attractor state in the nematic system depends much more sensitively on the imposed pressure gradient, and in turn, on the Reynolds number. For instance, the Reynolds numbers for which there are emergent attractor states in Fig. 5.5 are  $Re \simeq 0.48$  and  $Re \simeq 0.57$  and, even with this small increase in  $Re$ , the attractor position moves by almost one particle radius. Finally, the preferential migration in a nematic host phase happens more than an order of magnitude faster than in isotropic fluids. Let us illustrate this with an example. For a pressure gradient  $\Psi = 1.125 \times 10^{-5}$  (Fig. 5.5, green lines) the position of the emergent attractor in the nematic host phase and the Segré-Silberberg equilibrium position in the isotropic host phase almost coincide. The particles in a nematic host reach their equilibrium positions by the time they have travelled around  $z \simeq 5 \times 10^3$  along the



channel, and in an isotropic host phase (see Fig. 5.3), depending on the start positions  $x_s$ , the particles take at least an order of magnitude longer (in time or distance along the channel).

With regard to Ericksen numbers  $Er$ , our results indicate that the observed pattern of preferential migration occurs in a regime where viscous forces are larger than elastic forces [1]. Consequently, the director field is strongly affected by the flow field. At the lower end of this regime, for  $3.43 \leq Er \leq 16.55$ , the weak attractor state exists, as shown in the top row of the Fig. 5.6. The emergent attractor state occurs for  $Er \simeq 30$  and above. With increasing  $Er$ , viscous forces begin to dominate over elastic forces. This means the flow behaviour at higher Ericksen numbers is more similar to that of an isotropic fluid, which shows the classical Segré-Silberberg effect. However, the fact that a strongly flow-aligned liquid crystal forms the host phase leads always to certain qualitative differences. For instance, the trajectories shown in the two bottom rows of Fig. 5.6 featuring the emergent attractor state at  $33.33 \leq Er \leq 62.12$ , do show some similarities to the classic Segré-Silberberg effect. However, the movement of the emergent attractor region towards the walls with increasing Ericksen number, the attraction to the walls, or the existence of stable trajectories at the channel centre are all features that occur due to the anisotropic nature of the host phase and the interaction of flow-aligned director field with the defect structure around the particle. This is visible in the snapshots shown in Fig. 5.7(a)-(e).

### 5.2.3 Force effects

In order to investigate the presence of this emergent attractor, we consider the total force and the contributions to the total force on the particle in the steady state for particles that have equilibrated, see Fig. 5.8, as presented in [1]. An analysis of the individual force contributions shows that for a centre equilibrium position, as in Fig. 5.7(d), all three force components vanish. This is expected from symmetry. For a wall equilibrium position as seen in Fig. 5.7(b), all three force components are negative, forcing the particle to remain at the wall. For particle migration to an emergent attractor state as in Fig. 5.7(c), our simulation show that the particle feels a force

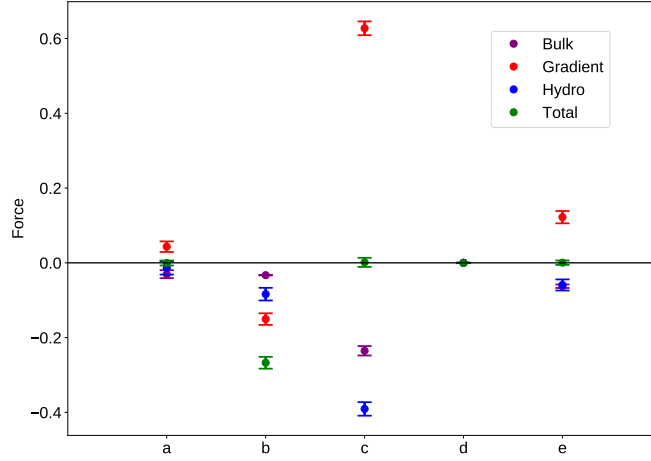


Figure 5.8: Total force and the contributions to the total force on the particle in the steady state for particles that have equilibrated to lie at (a) the centre with asymmetric defect, (b) at the wall, (c) at the emergent attractor, (d) at the centre with symmetric defect, and (e) at the weak off-centre attractor, for particle radius  $R = 9.6$ . The error bars indicate one standard deviation of the force data during a run over  $10^4$  algorithmic steps. All quantities are given in LBU.

towards the channel centre from the gradient, i.e. elastic, terms and forces towards the wall from both the bulk term and the hydrodynamic force component. This is also the case for particle migration to the centre with an asymmetric defect as in Fig. 5.7(a) and for particle migration to the weak attractor as in Fig. 5.7(e), although the individual force contributions are significantly smaller. A delicate force balance exists between these relatively large contributions leading to a zero total force at equilibrium.

Fig. 5.9 shows the time evolution of the different contributions to the force on the particle during its approach to an emergent attractor state, for pressure gradient  $\Psi = 1.125 \times 10^{-5}$  and particle radius  $R = 9.6$ . For these values of  $\Psi$  and  $R$  the attractor state is located at approximately the Segré-Silberberg equilibrium  $x$ -position (that is, one seen in Fig. 5.3). Trajectories for three starting positions are shown, for  $x = 34.5$  (light grey),  $x = 39.5$  (medium grey) and  $x = 59.5$  (dark grey), which cover a range of migration patterns to the attractor from below and above. Also shown are the contributions to the total force on the particle which arise from gradient (red), bulk (purple) and hydrodynamic (blue) terms with the hue (light, medium, dark)

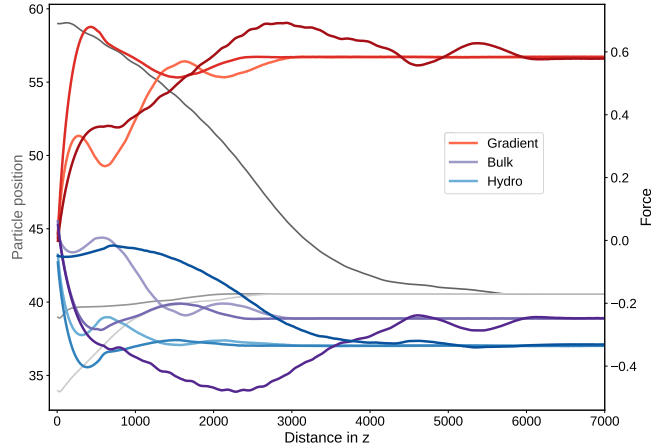


Figure 5.9: Time evolution of force contributions in the emergent attractor state with pressure gradient  $\Psi = 1.125 \times 10^{-5}$ . Trajectories for three starting positions are shown, for  $x = 34.5$  (light grey),  $x = 39.5$  (medium grey) and  $x = 59.5$  (dark grey). Also shown are the contributions to the total force on the particle which arise from gradient (red), bulk (purple) and hydrodynamic (blue) terms with the hue (light, medium, dark) corresponding to the equivalent starting position (light grey, medium grey, dark grey). All quantities are given in LBU.

corresponding to the equivalent starting position (light grey, medium grey, dark grey).

From Fig. 5.9 we observe initial transient behaviour before the particle reaches the same equilibrium position for all three starting positions. For all starting positions and for all time, the gradient contribution is positive, so that the elastic forces always act to move the particle towards the channel centre. For both bulk and hydrodynamic force contributions are negative for all starting positions and (almost all) time, so that they act to move the particle towards the wall. The exception is that for starting position  $x = 34.5$  the bulk force contribution is positive for a very short initial period, that is, for very small  $z$ -displacements of the particle from the initial position. Interestingly, all three force contributions are almost balanced, with a total force of zero, for all time. Variations in the total force are indiscernible on the same force scale used in Fig. 5.9.

This situation is in contrast to the Segré-Silberberg effect, in which the inertial component of the hydrodynamic force acts to move the particle across the shear gradient towards the wall, while the increased pressure caused by the particle moving towards the wall leads to a force acting to move the particle towards the centre of the channel.

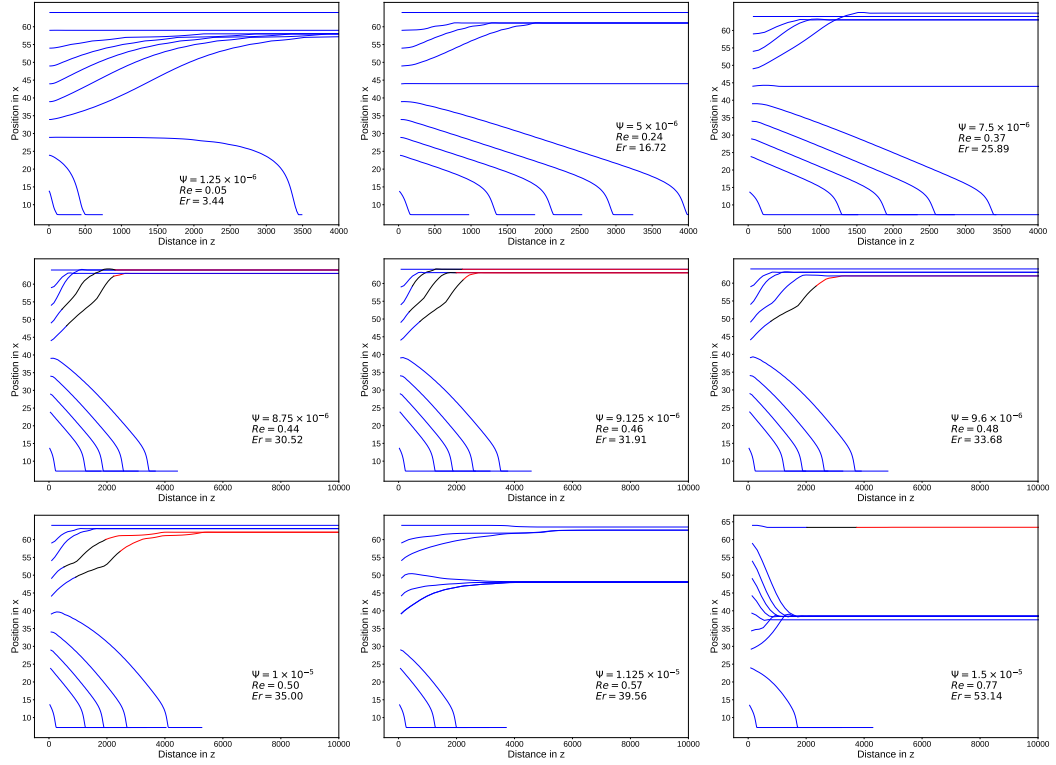


Figure 5.10: Particle trajectories in a nematic liquid crystal host phase for particle size  $R = 7.2$  and various applied pressure gradients from. Blue lines indicate that the director structure is in a bend state, red lines indicate the splay state and black sections denote the transition. The particle Ericksen numbers  $Er$  and particle Reynolds numbers  $Re$  are given in each sub-plot. All quantities are given in LBU.

At the Segré-Silberberg equilibrium position, the total hydrodynamic force vanishes. In a nematic host material, the gradient terms act with the inertial hydrodynamic forces to move the particle towards the wall, allowing much faster migration of the particle and the appearance of an attractor state at a much smaller Reynolds number.

The presence of a particle also leads to a distorted director structure, rather than a uniform director at the Leslie angle and so increased pressure gradients (equivalent to an increased Reynolds number) can align the director around the particle more closely to the Leslie angle, thus adapting the elastic force on the particle, and therefore control of the attractor equilibrium  $x$ -position through changes in pressure gradient is possible [1].

Additional results for smaller particles with  $R = 7.2$  show a similar pattern of

preferential migration, and are depicted Fig. 5.10 as trajectories. There are quantitative differences, for instance overshooting off-centre trajectories or trajectories with overshooting and pull-back to the channel centre are much less pronounced compared to larger particles with  $R = 9.6$ . This can be attributed to smaller inertia and reduced anchoring forces, which scale down with the surface area of the particle. For smaller particles the attractor state emerges at slightly larger pressure gradient around  $\Psi = 1.125 \times 10^{-5}$ , but shows the same characteristics, in particular the fast migration of the particle to the equilibrium regions, as well as the movement of the emergent attractor position towards the walls and its prominence in the phase diagram with increasing pressure gradient. These results suggest that this new effect depends to a certain extent also on particle size, and therefore on inertia. For higher inertia we expect the emergent attractor region in the phase diagram Fig. 5.7 and states as in Fig. 5.7(c) to extend towards lower pressure gradients. The middle regions with states as in Fig. 5.7(d),(e) are also likely to appear at lower pressure gradients and to grow in size. This would occur at the cost of the region with wall attraction and states as in Fig. 5.7(b), which is likely to have a smaller extent.

### 5.3 Summary

Through the investigation of single colloid behaviour this chapter investigated the particle migration patterns under flow conditions. The novel results in this nematic channel showed that particles could exhibit off-center, weak attractor, emergent attractor, and wall positions. Additionally, it was found that the emergent attractor region moves towards the walls with increasing Ericksen numbers, and there was a bend to splay transition at relatively narrow critical values. Importantly, shear and bulk viscosity changes did not affect equilibrium positions, as expected from the results presented in the previous chapter. We also observed particle-induced switching from bend to splay, and the regular Saturn ring defect was tilted due to particle position, changing shape and including a cap-like region in the bend state. Furthermore, fast migration of particles to equilibrium regions was noted, with the effect dependent on particle size, being

less pronounced for smaller particles and more pronounced for larger ones. In comparison to isotropic material the migration of the particle is much faster in the nematic. These findings provide valuable insights into factors influencing particle migration and liquid crystal defect behavior in flow, aligning with the stated project aims of defining factors strongly influencing particle migration and having a better understanding of the liquid crystal defect behaviour in flow.

Moving forward, controlling particle position through pressure gradients and conducting more experimental work in wider channels could yield further insights into the complex dynamics of particles in liquid crystals under flow conditions. The work presented in this chapter, which was also published in a peer-reviewed journal [1], could have future applications in flow sensing systems or in self assembly.

In the next chapter we also focus on the dynamics of a single particle in a nematic, as published in [2]. We bring focus to a much narrower microfluidic set up such that we can investigate the effects of confinement. Additionally, we will explore the effects of the particle anchoring strength, particularly focusing on the defect behaviour.

## Chapter 6

# Particle advection in confined liquid crystal flow

### 6.1 Simulation set up

Here we further investigate the dynamics of a single colloidal particle in a nematic liquid crystal environment. The simulation results we present show the scalar order parameter and director field at various confinement ratios and flow velocities and compare them to those obtained for simple Newtonian fluids, as published in [2].

Fig. 6.1 shows a diagram of the three-dimensional computational geometry, which consists of a duct of  $L_x = 24, 32$  or  $48$  and  $L_y \times L_z = 256 \times 384$  lattice sites. Solid walls are positioned at  $x = 0$  and  $x = L_x$ ,  $y = 0$  and  $y = L_y$  hence we refer to this geometry as a duct, in comparison to previous chapters where the solid walls were in the  $x$ - plane only creating a channel. We define the measure of confinement as the ratio of the particle diameter to the height of the duct, which here leads to confinement ratios  $2R/L_x = 0.8, 0.6$ , and  $0.4$ . The value of  $L_y$  means that, with the particle at the centre of the duct, the system is effectively unconfined in  $y$ -direction since  $2R/L_y = 0.075$ . Periodic boundary conditions are applied in the  $z$ -direction with the  $z$ -boundaries acting as inlet and outlet of the duct. A pressure gradient  $\Psi = \Delta p/L_z$  is applied in  $z$ -direction, leading to a body force density acting on all sites.

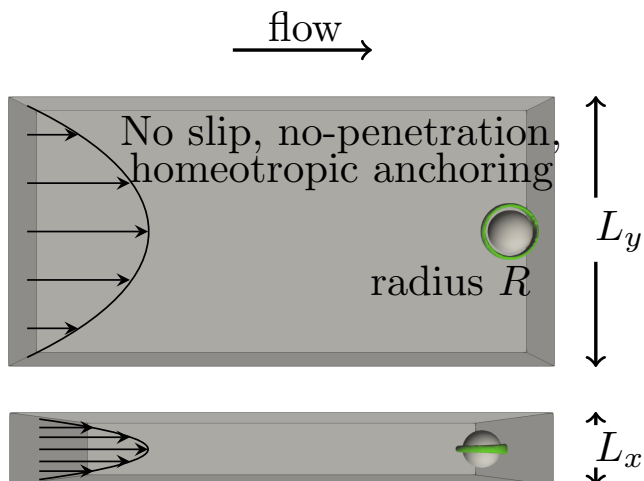


Figure 6.1: Overview of the computational geometry: We apply no-slip boundary conditions and homeotropic anchoring conditions at the walls in  $x$ -direction and  $y$ -direction, with periodic boundary conditions at the  $z$ -boundaries. The top part shows the top view, and the bottom part shows the side view.

The colloidal particle is discretised as a solid, mobile particle with a radius of  $R=9.6$  lattice sites. The longitudinal and angular momenta of the particle are evolved following the Newton's second law of motion. We use a mixed explicit-implicit velocity update, which minimises the number of linear equations that must be solved, while maintaining absolute stability [142]. Both the walls and the particle surface have no-slip and no-penetration boundary conditions which are applied by using a bounce-back on links scheme [109, 140, 141]. Lubrication corrections are applied normal to the walls within a distance of 0.1 lattice sites [142]. The chosen surface free energy creates a homeotropic anchoring condition with a preferred orientation of the director normal to the surfaces.

An overview of the simulation parameters used in this chapter is given in Tab. 6.1. A typical simulation is first initialised with no applied pressure gradient for  $5 \times 10^4$  iteration steps for each anchoring strength. After this initial equilibration phase, the simulations are restarted with various pressure gradients that are kept constant for  $4 \times 10^5$  iteration steps. Typical runtimes are approximately 26 hours using a hybrid MPI/OpenMP parallelisation with 2 MPI tasks each running on 20 OpenMP threads.

Before delving into our results, we shall first present some information relevant for



Table 6.1: Overview of simulation parameters

Variable		
Particle anchoring strength	$w_{\text{part}}$	0, 0.001, 0.01, 0.05
Invariable		
Bulk energy scale	$A_0$	0.01
Inverse temperature	$\gamma$	3.1
Elastic constants	$\kappa$	0.01
Wall anchoring strength	$w_{\text{wall}}$	0.02
Flow alignment parameter	$\xi$	0.7
Mobility parameter	$\Gamma$	0.5
Density	$\rho$	1.0
Dynamic viscosity	$\eta$	5/6
Bulk viscosity	$\zeta$	5/6
Particle radius	$R$	9.6

further context. As a reminder, the Ericksen number characterises the ratio of viscous to elastic forces and is defined as

$$\text{Er} = \frac{\eta u \Lambda}{\kappa}, \quad (6.1)$$

where  $u$  is a characteristic flow velocity, (here we use the velocity at the centre of the duct  $U_c$ ),  $\eta$  is the dynamic viscosity,  $\Lambda$  is a characteristic length scale, which we set here as the narrowest gap size  $L_x$  (see Tab. 6.2 for  $\Lambda = 2R$ , which allows direct comparison with Chapter 5), and  $\kappa$  is the bulk elastic constant of the liquid crystal.

The dynamic viscosity  $\eta$  is calculated as an apparent viscosity, defined as the ratio,  $\eta = \mu \Phi_0 / \Phi$  of the volumetric flux  $\Phi_0$  of a simple Newtonian fluid and the volumetric flux of the liquid crystalline system  $\Phi$ , through a plane perpendicular to the flow in the  $z$ -direction, namely

$$\Phi = \int_0^{L_x} \int_0^{L_y} u_z(x) dx dy, \quad (6.2)$$

with the flow being driven through the pressure gradient  $\Psi = \Delta p / L_z$  with  $\Delta p$  being the pressure difference between inlet and outlet. The volumetric flow rate  $\Phi_0$  of a Newtonian fluid with a dynamic viscosity  $\mu$  through a gap  $L_x$  driven by a pressure

gradient  $\Psi$  in plane Poiseuille flow can be calculated as

$$\Phi_0 = \int_0^{L_x} \int_0^{L_y} \frac{L_x^2}{2\mu} \Psi \left( \frac{x}{L_x} - \left( \frac{x}{L_x} \right)^2 \right) dx dy \quad (6.3)$$

$$= \frac{L_x^3 L_y \Psi}{12 \mu}. \quad (6.4)$$

Fig. 6.2 shows fluid velocity profiles for a representative confinement ratio of  $2R/L_x = 0.6$  that have been normalised to the peak flow velocity of a simple Newtonian fluid in Poiseuille flow at the same pressure gradient and scaled using the  $x$ -dimension of the duct. The apparent viscosity  $\eta$  is the ratio of the areas under the Poiseuille curve and the curves at finite Ericksen numbers.

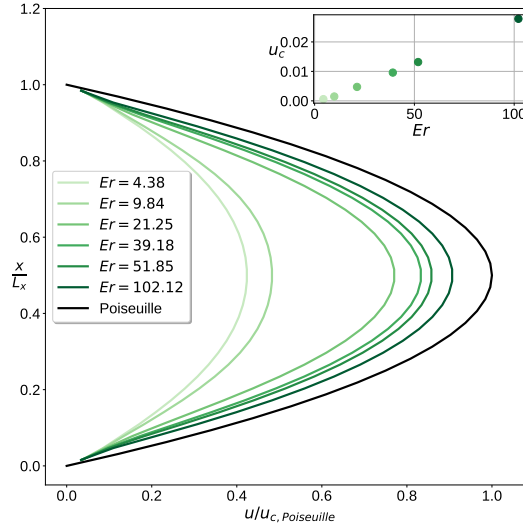


Figure 6.2: Scaled magnitude of the fluid velocity  $u(x) = |\mathbf{u}(x)|$ , normalised against the peak flow velocity  $u_{c,Poiseuille}$ , of a simple Newtonian fluid in Poiseuille flow at the centre line of the duct at  $x = L_x/2$ . The image shows representative results for the confinement ratio  $2R/L_x = 0.6$ . The black line is the parabolic flow profile of Poiseuille flow. Away from the walls the velocity profiles of the flowing nematic are parabolic. Deviations from the parabolic profile occur only close to the walls. The inset shows the dependence of the centre line fluid velocity  $u_c$  on the Ericksen number Er.

More specifically, in Fig. 6.2 the flow velocities have been normalised against the maximum flow velocity of the Poiseuille flow  $u_{c,Poiseuille}(x = L_x/2) = L_x^2 \Delta p / 8 \mu L_z$  at the centre line of the duct with  $\mu$  as dynamic viscosity and  $\Delta p$  as pressure difference

between inlet and outlet, respectively. Away from the walls at  $x/L_x = 0$  and  $x/L_x = 1$  the velocity profiles of the flowing nematic are parabolic and deviations from the parabolic profile occur only near the walls. This is a result of shear thinning as the director field flow-aligns further away from the walls, which is prevented by the normal wall anchoring in the vicinity of the walls. In all simulations that contain a colloidal particle the fluid flow velocity  $u_c$  at the centre line was taken at  $x = L_x/2$ , at a point in a distance  $L_z/2$  upstream/downstream from the particle. This is the point farthest away from the particle in the  $z$ -direction due to the periodic boundary conditions. However, owing to this large distance the values we obtained for  $u_c$  in this manner are virtually identical to those of a pure liquid crystal without particle. Profiles for other confinement ratios are not shown as they look very similar.

$2R/L_x = 0.4$		$2R/L_x = 0.6$		$2R/L_x = 0.8$	
Er ( $L_x$ )	Er (2R)	Er ( $L_x$ )	Er (2R)	Er ( $L_x$ )	Er (2R)
1.65	0.658	4.38	2.63	6.15	4.92
8.30	3.32	9.84	5.90	10.37	8.30
18.10	7.24	21.25	12.75	17.95	14.36
35.55	14.22	39.18	23.51	22.32	17.86
52.72	21.09	51.86	31.11	64.85	52.16
69.77	27.91	102.12	61.27	86.06	69.10

Table 6.2: Conversion of Ericksen numbers for different confinement ratios using different characteristic length scales, namely the size of the channel (odd columns) or, as in Chapter 5, the diameter of the particle (even columns).

## 6.2 Defect structure influenced by the director and fluid velocity fields

We study the advection behaviour of a single particle moving in a nematic host phase in highly confining ducts and investigate the effects of varying the pressure gradient  $\Psi$ , confinement ratio  $2R/L_x$  and homeotropic anchoring strength [2]. In a simple Newtonian fluid, or in a liquid crystal at temperatures above the isotropic-nematic transition point, the motion of a freely suspended spherical particle between two parallel plane walls has been studied previously theoretically [163, 164], with simulations [165] and

experimentally [166]. The main effect is that the retardation of the particle motion to the fluid motion is primarily independent of the applied pressure gradient. It is however greater for particles closer to either of the walls, and for highly confined particles due to the proximity to the walls. Therefore, it depends on the confinement ratio.

In a nematic liquid crystal with homeotropic anchoring conditions at the walls the director orientation is forced to be parallel to the wall normals. The degree of alignment depends on the strength of the anchoring, but also on the velocity gradient, and therefore the pressure gradient. At low pressure gradients, the nematic order will be enforced throughout the duct. But for higher pressure gradients the director field flow-aligns at the Leslie angle. As a reminder, the two conformations are persistent in flowing nematics, namely the so-called bend state or H-state and the splay state or V-state. For both H- and V-state the director flow-aligns to a positive (negative) Leslie angle in the lower (upper) half of the channel. The difference between the two states is determined by the way the director rotates between the positive and negative Leslie angles at the centre: in the bend state, the director at the centre is perpendicular to the walls, whereas in the splay state the director is almost parallel to the walls at the centre. The bend state is generally adopted at low flow velocities, whereas the nematic transitions to the splay state at higher flow velocities.

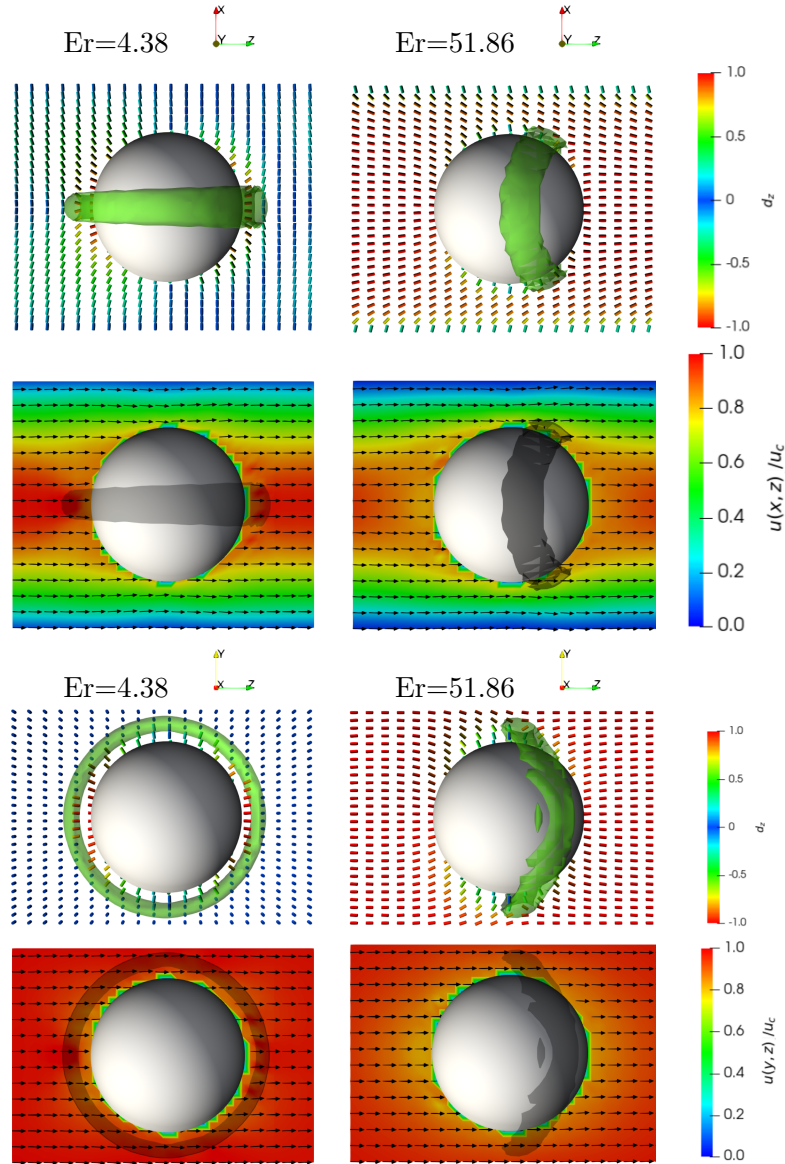


Figure 6.3: Director field, defect structure and fluid velocity profiles for confinement ratio  $2R/L_x = 0.6$  and anchoring parameter  $\omega = 48$  before and after the bend-to-splay transition. The left column shows the bend state, while the right column shows the splay state. The first and third row show the director field  $\mathbf{d}$  with the magnitude  $d_z$  of its  $z$ -component. The second and fourth row show the magnitude of the fluid velocity  $u(x, z)$  and  $u(y, z)$  through the centre of the particle, normalised to the maximum velocity  $u_c$  at the centre line of the duct. The two top rows represent slices through the middle of the channel in the  $xz$ -plane (narrowest duct and flow direction). The two bottom rows show slices in the  $yz$ -plane. The flow direction is from left to right. The opacity of the defect rings is reduced to for better visibility of the local director field.

Fig. 6.3 shows the director field, defect structure and magnitude of the fluid velocity at a medium confinement ratio  $2R/L_x = 0.6$  and different Ericksen numbers. The left column displays the bend state at  $Er=4.38$  prior to the transition to the splay state, whereas the right column shows the splay state at  $Er=51.86$  after transitioning from the bend state. The two top rows contain slices in the  $xz$ -plane (narrowest duct dimension and flow direction) at  $y = L_y/2$  with walls at the  $x$ -boundaries at the top and bottom, whereas the two bottom rows show slices in the  $yz$ -plane (widest duct dimension and flow direction) at  $x = L_x/2$  in the vicinity of the colloidal particle.

The director field in the first and third row is colour-coded with red indicating an orientation parallel to the flow or  $z$ -direction and blue indicating an orientation perpendicular to the flow direction or in  $xy$ -plane. The bend state at low Ericksen number shows the Saturn ring defect oriented parallel to the walls with only very minor deformations, while the splay state has the Saturn ring defect oriented approximately perpendicular to the walls and displaced slightly downstream from the meridian of the particle in positive  $z$ -direction.

The second and fourth row show the magnitude of the fluid velocity  $u(x, z) = |\mathbf{u}(x, z)|$  in the  $xz$ -plane and  $u(y, z) = |\mathbf{u}(y, z)|$  in the  $yz$ -plane normalised to the maximum velocity  $u_c$  at the centre line of the duct. It is interesting to see that despite the striking differences in the director field structure and defect ring orientation at the two different Ericksen numbers both flow profiles are very similar. A minor exception is that at the lower Ericksen number the peak velocity is attained very close to the particle, whereas at the higher Ericksen number the relative fluid velocity is slightly reduced around the particle. This is a consequence of the different differential velocities between the colloidal particle and the fluid in both cases (see Fig. 6.8).

As a quantitative overview of our findings, we include in Fig. 6.4, snapshots of the particle and its defect in the steady state for varying confinement ratios and Ericksen numbers [2]. In each cell the left images show the side view looking in the negative  $y$ -direction with walls at the top and bottom. The images on the right show the view from the top looking in the positive  $x$ -direction. The confinement increases from left to right from confinement ratios  $2R/L_x = 0.4$  to  $2R/L_x = 0.6$  to  $2R/L_x = 0.8$ , and

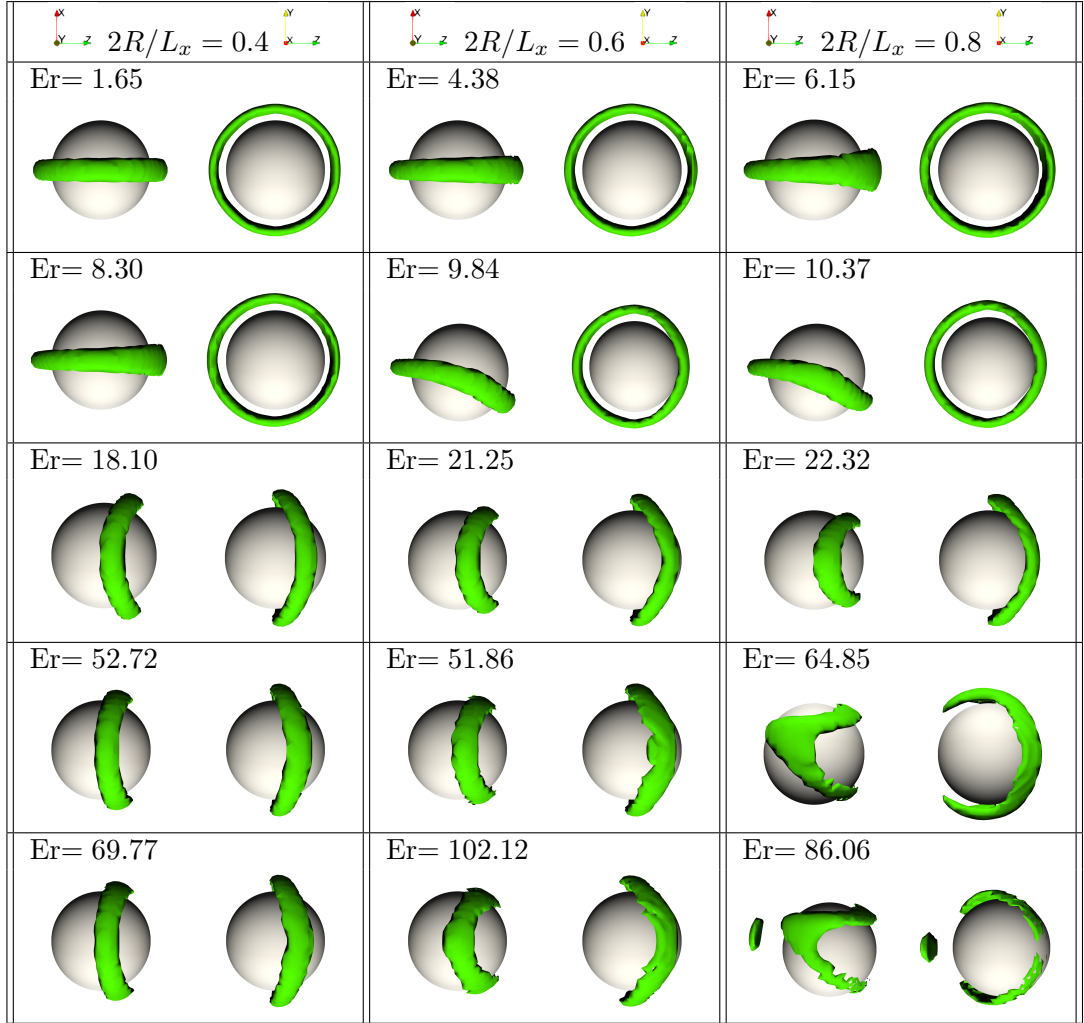


Figure 6.4: Snapshots of the director field and defect structure in the steady state at various Ericksen numbers and strongest particle anchoring parameter  $\omega = 48$ . The bright green region corresponds to the defect where liquid crystalline order is reduced. In each cell the left images in each cell show the side view looking in the negative  $y$ -direction with walls at the top and bottom. The images on the right in each cell show the view from the top looking in the positive  $x$ -direction. The confinement increases from left to right, and Ericksen numbers increase from top to bottom. While in most cases the particle stays at the centre of the duct throughout the simulation, there are a small number of cases where they migrate away from it. Specifically, there are two cases where the particle migrates fully to a wall (for the two highest Ericksen number and confinement ratio  $2R/L_x = 0.8$ ), and three cases where the particle migrates to a stable position between the wall and the centre (for Er= 18.10 and  $2R/L_x = 0.4$ , for Er= 9.84 and  $2R/L_x = 0.8$ , and for Er= 10.37 and  $2R/L_x = 0.8$ ).

Ericksen numbers increase from top to bottom. The defect is shown as a green isosurface defined by a local order parameter  $q \leq 0.188$  and the particle anchoring strength and dimensionless anchoring parameter are  $w_{part} = 0.05$  and  $\omega = 48$ , respectively, as lower anchoring strengths do not result in defects that could be distinctively visualised.

At low Ericksen numbers, below the bend-to-splay transition, the particle has a Saturn ring defect such that the ring plane remains parallel to the walls. This is the case for all confinement ratios and Ericksen numbers below  $Er = 10.37$ , as shown in the first and second row of Fig. 6.4. Two aspects are noteworthy. Firstly, there is a slight increase of the defect isosurface radius downstream of the particle, for which both Ericksen number (see images for  $2R/L_x = 0.4$  with  $Er = 1.65$  and  $Er = 8.30$ ) and confinement ratio (see image for  $2R/L_x = 0.6$ ,  $Er = 4.38$  and  $2R/L_x = 0.8$ ,  $Er = 6.15$ ) seem responsible. However, confinement appears to play a more important role in this context.

Secondly, at slightly increased Ericksen numbers (see images for  $2R/L_x = 0.6$ ,  $Er = 9.84$  and  $2R/L_x = 0.8$ ,  $Er = 10.37$ ), the Saturn ring becomes angled such that the part downstream of the particle is closer to the bottom wall, while the other part upstream of the particle remains virtually unchanged. These two particular cases reach steady state positions that are offset somewhere between the centre of the duct and the walls in the  $x$ -direction, which contributes to this asymmetric appearance. This can be explained with the migration to the weak attractor region that we observed in the previous chapter for low confinement conditions using a much wider microchannel and lower confinement ratio of  $2R/L_x = 0.15$ . For direct comparison, Tab. 6.2 gives an approximate conversion between particle Ericksen numbers, as used in the previous chapter, and Ericksen numbers based on the smallest duct dimension presented here.

Fig. 6.5 shows a direct comparison of the defect rings around the particle for the lowest and highest simulated Ericksen numbers below the bend-to-splay transition, at confinement ratios (a)  $2R/L_x = 0.4$  (b) 0.6 and (c) 0.8. The defects at the lowest Ericksen numbers, depicted in grey, are distinctive Saturn rings that are oriented parallel to the walls in the  $x$ -direction. As previously mentioned, increasing confinement leads to a defect ring that is thicker at the downstream side of the particle, while it remains



oriented parallel to the wall at the  $x$ -boundary. Increasing the Ericksen number alone does not change the orientation of the defect ring, but leads to a very slight shift in position upstream (see grey and yellow defect rings in Fig. 6.5a)). However, increasing the Ericksen number and confinement ratio induces a noticeable tilt of the defect ring, shown in Fig. 6.5b) and c), as the particle migrates into the off-centre steady state position somewhere between the centre of the duct and one of the walls. Despite the difference in confinement ratio and Ericksen number ( $2R/L_x = 0.6$  and  $0.8$ ,  $Er = 9.84$  and  $10.37$ , respectively) the shape of the defect rings is almost the same [2].

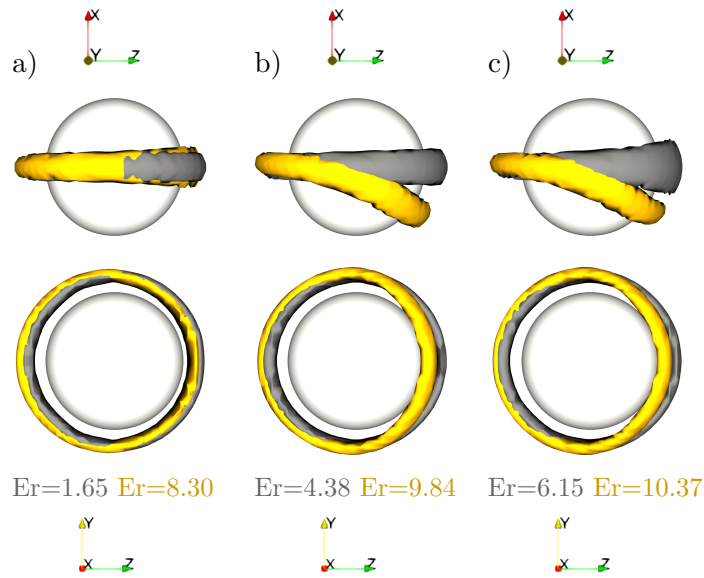


Figure 6.5: Disclination lines around the particle for the lowest — and highest — simulated Ericksen numbers below the bend-to-splay transition at confinement ratios a)  $2R/L_x = 0.4$ , b)  $2R/L_x = 0.6$  and c)  $2R/L_x = 0.8$ , respectively. The top row has the view in negative  $y$ -direction, the widest duct dimension, with the walls in the narrowest duct dimension at the  $x$ -boundaries situated closely above and below the particle. The bottom row shows the view in positive  $x$ -direction. The flow is in the horizontal positive  $z$ -direction from left to right.

Upon increasing the Ericksen number, a bend-to-splay transition takes place somewhere between  $8.30 < Er < 18.10$  (for  $2R/L_x = 0.4$ ),  $9.84 < Er < 21.25$  (for  $2R/L_x = 0.6$ ) and  $10.37 < Er < 17.95$  (for  $2R/L_x = 0.8$ ). The defect ring is now reoriented with its ring plane approximately perpendicular to the walls and flow direction, as shown in Fig. 6.4, for instance in the third row, and retains a similar shape at higher Erick-

sen numbers (see images for  $2R/L_x = 0.4$ ,  $Er = 18.10$ ,  $2R/L_x = 0.6$ ,  $Er = 21.25$ , and  $2R/L_x = 0.8$ ,  $Er = 22.32$ ). The case for  $2R/L_x = 0.4$ ,  $Er = 18.10$  forms an exception in that the particle moves very slightly away from the centre into a stable off-centre position, while in the other cases the particle remains at the centre of the duct, which can be also understood with the migration to the previously observed weak attractor region at similar Ericksen numbers [1] (see Tab. 6.2 for conversion of Ericksen numbers). A noticeable difference is that with increasing confinement the defect ring appears compressed in the smallest duct dimension due to the relative proximity of the walls (see image for  $2R/L_x = 0.8$ ,  $Er = 22.32$ ) [2].

With increasing Ericksen numbers the shape of the vertically oriented defect ring remains largely unchanged for low and medium confinement, as shown in the first and second column, fourth and fifth row, of Fig. 6.4 ( $2R/L_x = 0.4$  and  $0.6$ ) for Ericksen numbers  $Er = 52.72$ ,  $69.77$  and  $Er = 51.86$ ,  $102.12$ , respectively. At  $Er = 102.12$  a slight change occurs such that the defect close to the mid-plane of the duct in the  $x$ -direction are distorted and pulled in the upstream direction, i.e. against the flow. This effect is a precursor of the more dramatic elongation of the Saturn ring that will become even more evident as the confinement ratio increases.

At even higher Ericksen numbers  $Er = 64.85$  and  $Er = 86.06$  and confinement  $2R/L_x = 0.8$ , shown in the third column fourth and fifth row of Fig. 6.4, we observe defects that differ substantially from those discussed before. In these cases the particle migrates fully to one of the walls. This has also been previously observed for similar Ericksen numbers in much lower confinement [1], as shown in the previous chapter. There it occurred when the particle was within a distance of one and a half to two diameters from the walls, depending on the Ericksen number (see Tab. 6.2 for a conversion of  $Er$ ). Given the proximity of the walls with increased confinement, this means that attraction to the walls should occur in practically all situations. This, however, is not the case as we observe attraction to the walls only for the highest Ericksen numbers and the largest confinement. Hence, the increased confinement prevents particle migration to the walls and stabilises trajectories around the centre of the duct. The migration to one of the walls results in a different defect shape such that there is a pronounced elongation of

the Saturn ring defect in the upstream direction. There is also the indication of a small satellite region of low order, upstream of the particle that never merges up with the rest of the defect (see image for  $2R/L_x = 0.8$  and  $Er = 86.06$ ) [2].

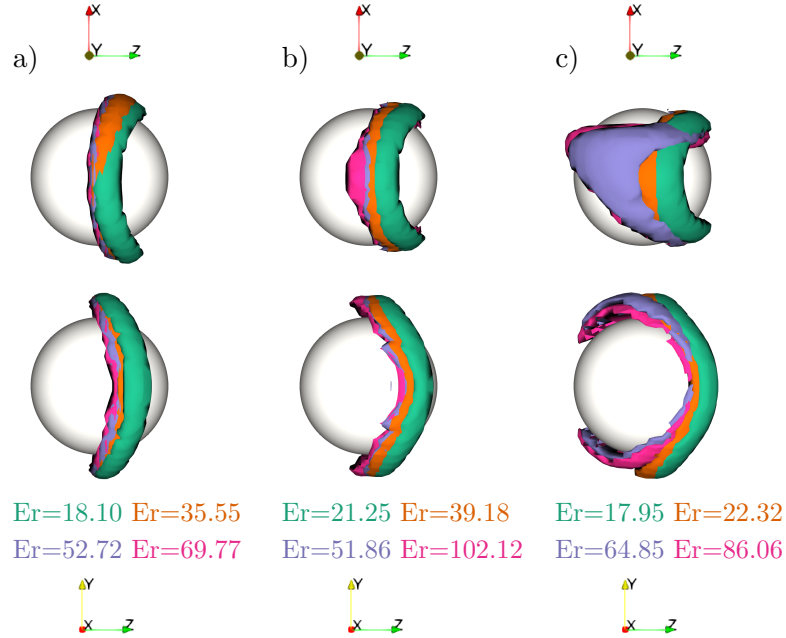


Figure 6.6: Saturn ring disclination lines around the particle for various Ericksen numbers after the bend-to-splay transition has taken place. The confinement ratios are a)  $2R/L_x = 0.4$ , b)  $2R/L_x = 0.6$  and c)  $2R/L_x = 0.8$ . In the top row the view is along the negative  $y$ -direction, the widest duct dimension, with the walls in the narrowest duct dimension at the  $x$ -boundaries situated above and below the particle. The bottom row is the view in the positive  $x$ -direction. The flow is in the horizontal  $z$ -direction from left to right.

Before focusing on the director structure at high Ericksen numbers and large confinement in more detail (see Fig. 6.7), we show the differences in the defect rings at different confinement ratios and Ericksen numbers. Fig. 6.6 shows superimposed, vertically oriented defect rings as they occur after the bend-to-splay transition has taken place. At the lowest confinement ratio  $2R/L_x = 0.4$ , shown in Fig. 6.6a), the defect ring remains relatively undistorted across a range of medium to high Ericksen numbers. However, comparing the images at the top with the view along the  $y$ -direction across the narrowest gap to those at the bottom with the view along the  $x$ -direction across

the widest gap gives evidence that the shape of the Saturn ring defects is sensitive to confinement. When confined, the defect rings are located slightly downstream from the particle's equator, whereas they remain situated along the equator in the dimension of no or very small confinement ( $2R/L_y = 0.075$ ). This feature becomes more pronounced as the confinement increases, discernible through the green defect rings at ratios  $2R/L_x = 0.6$  in Fig. 6.6b), and more so at  $2R/L_x = 0.8$  in Fig. 6.6c) where it results in the compressed appearance (Fig. 6.6c) top row). This applies to lower (green isosurfaces) and medium (orange isosurfaces) Ericksen numbers. Increasing both confinement and Ericksen numbers leads to the aforementioned different appearance of the defect rings (purple and magenta isosurfaces).

It is worth mentioning that the confinement ratios here are larger than those in similar studies [167, 168] ( $2R/L_x = 0.25$  and  $2R/L_x = 0.19$ , respectively), where the lower confinement has been chosen to eliminate possible effects on the results. However, our case [2] of  $2R/L_x = 0.4$  is low enough to feature defect rings that appear undeformed and occur at unaltered relative positions to the particle.

The director field, defect structure and magnitude of the fluid velocity at high Ericksen numbers and the largest confinement ratio  $2R/L_x = 0.8$  are shown in Fig. 6.7. At this confinement ratio the walls at the  $x$ -boundaries are close to the colloidal particle. The two top rows contain slices in the  $xz$ -plane (narrowest duct dimension and flow direction) at  $y = L_y/2$  with walls at the  $x$ -boundaries at the top and bottom, whereas the two bottom rows show slices in the  $yz$ -plane (widest duct dimension and flow direction) at  $x = L_x/2$  cropped to the vicinity of the colloidal particle. The director field in the first and third row is colour-coded with red indicating an orientation parallel to the flow or  $z$ -direction and blue indicating an orientation perpendicular to the flow direction or in  $xy$ -plane. The left column shows the situation at moderately high Ericksen numbers  $Er = 22.32$ .

The defect ring is vertically oriented, noticeably displaced downstream close to the walls at the boundary in  $x$ -direction (see Fig. 6.7 first row first column), and situated at the equatorial region of the particle in the non-confined  $y$ -dimension (see Fig. 6.7 third row first column). The director field structure in  $yz$ -plane shows that flow alignment

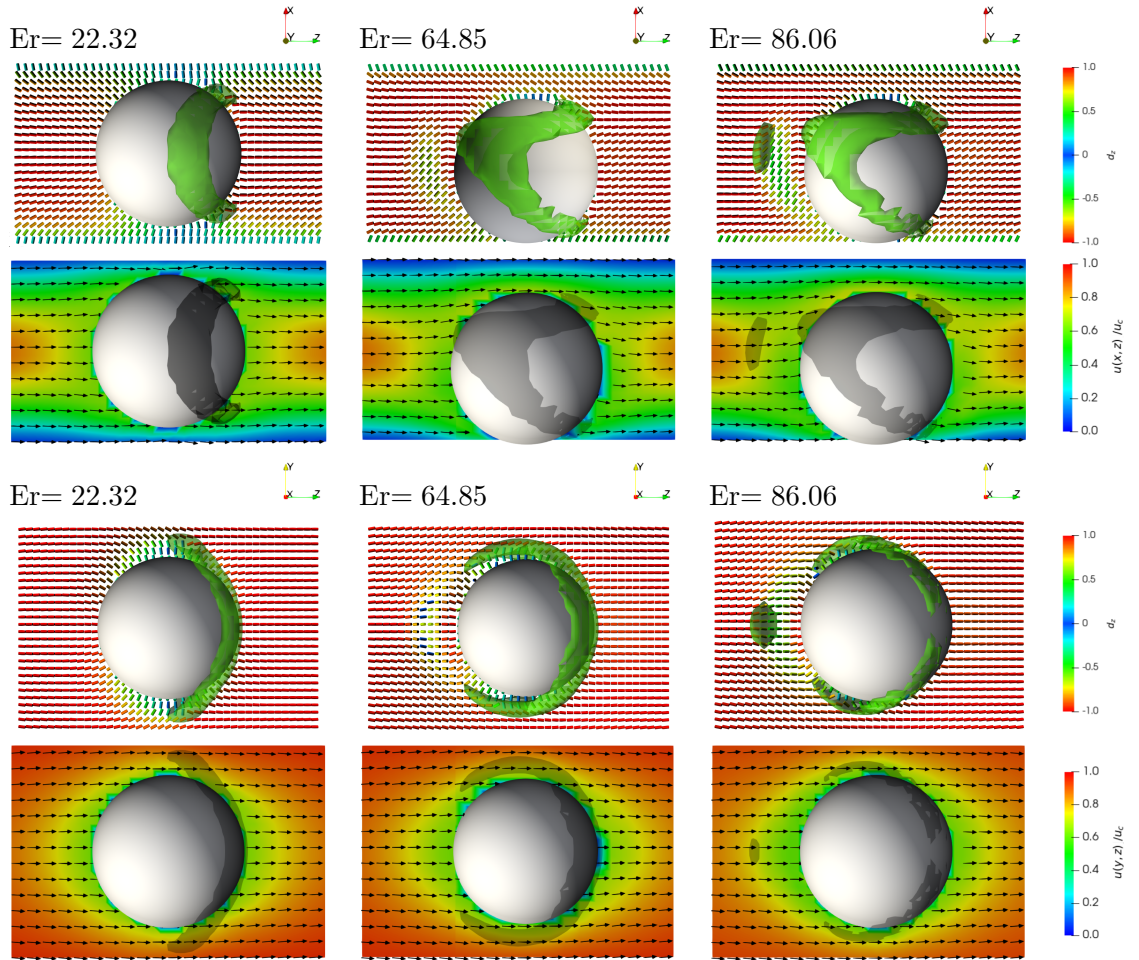


Figure 6.7: Director field, defect structure and fluid velocity profiles for confinement ratio  $2R/L_x = 0.8$  and anchoring parameter  $\omega = 48$  after the bend-to-splay transition for increasing Ericksen numbers  $Er = 22.32, 64.85$  and  $86.06$ , respectively. The first and third row show the director field  $\mathbf{d}$  with the magnitude  $d_z$  of its  $z$ -component indicated through the colour code. The second and fourth row show the magnitude of the fluid velocity  $u(x, z)$  and  $u(y, z)$  through the centre of the particle, normalised to the maximum velocity  $u_c$  at the centre line of the duct, where arrows give a sense of the vectorial dependence of the fluid velocity field. The images in the two top rows represent slices through the middle of the channel in the  $xz$ -plane (narrowest duct dimension and flow direction) and have the view along the negative  $y$ -dimension. Those in the two bottom rows show slices in the  $yz$ -plane (widest and narrowest duct dimension) and have the view in positive  $x$ -direction. The flow direction is from left to right in positive  $z$ -direction. The opacity of the defect rings (green isosurfaces) has been slightly reduced to enhance the visibility of the local director field.

occurs in a short distance from the particle and entails a defect in the equatorial region. Focusing again on the director field in  $xz$ -plane reveals that the situation is different in the confined  $x$ -dimension. Here, the homeotropic anchoring conditions at the wall and particle surfaces prevent any kind of flow alignment in the narrow gap between the particle and the walls. Considering the left-hand upstream side of the particle it becomes evident that both the normal anchoring conditions on the surface and the flow-alignment close to the surface work in the same sense and promote the same director orientation. This is different on the right-hand downstream side. While downstream directly right from the particle's centre flow-alignment and anchoring are also working in the same sense, this is not the case downstream above right and below right from the centre where flow-alignment invokes a northwest-southeast orientation of the director field, while surface anchoring promotes a northeast-southwest orientation. This leads to the slight downstream displacement of the defect ring.

At higher Ericksen numbers  $Er= 64.85$  and  $Er= 86.06$  the particle migrates readily to one of the walls [1] and the shape of the defect changes (see Fig. 6.7) first and third row, second and third column). The asymmetric positioning of the particle in the duct is only partly responsible for this. In fact, we observe large differential velocity between the particle and the fluid, which means the particle acts now increasingly as obstacle. Therefore, it is instructive to look again at fluid velocity profiles.

The second and fourth row in Fig. 6.7 show the magnitude of the fluid velocity  $u(x, z) = |\mathbf{u}(x, z)|$  in the  $xz$ -plane and  $u(y, z) = |\mathbf{u}(y, z)|$  in the  $yz$ -plane normalised to the maximum velocity  $u_c$  at the centre line of the duct. The profiles in  $xz$ -plane (second row) show that compared to Fig. 6.3 where the confinement ratio is  $2R/L_x = 0.6$ , the now larger confinement ratio of  $2R/L_x = 0.8$  leads to much lower relative fluid velocities upstream and downstream on the left and right of the particle. With increasing Ericksen number a region with enhanced flow velocities emerges immediately above the particle where the fluid is forced upwards (see Fig. 6.7 second row third column). The fluid velocity profiles in  $yz$ -plane (see Fig. 6.7 fourth row) demonstrate even further how the relative fluid velocity drops around the particle with increasing Ericksen number. However, what the colour code and normalisation to the peak flow velocity  $u_c$  hide is

that the velocity gradients in absolute terms are even larger for larger pressure gradient, a direct consequence of higher absolute values of the peak velocity  $u_c$ . In view of the director field and defect structure, it becomes evident that the regions with large fluid velocity gradients are also the regions where the director structure becomes noticeably distorted. This effect in combination with local flow-alignment and surface anchoring leads to local regions of low order, for instance the satellite region of very low order slightly upstream on the left of the particle (see Fig. 6.7 second and third column), and causes the defect ring to become extended further upstream, albeit never completely engulfing the particle [2].

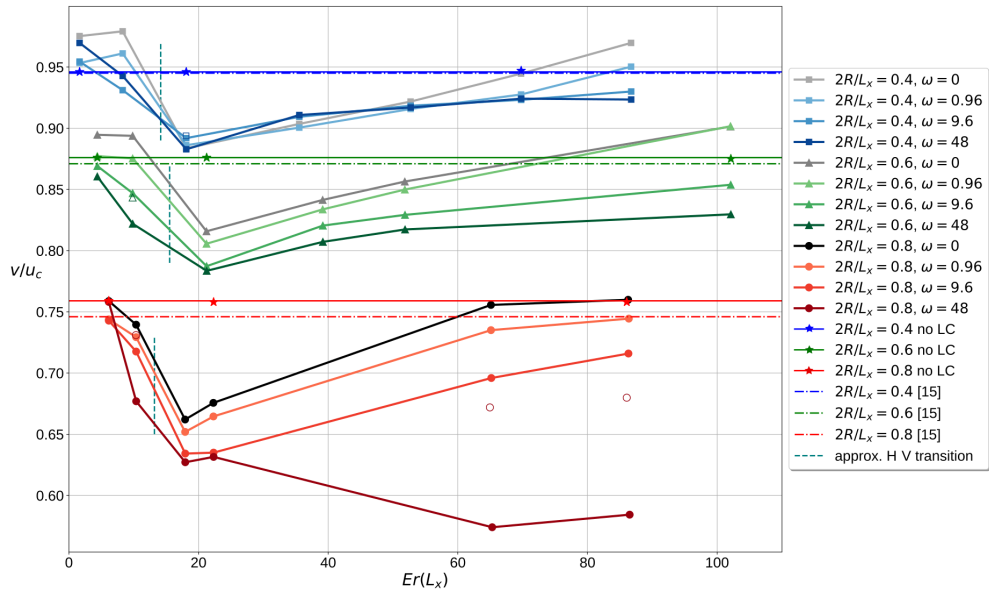


Figure 6.8: Comparison of retardation ratios  $v/u_c$  of particle velocity  $v$  to fluid velocity  $u_c$  at the centre of the rectangular duct for confinement ratios  $2R/L_x = 0.4$  (blue squares),  $0.6$  (green triangles) and  $0.8$  (red circles) and different particle anchoring strengths. Horizontal lines show results in a Newtonian fluid from Staben et al. [164] (dashed-dotted lines) and with our approach (in the isotropic phase (stars)). Open symbols indicate cases where the colloidal particle has been fixed in  $x$ -direction for comparison as it would normally migrate away from the centre of the duct to either an off-centre position or to the walls. The vertical lines indicate the approximate position of the bend-to-splay transition.

### 6.3 Advection behaviour

We now move on to the analysis of the advection behaviour of the colloidal particle at different Ericksen numbers and confinement ratios and compare it to that in a simple Newtonian fluid. For this purpose we draw on the theoretical results obtained by Staben et al. [164], which have been reproduced in a number of studies. While our Reynolds numbers are typically between  $\mathcal{O}(10^{-2})$  and  $\mathcal{O}(10^{-1})$  and therefore larger than those in Ref. [164], it is worth emphasising that the latter results form still a suitable reference as both regimes can be classed as low-Reynolds number ones.

A suitable measure to characterise the advection behaviour is the retardation ratio  $v/u_c$  of particle velocity  $v$  to fluid velocity  $u_c$  at the centre line of the duct. In an isotropic Newtonian fluid under Poiseuille flow this ratio is constant and depends only on the distance of the particle from the walls of the duct and the confinement ratio. In particular,  $v/u_c$  is independent of the Reynolds number. Without confinement the retardation ratio  $v/u_c$  is unity as the particle acts as a tracer and is simply advected with the fluid. At finite confinement ratios below  $2R/L_x = 1$  the movement of the particle is slowed down in the parabolic Poiseuille flow due to the no-slip boundary conditions on the walls of the duct. In our simulations the absolute value of  $u_c$  was taken as the flow velocity at the centre line  $x = L_x/2$  at the point farthest away from the colloidal particle in a distance  $L_z/2$  upstream/downstream in flow direction.

Fig. 6.8 shows the retardation ratio  $v/u_c$  for different confinement ratios  $2R/L_x$ , particle anchoring strengths and Ericksen numbers  $Er$ . Using the Ericksen number as abscissa has the advantage that the bend-to-splay transition occurs at similar values aiding the comparison across different confinement ratios. The straight, horizontal lines represent the results for a particle in a simple Newtonian fluid. Dashed-dotted lines give the results from Staben et al. [164] for particles at the centre of the duct. We measure retardation ratios of  $v/u_c = 0.946, 0.876$  and  $0.759$  for confinement ratios  $2R/L_x = 0.4, 0.6$  and  $0.8$ , respectively, shown in Fig. 6.8 with solid lines. These results compare well with those of Staben et al., which are  $v/u_c = 0.945, 0.871$  and  $0.746$  for the same confinement ratios and particles positioned at the centre of the duct. It is worth



emphasising that in our setup the largest confinement ratio  $2R/L_x = 0.8$  has less than 3 lattice sites between the particle surface and the walls on either side. Nevertheless, the relative deviation between ours and Staben's results for Newtonian host phases is less than 1.8% in the worst case, which means our method is remarkably accurate given the relatively sparse discretisation. However, it should be borne in mind that when modelling a liquid crystalline host phases the sparse discretisation affects also the tensor order parameter  $\mathbf{Q}$  in addition to the fluid-solid interaction in a Newtonian host phase. While these limitations affect the results in Fig. 6.8 to a certain extent, there are nevertheless clear and robust trends that we will examine.

At low Ericksen numbers we observe retardation ratios  $v/u_c$  that are close or identical to their corresponding values in Newtonian fluids. Interestingly, and primarily for no or low particle anchoring strength and low confinement ratios  $2R/L_x = 0.4$  and  $0.6$ , the retardation ratio can be slightly larger in the nematic host phase than in the Newtonian host phase (see light and medium grey and blue data points in Fig. 6.8). This could occur because for a particular pressure gradient the peak flow velocity is lower in the flowing nematic than in the Newtonian fluid. But as the same pressure gradients acts across the particle, the latter does not slow down to the same degree in the flowing nematic, leading to comparably higher retardation ratios. For larger anchoring strengths or in higher confinement both additional elastic forces are exerted on the particle and the effective viscosity in the vicinity of the particle increases, both to the effect of slowing down the particle, resulting in smaller retardation ratios.

As the Ericksen number increases, the nematic host phase undergoes a transition from the bend to the splay phase. This occurs at Ericksen numbers  $8.30 < \text{Er} < 18.10$  ( $2R/L_x = 0.4$ ),  $9.84 < \text{Er} < 21.25$  ( $2R/L_x = 0.6$ ) and  $10.37 < \text{Er} < 17.95$  ( $2R/L_x = 0.8$ ), respectively and is indicated by the vertical green dashed lines in Fig. 6.8. The transition is accompanied by a noticeable drop in the retardation ratio, which reaches a minimum around Ericksen numbers  $\text{Er} \simeq 20$ , so just beyond the bend-to-splay transition. The minimum is smaller the larger the particle anchoring strength is, but only for medium and large confinement (see medium grey and green curves as well as black and red curves in Fig. 6.8) and not so for small confinement (see light grey and blue

curves in Fig. 6.8).

Beyond Ericksen numbers in the range of  $Er \simeq 20$  the retardation ratio  $v/u_c$  begins to increase again, giving rise to an overall non-monotonic dependence on the Ericksen number. This is the case across all confinement ratios, and the retardation ratios begin to flatten out towards higher Ericksen numbers, approaching or reaching the values of Newtonian fluids again. This non-monotonic behaviour is therefore a consequence of the decreasing importance of liquid crystalline elasticity and consistent with the idea that with higher the Ericksen numbers the liquid crystal behaves rheologically more like a simple fluid.

Regarding how the retardation ratio  $v/u_c$  depends on the particle anchoring strength the same tends as for the minima prevail. Higher anchoring strengths entail smaller retardation ratios unless the confinement is small. For our largest confinement ratio  $2R/L_x = 0.8$  and strongest particle anchoring strength  $w_{part} = 0.05$  we observe a very strong decrease. This, however, originates also from the migration of the particles to the walls. The two empty circles in Fig. 6.8 (and similar empty symbols at the two other confinement ratios) permit us to estimate how the trend would continue if the particles had been prevented from leaving the region of maximum flow velocity at the centre of the duct.

In order to explain these findings, we have to look at several separate mechanisms: First of all, there is the transition from the bend to the splay state, which all particles regardless of their anchoring conditions are subject to. The data points for vanishing particle anchoring strength  $w_{part} = 0$  (light, medium and dark grey in Fig. 6.8) are indicative of this. The transition causes the general reduction of the retardation ratios from their initially approximately Newtonian values at low Ericksen numbers to their minima around  $Er \simeq 20$ . The reason for this decrease is the drop in apparent viscosity and increase in flow velocity  $u_c$  around the centre of the duct, whereas the regions of the particle closer to the walls act as anchor and do not allow the particle to pick up velocity  $v$  at the same proportion [2].

The second mechanism at work is the reorientation of the defect ring at the bend-to-splay transition, provided the particle anchoring strength is large enough for a defect to

emerge. The vertical orientation of the defect ring with its ring plane perpendicular to the flow direction and walls increases the effective particle radius in the narrowest duct dimension and therefore the effective confinement ratio. This leads to lower retardation ratio  $v/u_c$  the larger the anchoring strength is. However, our results suggest this is only the case provided the confinement is not too large. For instance, at  $2R/L_x = 0.4$  there is very little difference between vanishing and very strong particle anchoring up to Ericksen numbers  $Er \simeq 60$ , while at  $2R/L_x = 0.6$  and  $0.8$  differences are clearly visible at all Ericksen numbers. This subtlety can be understood by realising that at the different confinement ratios and flow velocities both velocity and order parameter gradients differ across the particle diameter. At a given flow velocity the gradients are largest in large confinement and vice versa. At a given confinement ratio the velocity gradient is largest at large flow velocities and Ericksen numbers. It is precisely this nonlinear order-flow coupling and the interactions between flow and order structure in the vicinity of the particle that cause the observed minor variations in the retardation ratio.

Finally, there is also the possibility of a direct interaction with the wall anchoring when Ericksen numbers and confinement ratios are large. In these situations the colloidal particle shows a tendency to leave the centre of the duct and migrate quickly to the wall regions. There, the advection velocity and therefore the retardation ratio are reduced as a result of the no-slip boundary conditions at the walls [2].

## 6.4 Summary

In this chapter we found that low anchoring strengths at the particle surface do not lead to visually distinct defects in the system under investigation, but we do obtain them for appropriately higher values. Once again, a transition from bend to splay occurs within the more confined set ups than in Chapter 5. The critical value for the transition was observed to be dependent on the pressure gradient. During this transition, the Saturn ring remains parallel to the x-direction walls and an increase in velocity results in an expansion of the isosurface radius downstream of the particle. Additionally, a

tilt of the defect ring was noted after the transition, indicating a reorientation of the Saturn ring defect. Furthermore, as confinement increased in the system, the defect ring appeared compressed in the smallest duct dimension due to the walls' relative proximity and attraction. This compression was particularly evident for high Ericksen numbers and significant confinement levels. The increased confinement also played a role in preventing particle migration to the walls, instead stabilizing trajectories around the center of the duct. This transition caused a general reduction in retardation ratios at low Ericksen numbers, with the vertical orientation of the defect ring leading to lower retardation ratios ( $\frac{v}{u_c}$ ). Our findings indicated that the larger the anchoring strength, the more pronounced the effects observed, with the confinement playing a crucial role in determining the system's behavior. Overall, these novel results shed light on the intricate dynamics of the system under varying conditions of anchoring strength, pressure gradients, and confinement levels, providing valuable insights into the behavior of the Saturn ring defect and particle migration within the system, fully aligning with our stated project aims.

As our simulation of ducts resemble modern microfluidic experimental set ups in the liquid crystal field, in terms of narrow channels, there is possibility of doing further future experiments. Especially focusing on the Saturn ring defect types, as currently more work is done on hyperbolic hedgehog defects as we found through our collaboration with Prof Uroš Tkalec. Additionally, there are potential applications in using colloids and nematic mixtures in safety shut offs using narrow ducts - if particles drop to the walls the flow is too high.

Having presented our research results focused on single particles within microfluidic simulation set ups, we can now apply what we have found to large scale simulations with many particles. This is what we will explore in the next chapter of this thesis where our observations of single particle migration and changes in the defect shape, size, and tilt under different fluid velocity conditions can be used to comment on the behaviour of many particles that are able to interact with each other.

## Chapter 7

# Many particle liquid crystal flow

### 7.1 Simulation set up

In this chapter we investigate a large scale system with many colloidal particles in a microfluidic channel with a nematic liquid crystal subjected to flow. As in our previous results we use the lattice Boltzmann scheme from Chapter 3. This is done using the *Ludwig* code that applies the lattice Boltzmann method to the hydrodynamics and models the liquid crystal using the  $Q$ -tensor approach with a finite difference scheme. We now include many particles of the same size placed in the system before any flow is applied. An additional step is needed to handle the inclusion of many particles. In most cases this is done through random allocation of particle positions until all particles are placed within the system with no overlap between the walls or each other. In geometry, the close packing of identical spheres can be described through the packing fraction (or packing density)  $pf$  that relates the volume occupied by the spheres with the volume of the system size. As this can take a very long time for tightly packed systems, at packing fractions above 0.35 the *Ludwig* code places the chosen number of colloids on a 3D lattice and then performs a number of Monte Carlo moves, consisting of independent displacements, looping over all colloids. The lattice is of a body centered cubic type (one point in the center, and eight points on the corners). The investigated system is a three dimensional rectangular channel of size  $L_x \times L_y \times L_z = 66 \times 128 \times 256$  lattice

sites. Solid walls exist at the top and bottom in the  $x$ - plane with no slip boundary conditions and the walls in the the  $y$ - and  $z$ - directions are periodic. The anchoring on the walls and the particles is homeotropic. The boundaries in the  $z$ -direction act as the inlet and outlet of the channel. A pressure gradient  $\Psi = \Delta p/L_z$  is applied in the  $z$ - direction as a body force density acting on all fluid sites. A sketch of the geometry is shown in Fig. 7.1. All particles are discretised to be of the same size, with

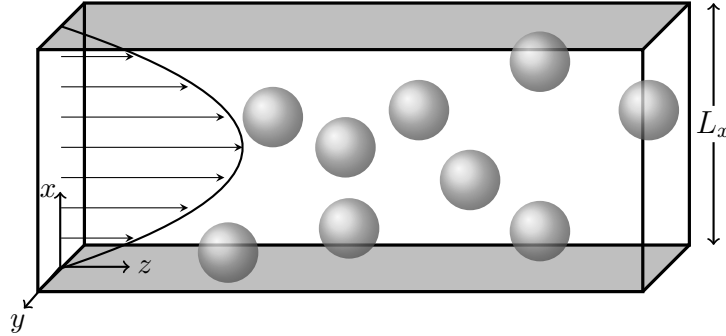


Figure 7.1: Sketch of the computational geometry: We apply no-slip boundary conditions and homeotropic anchoring conditions at the walls in  $x$ -direction and periodic boundary conditions at the  $y$ - and  $z$ -boundaries. The direction of flow is to the right, as shown by the parabolic flow profile at the inlet. Not to scale.

a radius of  $R = 5$  lattice sites and are free to move. The volume packing fraction  $pf$  determines the percentage of the system volume taken up by the initialised colloidal particles. The surface free energy has weak homeotropic anchoring both on the walls and particle surfaces. The initial set up is left to relax for 100,000 timesteps without flow, after which a pressure gradient is applied. For high values of the pressure gradient the simulations are ran for approximately 2.5 million timesteps to reach a steady state, while for the low values they are extended to around 8-9 million timesteps. We explore the effect of low, medium, and high fluid velocity on different packing fractions. The results are also further compared with the behaviour of the same packing density and applied pressure gradient combination in an isotropic fluid instead of a nematic. The simulation parameters are given in Tab. 7.1. We apply three different values of pressure gradient to each simulation resulting in low, medium, and high fluid velocity.

Variable		
Packing fraction	$pf$	0.01, 0.03, 0.05, 0.07, 0.10, 0.20, 0.30, 0.40
Pressure gradient	$\Psi$	$10^{-5}, 10^{-6}, 10^{-7}$
Invariable		
Elastic constants	$\kappa$	0.01
Dynamic viscosity	$\eta$	0.8333333
Bulk viscosity	$\zeta$	0.8333333
Mobility parameter	$\Gamma$	0.3
Bulk energy scale	$A_0$	0.084
Inverse temperature	$\gamma$	3.085
Wall anchoring strength	$w_{\text{wall}}$	0.006
Particle anchoring strength	$w_{\text{part}}$	0.006
Flow alignment parameter	$\xi$	0.7
Density	$\rho$	1.0
Particle radius	$R$	5

Table 7.1: Overview of simulation parameters

## 7.2 Particle Migration

We can now investigate the particle behaviour for different flow velocities at increasing packing fractions. The flow profile is parabolic, and as such we expect particles near the center of the channel to move faster than one that are near the walls. The observed particle migration shows distinction between low and high colloidal densities. At the highest packing fractions of  $pf = 0.3$  and  $pf = 0.4$  the system is very tightly packed with limited migration ability, especially for the  $pf = 0.4$  case. To explore the migration effects in depth we create and use 3D histograms. Each histogram shows the number of colloids in equal numerical ranges across the channel width with an additional axis of time. This gives a visual representation of the particle position distribution and its change over time. The numerical range is called a bin, and here the chosen bin size is 6 LBU. It is just above the particle radius of  $R = 5$  LBU and divides the channel width into 11 equal sections with the central bin including the center-line of the channel in the middle of it.

## 7.2.1 Low colloidal density

Initially we shall explore the particle migration at low packing fractions, that is for  $pf = 0.01, 0.03, 0.05, 0.07$  in a nematic. For comparison, we include the results for the same number of particles in an isotropic material. For a packing fraction of 0.01, the number of initialised particles in the system is 41. The resulting histograms are shown in Fig. 7.2.

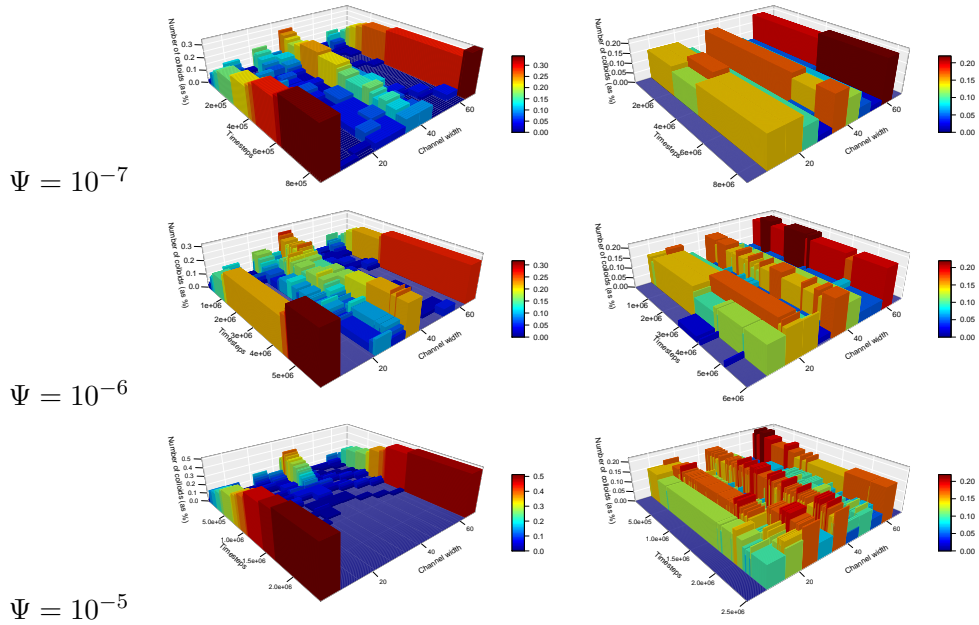


Figure 7.2: Evolution of particle position in the channel over time. Left column shows the particles in a nematic, while the right column shows particles in an isotropic fluid. The first row has the lowest fluid velocity, the second has medium with the highest shown in the last row. The packing fraction is  $pf = 0.01$ .

At the lowest applied pressure gradient with a random distribution of a small number of particles in a nematic, as shown in the top left graph of Fig. 7.2, we can see that the particles tend to migrate towards the top and bottom walls in the  $x$ - direction if they start away from the center of the channel. For particles that start at the center, they remain in a central position, not near the walls over time. This behaviour, meaning migration to the walls or staying in a stable position at the center, was also observed for a single particle at low fluid flows in Chapter 5 [1]. In an isotropic fluid with the



same pressure gradient and packing fraction, we can see that the particles remain in the same positions over time. This is shown in top right graph in Fig. 7.2 with slight deviations being the result of the particles moving slightly near the boundary of the bins. The fluid flow is low, and in an isotropic fluid there are no liquid crystal effects that would affect the particles.

For a medium applied pressure gradient and a packing fraction of 0.01 in a nematic liquid crystal, shown in the second row of the first column of Fig. 7.2 we observe the same migration pattern as for the lowest pressure gradient. Meaning that over time the particles that began near the walls migrate towards them, while the particles that began near the center of the channel stay in the center position. With the slightly higher fluid velocity the particles in the center are now also tending to stay at that central position more than for the lower fluid velocity case. Comparing with an isotropic fluid case of the same pressure gradient and colloid concentration shown in the second row of the second column of Fig. 7.2 the contrast between the behaviour can be immediately seen. Without liquid crystal, none of the particles end up near walls and instead tend to remain near their starting positions in the  $x$ - direction.

The biggest difference in particle migration between a nematic and isotropic fluid occurs for the highest fluid velocity, as shown in the last row of Fig. 7.2. Under high flow particles in a nematic completely move towards the walls with no particles anywhere in the middle of the channel. That does not happen in an isotropic fluid. Instead, similarly to lower fluid velocities the particles remain in the middle of the channel at various position and not near the walls. There is some variation in final particle position, however most particles remain close to their starting position.

The migration behaviour at the remaining low packing fractions of  $pf = 0.03, 0.05, 0.07$  follows the same trends, and as such we can choose a representative case that applies to them all. To that effect, we show the change in time of the distribution of the particle position of  $pf = 0.07$  in Fig. 7.3. Additionally, the number of particles in the system for  $pf = 0.03, 0.05, 0.07$  is 123, 206, and 289 respectively. The main difference between the case for  $pf = 0.01$  shown in Fig. 7.2 and the other low colloidal densities is that at low flow velocities for  $pf = 0.01$  there is an attraction to the central

position in the channel, while for the other low packing fractions that is no longer present in the position distribution. There are some particles that are in the middle of the channel, but that is a result of particle entanglement/clustering facilitated through the disclination lines.

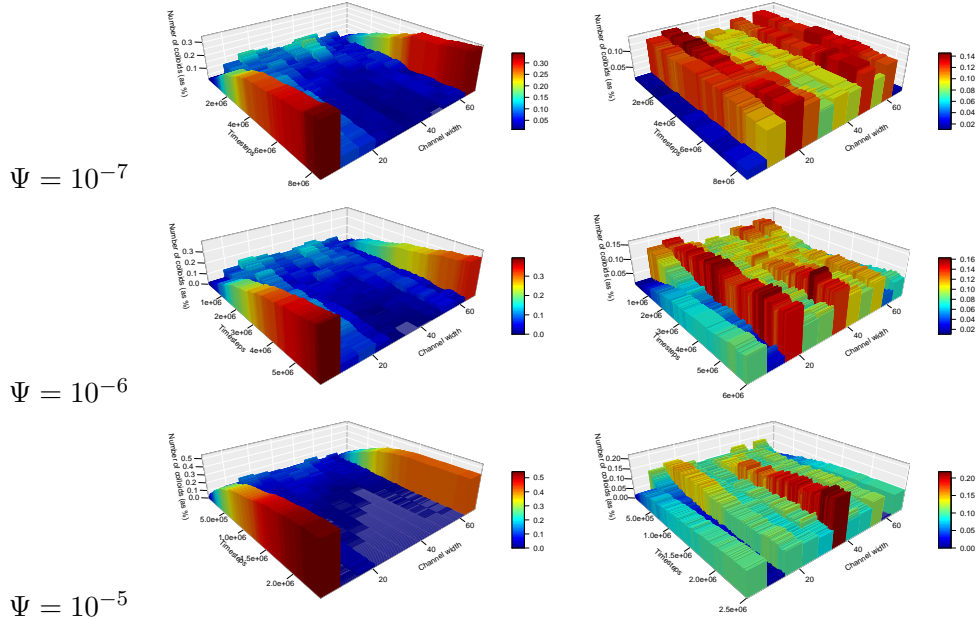


Figure 7.3: Evolution of particle position between the top and bottom walls of the channel over time. Left column shows the particles in a nematic, while the right column shows particles in an isotropic fluid. The first row has the lowest fluid velocity, the second is of medium fluid velocity with the highest shown in the last row. The packing fraction is  $pf = 0.07$ .

Fig. 7.3 shows the particle migration for a packing density of  $pf = 0.07$  at three different flow velocities for a nematic and an isotropic fluid. At the low and medium flow velocity the particle migration is very similar in that most particles end up very close to the top and bottom walls, with some particles in between. This is shown in the first and second row of the left column. The few colloids that are in the middle are either close to the walls, or they form clusters with other particles that are at the walls. In comparison, in an isotropic case very few particles are close to the walls with the majority located inside the channel at the lowest fluid velocity. In fact, the position distribution is bimodal, with particles preferring a position at 0.25 channel

length from either walls. This is consistent with the expected Segré -Silberberg effect we discussed in previous a chapter. For an isotropic fluid with a medium flow velocity, the particles do tend to go to the Segré -Silberberg distance, but a significant number also is located at the center of the channel and at the top and bottom walls. This is a result of increased velocity.

Finally, there are also differences at the highest flow velocity imposed through the pressure gradient of  $\Psi = 10^{-5}$  show in the bottom row of Fig. 7.3. In a liquid crystal, the flow is so large, that all particles end up either near the top or the bottom wall with no colloids in the middle. That is not the case for the comparable scenario in an isotropic fluid, where most particles are exactly in the center of the channel. In this case some particles that start close to the walls do end up near them over time. Additionally, many are as close to the middle of the channel as it is possible showing a symmetric unimodal distribution.

The distribution of particle positions and the colloid migration over time is one of many effects that occurs within this system, especially for liquid crystal. Before looking into those, we shall focus on what happens at higher colloidal densities. With increasing particle numbers, clustering effects have a large influence.

## 7.2.2 High colloidal density

With increasing numbers of particles introduced to the system, the interactions between them affect the evolution of the position migration. For our purposes, we consider the packing fractions of  $pf = 0.1, 0.2, 0.3, 0.4$  to be of high colloidal density. While the case of  $pf = 0.1$  could be considered to be one of medium density, due to the clustering and the propensity for the particles to form a connected network it is more appropriate to consider it together with the high colloidal density cases. At a packing fraction higher than approximately  $pf = 0.12$  it is not possible for all particles to occupy spaces fully on the top and bottom walls due to geometrical constraints. At highly packed cases of  $pf = 0.3$  and  $pf = 0.4$ , and especially for  $pf = 0.4$  the colloids are packed so closely together that little migration can occur. We will focus our analysis on the migration behaviour in the  $pf = 0.1$  and  $pf = 0.2$  cases.

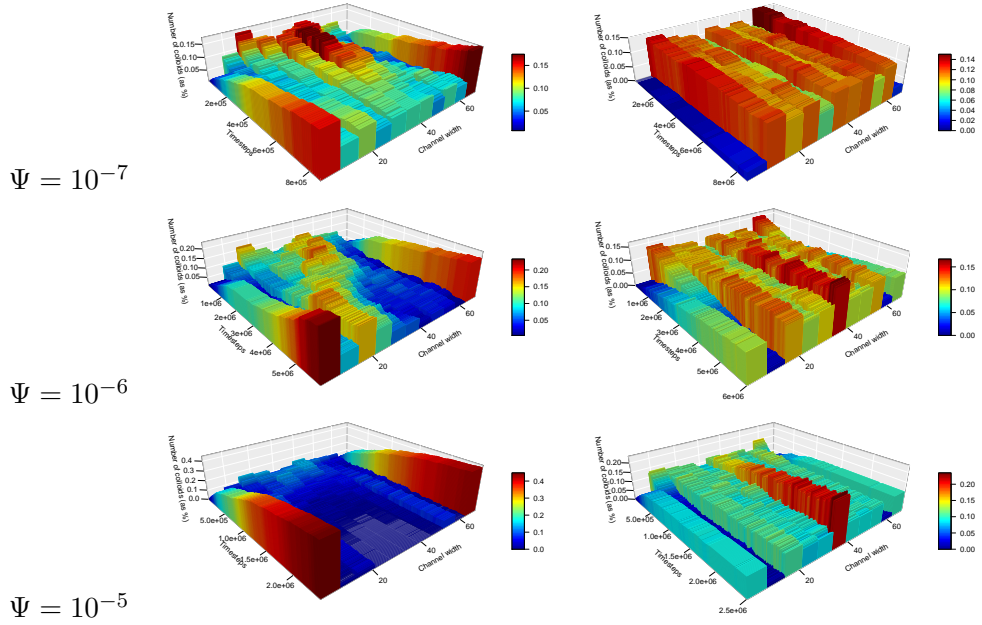


Figure 7.4: Evolution of particle position in the channel over time. Left column shows the particles in a nematic, while the right column shows particles in an isotropic fluid. The first row has the lowest, the second has medium, and the last row has the highest flow velocity. The packing fraction is  $pf = 0.1$ .

Fig. 7.4 shows the histogram of time evolution of the particle distribution for a packing density of  $pf = 0.1$ . The number of colloids inside the system is 413. At the lowest applied pressure gradient in a nematic liquid crystal the particles tend to aggregate at the top and bottom walls, with some present throughout the channel width. The attraction to the wall is as expected, similarly to what happens at lower packing fractions. At the low fluid velocity the particles also become entangled through the defect structure around them leading to clusters of colloids that join together. In this case, as there is a larger number of particles, they are able to create a network that spans the width of the channel. The elastic forces of the defects are larger than the viscous forces, with the fluid velocity not being large enough to prevent the particles from creating percolating networks that form a bridge between the top and bottom walls. At the same applied pressure gradient in an isotropic fluid the velocity is low and the particle migration is different than in the nematic. Very few particles are close to the walls, and not many end up at those positions. Most particles are near their

original starting positions with a random distribution over all bins that are not directly next to the top and bottom walls.

Medium flow velocity for a packing fraction of  $pf = 0.1$  in a nematic and isotropic phase is shown in the second row of Fig. 7.4. For a nematic, the particles as usual migrate towards the top and bottom walls of the channel over time. Another interesting effect that can be seen is that colloids that started close together in the middle of the channel form a cluster that over time moves from the top part of the channel towards the bottom. This is a result of particle interaction and entanglement combined with flow effects. Particles that are close together end up pulling each other into an energetically favourable position that minimises the defect loops around them, while the fluid velocity is still not high enough to completely force the particles to move to their preferred positions near the walls. In an isotropic fluid the histogram shows a fully symmetric unimodal pattern for colloid position distribution. The most favoured position of the particles is at the center of the channel. In contrast to the lower fluid velocity in an isotropic fluid, the increase in fluid flow velocity now makes a portion of the colloids to be pushed towards the walls. There is no particle entanglement as there is no director or disclination lines, but the particles do aggregate in the middle of the channel.

At the highest applied pressure gradient of  $\Psi = 10^{-5}$  the migration behaviour follows the same patterns that were initially observed for lower colloidal densities in the comparable nematic and isotropic fluid cases. For the nematic case, nearly all particles end at the walls, with a small proportion in the middle of the channel. In the isotropic case, once again we can observe a very symmetric unimodal pattern with the center of the channel being the most preferred position for the colloids. With this higher fluid velocity more particles than before tend to be directed to that central position, while the ones that are not in the middle represent a smaller proportion of all the colloids and are located either near the wall or at evenly distributed near in the middle around the most central location.

The final evolution of particle distribution across the channel width we will discuss is shown in Fig. 7.5. Here, the packing density is  $pf = 0.2$ , and the number of particles introduced to the channel is 826. It is no longer physically possible for all particles to

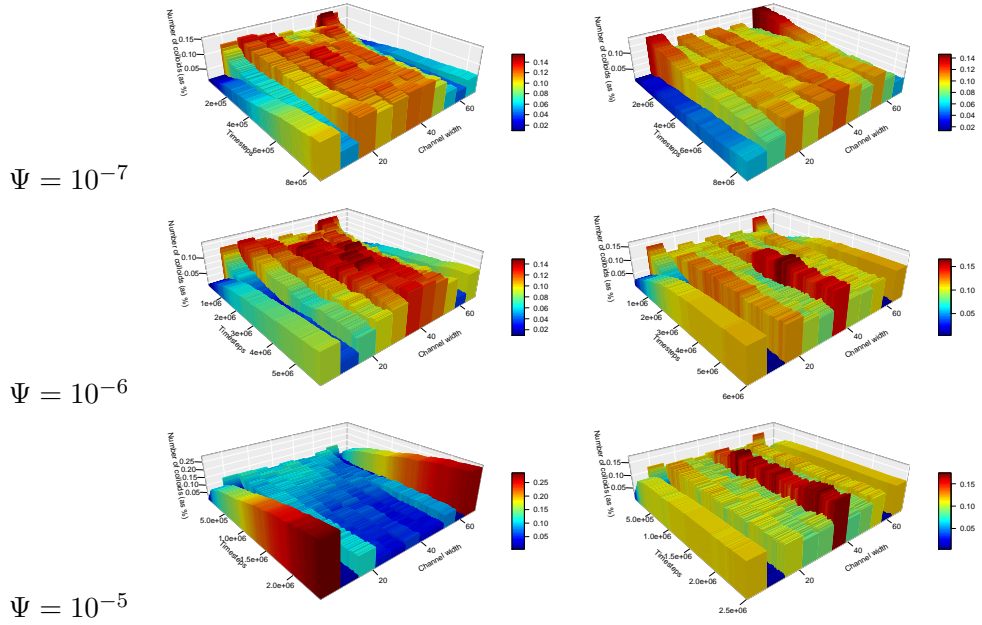


Figure 7.5: Particle position in the channel over time. Left column shows the particles in a nematic phase, while the right column shows particles in an isotropic one. The first row has the lowest pressure gradient, the second has medium, and the last row has the highest. The packing fraction is  $pf = 0.2$ .

only occupy positions at the walls due to the high colloid density. Particle movement is heavily impacted by interactions between the particles, however there are still emerging trends that are present. In a liquid crystal at low pressure gradient the particles have a roughly symmetrical distribution over the width of the channel, with the center of the channel and the walls being the preferred positions. The particles are fully entangled forming an interconnected cluster through the disclination lines. At the same applied pressure gradient and fluid velocity in an isotropic fluid the colloids are distributed very symmetrically across the channel, and mostly away from the walls. The most likely position for an individual particle after the system is in a steady state is at the very center of the channel, with the second most likely positions a diameter away from the center line in either direction.

At a medium pressure gradient and a packing fraction of 0.2, the colloidal migration in a nematic liquid crystal and in an isotropic fluid is very similar, which has not occurred for other packing fractions. In both cases, the resulting histogram showing the

distribution of the particles over the width of the channel is unimodal and symmetric, with the most likely particle positions being either at the center of the channel or at the walls. The colloids in the isotropic fluid show a higher degree of uniformity and symmetry in their position distribution.

While at medium pressure the particle behaviour is similar in both a liquid crystal and an isotropic fluid, the differences are very stark at a higher applied pressure gradient. In a nematic, the high fluid velocity leads to most particles ending up at the top and bottom walls. As there are more particles than the available space at the walls, a proportion of the particles migrates to positions creating a second layer over the particles at the wall. The remaining particles are in the middle of the channel. For an isotropic fluid however, the majority of colloids migrate towards the middle of the channel as shown in the histogram in the bottom right column of Fig. 7.5. Those stark differences in migration of the particles allow to easily differentiate between a liquid crystal and an isotropic state, which could have potential future applications.

For higher packing fractions of 0.3 and 0.4 the migration behaviour is limited due to the high number of particles occupying the space. The tightly packed particles bump into each other and are restricted in their movements resulting in reduced colloid velocities and a certain proportion of particles with negative velocity, that is, moving in the direction opposite to the direction of the flow.

### 7.3 Colloid velocity and defects

Colloidal velocity is another facet of many particle liquid crystal flow. There are differences related to the changes in the colloidal density together with varying behaviour present for high and low applied pressure gradients. We will discuss the colloidal velocity, observed changes in the Saturn ring defects and the phenomenon of negative colloid velocity. To achieve this we will look at two examples with low colloid density (with packing fractions of 0.03 and 0.07) and two examples with high colloid density (with packing fractions of 0.1 and 0.3 respectively).

In the first instance, Fig. 7.6 shows a still from the simulation at a steady state for

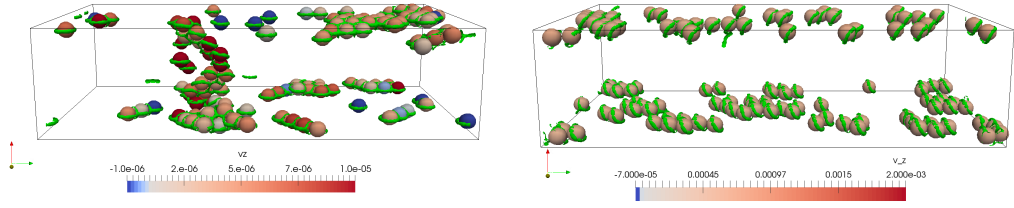


Figure 7.6: Colloid velocity for a packing fraction of 0.03. In both cases the colloidal particles are color coded by their velocity and shown together with the defect structure (green) around them. The left image shows the system subjected to a low pressure gradient of  $\Psi = 10^{-7}$ , while on the right a high pressure gradient of  $\Psi = 10^{-5}$  is used.

a colloidal density of 0.03. The left image shows the a low applied pressure gradient of  $\Psi = 10^{-7}$  while the right shows a high pressure gradient of  $\Psi = 10^{-5}$ . The green lines show the defect lines, with the colour of the colloids showing positive velocity for shades of red and negative velocity for the shades of blue. At the lower pressure gradient, and consequently lower fluid and colloid velocities, the Saturn ring defects around the colloids are oriented parallel to the top and bottom walls in the  $x$ - direction, and in line with the direction of the flow. They are flow aligned, as expected from the previously studied single particle systems. The Ericksen number is lower here than for the higher pressure gradient, meaning that the viscous effects have lower impact here. This leads to the observed clustering that is mediated through the joint defect structure around the colloids, a result of the tendency of the system to minimise its internal elastic energy. Another effect that can be noted here, is the negative colloid velocity noted for some of the colloids that migrated to the the top and bottom walls. In essence, some of the particles get ‘stuck’ on the wall for short periods of time, while others are pulled back due to the entangled defect structure within the clusters. Additionally, even at this low colloid velocity, some percolation occurs - with a joined structure of colloids joining from top to bottom. Moving on to what happens at the same colloidal density, but for a larger pressure gradient, we observe significant differences, as shown in the right image of Fig. 7.6. The Saturn ring defects are now oriented at an angle to the direction of flow and the top and bottom walls. This is a result of the flow aligning at this high velocity. Additionally, as the viscous effects dominate over the elastic effects



there is no colloid clusters created by the entanglement of the defects, rather individual colloids have Saturn ring defects present around them at the appropriate flow aligned angle. There are no more cases of particles having negative velocities in any significant way. As discussed in the previous section, all the colloids migrate to either the top or the bottom wall of the channel.

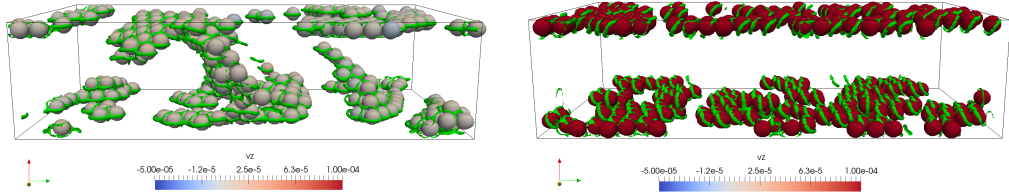


Figure 7.7: Colloid velocity for a packing fraction of 0.07. The colloidal particles are marked with their velocity and shown together with the defect structure (green). The left image shows the colloids subjected to a low pressure gradient of  $\Psi = 10^{-7}$ , while the image on the right shows a high pressure gradient of  $\Psi = 10^{-5}$ .

Fig. 7.7, similarly to Fig. 7.6, shows a snapshot of a system of colloidal particles in a liquid crystal in a steady state with a packing fraction of 0.07 for a constant applied pressure gradient of  $\Psi = 10^{-7}$  on the left and  $\Psi = 10^{-5}$  on the right. As before, the green lines correspond to the defects and the colour scheme of the particles is red for positive velocity and blue for negative velocity. For the left hand side, which represent the lower applied pressure gradient, we see more clusters of particles present than for a lower packing fractions. The Saturn ring defects are oriented parallel to the direction of flow and the  $x$ - walls around particles and form networks around the colloids creating clusters. This is because the elastic and viscous forces are competing here, with the elastic forces favouring energetically to join together to minimise their total elastic energy and creating clusters that over time resemble percolating networks. There is a small proportion of the particles with negative velocity, marked with light blue. In contrast within the same figure the higher velocity shows markedly different behaviour. With the higher applied pressure gradient, the viscous effects dominate, resulting in the reorientation of the Saturn ring defect to a flow aligning angle. There is no entanglement of the defects around multiple particles, and as expected all particles are either at the

top or bottom boundary walls. At this high velocity there is very limited occurrences of negative colloid velocity, none of which can be seen in this figure.

Focusing on higher colloidal densities, we will now investigate the behaviour and defect structures for the cases with 0.1 and 0.3 packing fractions, as show in Fig. 7.8 and Fig. 7.9. Starting with a packing fraction of 0.1 shown in Fig. 7.8, we once again

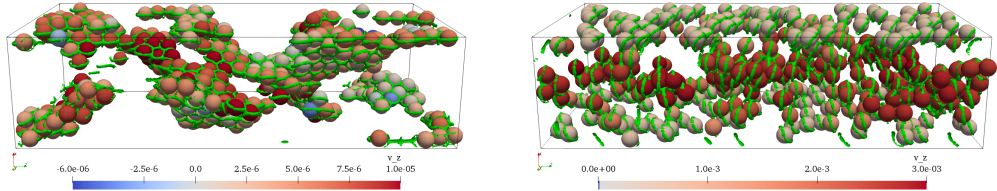


Figure 7.8: Images showing the colloid velocity for a packing fraction of 0.1. The colour of the colloids shows their velocity in the direction of flow, with the green regions representing the defect structure. On the left, we show the lower pressure gradient of  $\Psi = 10^{-7}$ , while on the right the applied pressure gradient is  $\Psi = 10^{-5}$ .

observe the colloidal behaviour at two different applied pressure gradients,  $\Psi = 10^{-7}$  and  $\Psi = 10^{-5}$  on the left and right side respectively. For the lower velocity example, the defects around the individual particles are Saturn rings around individual colloids that have entangled and created clusters. Those clusters are mostly interconnected creating a percolating network such that the orientation of the Saturn ring like defects is now more significantly influenced by the cluster network than orienting exactly parallel to the flow. There are colloids with negative velocity, resulting from the tight clusters of particles where individual colloids are unable to move in a different direction. The degree of interconnectedness is higher than in the low density cases as colloids are more likely to get within a close distance and join together with their defects than at lower density cases. The biggest difference in migration behaviour at high flow velocities between the low and high packing fractions, as seen on the right of Fig. 7.7 and Fig. 7.8 is that the particles no longer only migrate towards the top and bottom walls. The right side of Fig. 7.8 shows the colloid velocities and the director structure for this higher packing fraction and higher velocity scenario. As it can be seen, the defects around the particles are Saturn rings around individual colloidal particles with no overarching connected networks. These Saturn ring defects are reoriented completely. At the walls

they align to the angle of flow, with some reorientation adjusted through the closeness to the wall. In the middle of the channel, the defects are now perpendicular to the direction of flow - a result of the dominating viscous effects of the flow over the elastic effects. The clustering effects are minimal, and very few particles have negative velocity.

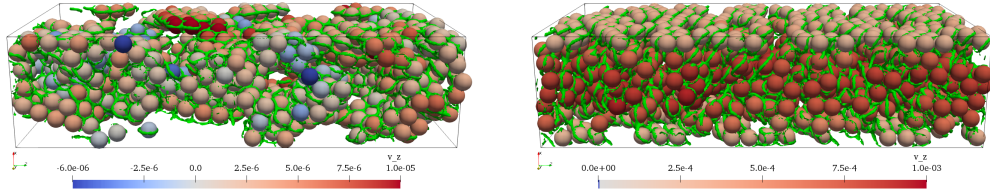


Figure 7.9: Colloid velocity for a packing fraction of 0.3. The colloidal particles are color coded with their velocity and shown together with the defect structure (green). The left image shows the colloids subjected to a low pressure gradient of  $\Psi = 10^{-7}$ , while the image on the right shows a high pressure gradient of  $\Psi = 10^{-5}$ .

The final example we will examine is for a high packing fraction of 0.3, as shown in Fig. 7.9. The left hand side of the figure shows the lower applied pressure gradient  $\Psi = 10^{-7}$ , with the right hand side showing the much larger pressure gradient of  $\Psi = 10^{-5}$ . At this colloidal density the system is tightly packed with many particles with not a lot of space for all of them to move around. As such the instances of negative colloid velocity are much higher. For the lower fluid velocity, shown on the left of the figure, the particles form a large cluster of defect bound particles. The Saturn ring like defects on the top and bottom walls remain oriented parallel to the flow, while the defect network in the middle of the channel does not have a clear preferred orientation in the flow direction but rather aims to minimise the total elastic energy of the system in the most favourable way. For the higher flow velocity on the left, some differences can be immediately seen. The colloids are still pushed towards the top and bottom walls due to the high applied pressure gradient, with the particles that are not able to fill the space on the wall being about evenly distributed across the center of the channel. Even though the channel is tightly packed, the flow velocity is very high and not many particles end up having negative velocity. As before, the Saturn ring like defects on particles that are on the top and bottom walls are reoriented such that they are no longer parallel to the direction of flow. Additionally, a major difference is observed

at this high packing fractions as the defect structure consists of a connected network around the cluster of particles, rather than individual defects. This has not occurred at any of the lower colloidal densities, and is only present in the middle of the channel - the colloids at the top and bottom walls still tend to be individual Saturn ring defects flow aligned to the appropriate angle.

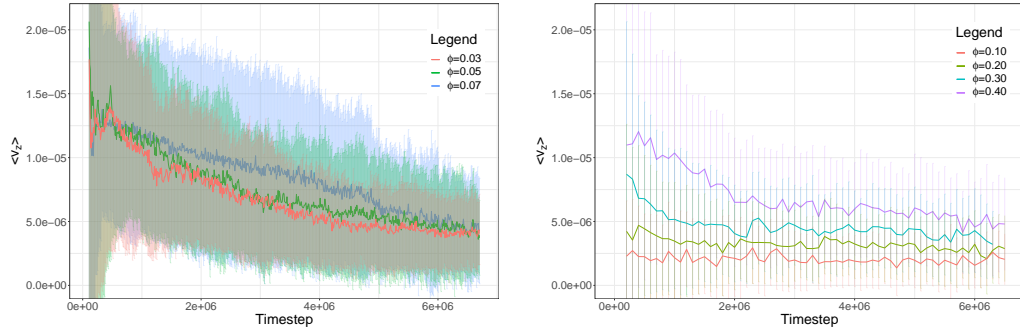


Figure 7.10: Mean colloid velocity in the direction of flow for various packing fractions with an applied pressure gradient of  $\Psi = 10^{-6}$ . Error bars shown are one standard deviation of the mean. Left graph shows results for the low colloidal densities and right hand side shows the result for high colloidal densities.

The final figure to be presented includes the graphs of the mean colloid velocity for different colloidal densities shown in Fig. 7.10. The left graph shows the results for the low packing fractions, while the graph on the right shows the results for high packing fractions. The main trend that can be observed is that the mean colloid velocity is reduced over time for all cases. This is a result of some proportion of particles migrating towards the walls. As the flow profile is parabolic, more particles at the top and bottom walls will mean lower velocity for those particles in comparison to the ones that are in the center of the channel. This also explains the trend of higher average colloidal velocity for higher packing fractions, as with more particles present more of them end up at central locations that will experience higher flow velocity. This is especially true for the higher colloid densities, as there is a geometrical limit of positions close to the walls, with each subsequent additional particle being closer to the middle of the channel.

## 7.4 Summary

In summary, the behavior of colloidal particles in a liquid crystal under different flow velocities is complex and influenced by the inherent anisotropy of liquid crystals as compared to isotropic fluids. This can lead to unique and interesting phenomena such as wall or center migration, percolating networks of colloids bound by defects and changes in Saturn ring tilt angles. The observed migration behaviour differed for low and high colloidal densities. For low colloidal density, the particles showed a tendency to migrate towards the walls or remain stable at the center for low and medium flow rates, while isotropic fluid particles exhibited minimal migration at low and medium velocities and preference towards the center at high velocities. However, for higher colloidal density, differences in migration behavior between liquid crystal and isotropic particles were more pronounced. The particles in a nematic tended to migrate towards the walls, while isotropic particles migrated towards the center, with this trend becoming more pronounced at higher flow velocities. Additionally, at low and medium flow velocities, percolating networks of colloidal particles were observed in the liquid crystal, leading to some instances of negative velocity due to clustering. However, no clusters were formed at the highest velocity as the viscous forces are much larger than the elastic forces. We also found that the Saturn ring defect near walls tilted at an increasing angle as the fluid velocity increased to the appropriate Leslie angle. Furthermore, higher packing fractions were associated with higher average colloidal velocity, indicating a relationship between particle density and velocity. Overall, the novel results of the study shed light on the migration behavior of colloidal particles in different flow conditions and the unique characteristics related to the nematic environment. The key observed novel results that include the migration patterns and clustering effects summarised earlier align with our stated project aims of having a better understanding of defect behaviour in flow as well as defining the factors strongly influencing particle migration. Our previously obtained results in Chapters 5 and 6 (published in [1] and [2] respectively) contributed greatly to our analysis of the large scale systems discussed in this chapter.

We hope that through our observation of the large scale nematic colloids more

experimental work will be done in this area. Especially when it comes to dynamic and flow driven systems, as a lot of the current work is focused equilibrium conditions [169]. In general, there is scope for applications in self-assembly driven by the understanding of the novel types of behavior and emergent effects.

## Chapter 8

# Conclusions and Future work

### 8.1 Conclusions

In conclusion, in chapter 4 we investigate the appropriate simulation parameters to obtain a well defined colloidal particle with appropriate anchoring conditions on the walls and particle surface fixed in place in a microchannel with a flowing nematic liquid crystal. This allows us to observe the elongation of the ring defects around the static particle and the bend to splay transition dependent on the simulation parameters including fluid velocity and viscosity.

The summary of chapter 5 is that we observe multiple equilibrium particle positions and a new pressure-controllable particle attractor state for a colloidal particle with nematic liquid crystalline host phase. At low pressure gradients particles migrate either to the channel centre or the walls but at higher pressure gradients a third attractor state emerges spontaneously, whose position in the channel depends sensitively on the pressure gradient. These results are in contrast to the classical Segré-Silberberg effect in isotropic fluids, where the equilibrium position is reached more slowly. The discovery of these controllable attractor positions creates interesting routes for tailored particle separation. While our results were obtained in pressure-driven flow, we expect them to hold as well in flux-driven flow as long as there is no significant drag between particle and fluid.

In chapter 6 we explore how defects influence the advection behaviour of colloidal particles in moderate and large confinement. The interaction between nematic order and flow together with the fluid-solid interaction results in a non-monotonic dependence of the retardation ratio, that is the ratio of particle advection velocity to the maximum velocity at the centre of the duct, on the Ericksen number. When the Ericksen number is low, the retardation ratio is close to values observed in a Newtonian host phase in all confinement ratios and particle anchoring conditions. This is also the case for vanishing or low anchoring strength and at high Ericksen numbers, where the nematic liquid crystal behaves increasingly like a simple Newtonian fluid. This is because the relative importance of elastic effects decreases. At intermediate Ericksen numbers there is a pronounced minimum in the retardation ratio. We attribute this to a combination of two effects. The first is the bend-to-splay transition, to which particles in all anchoring conditions are subject. The second effect is the defect ring undergoing a reorientation from horizontal alignment with the ring plane parallel to the walls to a vertical orientation, which has the ring plane perpendicular to the flow direction and the walls. This increases the effective particle radius and therefore the confinement. The second effect is only present when the defect ring is properly formed, i.e. for stronger particle anchoring strengths, and when the confinement is lower. This is because the increased retardation that the particle experiences is a consequence of the interaction of the defect with the gradients of the flow velocity and liquid crystalline order. We do not observe migration to the walls for all but the highest Ericksen numbers and confinement ratios that we tested in contrast to the much lower confinement in chapter 5. Hence the increased confinement leads to the stabilisation of trajectories at the centre of the duct.

Finally, chapter 7 presents the results of many particle liquid crystal flow. The observed behaviour includes advanced particle migration behaviour that is highly dependent on both the packing fraction and the velocity of the fluid, the reorientation of the Saturn ring defect, formation of percolating clusters of colloids bound by their entangled defect, and cases of negative colloidal velocity.

We can now reflect on how the work that we did aligns with the project aims. As



a reminder, the stated goals of our work are to define the factors strongly influencing particle migration and to better understand liquid crystal defect behaviour in flow. When it comes to the particle migration, our results in chapters 5 and 7 provide the most insight. In the former we find that the particle migration is influenced by its starting position in the system, the bend to splay transition, and increasing Ericksen numbers. Those are factors affecting an individual particle, and in the case of many particle systems presented in Chapter 7 we additionally note that the packing fraction and clustering effects affect particle migration. The second aim of our research, focusing on defect behaviour in flow, has been met in all of the results chapters. Specifically, we observed the elongation and changes in defect shapes in Chapter 4, the tilting of the Saturn ring defect and reorientation during the bend to splay transition in Chapters 5 and 7, changes in shape due to the combination of high confinement and large Ericksen numbers in 6, and defect structures around clusters of particles in 7. In summary, the original contribution of the work done by the thesis author is in the running of fully three-dimensional simulations of nematic colloids in microfluidic flow and analysing the key results which relate and add to the current understanding of nematic colloids. The implications of this research is in potential for further experimental research that can be done to further explore the novel mechanisms of particle control through the found factors strongly influencing their migration.

## 8.2 Future Work

There is scope for further investigation based on the work presented in this thesis. The simulations of a single small fixed particle can be explored for larger sizes that would lead to differences in the defect type. This would allow to simulate the behaviour of hyperbolic hedgehog defects and compare it to experimental results. Additionally, the type of ordering at the particle can be changed to planar, leading to obtaining bojuum defects and an exploration of the changes in the system behaviour. It is not clear how these topological differences would affect the advection and migration behaviour. The same changes can be introduced to the motile particle explored in Chapter 5, the

confined colloid in Chapter 6 and the many particle systems in Chapter 7.

As another example, there is scope to explore how planar or hybrid anchoring conditions affects the defect morphology, migration, and advection behaviour of the particles in the differing systems presented in the different results chapters of this thesis. Planar wall anchoring is fully compatible with the flow alignment that takes place at higher Ericksen numbers. This means that there is no bend-to-splay transition, rather a more gradual transition to a state where the director field is flow-aligned at the Leslie angle.

There is also a lot of possibilities for investigating particle effects for large scale systems of many colloids placed in a liquid crystal and subjected to flow. The thesis has set up the groundwork to explain single particle behaviour in flow which can then be used to analyse more effects that occur as a result of particle interactions, clustering effects, and entanglement. This is beyond the scope of this project, nonetheless there is unique opportunities for discovering novel behaviour.

# Appendix A

## Chapman-Enskog analysis

### A.1 Connecting the lattice-Boltzmann and Navier Stokes equations

Assuming that the distribution function  $f$  is such that  $f \simeq f_{eq}$ , the general momentum and the internal energy conservation equations lead to the Euler and energy equations

$$\frac{\partial(\rho u_\alpha)}{\partial t} + \frac{\partial(\rho u_\alpha u_\beta)}{\partial x_\beta} = -\frac{\partial p}{\partial x_\alpha} + F_\alpha, \quad \frac{\partial(\rho e)}{\partial t} + \frac{\partial(\rho u_\beta e)}{\partial x_\beta} = -p \frac{\partial u_\beta}{\partial x_\beta}. \quad (\text{A.1})$$

These equations do not contain the viscous stress tensor  $\boldsymbol{\sigma}'$  and the heat flux  $\mathbf{q}$  found in the Navier-Stokes-Fourier momentum and energy equations. Having found the Euler equations for  $f$  at equilibrium without the viscous dissipation and the heat diffusivity, implies that these phenomena occur out of equilibrium. Those contributions in that case will occur at some non-equilibrium deviation  $f_{neq} = f - f^{eq}$ . This also applies in a discretised velocity space, as we have established that the moments of  $f$  are equal to the corresponding moments of  $f_i$ .

Now is the time to use the Chapman-Enskog analysis, which finds the non-equilibrium contributions to  $f_i$  to connect the kinetic and continuum methods together. The underlying thought is to represent  $f$  as a perturbation expansion about  $f_i^{eq}$ , using the

Knudsen number  $\text{Kn}$  as the expansion parameter like so:

$$f_i = f_i^{eq} + \epsilon f_i^{(1)} + \epsilon^2 f_i^{(2)} + \dots \quad , \quad (\text{A.2})$$

where  $\epsilon^n$  is used as a smallness label to indicate the terms of order of  $\text{Kn}^n$ . It is common to write  $f_i^{eq}$  as  $f_i^{(0)}$ , resulting in a fully consistent notation. By using  $\epsilon$  it is easy to group the terms according to their Knudsen number order. This is important, as within the framework of the perturbed equation each order of  $\text{Kn}$  is treated itself as a semi-independent equation. The lowest order terms give the Euler momentum equation, with the higher order terms marked as correction terms, similarly to how the viscous stress tensor in the NSE can be seen as a correction term to the Euler equation. The perturbation is completed in such a way that the equations of different  $\text{Kn}$  orders still retain a link to each other with higher-order terms connecting to the lower-order equations. A sufficiently accurate description can be often obtained by using the lowest two orders. As follows, we can assume an ansatz consisting of  $f_i^{eq}$  and  $f_i^{(1)}$  only. The Chapman-Enskog analysis approach be used for any collision operators, and as we use the BGK operator we will use the derivation that includes it.

The BGK operator must conserve mass and momentum, we express that using

$$\sum_i f_i^{\text{neq}} = 0, \quad \sum_i \mathbf{c}_i f_i^{\text{neq}} = \mathbf{0}. \quad (\text{A.3})$$

Once again, we assume that those conditions hold true individually, such that

$$\sum_i f_i^{(n)} = 0, \quad \sum_i \mathbf{c}_i f_i^{(n)} = \mathbf{0} \quad \text{for all } n \geq 1. \quad (\text{A.4})$$

These assumptions are often called the solvability conditions in the literature.

We now use the Taylor expansion of the discrete-velocity Boltzmann equation to obtain

$$\Delta t (\partial_t + c_{i\alpha} \partial_\alpha) f_i + \frac{\Delta t^2}{2} (\partial_t + c_{i\alpha} \partial_\alpha)^2 f_i + \mathcal{O}(\Delta t^3) = -\frac{\Delta t}{\tau} f_i^{\text{neq}} \quad (\text{A.5})$$

which is an expression continuous in space and time while maintaining the discretisation

error of the original equation. In this analysis, the terms with third-order derivatives or higher are omitted, as they tend to be very small and their effect on the macroscopic behaviour is largely insignificant. It also follows our previously assumed ansatz of only using the two lowest orders in the Knudsen number to find the Navier-Stokes equations solutions.

This presumption operates under the condition that changes in  $f_i$  are slow and occur on the macroscale. For rapidly changing  $f_i$ , as a result of numerical errors or otherwise, the Champan-Enskog analysis is no longer appropriate and the resulting macroscopic equations are invalid for the purposes of connecting the lattice-Boltzmann and Navier Stokes equations.

As we focus on second-order terms only, we neglect the  $\mathcal{O}(\Delta t^3)$  terms, and then we get rid of the second-order derivative terms by subtracting  $(\Delta t/2)(\partial_t + c_{i\alpha}\partial_\alpha)$  in the Eq.(A.5). Hence we get the following

$$\Delta t(\partial_t + c_{i\alpha}\partial_\alpha)f_i = -\frac{\Delta t}{\tau}f_i^{\text{neq}} + \Delta t(\partial_t + c_{i\alpha}\partial_\alpha)\frac{\Delta t}{2\tau}f_i^{\text{neq}} \quad (\text{A.6})$$

where  $f_i^{\text{neq}}$  derivative on the right hand side are the only remnants of the discretisation error. Another assumption that is made here is that the time derivative is expanded into terms spanning several orders in Kn. Using that to relabel the spatial derivative without expanding it, the time and space derivatives will end up as

$$\Delta t\partial_t f_i = \Delta t\left(\epsilon\partial_t^{(1)}f_i + \epsilon^2\partial_t^{(2)}f_i + \dots\right), \quad \Delta t c_{i\alpha}\partial_\alpha f_i = \Delta\left(\epsilon c_{i\alpha}\partial_t^{(1)}\right)f_i. \quad (\text{A.7})$$

The different components of  $\partial_t$  at different orders in Kn are not considered to be time derivatives by themselves [112], rather they are terms at various orders in Kn that when summed together will equal the time derivative. The approach to the expansions of derivatives is commonly used in the general perturbation theory and is referred to as the multiple-scale expansion. It is used to prevent from creating terms that grow with no bounds at one order but are cancelled by similar terms at higher orders [170].

To tie in these expansions together, we use the  $f_i$  form from Eq. A.2 and the multi-

scale expansion from Eq. A.7 applied to Eq. A.6. Separating the equation by their Kn order, the two lowest orders in Kn are

$$\mathcal{O}(\epsilon) : \left( \partial_t^{(1)} + c_{i\alpha} \partial_\alpha^{(1)} \right) f_i^{\text{eq}} = -\frac{1}{\tau} f_i^{(1)}, \quad (\text{A.8a})$$

$$\mathcal{O}(\epsilon^2) : \partial_t^{(2)} f_i^{\text{eq}} + \left( \partial_t^{(1)} + c_{i\alpha} \partial_\alpha^{(1)} \right) \left( 1 - \frac{\Delta t}{2\tau} \right) f_i^{(1)} = -\frac{1}{\tau} f_i^{(2)}. \quad (\text{A.8b})$$

From here, we can find the moment equations in  $\mathcal{O}(\epsilon)$  by taking the zeroth to second moments of Eq. A.8a. To do that, we multiply by 1,  $c_{i\alpha}$  and  $c_{i\alpha}c_{i\beta}$  and then sum over  $i$  resulting in:

$$\partial_t^{(1)} \rho + \partial_\gamma^{(1)} (\rho u_\gamma) = 0, \quad (\text{A.9a})$$

$$\partial_t^{(1)} (\rho u_\alpha) + \partial_\beta^{(1)} \Pi_{\alpha\beta}^{\text{eq}} = 0, \quad (\text{A.9b})$$

$$\partial_t^{(1)} \Pi_{\alpha\beta}^{\text{eq}} + \partial_\gamma^{(1)} \Pi_{\alpha\beta\gamma}^{\text{eq}} = -\frac{1}{\tau} \Pi_{\alpha\beta}^{(1)}. \quad (\text{A.9c})$$

These equations contain the moments

$$\Pi_{\alpha\beta}^{\text{eq}} = \sum_i c_{i\alpha} c_{i\beta} f_i^{\text{eq}} = \rho u_\alpha u_\beta + \rho c_s^2 \delta_{\alpha\beta}, \quad (\text{A.10a})$$

$$\Pi_{\alpha\beta\gamma}^{\text{eq}} = \sum_i c_{i\alpha} c_{i\beta} c_{i\gamma} f_i^{\text{eq}} = \rho c_s^2 (u_\alpha \delta_{\beta\gamma} + u_\beta \delta_{\alpha\gamma} + u_\gamma \delta_{\alpha\beta}), \quad (\text{A.10b})$$

$$\Pi_{\alpha\beta}^{(1)} = \sum_i c_{i\alpha} c_{i\beta} f_i^{(1)}, \quad (\text{A.10c})$$

where the first two are explicit equilibrium moments in discretised velocity space, with the third one explained later. Note that the  $\Pi_{\alpha\beta\gamma}^{\text{eq}}$  lacks a term  $\rho u_\alpha u_\beta u_\gamma$  as we only include  $f_i^{\text{eq}}$  containing terms up to  $\mathcal{O}(u^2)$ . Taking the moment equations in Eq. A.8 and reverse the Eq. A.7 expansions while neglecting the higher-order Kn contributions such that  $\partial_t f_i \approx \epsilon \partial_t^{(1)} f_i$ , we get the first equation to be the continuity equation, and the second equation being the Euler equation, with the third one currently to be kept in mind to get back to.

Using the same method to take the zeroth and first moments of Eq. A.8b, we find

the moments equations in  $\mathcal{O}(\text{Kn}^2)$ :

$$\partial_t^{(2)}\rho = 0, \quad (\text{A.11a})$$

$$\partial_t^{(2)}(\rho u_\alpha) + \partial_\beta^{(1)}\left(1 - \frac{\Delta t}{2\tau}\right)\Pi_{\alpha\beta}^{(1)} = 0. \quad (\text{A.11b})$$

Both of these equations can be thought of as the  $\mathcal{O}(\epsilon^2)$  corrections to the earlier  $\mathcal{O}(\epsilon)$  equations. The continuation equation is exact at  $\mathcal{O}(\epsilon)$ , which is now confirmed with the  $\mathcal{O}(\epsilon^2)$  being equal to 0. The  $\mathcal{O}(\epsilon^2)$  correction to the Euler equation is non-zero, given by the currently unexplored moment  $\Pi_{\alpha\beta}^{(1)}$ .

Aggregating the  $\mathcal{O}(\epsilon)$  and  $\mathcal{O}(\epsilon^2)$  component equations from the equations detailed above in the equation sets Eq. A.9 and Eq. A.11 respectively to construct the mass and momentum equations, we obtain

$$\left(\epsilon\partial_t^{(1)} + \epsilon^2\partial_t^{(2)}\right)\rho + \epsilon\partial_\gamma^{(1)}(\rho u_\gamma) = 0, \quad (\text{A.12a})$$

$$\left(\epsilon\partial_t^{(1)} + \epsilon^2\partial_t^{(2)}\right)(\rho u_\alpha) + \epsilon\partial_\beta^{(1)}\Pi_{\alpha\beta}^{\text{eq}} = -\epsilon^2\partial_\beta^{(1)}\left(1 - \frac{\Delta t}{2\tau}\right)\Pi_{\alpha\beta}^{(1)}. \quad (\text{A.12b})$$

Using the reverse of the derivative expansion from Eq. A.7, the above equations emerge as the continuity equation and a momentum conservation equation with thus far unidentified viscous stress tensor

$$\sigma'_{\alpha\beta} = -\left(1 - \frac{\Delta t}{2\tau}\right)\Pi_{\alpha\beta}^{(1)}. \quad (\text{A.13})$$

It is important to note that we use the expanded time derivative to recombine the two different orders of  $\epsilon$ . Were it not done in this way Eq. A.11b would omit the  $\partial_1^{(2)}(\rho u_\alpha)$  term and as a result incorrectly concluding  $\partial_\beta^{(1)}\Pi_{\alpha\beta}^{(1)} = 0$ .

We now get back to the  $\Pi_{\alpha\beta}^{(1)}$  moment, looking for an explicit expression. We can call it a perturbation moment and it can be directly found from the derivatives of the equilibrium moments by using Eq. A.9c. To this end, a tedious amount of algebra is required, the details of which can be found in the Appendix A.2.2 of reference [109].

The final result using the equilibrium distribution function  $f_{i\text{eq}}$  expanded to  $\mathcal{O}(u^2)$

$$\Pi_{\alpha\beta}^{(1)} = -\rho c_s^2 \tau \left( \partial_\beta^{(1)} u_\alpha + \partial_\alpha^{(1)} u_\beta \right) + \tau \partial_\gamma^{(1)} (\rho u_\alpha u_\beta u_\gamma). \quad (\text{A.14})$$

This derivation does not assume that  $\partial_t \tau = 0$  or  $\partial_\alpha \tau = 0$  which means that the expression found holds for  $\tau$  being a function of space and time. The first term on the right hand side is the corresponding Navier-Stokes viscous stress tensor and the second is an error term emerging from the absence of an appropriate ( $u^3$ ) term in the equilibrium  $f_i^{\text{eq}}$ . In most cases, this error term is negligible. In fact, when looking at magnitudes of the two terms the error term can be neglected for  $u^2 \ll c_s^2$ . The last part is actually equivalent to  $\text{Ma}^2 \ll 1$  for a Mach number  $\text{Ma} = u/c_s$  [171]. As a result, the commonly held view is that the lattice-Boltzmann method is valid for weakly compressible phenomena only (subsonic) [172], [173], and not suitable for strongly compressible phenomena of flows with  $\text{Ma}$  at unity or above (supersonic) [77].

Having done all of the above it is now the time to put it together to determine the macroscopic equations outlined by the lattice Boltzmann method. To achieve this we use the perturbation moment in Eq. A.14, omitting the  $\mathcal{O}(u^3)$  term, in Eq. A.11, as well as reversing the expansion of derivatives in Eq. A.7. Subsequently, it is found that the lattice-Boltzmann equation solves the continuity and the Navier-Stokes equation like so:

$$\partial_t \rho + \partial_\gamma (\rho u_\gamma) = 0, \quad (\text{A.15a})$$

$$\partial_t (\rho u_\alpha) + \partial_\beta (\rho u_\alpha u_\beta) = -\partial_\alpha p + \partial_\beta [\eta (\partial_\beta u_\alpha + \partial_\alpha u_\beta)] \quad (\text{A.15b})$$

where

$$p = \rho c_s^2, \quad \eta = \rho c_s^2 \left( \tau - \frac{\Delta t}{2} \right), \quad \eta_B = \frac{2}{3} \eta. \quad (\text{A.16})$$

The bulk viscosity  $\eta_B$  is of the same order as the shear viscosity  $\eta$  here, where as in monoatomic kinetic theory it is usually found to be zero. The discrepancy comes from using the isothermal equation of state [134] such that  $p/p_0 = (\rho/\rho_0)^\gamma$  resulting in the expression for bulk viscosity being  $\eta_B = \eta(5/3 - \gamma)$  [123]. At the monoatomic limit



$\gamma = 5/3$ , resulting in  $\eta_B$ , while at the isothermal limit  $\gamma = 1$  leading to  $\eta_B = 2\eta/3$ . As a result of Eq. A.16 we find a stability condition such that  $\tau/\Delta t \geq 1/2$ , as otherwise for  $\tau/\Delta < 1/2$  the viscosity would be negative, which is macroscopically unstable.

As a final note on the Chapman-Enskog analysis, the same method of deriving the macroscopic Navier-Stokes equations from the mesoscopic lattice-Boltzmann equations set that uses the BGK operator could be used for more general collision operators. The  $\tau$  exclusively appears as the relaxation time of the moment  $\Pi_{\alpha\beta}$  in Eq. A.9c. While using the commonplace multiple-relaxation-time (MRT) collision operators each moment relaxes to equilibrium at a different rate, with good choices for the relaxation times increasing the stability and accuracy of the lattice-Boltzmann simulations. There is also potential to modify the shear and bulk viscosities separately through a more involved relaxation of the  $\Pi_{\alpha\beta}$  moment.

## Appendix B

# Hermite Polynomials

### B.1 Expansion of the equilibrium and particle distribution functions

The Hermite polynomials are commonly used in quantum mechanics for the wave functions of harmonic potentials and use tensor notation. In one-dimension, the weight function (also known as the generating function)

$$\omega(x) = \frac{1}{\sqrt{2\pi}} e^{-x^2/2}, \quad (\text{B.1})$$

can be used to describe the Hermite polynomial of the  $n$ -th order as

$$H^{(n)}(x) = (-1)^n \frac{1}{\omega(x)} \frac{d^n}{dx^n} \omega(x) \quad (\text{B.2})$$

where  $n \geq 0$  is an integer. Writing them out explicitly, the first four of these polynomials are

$$\begin{aligned} H^{(0)}(x) &= 1, & H^{(1)}(x) &= x, \\ H^{(2)}(x) &= x^2 - 1, & H^{(3)}(x) &= x^3 - 3x. \end{aligned} \quad (\text{B.3})$$

This definition can be extended to multiple dimensions  $d$  [117, 174], resulting in

$$\mathbf{H}^{(n)}(\mathbf{x}) = (-1)^n \frac{1}{\omega(\mathbf{x})} \nabla^{(n)} \omega(\mathbf{x}), \quad \omega(\mathbf{x}) = \frac{1}{(2\pi)^{d/2}} e^{-x^2/2}. \quad (\text{B.4})$$

In this notation, both  $\mathbf{H}^{(n)}$  and  $\nabla^{(n)}$  are tensors with rank  $n$ . That is, they can be represented by their  $d^n$  components  $H_{\alpha_1 \dots \alpha_n}^{(n)}$  and  $\nabla_{\alpha_1 \dots \alpha_n}^{(n)}$ , where  $n$  are indices running from 1 to  $d$  each.  $\nabla_{\alpha_1 \dots \alpha_n}^{(n)}$  term is a short notation indicative of  $n$  consecutive spatial derivatives

$$\nabla_{\alpha_1 \dots \alpha_n}^{(n)} = \frac{\partial}{\partial x_{\alpha_1}} \cdots \frac{\partial}{\partial x_{\alpha_n}}. \quad (\text{B.5})$$

For sufficiently smooth functions the derivatives commute such that, for example,  $\nabla_{xyy}^{(3)} = \nabla_{yxy}^{(3)} = \nabla_{yyx}^{(3)}$ . Under that assumption, the derivatives are symmetric upon permutation of the indices. For our purposes the cases that are of interest are for  $d = 2$  or  $d = 3$ , where the  $\alpha_1, \dots, \alpha_n \in \{x, y\}$  or  $\{x, y, z\}$ , respectively. For additional clarity, we can explicitly write down the two-dimensional ( $d = 2$ ) Hermite polynomials for the first two orders ( $n = 0, 1$ ), such that for  $n = 0$ :

$$H^{(0)} = 1, \quad (\text{B.6})$$

and for  $n=1$ :

$$\begin{aligned} H_x^{(1)} &= -\frac{1}{e^{-(x^2+y^2)/2}} \partial_x e^{-(x^2+y^2)/2} = x, \\ H_y^{(1)} &= -\frac{1}{e^{-(x^2+y^2)/2}} \partial_y e^{-(x^2+y^2)/2} = y. \end{aligned} \quad (\text{B.7})$$

Another mathematical property of the Hermite polynomials is that they are orthogonal. Considering the one dimensional case, the following holds true

$$\int_{-\infty}^{\infty} \omega(x) H^{(n)}(x) H^{(m)}(x) dx = n! \delta_{nm}^{(2)} \quad (\text{B.8})$$

with  $\delta_{nm}^{(2)}$  being the Kronecker delta. Extending the orthogonality to many dimensions

$d$ , the following is obtained:

$$\int \omega(\mathbf{x}) \mathbf{H}_{\alpha}^{(n)}(\mathbf{x}) \mathbf{H}_{\beta}^{(m)}(\mathbf{x}) d^d x = \prod_{i=1}^d n_i! \delta_{nm}^{(2)} \delta_{\alpha\beta}^{(n+m)}. \quad (\text{B.9})$$

The generalised Kronecker delta  $\delta_{\alpha\beta}^{(n+m)}$  is equal to 1 only if  $\alpha = (\alpha_1, \dots, \alpha_n)$  is a permutation of  $\beta = (\beta_1, \dots, \beta_n)$ , and 0 otherwise. As an example  $(x, y, z)$  is a permutation of  $(z, x, y)$ , but not of  $(x, x, z)$ . Additionally,  $n_x, n_y, n_z$  are the numbers of occurrences of  $x, y$ , and  $z$  in  $\alpha$ . Giving an example again, for  $\alpha = (y, y, z)$   $n_x = 0, n_y = 2, n_z = 1$ . For the 3D case, the orthogonality expressed in Eq. B.9 is given by

$$\int \omega(\mathbf{x}) \mathbf{H}_{\alpha}^{(n)}(\mathbf{x}) \mathbf{H}_{\beta}^{(n)}(\mathbf{x}) d^3 x = n_x! n_y! n_z! \delta_{nm}^{(2)} \delta_{\alpha\beta}^{(n+m)}. \quad (\text{B.10})$$

Having introduced orthogonality, we can now also talk about orthonormality. To do that, we can remind ourselves of some aspects of linear algebra. A basis is a set of vectors in a vector space such that every element of the space can be written as a linear combination of the elements of the set of vectors. The elements of a basis are also referred to as basis vectors. An orthonormal basis is one where all the vectors are orthonormal, i.e. the vectors are linearly independent unit vectors that are orthogonal to each other. A basis is complete for a vector space  $H$   $\{x \in H : \forall i \in I < x_i, x >= 0\} = \{0\}$ . Bringing that back to the Hermite polynomials, in one dimension they form a complete basis in  $\mathbb{R}$ , meaning that any sufficiently well behaved continuous function  $f(x) \in \mathbb{R}$  can be obtained through a series of Hermite polynomials:

$$f(x) = \omega(x) \sum_{n=0}^{\infty} \frac{1}{n!} a^{(n)} H^{(n)}(x), \quad a^{(n)} = \int f(x) H^{(n)}(x) dx. \quad (\text{B.11})$$

As before, we can extend this representation to  $d$  dimensions:

$$f(x) = \omega(\mathbf{x}) \sum_{n=0}^{\infty} \frac{1}{n!} \mathbf{a}^{(n)} \cdot \mathbf{H}^{(n)}(\mathbf{x}), \quad \mathbf{a}^{(n)} = \int f(\mathbf{x}) \mathbf{H}^{(n)}(\mathbf{x}) d^d x. \quad (\text{B.12})$$

The expansion coefficients  $\mathbf{a}^{(n)}$  are tensors of rank  $n$ . The scalar product  $\mathbf{a}^{(n)} \cdot \mathbf{H}^{(n)}$  is

given by the summation over all possible indices of  $a_{\alpha_1 \dots \alpha_n}^{(n)} H_{\alpha_1 \dots \alpha_n}^{(n)}$ .

We now have all the tools to apply the Hermite series expansion to the equilibrium function that will ultimately lead to the velocity discretisation. Implementing this Hermite series expansion from Eq. B.12 to  $f^{\text{eq}}$  in  $\boldsymbol{\xi}$ -space we obtain

$$\begin{aligned} f^{\text{eq}}(\rho, \mathbf{u}, \theta, \boldsymbol{\xi}) &= \omega(\boldsymbol{\xi}) \sum_{n=0}^{\infty} \frac{1}{n!} \mathbf{a}^{(n), \text{eq}}(\rho, \mathbf{u}, \theta) \cdot \mathbf{H}^{(n)}(\boldsymbol{\xi}), \\ \mathbf{a}^{(n), \text{eq}}(\rho, \mathbf{u}, \theta) &= \int f^{\text{eq}}(\rho, \mathbf{u}, \theta, \boldsymbol{\xi}) \mathbf{H}^{(n)}(\boldsymbol{\xi}) d^d \boldsymbol{\xi}. \end{aligned} \quad (\text{B.13})$$

An important realisation is that the equilibrium distribution function is of the same form as the weight function in Eq. B.1 :

$$f^{\text{eq}}(\rho, \mathbf{u}, \theta, \boldsymbol{\xi}) = \frac{\rho}{(2\pi\theta)^{d/2}} e^{-(\boldsymbol{\xi}-\mathbf{u})^2/(2\theta)} = \frac{\rho}{\theta^{d/2}} \omega\left(\frac{\boldsymbol{\xi}-\mathbf{u}}{\sqrt{\theta}}\right). \quad (\text{B.14})$$

Through this relation, we can calculate the series coefficients

$$\mathbf{a}^{(n), \text{eq}} = \frac{\rho}{\theta^{d/2}} \int \omega\left(\frac{\boldsymbol{\xi}-\mathbf{u}}{\sqrt{\theta}}\right) \mathbf{H}^{(n)}(\boldsymbol{\xi}) d^d \boldsymbol{\xi}, \quad (\text{B.15})$$

where the substitution  $\boldsymbol{\eta} = (\boldsymbol{\xi} - \mathbf{u})/\sqrt{\theta}$  results in

$$\mathbf{a}^{(n), \text{eq}} = \rho \int \omega(\boldsymbol{\eta}) \mathbf{H}^{(n)}(\sqrt{\theta}\boldsymbol{\eta} + \mathbf{u}) d^d \boldsymbol{\eta}. \quad (\text{B.16})$$

These integrals can be directly found, with the help of mathematical software package of choice, to give

$$\begin{aligned} a^{(0), \text{eq}} &= \rho, \\ a_{\alpha}^{(1), \text{eq}} &= \rho u_{\alpha}, \\ a_{\alpha\beta}^{(2), \text{eq}} &= \rho(u_{\alpha} u_{\beta} + (\theta - 1)\delta_{\alpha\beta}), \\ a_{\alpha\beta\gamma}^{(3), \text{eq}} &= \rho[u_{\alpha} u_{\beta} u_{\gamma} + (\theta - 1)(\delta_{\alpha\beta} u_{\gamma} + \delta_{\beta\gamma} u_{\alpha} + \delta_{\gamma\alpha} u_{\beta})]. \end{aligned} \quad (\text{B.17})$$

By having a closer look at the equations above, it can be noted that the coefficients in this Hermite series expansion of the equilibrium distribution function  $f^{\text{eq}}$  are related to

the conserved moments. The three outlined coefficients are connected to the density, momentum, and energy. Simultaneously, the Hermite series expansion can also be applied to the particle distribution function  $f$  such that the conserved quantities are given by the expansion coefficients.

$$\begin{aligned}
a^{(0),eq} &= \int f^{\text{eq}} d^d\xi = \rho = \int f d^d\xi = a^{(0)}, \\
a_{\alpha}^{(1),eq} &= \int f^{\text{eq}} \xi_{\alpha} d^d\xi = \rho u_{\alpha} = \int f \xi_{\alpha} d^d\xi = a_{\alpha}^{(1)}, \\
\frac{a_{\alpha\alpha}^{(2),eq} + \rho d}{2} &= \int f^{\text{eq}} \frac{|\xi|^2}{2} d^d\xi = \rho E = \int f \frac{|\xi|^2}{2} d^d\xi = \frac{a_{\alpha\alpha}^{(2)} + \rho d}{2}.
\end{aligned} \tag{B.18}$$

For this reason the Hermite series expansion is so useful for the Boltzmann equation approach. The series coefficients are directly connected to the conserved moments, with the first three  $n = 0, 1, 2$  being enough to satisfy the conservation laws and hence represent the macroscopic equations for the hydrodynamics of the system. It's also possible to include higher order expansion terms, which has been argued to improve the numerical stability and accuracy. For our purposes it is enough to consider the first three terms which results in significant reduction in the numerical resources needed in comparison to focusing on the full mesoscopic equilibrium. Using what we have outlined above, we can now explicitly write the approximation of the equilibrium distribution function up to the third moment (that corresponds to the second order in  $\xi$  ( $N = 2$ )):

$$\begin{aligned}
f^{\text{eq}}(\rho, \mathbf{u}, \theta, \xi) &\approx \omega(\xi) \rho [1 + \xi_{\alpha} u_{\alpha} + (u_{\alpha} u_{\beta} + (\theta - 1) \delta_{\alpha\beta}) (\xi_{\alpha} \xi_{\beta} - \delta_{\alpha\beta})] \\
&= \omega(\xi) \rho Q(\mathbf{u}, \theta, \xi).
\end{aligned} \tag{B.19}$$

As an aside, we can briefly mention the Mach number expansion. By expanding the equilibrium distribution function from Eq. 3.18 up to the second order in  $\mathbf{u}$  we get the same equation as Eq. B.19. Nevertheless for the next order expansion, corresponding to energy conservation, the Mach number expansion differs from the Hermite series. Thanks to the orthogonality of the Hermite polynomials, the Hermite series expansion does not mix the lower order moments (related to the Navier-Stokes equations) with the higher order moments related to the energy equation and beyond. The Mach number

expansion does [175], making the Hermite series expansion largely preferable.

Another reason for the preference of using the Hermite polynomials is that we can obtain discrete velocity sets by taking integral function values at a small number of discrete points, called the abscissae. First, lets assume we have a one dimensional polynomial  $P^{(N)}(x)$  of order  $N$ . Then, we look for the exact solution of the integral  $\int \omega(x)P^{(N)}(x)dx$ . Through considering integral function values in certain points  $x_i$  we can achieve just that by using what is called the Gauss-Hermite quadrature rule

$$\int_{-\infty}^{+\infty} \omega(x)P^{(N)}(x)dx = \sum_{i=1}^n w_i P^{(N)}(x_i). \quad (\text{B.20})$$

Here, the  $n$  values of  $x_i$  are the roots of the Hermite polynomials  $H^{(n)}(x)$ , that is  $H^{(n)}(x_i) = 0$ , and  $N \leq 2n - 1$ . This implies that in order to exactly integrate a polynomial of order  $N$ , the minimum number of  $x_i$  abscissae with associated weights  $w_i$  required is  $n = (N + 1)/2$ . Higher order polynomials will require more abscissae and subsequently higher-order Hermite polynomials. We can generalise Eq. B.20 to  $d$  dimensions

$$\int \omega(\mathbf{x})P^{(N)}(\mathbf{x})d^d x = \sum_{i=1}^n w_i P^{(N)}(\mathbf{x}_i). \quad (\text{B.21})$$

where each component of the multidimensional point  $\mathbf{x}_i$  (that is,  $x_{i\alpha}$  with  $\alpha = 1, \dots, d$ ) is a root of one-dimensional Hermite polynomial  $H^{(n)}(x_{i\alpha}) = 0$ .

The Gauss-Hermite rule can be used to calculate moments and coefficients of the Hermite expansions. By examining the definition of the coefficients for the equilibrium function in more detail we find that

$$\mathbf{a}^{(n),\text{eq}} = \rho \int \omega(\boldsymbol{\eta})\mathbf{H}^{(n)}(\sqrt{\theta}\boldsymbol{\eta} + \mathbf{u}) d^d \boldsymbol{\eta} = \rho \int \omega(\boldsymbol{\eta})\mathbf{P}^{(n)}(\boldsymbol{\eta}) d^d \boldsymbol{\eta}. \quad (\text{B.22})$$

The tensor-valued Hermite polynomial  $\mathbf{H}^{(n)}(\boldsymbol{\eta})$  is actually a polynomial of order  $n$ , and as a result it can be rewritten as  $\mathbf{P}^{(n)}(\boldsymbol{\eta})$ . We can apply the Gauss-Hermite quadrature rule to the integral on the right-hand side. Unfortunately, it is somewhat of an endeavour to calculate the  $\mathbf{P}^{(n)}(\boldsymbol{\eta})$  from the Hermite polynomial  $\mathbf{H}^{(n)}(\sqrt{\theta}\boldsymbol{\eta} + \mathbf{u})$ .

Alternatively, we choose a different method and use the truncated series expansion of the equilibrium distribution function  $f^{\text{eq}}$  that gives the same macroscopic moments.

Using Eq. B.13 and Eq. B.19 we get the relation

$$\mathbf{a}^{(n),\text{eq}} = \int f^{\text{eq}}(\boldsymbol{\xi}) \mathbf{H}^{(n)}(\boldsymbol{\xi}) d^d \xi = \rho \int \omega(\boldsymbol{\xi}) Q(\boldsymbol{\xi}) \mathbf{H}^{(n)}(\boldsymbol{\xi}) d^d \xi \quad (\text{B.23})$$

that once again only notes down the  $\boldsymbol{\xi}$ -dependence. Next, we take the composed polynomial  $\mathbf{R} = Q(\boldsymbol{\xi}) \mathbf{H}^{(n)}(\boldsymbol{\xi})$  and implement the Gauss-Hermite quadrature rule

$$\mathbf{a}^{(n),\text{eq}} = \rho \int \omega(\boldsymbol{\xi}) \mathbf{R}(\boldsymbol{\xi}) d^d \xi = \rho \sum_{i=1}^n w_i \mathbf{R}(\boldsymbol{\xi}_i) = \rho \sum_{i=1}^n w_i Q(\boldsymbol{\xi}_i) \mathbf{H}^{(n)}(\boldsymbol{\xi}_i). \quad (\text{B.24})$$

We have now obtained the discretised Hermite series expansion with  $n$  being the essential number of abscissae.

A remark on the abscissae would not go amiss here. In order to make sure that all the relevant conservation laws are obeyed, the polynomial of the highest degree needs to be correctly integrated. In our example, this is the last polynomial in Eq. B.18, which is related to the energy and also connected to the second-order Hermite polynomial  $\mathbf{H}^{(2)}(\boldsymbol{\xi})$ . Making an assumption that the polynomial  $Q(\boldsymbol{\xi})$  is also of second order, the composed polynomial  $\mathbf{R} = Q(\boldsymbol{\xi}) \mathbf{H}^{(2)}(\boldsymbol{\xi})$  is then of fourth order,  $N = 4$ . Following the conditions of the Gauss-Hermite quadrature rule,  $n \geq (N + 1)/2$ , meaning that at the minimum we need  $n = 3$  for the exact calculation of moments. Therefore we are looking for the roots of  $H^3(\xi_{i\alpha})$  that will give us the abscissae. The details of the proper choice and the complex mathematical background of the Gauss-Hermite rule is available in the Appendix A.4 of [109]. The exact abscissae outlined there contain unwieldy factors of  $\sqrt{3}$ . This can be simplified by introducing a new particle velocity

$$\mathbf{c}_i = \frac{\mathbf{x} \mathbf{i}_i}{\sqrt{3}} \quad (\text{B.25})$$

meaning that the velocity sets will consist of integer abscissae.



# Appendix C

## Input options

To reproduce the data a parallel configuration of Ludwig v0.19.1 should be compiled on the machine used for the simulations. The resulting executable (Ludwig.exe) should be placed in a directory together with an input file. The results were obtained using Open MPI, by loading module version openmpi/gcc-8.5.0/4.1.1 . Here we present an example of an input script, annotated with appropriate comments, used to run a single simulation. This illustrates the process to follow to reproduce the simulations ran to obtain the data presented in this thesis. For more details on how to use Ludwig, detailed information can be found in the Ludwig code repository [143]. The input script is given below.

```
#####  
#  
# Ludwig input file  
# Reference  
#  
# Lines introduced with # and blank lines are ignored.  
#  
# The file is made up of a series of (case-sensitive) keyword value  
# pairs which should be separated by a space:  
#
```



```

# grid PX_PY_PZ      is the processor decomposition
#                   If PX*PY*PZ is not equal to the number of processors,
#                   MPI will choose a default (may be implementation-dependent).
#
# periodicity        Periodicity of MPI Cartesian communicator
#
# reduced_halo [yes|no]  use reduced or full halos. Using reduced halos
#                       is *only* appropriate for fluid only problems.
#                       Default is no.
#
#####

size          128_64_256
grid          1_1_4
periodicity   0_1_1

#####

# Fluid parameters
#
# viscosity        shear viscosity [default is 1/6, ie., relaxation time 1]
# viscosity_bulk   bulk viscosity [default = shear viscosity]
#
# isothermal_fluctuations [on—off]    Default is off.
# temperature      isothermal fluctuation 'temperature'
#
# ghost_modes [on—off]    Default is on.
# force FX_FY_FZ      Uniform body force on fluid (default zero)
#
#####

```



















# Bibliography

1. Lesniewska, M., Mottram, N. & Henrich, O. Controllable particle migration in liquid crystal flows. *Soft Matter* **18**, 6942–6953 (36 2022).
2. Lesniewska, M., Mottram, N. & Henrich, O. Defect-influenced particle advection in highly confined liquid crystal flows. *Soft Matter* **20**, 2218–2231 (10 2024).
3. Barrat, J.-L. & Hansen, J.-P. *Basic concepts for simple and complex liquids* (Cambridge University Press, 2003).
4. Ingebrigtsen, T. S., Schrøder, T. B. & Dyre, J. C. What Is a Simple Liquid? *Phys. Rev. X* **2**, 011011 (1 2012).
5. Schowalter, W. R. *Mechanics of non-newtonian fluids* (Pergamon Press, 1978).
6. Bird, R. B., Armstrong, R. C. & Hassager, O. *Dynamics of polymeric liquids* (John Wiley & Sons, 1987).
7. Larson, R. *The Structure and Rheology of Complex Fluids* (OUP USA, 1999).
8. De Gennes, P.-G. & Prost, J. *The Physics of Liquid Crystals* (Oxford University Press, New York, 1993).
9. Castellano, J. *Liquid Gold: The Story of Liquid Crystal Displays and the Creation of an Industry* 1–302 (Jan. 2005).
10. Lagerwall, J. P. & Scalia, G. A new era for liquid crystal research: Applications of liquid crystals in soft matter nano-, bio- and microtechnology. *Current Applied Physics* **12**, 1387–1412 (2012).

11. Whitesides, G. M. The origins and the future of Microfluidics. *Nature* **442**, 368–373 (2006).
12. Tabeling, P. *Introduction to Microfluidics* (Oxford University Press, 2023).
13. Squires, T. M. & Quake, S. R. Microfluidics: Fluid physics at the nanoliter scale. *Rev. Mod. Phys.* **77**, 977–1026 (3 2005).
14. Thorsen, T., Maerkl, S. J. & Quake, S. R. Microfluidic Large-Scale Integration. *Science* **298**, 580–584 (2002).
15. Reinitzer, F. Contributions to the knowledge of cholesterol. *Liquid Crystals* **5**, 7–18 (1989).
16. Smalyukh, I. I. Liquid Crystal Colloids. *Annual Review of Condensed Matter Physics* **9**, 207–226 (2018).
17. Meeker, S. P., Poon, W. C. K., Crain, J. & Terentjev, E. M. Colloid–liquid-crystal composites: An unusual soft solid. *Phys. Rev. E* **61**, R6083–R6086 (6 2000).
18. Petrov, P. G. & Terentjev, E. M. Formation of Cellular Solid in Liquid Crystal Colloids. *Langmuir* **17**, 2942–2949 (2001).
19. Muševič, I., Škarabot, M., Tkalec, U., Ravnik, M. & Žumer, S. Two-Dimensional Nematic Colloidal Crystals Self-Assembled by Topological Defects. *Science* **313**, 954–958 (2006).
20. Ravnik, M. *et al.* Entangled Nematic Colloidal Dimers and Wires. *Phys. Rev. Lett.* **99**, 247801 (24 2007).
21. Muševič, I. & Škarabot, M. Self-assembly of nematic colloids. *Soft Matter* **4**, 195–199 (2 2008).
22. Škarabot, M. *et al.* Interactions of quadrupolar nematic colloids. *Phys. Rev. E* **77**, 031705 (3 2008).
23. Škarabot, M. *et al.* Hierarchical self-assembly of nematic colloidal superstructures. *Phys. Rev. E* **77**, 061706 (6 2008).

24. Hung, F. R. Quadrupolar particles in a nematic liquid crystal: Effects of particle size and shape. *Phys. Rev. E* **79**, 021705 (2 2009).
25. Fukuda, J.-i. Liquid Crystal Colloids: A Novel Composite Material Based on Liquid Crystals. *Journal of the Physical Society of Japan* **78**, 041003 (2009).
26. Tkalec, U., Ravnik, M., Žumer, S. & Muševič, I. Vortexlike Topological Defects in Nematic Colloids: Chiral Colloidal Dimers and 2D Crystals. *Phys. Rev. Lett.* **103**, 127801 (12 2009).
27. Collings, P. J. & Goodby, J. W. *Introduction to liquid crystals: Chemistry and physics, Second edition* (Taylor & Francis Ltd, 2019).
28. Fréedericksz, V. & Zolina, V. Forces causing the orientation of an anisotropic liquid. *Trans. Faraday Soc.* **29**, 919–930 (140 1933).
29. Neubert, M. E. Glenn Halstead Brown, 1915–1995. *Liquid Crystals Today* **5**, 1–2 (1995).
30. Imrie, C. Recollections of Professor George W. Gray. *Liquid Crystals* **42**, 564–592 (2015).
31. Goulding, M. & Geelhaar, T. Merck and George Gray: a 30-year relationship. *Liquid Crystals* **42**, 643–645 (2015).
32. Bunning, T. Cholesteric liquid crystals: properties and applications. *Liquid Crystals Today* **23**, 23–24 (2014).
33. Williams, V. *Liquid Crystal Microscopy* <http://lcmicroscopy.weebly.com/lc-photogallery.html>. Accessed: 2023-12-01.
34. Allen, M. P. Molecular simulation of liquid crystals. *Molecular Physics* **117**, 2391–2417 (2019).
35. Wilson, M. R. Molecular simulation of liquid crystals: progress towards a better understanding of bulk structure and the prediction of material properties. *Chem. Soc. Rev.* **36**, 1881–1888 (12 2007).
36. Stewart, I. W. *The Static and Dynamic Continuum Theory* (Taylor, Francis, London, and New York, 2004).

37. Carlsson, T. & Leslie, F. M. The development of theory for flow and dynamic effects for nematic liquid crystals. *Liquid Crystals* **26**, 1267–1280 (1999).
38. Frank, F. C. I. Liquid crystals. On the theory of liquid crystals. *Discuss. Faraday Soc.* **25**, 19–28 (0 1958).
39. Ericksen, J. L. Conservation Laws for Liquid Crystals. *Transactions of The Society of Rheology* **5**, 23–34 (1961).
40. Leslie, F. M. Some constitutive equations for anisotropic fluids. *The Quarterly Journal of Mechanics and Applied Mathematics* **19**, 357–370 (1966).
41. Leslie, F. M. Some constitutive equations for liquid crystals. *Archive for Rational Mechanics and Analysis* **28**, 265–283 (1968).
42. Atkin, R. J. Poiseuille flow of liquid crystals of the nematic type. *Archive for Rational Mechanics and Analysis* **38**, 224–240 (1970).
43. Fisher, J. & Fredrickson, A. G. Interfacial Effects on the Viscosity of a Nematic Mesophase. *Molecular Crystals* **8**, 267–284 (1969).
44. Ericksen, J. L. Liquid crystals with variable degree of orientation. *Archive for Rational Mechanics and Analysis* **113**, 97–120 (1991).
45. Kinderlehrer, D. *Recent Developments in Liquid Crystal Theory* in (1989).
46. Virga, E. G. *Variational theories for Liquid Crystals* (Chapman & Hall, 1994).
47. Mottram, N. J. & Newton, C. J. P. Introduction to Q-tensor theory. *arXiv: Soft Condensed Matter* (2014).
48. Beris, A. N. & Edwards, B. J. *Thermodynamics of flowing systems* (Oxford Univ. Press, 1994).
49. Ravnik, M. *Colloidal structures confined to thin nematic layers* PhD thesis (Faculty of Mathematics and Physics, Univeristy of Ljubljana, Slovenia, 2009).
50. Ericksen, J. L. Inequalities in Liquid Crystal Theory. *The Physics of Fluids* **9**, 1205–1207 (1966).

51. Bradshaw, M. J., Raynes, E. P., Bunning, J. D. & Faber, T. E. The Frank constants of some nematic liquid crystals. *Journal De Physique* **46**, 1513–1520 (1985).
52. Luckhurst, G., Dunmur, D., Fukuda, A. & Group, I. E. *Physical Properties of Liquid Crystals: Nematics* (Institution of Electrical Engineers, 2001).
53. Madhusudana, N. V. & Pratibha, R. Elasticity and Orientational Order in Some Cyanobiphenyls: Part IV. Reanalysis of the Data. *Molecular Crystals and Liquid Crystals* **89**, 249–257 (1982).
54. Iglesias, W., Abbott, N. L., Mann, E. K. & Jákli, A. Improving Liquid-Crystal-Based Biosensing in Aqueous Phases. *ACS Applied Materials & Interfaces* **4**, 6884–6890 (2012).
55. Muševič, I. *Liquid Crystal Colloids* ISBN: 9783319549163 (Springer International Publishing, 2017).
56. Landau, L. D. & Lifšic, E. M. *Fluid mechanics* (Pergamon Press, 1987).
57. Andrienko, D. Introduction to liquid crystals. *Journal of Molecular Liquids* **267**. Special Issue Dedicated to the Memory of Professor Y. Reznikov, 520–541. ISSN: 0167-7322 (2018).
58. Jérôme, B. Surface effects and anchoring in liquid crystals. *Reports on Progress in Physics* **54**, 391 (1991).
59. Berteloot, B., Nys, I., Poy, G., Beeckman, J. & Neyts, K. Ring-shaped liquid crystal structures through patterned planar photo-alignment. *Soft Matter* **16**, 4999–5008 (21 2020).
60. Zhang, B., Lee, F. K., Tsui, O. K. C. & Sheng, P. Liquid Crystal Orientation Transition on Microtextured Substrates. *Phys. Rev. Lett.* **91**, 215501 (21 2003).
61. Fournier, J.-B. & Galatola, P. Modeling planar degenerate wetting and anchoring in nematic liquid crystals. *Europhysics Letters* **72**, 403 (2005).



62. Alexander, G. P., Chen, B. G.-g., Matsumoto, E. A. & Kamien, R. D. Colloquium: Disclination loops, point defects, and all that in nematic liquid crystals. *Rev. Mod. Phys.* **84**, 497–514 (2 2012).
63. Kléman, M. & Mermin, N. D. Points, Lines, and Walls in Liquid Crystals, Magnetic Systems, and Various Ordered Media. *American Journal of Physics* **52**, 188–189 (1984).
64. Mermin, N. D. The topological theory of defects in ordered media. *Rev. Mod. Phys.* **51**, 591–648 (3 1979).
65. Trebin, H.-R. The topology of non-uniform media in condensed matter physics. *Advances in Physics* **31**, 195–254 (1982).
66. Volovik, G. E. *The Universe in a Helium Droplet* (Oxford University Press, 2009).
67. Sengupta, A. *Nematic liquid crystals and nematic colloids in microfluidic environment* PhD thesis (2012).
68. Chandrasekhar, S. *Liquid Crystals* 2nd ed. (Cambridge University Press, 1992).
69. Oswald, P. & Pieranski, P. *Nematic and Cholesteric Liquid Crystals: Concepts and physical properties illustrated by experiments* (Taylor & Francis, 2005).
70. Peroli, G. G. & Virga, E. G. Annihilation of point defects in nematic liquid crystals. *Phys. Rev. E* **54**, 5235–5241 (5 1996).
71. Miesowicz, M. The three coefficients of viscosity of anisotropic liquids. *Nature* **158**, 27–27 (1946).
72. Gähwiller, C. Temperature Dependence of Flow Alignment in Nematic Liquid Crystals. *Phys. Rev. Lett.* **28**, 1554–1556 (24 1972).
73. Miesowicz, M. Liquid crystals in my memories and now—the role of anisotropic viscosity in liquid crystals research. *Molecular Crystals and Liquid Crystals* **97**, 1–11 (1983).
74. Ericksen, J. L. Anisotropic fluids. *Archive for Rational Mechanics and Analysis* **4**, 231–237 (1959).

75. Parodi, O. Stress tensor for a nematic liquid crystal. *Journal de Physique* **31**, 581–584 (1970).
76. Yu, H. & Zhang, P. A Kinetic–hydrodynamic simulation of microstructure of liquid crystal polymers in plane shear flow. *Journal of Non-Newtonian Fluid Mechanics* **141**, 116–127 (2007).
77. Thompson, P. D. *Compressible-fluid dynamics* (McGraw-Hill, 1972).
78. Kinsler, L. E., Frey, A. R., Coppers, A. B. & Sanders, J. V. *Fundamentals of Acoustics* (Wiley, 2000).
79. Ericksen, J. L. Hydrostatic theory of liquid crystals. *Archive for Rational Mechanics and Analysis* **9**, 371–378 (1962).
80. Qian, T. & Sheng, P. Generalized hydrodynamic equations for nematic liquid crystals. *Physical Review E* **58**, 7475 (1998).
81. Wu, H., Xu, X. & Liu, C. On the general Ericksen–Leslie system: Parodi’s relation, well-posedness and stability. *Archive for Rational Mechanics and Analysis* **208**, 59–107 (2013).
82. Liu, C. & Sun, H. On energetic variational approaches in modeling the nematic liquid crystal flows. *Discrete and Continuous Dynamical Systems* **23**, 455–475 (2008).
83. Denniston, C., Orlandini, E. & Yeomans, J. M. Lattice Boltzmann simulations of liquid crystal hydrodynamics. *Phys. Rev. E* **63**, 056702 (5 2001).
84. Elger, D. F., LeBret, B. A., Crowe, C. T. & Roberson, J. A. *Engineering fluid mechanics* (John Wiley & Sons, Inc., 2022).
85. *Compendium of polymer terminology and nomenclature: IUPAC recommendations, 2008* (RSC Pub., 2008).
86. Dukhin, A. S. & Goetz, P. J. in *Characterization of Liquids, Nano- and Microparticulates, and Porous Bodies Using Ultrasound* (eds Dukhin, A. S. & Goetz, P. J.) 21–89 (Elsevier, 2010).

87. Muševič, I. Nematic Liquid-Crystal Colloids. *Materials* **11** (2018).
88. Stark, H. Physics of colloidal dispersions in nematic liquid crystals. *Physics Reports* **351**, 387–474. ISSN: 0370-1573 (2001).
89. Brochard, F. & de Gennes, P. G. Theory of magnetic suspensions in liquid crystals. *Journal De Physique* **31**, 691–708 (1970).
90. Poulin, P., Stark, H., Lubensky, T. C. & Weitz, D. A. Novel Colloidal Interactions in Anisotropic Fluids. *Science* **275**, 1770–1773 (1997).
91. Ashkin, A., Dziedzic, J. M. & Yamane, T. Optical trapping and manipulation of single cells using infrared laser beams. *Nature* **330**, 769–771 (1987).
92. Muševič, I. *et al.* Laser Trapping of Small Colloidal Particles in a Nematic Liquid Crystal: Clouds and Ghosts. *Phys. Rev. Lett.* **93**, 187801 (18 2004).
93. Škarabot, M. *et al.* Laser trapping of low refractive index colloids in a nematic liquid crystal. *Phys. Rev. E* **73**, 021705 (2 2006).
94. Hotta, J.-i., Sasaki, K. & Masuhara, H. Manipulation of liquid crystal textures with a focused near infrared laser beam. *Applied Physics Letters* **71**, 2085–2087 (1997).
95. Smalyukh, I. I., Kuzmin, A. N., Kachynski, A. V., Prasad, P. N. & Lavrentovich, O. D. Optical trapping of colloidal particles and measurement of the defect line tension and colloidal forces in a thermotropic nematic liquid crystal. *Applied Physics Letters* **86**, 021913 (2005).
96. Smalyukh, I., Shiyanovskii, S. & Lavrentovich, O. Three-dimensional imaging of orientational order by fluorescence confocal polarizing microscopy. *Chemical Physics Letters* **336**, 88–96 (2001).
97. Posnjak, G., Čopar, S. & Muševič, I. Points, Skyrmions and torons in chiral nematic droplets. *Scientific Reports* **6** (2016).

98. Smalyukh, I. I., Lavrentovich, O. D., Kuzmin, A. N., Kachynski, A. V. & Prasad, P. N. Elasticity-Mediated Self-Organization and Colloidal Interactions of Solid Spheres with Tangential Anchoring in a Nematic Liquid Crystal. *Phys. Rev. Lett.* **95**, 157801 (15 2005).
99. P. V. Dolganov, P. C. & Dolganov, V. K. Interaction and self-organization of inclusions in two-dimensional free-standing smectic films. *Liquid Crystals Reviews* **7**, 1–29 (2019).
100. Sengupta, A. Topological microfluidics: present and prospects. *Liquid Crystals Today* **24**, 70–80 (2015).
101. Sengupta, A., Tkalec, U. & Bahr, C. Nematic textures in microfluidic environment. *Soft Matter* **7**, 6542–6549 (14 2011).
102. Sengupta, A., Pieper, C., Enderlein, J., Bahr, C. & Herminghaus, S. Flow of a nematogen past a cylindrical micro-pillar. *Soft Matter* **9**, 1937–1946 (6 2013).
103. Sengupta, A., Bahr, C. & Herminghaus, S. Topological microfluidics for flexible micro-cargo concepts. *Soft Matter* **9**, 7251–7260 (30 2013).
104. Sengupta, A., Schulz, B., Ouskova, E. & Bahr, C. Functionalization of microfluidic devices for investigation of liquid crystal flows. *Microfluidics and Nanofluidics* **13**, 941–955 (2012).
105. Gerus, I., Glushchenko, A., Kwon, S.-B., Reshetnyak, V. & Reznikov, Y. Anchoring of a liquid crystal on a photoaligning layer with varying surface morphology. *Liquid Crystals* **28**, 1709–1713 (2001).
106. Fukuhara, K., Nagano, S., Hara, M. & Seki, T. Free-surface molecular command systems for photoalignment of liquid crystalline materials. *Nature Communications* **5** (2014).
107. Araùjo, N. A. M. *et al.* Steering self-organisation through confinement. *Soft Matter* **19**, 1695–1704 (9 2023).
108. Sudha, D. G., Ochoa, J. & Hirst, L. S. Colloidal aggregation in anisotropic liquid crystal solvent. *Soft Matter* **17**, 7532–7540 (32 2021).

109. Krüger, T. *et al.* *The Lattice Boltzmann Equation* ISBN: 978-3-319-44649-3 (Springer International Publishing, Cham, 2017).
110. Cercignani, C. *The boltzmann equation and its applications* (Springer-Verlag, 1988).
111. Adhikari, R., Stratford, K., Cates, M. E. & Wagner, A. J. Fluctuating lattice Boltzmann. *Europhysics Letters* **71**, 473 (2005).
112. Chapman, S., Cowling, T. G. & Burnett, D. *The mathematical theory of non-uniform gases: An account of the kinetic theory of viscosity, thermal conduction and diffusion in gases* (Cambridge U.P, 1970).
113. Sone, Y. in *Kinetic Theory and Fluid Dynamics* 1–4 (Birkhäuser Boston, Boston, MA, 2002).
114. E. Ikenberry, C. T. On the Pressures and the Flux of Energy in a Gas according to Maxwell’s Kinetic Theory, II. *Journal of Rational Mechanics and Analysis* **5**, 55–128 (1956).
115. Wagner, A. J. Thermodynamic consistency of liquid-gas lattice Boltzmann simulations. *Phys. Rev. E* **74**, 056703 (5 2006).
116. Caiazzo, A., Junk, M. & Rheinländer, M. Comparison of analysis techniques for the lattice Boltzmann method. *Comput. Math. Appl.* **58**, 883–897 (2009).
117. Shan, X. & Chen, H. Kinetic theory representation of hydrodynamics: A way beyond the Navier-Stokes equation. *Journal of Fluid Mechanics* **550**, 413–441 (2006).
118. He, X. & Luo, L.-S. Theory of the lattice Boltzmann method: From the Boltzmann equation to the lattice Boltzmann equation. *Phys. Rev. E* **56**, 6811–6817 (6 1997).
119. Taylor, G. K., Nudds, R. L. & Thomas, A. L. Flying and swimming animals cruise at a Strouhal number tuned for high power efficiency. *Nature* **425**, 707–711 (2003).

120. Wolf-Gladrow, D. *Lattice-gas cellular automata and lattice Boltzmann models: An introduction* (Springer, 2005).
121. Qian, Y. H., d’Humières, D. & Lallemand, P. Lattice BGK Models for Navier-Stokes Equation. *EPL (Europhysics Letters)* **17**, 479–484 (1992).
122. Frisch, U., Hasslacher, B. & Pomeau, Y. Lattice-Gas Automata for the Navier-Stokes Equation. *Phys. Rev. Lett.* **56**, 1505–1508 (14 1986).
123. Vigen, E. M. *The lattice Boltzmann method: Fundamentals and acoustics* PhD thesis (2014).
124. Silva, G. & Semiao, V. Truncation errors and the rotational invariance of three-dimensional lattice models in the lattice Boltzmann method. *Journal of Computational Physics* **269**, 259–279 (2014).
125. Ginzburg, I., d’Humières, D. & Kuzmin, A. Optimal Stability of Advection-Diffusion Lattice Boltzmann Models with Two Relaxation Times for Positive/Negative Equilibrium. *Journal of Statistical Physics* **139**, 1090–1143 (2010).
126. Yudistiawan, W. P., Kwak, S. K., Patil, D. V. & Ansumali, S. Higher-order Galilean-invariant lattice Boltzmann model for microflows: single-component gas. *Physical review. E, Statistical, nonlinear, and soft matter physics* **82** **4 Pt 2**, 046701 (2010).
127. Suga, K., Kuwata, Y., Takashima, K. & Chikasue, R. A D3Q27 multiple-relaxation-time lattice Boltzmann method for turbulent flows. *Comput. Math. Appl.* **69**, 518–529 (2015).
128. Kuwata, Y. & Suga, K. Anomaly of the lattice Boltzmann methods in three-dimensional cylindrical flows. *Journal of Computational Physics* **280**, 563–569 (2015).
129. Pontrelli, G., Ubertini, S. & Succi, S. The unstructured lattice Boltzmann method for non-Newtonian flows. *Journal of Statistical Mechanics: Theory and Experiment* **2009**, P06005 (2009).

130. Misztal, M. K., Hernandez-Garcia, A., Matin, R., Sørensen, H. O. & Mathiesen, J. Detailed analysis of the lattice Boltzmann method on unstructured grids. *J. Comput. Phys.* **297**, 316–339 (2014).
131. Sandoval, L. *Revisiting grid refinement algorithms for the lattice Boltzmann method* PhD thesis (2012).
132. Ubertini, S., Asinari, P. & Succi, S. Three ways to lattice Boltzmann: A unified time-marching picture. *Phys. Rev. E* **81**, 016311 (1 2010).
133. Hoffman, J. D. *Numerical methods for engineers and scientists* (McGraw-Hill, 1992).
134. Dellar, P. J. Bulk and shear viscosities in lattice Boltzmann equations. *Phys. Rev. E* **64**, 031203 (3 2001).
135. Tolke, J. & Krafczyk, M. Teraflop computing on a desktop PC with GPUs for 3D CFD. *International Journal of Computational Fluid Dynamics* **22**, 443–456 (2008).
136. He, X., Chen, S. & Doolen, G. D. A Novel Thermal Model for the Lattice Boltzmann Method in Incompressible Limit. *Journal of Computational Physics* **146**, 282–300 (1998).
137. Sterling, J. D. & Chen, S. Stability Analysis of Lattice Boltzmann Methods. *Journal of Computational Physics* **123**, 196–206 (1996).
138. Bhatnagar, P. L., Gross, E. P. & Krook, M. A Model for Collision Processes in Gases. I. Small Amplitude Processes in Charged and Neutral One-Component Systems. *Phys. Rev.* **94**, 511–525 (3 1954).
139. Chorin, A. J. & Marsden, J. E. *Mathematical introduction to fluid mechanics* (Springer, 2000).
140. Ladd, A. Numerical simulations of particulate suspensions via a discretised Boltzmann equation. Part 1. Theoretical foundation. *J. Fluid. Mech.* **271**, 285 (1994).
141. Ladd, A. Numerical simulations of particulate suspensions via a discretised Boltzmann equation. Part 2. Numerical results. *J. Fluid. Mech.* **271**, 311 (1994).

142. Nguyen, N. Q. & Ladd, A. J. Lubrication corrections for lattice-Boltzmann simulations of particle suspensions. *Phys. Rev. E* **66**, 046708. ISSN: 1063651X (2002).
143. Ludwig GitHub repository. <https://github.com/ludwig-cf/ludwig>. Accessed: 2023-11-01.
144. Wright, D. C. & Mermin, N. D. *Rev. Mod. Phys.* **61**, 385–432 (1989).
145. Desplat, J. C., Pagonabarraga, I. & Bladon, P. Ludwig: A parallel Lattice-Boltzmann code for complex fluids. *Comput. Phys. Commun.* **134**, 273–290. ISSN: 00104655. eprint: 0005213 (2001).
146. Adhikari, R., Stratford, K., Cates, M. E. & Wagner, A. J. Fluctuating lattice Boltzmann. *Europhys. Lett.* **71**, 473–479. ISSN: 02955075. eprint: 0402598 (cond-mat) (2005).
147. Mougin, G. & Magnaudet, J. The generalized Kirchhoff equations and their application to the interaction between a rigid body and an arbitrary time-dependent viscous flow. *International Journal of Multiphase Flow* **28**, 1837–1851 (2002).
148. Anderson, J. *Fundamentals of Aerodynamics* (McGraw-Hill Education, 2010).
149. JOHNSON, T. A. & PATEL, V. C. Flow past a sphere up to a Reynolds number of 300. *Journal of Fluid Mechanics* **378**, 19–70 (1999).
150. Taneda, S. Experimental Investigation of the Wake behind a Sphere at Low Reynolds Numbers. *Journal of the Physical Society of Japan* **11**, 1104–1108 (1956).
151. Natarajan, R. & Acrivos, A. The instability of the steady flow past spheres and disks. *Journal of Fluid Mechanics* **254**, 323–344 (1993).
152. Nakamura, I. Steady wake behind a sphere. *Physics of Fluids* **19**, 5–8 (1976).
153. Kiya, M., Ishikawa, H. & Sakamoto, H. Near-wake instabilities and vortex structures of three-dimensional bluff bodies: a review. *Journal of Wind Engineering and Industrial Aerodynamics* **89**. Bluff Body Aerodynamics and Applications, 1219–1232 (2001).



154. Marenduzzo, D., Orlandini, E., Cates, M. E. & Yeomans, J. M. Steady-state hydrodynamic instabilities of active liquid crystals: Hybrid lattice Boltzmann simulations. *Phys. Rev. E - Stat. Nonlinear, Soft Matter Phys.* **76**, 1–18 (2007).
155. Segré, G. & Silberberg, A. Radial Particle Displacements in Poiseuille Flow of Suspensions. *Nature* **189**, 209–210 (1961).
156. Kilimnik, A., Mao, W. & Alexeev, A. Inertial migration of deformable capsules in channel flow. *Phys. Fluids* **23**, 123302 (2011).
157. Lashgari, I., Ardekani, M., Banerjee, I., Russom, A. & brandt, L. Inertial migration of spherical and oblate particles in straight ducts. *J. Fluid Mech.* **819**, 540–561 (2017).
158. Ho, B. P. & Leal, L. G. Inertial migration of rigid spheres in two-dimensional unidirectional flows. *J. Fluid Mech.* **65**, 365–400 (1974).
159. Schonberg, J. A. & Hinch, E. J. Inertial migration of a sphere in Poiseuille flow. *J. Fluid Mech.* **203**, 517–524 (1989).
160. Anderson, T., Mema, E., Kondic, L. & Cummings, L. Transitions in Poiseuille flow of nematic liquid crystal. *Int. J. Non-Linear Mech.* **75**, 15–21. ISSN: 0020-7462 (2015).
161. Čopar, S., Kos, Ž., Emeršič, T. & Tkalec, U. Microfluidic control over topological states in channel-confined nematic flows. *Nat. Commun.* **11**, 59 (2020).
162. Segré, G. & Silberberg, A. Behaviour of macroscopic rigid spheres in Poiseuille flow: Part 2. Experimental results and interpretation. *J. Fluid Mech.* **14**, 136–157 (1962).
163. Ganatos, P., Pfeffer, R. & Weinbaum, S. A strong interaction theory for the creeping motion of a sphere between plane parallel boundaries .2. Parallel motion. *Journal of Fluid Mechanics* **99**, 755–783 (1980).
164. Staben, M. E., Zinchenko, A. Z. & Davis, R. H. Motion of a particle between two parallel plane walls in low-reynolds-number Poiseuille Flow. *Phys. Fluids* **15**, 1711–1733 (2003).

165. Nikoubashman, A., Likos, C. N. & Kahl, G. Computer simulations of colloidal particles under flow in microfluidic channels. *Soft Matter* **9**, 2603–2613 (2013).
166. Staben, M. E. & Davis, R. H. Particle transport in Poiseuille flow in narrow channels. en. *Int. J. Multiph. Flow* **31**, 529–547. (2023) (2005).
167. Stieger, T., Schoen, M. & Mazza, M. G. Effects of flow on topological defects in a nematic liquid crystal near a colloid. *J. Chem. Phys.* **140**, 054905 (2014).
168. Stieger, T., Püschel-Schlotthauer, S., Schoen, M. & Mazza, M. G. Flow-induced deformation of closed disclination lines near a spherical colloid immersed in a nematic host phase. *Molecular Physics* **114**, 259–275 (2016).
169. Senyuk, B., Meng, C. & Smalyukh, I. I. Design and preparation of nematic colloidal particles. *Langmuir* **38**, 9099–9118 (2022).
170. Bender, C. M. & Orszag, S. A. *Advanced mathematical methods for scientists and Engineers* (McGraw-Hill, 1978).
171. Qian, Y. H. & Orszag, S. A. Lattice BGK Models for the Navier-Stokes Equation: Nonlinear Deviation in Compressible Regimes. *Europhysics Letters* **21**, 255. <https://dx.doi.org/10.1209/0295-5075/21/3/001> (1993).
172. Geller, S., Tölke, J. & Krafczyk, M. *Lattice-Boltzmann Method on Quadtree-Type Grids for Fluid-Structure Interaction* in *Fluid-Structure Interaction* (eds Bungartz, H.-J. & Schäfer, M.) (Springer Berlin Heidelberg, Berlin, Heidelberg, 2006), 270–293.
173. Latt, J., Chopard, B., Malaspinas, O., Deville, M. & Michler, A. Straight velocity boundaries in the lattice Boltzmann method. *Phys. Rev. E* **77**, 056703 (5 2008).
174. Grad, H. Note on N-dimensional hermite polynomials. *Communications on Pure and Applied Mathematics* **2**, 325–330 (1949).
175. Guo, Z., Zheng, C., Shi, B. & Zhao, T. S. Thermal lattice Boltzmann equation for low Mach number flows: Decoupling model. *Phys. Rev. E* **75**, 036704 (3 2007).